

Nanofluidic technology for chemical neurostimulation

Dissertation

der Mathematisch-Naturwissenschaftlichen Fakultät
der Eberhard Karls Universität Tübingen
zur Erlangung des Grades eines
Doktors der Naturwissenschaften
(Dr. rer. nat.)

vorgelegt von
Peter D. Jones
aus London, Kanada

Tübingen
2017

Gedruckt mit Genehmigung der Mathematisch-Naturwissenschaftlichen Fakultät
der Eberhard Karls Universität Tübingen.

Tag der mündlichen Qualifikation:

19. Juli 2017

Dekan:

Prof. Dr. Wolfgang Rosenstiel

1. Berichterstatter

Prof. Dr. Dieter P. Kern

2. Berichterstatter

Dr. Martin Stelzle

Richard Feynman is well known among nanotechnologists for his 1959 talk: “There’s Plenty of Room at the Bottom.” Physicists admire how he could unravel complex topics in his clear writings and lectures.

His discussions of the scientific method helped me to overcome my internal biases, to examine my own work with increased rigour, and to become a better scientist and engineer.

“The first principle is that you must not fool yourself
—and you are the easiest person to fool.”

— Richard Feynman

Die vorliegende Arbeit wurde in der Zeit von Januar 2012 bis Juni 2016 unter Betreuung von Dr. Martin Stelzle am Naturwissenschaftlichen und Medizinischen Institut an der Universität Tübingen und Prof. Dr. Dieter P. Kern an der Universität Tübingen angefertigt.

Finanziell wurde das Vorhaben von der Europäischen Kommission unter dem Förderkennzeichen 264872 (7th Framework Programme, Marie Curie Initial Training Network „NAMASEN“) und von der Volkswagen Stiftung unter der Förderinitiative „Experiment!“ unterstützt.

Summary

The goal of this work was to develop technology for local chemical stimulation of neurons. Recent years have seen impressive treatment of neurodegenerative diseases by electrical neuroprostheses, including restoration of vision by retinal implants. Despite their success, these prostheses interact by unnatural mechanisms of electrical neurostimulation, which cannot fully mimic biological specificity or resolution. Stimulation by artificial chemical signals could provide a more natural means of restoring neurological functions, but technology for precise, high-resolution chemical release remains primitive in comparison with microelectronics. Current micro- or nanofluidic technology cannot control chemical release with sufficient precision to imitate synaptic release.

This work has focused on two main topics. First, the investigation of hydrophobically gated nanopores has been pursued towards developing precise nanovalves for absolute, diffusion-free control of chemical release. Second, a platform for in vitro chemical stimulation of cells or tissues by chemical release from nanopores integrated with microfluidic control and microelectrodes has been developed. In support of these topics, issues of nanofluidic chemical control and future chemical neuroprostheses have been investigated.

Hydrophobically gated nanopores may provide ideal control for high-resolution chemical release, but previous reports in artificial nanopores suffered from limited reversibility and reproducibility. These challenges were compounded by limited understanding of the physical mechanisms governing the observed behaviour. Extensive literature review was carried out to understand the liquid–vapour behaviour in artificial hydrophobic nanopores. The contributing mechanisms are distinct from hydrophobic gating in biological nanopores with dimensions an order of magnitude smaller. Electrowetting – more specifically, electromechanical force on the liquid–vapour surface – was identified as the principal mechanism. Models of electrowetting in nanopores were developed, including for nanopores with integrated gate electrodes for individual control of nanopores in contact with a shared reservoir. Because reversibility of hydrophobic gating in large hydrophobic nanopores requires trapped bubbles, a novel mechanism was proposed to trap bubbles in circumferential cavities within nanopores. Hydrophobic gating behaviour was investigated by current–voltage recordings of silicon nitride (SiN_x) nanopores modified with monofunctional hydrophobic silanes and gold nanopores modified with hydrophobic thiols. Differences observed in SiN_x –silane and gold–thiol nanopores demonstrated the importance of material selection for precise, stable nanopore fabrication, and suggested that molecular effects contribute to electrowetting behaviour. Limited stability of thiol-coated gold prevented investigation of electrowetting by integrated electrodes. Through analysis of theoretical and experimental results, next experiments towards reversible hydrophobic gating were proposed.

A nanopore-based in vitro chemical stimulation platform was developed for biological experiments with localized chemical release. A nanopore/microelectrode array (NPMEA) was produced based on established microelectrode arrays (MEAs). MEAs are widely used for in vitro neuroscience research, and established systems for cell culture and tissue preparations can be transferred to the NPMEA. Although many microfluidic platforms for chemical stimulation of cells have been reported, none have reached submicrometre dimensions. Integrating nanofluidic structures introduced unique challenges, but also opened new possibilities for nanofluidic control of chemical release. The NPMEA integrated focused-ion-beam-milled nanopores by dry bonding with microfluidic channels produced by photolithography. The process was designed to ensure future compatibility with alternative nanopore designs, such as hydrophobically gated nanopores. The resulting NPMEA has 29 microelectrodes for electrophysiological recording and stimulation, and 30 nanopores individually addressed by microfluidic channels and electrodes. A robust microfluidic connector was produced to connect the 30 microfluidic channels, which surpassed the complexity of many microfluidic applications. The NPMEA was applied in first biological experiments towards proof of local nanopore-based chemical stimulation, but a positive demonstration has not yet been obtained.

This work presents concrete steps towards precise, high-resolution chemical stimulation of neurons. Challenges remain before hydrophobically gated nanopores may be achieved, and nanopore-based chemical release from the developed in vitro system must be verified with biological experiments. The path towards chemical neuroprostheses extends far into the future, but the continuation of this work will be moving in the right direction.

Zusammenfassung

Ziel dieser Arbeit war es, Technologien für die lokale chemische Stimulation von Neuronen zu entwickeln. In den letzten Jahren entstanden beeindruckende Behandlungsmöglichkeiten für neurodegenerative Krankheiten durch elektrische Neuroprothesen, einschließlich der Wiederherstellung des Sehvermögens durch Netzhautimplantate. Trotz ihres Erfolgs interagieren diese Prothesen durch den an sich unnatürlichen Mechanismus der elektrischen Neurostimulation, der Spezifität und Auflösung des biologischen Vorbilds nicht vollständig nachahmen kann. Die Stimulation durch chemische Signale appliziert durch künstliche Systeme könnte einen physiologischeren Weg zur Wiederherstellung neurologischer Funktionen eröffnen. Bisher allerdings sind die für eine präzise, hochauflösende chemische Freisetzung verfügbaren Technologien im Vergleich zur Mikroelektronik nicht hinreichend weit entwickelt. Die aktuell verfügbare Mikro- oder Nanofluidik-Technologie kann die Freisetzung chemischer Stoffe nicht mit ausreichender Genauigkeit steuern, um synaptische Transmitterfreisetzung angemessen zu imitieren.

Diese Arbeit konzentrierte sich auf zwei Hauptthemen. Zum einen wurden Untersuchungen zu hydrophob schaltbaren Nanoporen unternommen, um präzise Nanoventile für die leakage- und diffusionsfreie Kontrolle der Freisetzung chemischer Stoffe zu entwickeln. Zum anderen wurde eine Testplattform entwickelt, welche Nanoporen mit Mikrofluidik und Mikroelektroden integriert, um die chemische Stimulation von Zellen oder Geweben durch die Freisetzung chemischer Stoffe aus Nanoporen zu testen. Zusätzlich wurden Aspekte zur nanofluidischen, chemischen Steuerung und zu zukünftigen chemischen Neuroprothesen diskutiert.

Hydrophob geschaltete Nanoporen sind ideale Kandidaten für die Steuerung räumlich hochauflösender Freisetzung chemischer Stoffe, jedoch zeigten bisherige Berichte über künstliche Nanoporen deutliche Mängel hinsichtlich der Reversibilität und Reproduzierbarkeit des Schaltverhaltens. Dies ist auf das bislang begrenzte Verständnis der diesen Phänomenen zugrunde liegenden physikalischen Mechanismen zurückzuführen. Eine umfangreiche Literaturrecherche wurde durchgeführt, um das Flüssigkeit-Dampf-Verhalten in künstlichen, hydrophoben Nanoporen zu verstehen. Die dort auftretenden Mechanismen unterscheiden sich grundsätzlich von den Verhältnissen in biologischen Nanoporen, die zwar ebenfalls mittels hydrophobem Schalten funktionieren, jedoch um eine Größenordnung kleiner sind. Als Hauptmechanismus wurde die Elektrobenetzung (im Englischen „electrowetting“) – genauer gesagt die auf die Flüssigkeits-Dampf-Grenzfläche wirkende elektromechanische Kraft – identifiziert. Es wurden verschiedene Modelle der Elektrobenetzung in Nanoporen entwickelt, darunter eines für Nanoporen mit integrierten Gate-Elektroden zur individuellen Steuerung von Nanoporen in Kontakt mit einem gemeinsamen Reservoir. Da in großen hydrophoben Nanoporen das permanente Vorhandensein von Gasblasen notwendig ist, um die Reversibilität des hydrophoben Schaltens sicherzustellen, wurde ein neuer Mechanismus vorgeschlagen, bei dem solche Gasblasen in umlaufenden Hohlräumen der Nanopore gehalten werden. Das fluidische Schaltverhalten der hydrophoben Nanoporen wurde mit Hilfe von Strom-Spannungs-Messungen untersucht. Diese Nanoporen bestanden entweder aus Siliziumnitrid (SiN_x) modifiziert mit monofunktionellem Silan oder aus Gold modifiziert mit Thiol. Die in SiN_x -Silan- und Gold-Thiol-Nanoporen beobachteten Unterschiede unterstreichen die Bedeutung der Materialauswahl für die präzise, stabile Nanoporen-Herstellung und zeigten, dass molekulare Effekte das Elektrobenetzungsverhalten beeinflussen. Die begrenzte Beständigkeit des Thiol-beschichteten Goldes verhinderte weitere Untersuchungen an Nanoporen mit integrierten Elektroden. Auf der Grundlage der theoretischen und experimentellen Ergebnisse werden weiterführende Experimente zum reversiblen, hydrophoben Schalten vorgeschlagen.

Eine Nanoporen-basierte in vitro Stimulationsplattform wurde entwickelt, um Zellen und Gewebe mittels lokaler Freisetzung chemischer Stoffe zu stimulieren. Ein Nanoporen/Mikroelektroden-Array (NPMEA) wurde basierend auf etablierten Mikroelektroden-Arrays (MEAs) hergestellt. MEAs sind weit verbreitet in der neurowissenschaftlichen in vitro Forschung und etablierte Kultivierungsverfahren für

Zellen und Gewebepräparate können auf NP-MEAs übertragen werden. Obwohl bereits viele mikrofluidische Plattformen für die chemische Stimulation von Zellen beschrieben wurden, wies keines davon Dimensionen kleiner als 1 μm auf. Die Integration nanofluidischer Strukturen stellt eine sehr hohe technologische Herausforderung dar, eröffnet aber auch neue Möglichkeiten der nanofluidischen Kontrolle der Freisetzung chemischer Stoffe. Das NPMEA integriert mittels fokussiertem Ionenstrahl erzeugte Nanoporen mit photolithographisch hergestellten mikrofluidischen Kanälen mit Hilfe eines Trockenverklebungsverfahrens. Dieses Verfahren wurde entwickelt, um die zukünftige Kompatibilität der Technologie mit alternativen Nanoporen – zum Beispiel mit hydrophobem Schalten – sicherzustellen. Das resultierende NPMEA hat 29 Mikroelektroden zur elektrophysiologischen Aufzeichnung und Stimulation und 30 Nanoporen, die einzeln durch mikrofluidische Kanäle und Elektroden adressiert werden. Ein robuster mikrofluidischer Aufbau wurde entwickelt, der es ermöglicht, simultan 30 mikrofluidischen Kanäle mit der Peripherie zu verbinden, was hinsichtlich Komplexität viele bisherige mikrofluidische Anwendungen deutlich übertrifft. Das NPMEA wurde in ersten biologischen Experimenten zur lokalen Nanoporen-basierten chemischen Stimulation eingesetzt, ein positiver Nachweis wurde jedoch noch nicht erzielt.

Diese Arbeit verbindet eine systematische Analyse der physikalischen Grundlagen schaltbarer nanofluidischer Poren mit konkreten technologischen Schritten für ihre Realisierung, mit dem Ziel der präzisen, hochauflösenden und chemischen Stimulation von Neuronen. Allerdings bleibt die Herausforderung, zuverlässig und reproduzierbar hydrophob geschalteter Nanoporen bestehen und die Nanoporen-basierte Freisetzung chemischer Stoffe aus dem entwickelten *in vitro* System muss mit weiteren biologischen Experimenten überprüft werden. Der Weg zu chemischen Neuroprothesen reicht sicherlich noch weit in die Zukunft, diese Arbeit hat jedoch wichtige Grundlagen dafür gelegt.

Acknowledgements

I would like to thank Dr. Martin Stelzle, for the opportunity to pursue this research, and for his support and our scientific discussions. I am also grateful to Prof. Dr. Dieter P. Kern for scientific discussions and his critical feedback of my work.

Thank you to everyone in the BioMEMS & Sensors group for providing a stimulating and supportive environment. I am especially grateful to Clemens Barthold, Dr. Meike Beer, Madeleine Fries, Kai Fuchsberger, Dr. Raiah Gottheil, Britta Hagemeyer, Steve Link, Heiko Kießling, Dr. Massimo Kubon, Dr. Ramona Samba, Dr. Julia Schütte, and Simon Werner. I would like to specifically thank Madeleine Fries for working with me to study gold–thiol nanopores, and Chirayu Gandhi for performing measurements of SiN_x nanopores.

My gratitude extends to the entire Microsystems & Nanotechnology group of Dr. Claus Burkhardt. I would especially like to thank Dr. Gerhard Heusel, Stefan Klaus, and Angelika Stumpf for support in the cleanroom; Manuel Martina and Sebastian Röhler for introducing me to lithography of SU-8 and dry film resists; and Dr. Birgit Schröppel for teaching me how to make and study nanopores.

I am grateful for the excellent multi- and interdisciplinary environment provided by the NMI. Developing the concepts and carrying out the work described in this dissertation were only possible with support from a wide spectrum of scientists, who were always available to help me learn and excited to discuss new ideas. I am especially grateful to Dr. Paolo Cesare, Prof. Dr. Elke Guenther, Dr. Udo Kraushaar, Dr. Alfred Stett, and Dr. Günther Zeck. I am grateful to the Neurophysics group of Dr. Günther Zeck and the Molecular Neurobiology group of Prof. Dr. Hansjürgen Volkmer for supporting biological experiments. I would specifically like to thank Florian Jetter and Dr. Henrike Stutzki for preparing retinas and Christine Dürr for preparing cortical neurons. I would also like to thank Anita Niedworok for performing confocal microscopy.

I would like to thank Dr. Ronny Löffler at the LISA+ in Tübingen for assistance with metal evaporation. I am grateful to Dr. Maria Eugenia Toimil Molares and Prof. Dr. Christina Trautmann at the GSI for providing track-etched membranes for my first experiments with nanopores.

I am grateful for the support of the European Commission in their funding of the NAMASEN project. I would like to thank all partners for everything that I learned in our project meetings, and especially Prof. Michele Giugliano for his scientific leadership. I am very grateful for the support of the Volkswagen Foundation, which allowed me to arrive at the submission of this dissertation.

Finally, thank you to my friends and family for your support! To my parents, Marlene and Bruce, and to Dylan and Mel: I'm grateful that family is only a phone call (or plane ride) away. Thank you to everyone who flew across the ocean to visit me; to those who remain close despite the long distance; and to new friends in Germany.

To Alex: thank you for your support and your patience always, and your pressure when I needed it.

Abbreviations

Materials

ADEX	a dry film photoresist
APDMES	3-aminopropyldimethylethoxysilane
APTMS	3-aminopropyltrimethoxysilane
Ag/AgCl	silver–silver chloride, used for reference electrodes
CAM	calcein AM; calcein acetoxymethyl ester
CNT	carbon nanotube
COC	cyclic olefin copolymer
DRAQ5	a far-red cell-permeant DNA stain
FEP	fluorinated ethylene propylene
H ₂ O ₂	hydrogen peroxide
H ₂ SO ₄	sulphuric acid
ODMCS	octyldimethylchlorosilane
OSTE	off-stoichiometry thiol-ene
OSTE+	off-stoichiometry thiol-ene-epoxy
PBS	phosphate-buffered saline
PEDOT	poly(3,4-ethylenedioxythiophene)
PEDOT-CNT	PEDOT-CNT composite
PET	polyethylene terephthalate
PFDT	1H,1H,2H,2H-perfluorodecanethiol
PFOTCS	1H,1H,2H,2H-perfluorooctyltrichlorosilane
PDMS	polydimethylsiloxane
SiN _x	silicon nitride (low stress, non-stoichiometric)
SU-8	an epoxy photoresist
TiN	titanium nitride

Devices

MEA	microelectrode array
NPA	nanopore array
NPMEA	nanopore/microelectrode array

Tools

FIB	focused ion beam
SEM	scanning electron microscope
TEM	transmission electron microscope

Miscellaneous

EWOD	electrowetting-on-dielectric
SAM	self-assembled monolayer
DBS	deep brain stimulation
UV	ultraviolet

Symbols

c	concentration [amount/volume]
C	specific capacitance [current-time/(voltage·area)]
$d, D_i, L, R_i, r, x, y, z$	spatial dimensions [distance]
D	diffusion constant [area/time]
F	Faraday constant [96 485 C mol ⁻¹]
G	conductance [current/voltage]
I	current
J	chemical flux [amount/(area·time)]
k_B	Boltzmann constant [1.381×10^{-23} J K ⁻¹]
N	amount
\dot{N}	molar flow rate [amount/time]
ΔP	pressure difference [pressure]
Q	volumetric flow rate [volume/time]
R	resistance [voltage/current]
R_H	hydraulic resistance [volume/(time·pressure)]
t	time
T	temperature
V	voltage
z	valence [dimensionless]
γ	surface energy or tension [energy/area or force/distance]
ϵ_0	electric constant [8.854×10^{-12} F m ⁻¹]
ϵ_r	relative permittivity [dimensionless]
η	dynamic viscosity [pressure·time]
θ	contact angle [degree]
λ	slip length [distance]
λ_D	Debye length [distance]
ρ	density [mass/volume]
σ	conductivity [current/(voltage·distance)]

Contents

Summary	v
Zusammenfassung	vii
Acknowledgements	ix
Abbreviations	xi
Symbols	xiii
1 Introduction	1
2 Background	3
2.1 Neurophysiology	3
2.2 Neurostimulation	6
2.2.1 Electrical stimulation	6
2.2.2 Chemical stimulation	7
2.2.3 Optical stimulation	9
2.3 Argument for neuroprostheses	12
2.4 Physics	12
2.4.1 Artificial nanopores	12
2.4.2 Fluid dynamics at small dimensions	14
2.4.3 Pressure-driven flow	15
2.4.4 Diffusion	16
2.4.5 Electrokinetic effects	17
2.4.6 Electrostatic gating in nanopores	18
2.4.7 Hydrophobic gating in nanopores	18
2.4.8 Liquid–vapour fluid dynamics	19
2.4.9 Contact angle	20
2.4.10 Electrowetting	20
3 Vision	25
4 Nanopores enable local, high-resolution chemical release	27
5 Nanovalves	33
5.1 Literature review	33
5.1.1 Previous experimental observations of hydrophobic gating	34
5.1.2 Biological hydrophobic gating is a separate phenomenon	35
5.1.3 Fully wet, hydrophobic nanopores remain wet	36
5.1.4 Trapped bubbles allow drying	37
5.2 New nanopore designs	37
5.3 Theories of hydrophobic gating in nanopores	42
5.3.1 Electromechanical models of nanopore electrowetting	43
5.3.2 Nanopore electrowetting by a transmembrane voltage across an insulating membrane	44
5.3.3 Nanopore electrowetting with gate electrodes	46
5.3.4 Nanopore electrowetting at high pressures	47
5.3.5 Bubble traps will enable dewetting of nanopores	48

5.3.6	Field emission	51
5.3.7	Related electrohydrodynamic effects	52
5.4	Experimental explorations	52
5.4.1	Characterization of nanopores	52
5.4.2	Nanopore fluidic cell	55
5.4.3	Hydrophobic nanopores stay dry	56
5.4.4	Some hydrophobic nanopores are spontaneously wet	60
5.4.5	Electrowetting of hydrophobic SiN _x nanopores	62
5.4.6	Electrowetting of hydrophobic gold–thiol nanopores	73
5.5	Conclusions and outlook	82
6	Nanopore arrays for chemical stimulation	85
6.1	Design constraints with commercial MEAs and SiN _x membranes	87
6.2	Development of thin film microfluidic networks	87
6.2.1	Off-stoichiometry thiol-ene-epoxy	90
6.2.2	SU-8 and ADEX film	92
6.3	Bonding nanopore arrays to microfluidic networks	96
6.3.1	Adhesive bonding	97
6.3.2	Dry bonding	98
6.4	How to connect tubes	102
6.5	Microfluidic control of chemical release from nanopores	106
6.5.1	Electrical characterization of nanopore array functionality	109
6.6	Towards stimulation of cells and tissues	110
6.6.1	Cortical neurons	111
6.6.2	Retinas	111
6.7	Summary	117
7	Outlook	119
7.1	Current results	119
7.2	Next steps towards hydrophobic gating in nanopores	120
7.3	Next steps towards local chemical stimulation of cells	121
7.4	Future challenges	122
7.4.1	Materials for nanopores	122
7.4.2	Individual control of large numbers of nanopores	122
7.4.3	Chemical elimination	122
7.4.4	In vivo chemical neurostimulation technology	122
7.4.5	The structural component of synapses	123
7.5	Other applications	123
8	Methods	125
8.1	Nanopore fabrication	125
8.1.1	Nanopore membranes	125
8.1.2	Metal deposition	125
8.1.3	Nanopore milling	125
8.1.4	Nanopore cleaning	125
8.2	Thiol modification	126
8.3	Hydrophobic silane modification of nanopores	126
8.4	Non-sticking coating for soft lithography	126
8.5	Photolithographic microfluidic fabrication	127
8.6	Amine modification of silicon nitride for bonding	127
8.7	PDMS soft lithography	127
8.8	CNC milling	128
8.9	Electrochemistry	128
8.10	Nanopore measurements	128
8.11	Fluorescence microscopy	129

8.12 Biological experiments	129
8.13 Data analysis, graphing, and document preparation	129
Bibliography	I
About the author	XV

List of Figures

2.1	Signal propagation in neurons	4
2.2	Structure of a photoreceptor terminal	5
2.3	Comparison of microfluidic chemical stimulation techniques	10
2.4	Schematic of nanopore measurements	13
2.5	Young–Laplace equation	19
2.6	Behaviour of water in narrow capillaries	20
2.7	Electrowetting	21
2.8	Failure of the electrochemical model of electrowetting	22
4.1	Schematic of chemical release from a nanopore	27
4.2	Chemical release rates through a single nanopore	29
4.3	Spread of a chemical signal released from a nanopore	30
4.4	Release and spread of chemical signals by diffusion	31
4.5	Rise and decay of vesicular chemical release	32
4.6	Chemical release from an array of nanopores	32
5.1	Nanopore configurations	38
5.2	Nanopore diameters obtained by FIB milling	39
5.3	Nanopore Design 1	41
5.4	Nanopore Design 2	41
5.5	Nanopore Design 3	42
5.6	Nanopore electrowetting combines planar electrowetting with the Young–Laplace equation	43
5.7	Electromechanical model of electrowetting in nanopores	44
5.8	Transmembrane contact-angle-driven electrowetting in a hydrophobic nanopore	45
5.9	Transmembrane contact-angle-driven electrowetting voltages	45
5.10	Gate electrode contact-angle-driven electrowetting in a hydrophobic nanopore	46
5.11	Gate electrode contact-angle-driven nanopore electrowetting, under pressure	47
5.12	Predicted electrowetting gate voltages for gold–thiol nanopores at increased pressures	48
5.13	Geometry of the bubble trap in the nanopore wall	49
5.14	Predicted contact-angle-driven electrowetting conditions for a nanopore with a bubble trap	50
5.15	Schematic of nanopore measurements	53
5.16	Voltage scan of a hydrophilic nanopore	54
5.17	Impedance spectroscopy of a hydrophilic nanopore	54
5.18	Illustrations of bubbles in hydrophobic nanopores	55
5.19	Nanopore fluidic cell	57
5.20	Nanopore fluidic cell validation	58
5.21	Filling of the fluidic cell can trap bubbles	58
5.22	Impedance spectra can reveal bubble in the fluidic cell	59
5.23	Electrical measurements of a hydrophobically blocked SiN _x –silane nanopore	59
5.24	Electrical measurements of a hydrophobically blocked gold–thiol nanopore	60
5.25	An array of twenty-five nanopores, most of which were dry after modification with PFDT	61
5.26	An array of twenty-five nanopores, half of which were dry after modification with PFDT	62
5.27	SEM of SiN _x nanopores	64
5.28	Electrowetting of a hydrophobic nanopore, SiN _x -1	66
5.29	Electrowetting of a hydrophobic nanopore, SiN _x -2	67
5.30	Electrowetting of a hydrophobic nanopore, SiN _x -3	68
5.31	Electrowetting of a hydrophobic nanopore, SiN _x -4	69
5.32	Electrowetting of a hydrophobic nanopore, SiN _x -5	70

5.33	Examples of electrolyte or field emission currents in hydrophobic nanopores	71
5.34	Conformation of menisci within a nanopore will increase local electric fields	71
5.35	Fowler–Nordheim plot of nanopore measurements	73
5.36	Electrowetting of a gold–thiol nanopore array	75
5.37	Conductive membranes act as bipolar electrodes	76
5.38	Attempted gate-electrode–controlled electrowetting	78
5.39	Fabrication of nanopores with bubble traps	79
5.40	Electrowetting of a hydrophobic gold nanopore	80
5.41	Behaviour of a single hydrophobic nanopore with a bubble trap	81
5.42	Discrete conductance levels suggest metastable water channels	82
6.1	Comparison of nanopore arrays with microelectrode arrays	85
6.2	A commercial MEA	86
6.3	MEA in recording setup	87
6.4	Schematic of a nanopore addressed by a buried microfluidic channel on a MEA	88
6.5	Design of the NPMEA	89
6.6	Process for NPMEA fabrication with OSTE+	91
6.7	Testing of OSTE+	91
6.8	Failed OSTE+ fabrication	92
6.9	NPMEA fabrication process with SU-8 and ADEX	94
6.10	Microfluidics produced with SU-8 and ADEX	95
6.11	Reflow of ADEX into SU-8 channels	95
6.12	SEM of a nanopore array membrane	96
6.13	NPA bonding to microfluidics with liquid adhesive	98
6.14	Adhesive bonding failed after prolonged exposure to water	98
6.15	Chemistry of dry bonding	99
6.16	Dry bonding of nanopore arrays	100
6.17	Dry bonding results	101
6.18	SEM of NPA bonded on microfluidic channels	101
6.19	Dry bonding results with a fractured membrane	102
6.20	Dry bonding survived 16 days in an incubator	102
6.21	Silicone connectors bonded on the surface of the NPMEA	103
6.22	Dolomite-inspired tubing connector	104
6.23	Final connector design	105
6.24	Mould for silicone seals	105
6.25	Release from a nanopore observed by fluorescence microscopy	106
6.26	Provisional control setup	107
6.27	Filling and rinsing of a microfluidic channel	107
6.28	Hydraulic analysis of the NPMEA	108
6.29	SEM of nanopores from a NPMEA	109
6.30	Electrical characterization of nanopores in a NPMEA	110
6.31	Retina electrophysiology	112
6.32	Calcein staining of a retina on a NPMEA	113
6.33	Concept for local fluorescence staining by chemical release from a nanopore	114
6.34	Retina stained with CAM and DRAQ5	114
6.35	DRAQ5 and attempted local CAM staining with an electrode-free NPMEA	116
6.36	Electrical characterization before and after a retina experiment	117
7.1	A proposed experiment for chemical stimulation of the retina	121
8.1	Contact angle on PFDT-coated gold	126

List of Tables

2.1	Overview of microfluidic chemical stimulation techniques.	11
4.1	Parameters for chemical release calculations.	28
5.1	Designs for hydrophobic nanopores, ordered chronologically.	40
5.2	Summary of SiN _x nanopore results.	65
6.1	Hydraulic analysis of the microfluidic network.	108

1 Introduction

This work lays a foundation for high-resolution artificial chemical neurostimulation by nanofluidic technology. Neurotransmitter-based neuroprostheses require development of radically new technology to enable functional chemical stimulation. This goal is not simply drug delivery or neuromodulation, which may be achieved with spatial resolution of hundreds of micrometres or larger and time scales of minutes or longer. Rather, functional chemical stimulation refers to information delivery. The envisioned chemical release should imitate biological synapses, with transmission of chemical signals at sub-micrometre and millisecond scales.

The motivation for this work stems from a desire to artificially communicate with neurons with optimal precision and specificity. Electrical retinal neuroprostheses are now clinically approved in Europe and the United States to restore vision to the blind. Inherent limits of electrical neurostimulation have been revealed during the development of these neuroprostheses. Biological neurotransmission generates electrical activity in neurons in response to specific, local chemical signals. Artificial electrical stimulation can stimulate any nearby cellular structures, so it cannot achieve the resolution or specificity of neurotransmission. Electrical stimulation is analogous to attempting a conversation with another person by blowing a whistle. Yes, a message is transmitted and the person will react – but wouldn't it be better to speak to him in a language he understands?

First, a discussion of neurophysiology will introduce the brain, as the target of future chemical neuroprostheses. Natural neurotransmission will be presented, as this is the process that this work will attempt to mimic. A review of state-of-the-art artificial neurostimulation techniques will highlight the limitations of electrical stimulation as well as the primitive state of chemical stimulation methods. Necessary background for understanding the technical developments in this dissertation is also provided.

In chapter 3, an inspirational vision of future chemical neuroprostheses will be described. In consideration of current technological capabilities, a plausible model is proposed, which still requires development before its realization. This model would allow for *in vitro* validation of functional chemical stimulation. Critical steps towards this model were chosen for development and comprise the majority of this dissertation. The vision is based on nanofluidic elements which may enable the necessary degree of control. The properties of envisioned nanofluidic chemical release will be described theoretically in chapter 4.

Chapters 5 and 6 describe the experimental work towards chemical neurostimulation technology. First, investigations towards precisely controllable nanopores are presented in chapter 5. Electrically controlled hydrophobic gating was proposed as a mechanism to control chemical release. This chapter explores this mechanism through theory and experiments. The results can guide continued efforts towards achieving robust, reversible control of nanopores. Chapter 6 describes the integration of nanopores into an *in vitro* system for chemical neurostimulation. The system has been designed to allow integration of future nanopores as improved hydrophobic gating is developed. Preliminary proof-of-concept biological experiments are described, although a positive demonstration of local nanopore-based chemical stimulation of cells or tissues remains to be achieved.

Finally, the next steps required for continued development of nanopore-based chemical neurostimulation will be suggested. The progress made in this work will be discussed in the context of the goal of achieving functional chemical neurostimulation. Additional challenges will be uncovered as research in this area continues, some of which will be briefly discussed. Although work remains before the goals of functional chemical neurostimulation and neurotransmitter-based prostheses can be achieved, the presented results are concrete steps forward towards these goals. Continued development of the new technology presented here may enable fundamentally new techniques for artificial interfacing with neurons and biological systems.

2 Background

This chapter will review some fundamentals of neurophysiology to provide context for the following technical discussion. The neurophysiological discussion has three intentions: to provide a background for readers who may be unfamiliar with neurobiology, to describe the brain as a potential target for artificial chemical stimulation, and to describe the mechanisms of neurotransmissions as guidance for designing artificial chemical release. The discussion follows from Purves et al., which is an excellent resource for those unfamiliar with neurobiology [1].

The current state of neuromodulation technology will be discussed. The impressive results of current neuroprostheses will be presented, to highlight the critical differences which separate electrical neurostimulation from biological neurotransmission. State-of-the-art chemical stimulation methods will be discussed, demonstrating their limited capabilities. The development of advanced chemical-based neuroprostheses will be justified in light of alternatives which include therapies based on optogenetics or stem cell treatments.

Requirements of technology development will be presented, which will be expanded upon in the following chapters. The end of this section will provide background on the important physical phenomena involved in the technological developments in this thesis.

2.1 Neurophysiology

The human brain has a volume of 1.2l, containing around 10^{11} neurons and a similar number of non-neuronal cells [2]. Although extracellular fluid occupies some of this volume, a first order estimate suggests the average volume per neuron is 5–10 pl, which is roughly the volume of a 20–25 μm droplet.

Neurons comprise a body (the soma) and complex branched projections (neurites). These neurites may be dendrites, which receive and integrate signals, or axons, which transmit signals. Dendrites may be simple linear structures or complex structures with hundreds of branches. Neurons usually have one axon, which can also be highly branched. Mammalian axons have diameters of 0.2–20 μm but are typically 2 μm . Their lengths may be only a few micrometres or greater than 1 m, connecting the brain to distal areas of the body. Neurons form connections between each other at synapses. Each neuron receives input from an average of 10^4 synapses, which together determine the neuron's behaviour. Individual synapses are regions defined by close structural connections between two cell membranes. The synaptic cleft between neurons is 20–40 nm wide, and the width of the synapse is typically hundreds of nanometres. In the classical example of a synapse, the axon of the presynaptic neuron transmits a signal to a dendrite of the postsynaptic neuron. However, synapses can also project onto the soma, axons, or into the extracellular fluid. Communication at synapses depends on the rapid release of a neurotransmitter by the presynaptic neuron, recognition by receptors on the postsynaptic neuron, and removal of the neurotransmitter. Synapses may also allow diffusion of the neurotransmitter into the extracellular fluid, which can modulate activity at larger distances.

Communication in neurons relies on both electrical and chemical processes (Figure 2.1). Neurotransmission occurs when an action potential is generated in a presynaptic neuron. The action potential propagates along the axon by ion channel-mediated movement of ions across the cell membrane. When the action potential reaches an axon terminal, voltage-gated calcium channels allow calcium into the cell. The rise in calcium concentration causes synaptic vesicles containing neurotransmitter to fuse with the cell membrane and release their contents into the synaptic cleft. Diffusion across the narrow synaptic cleft occurs rapidly, and receptors on the membrane of the postsynaptic neuron recognize the presence of the released neurotransmitter. Depending on the specific neurotransmitters and receptors involved, the response of the postsynaptic neuron may be either to increase (excitation) or decrease (inhibition) its probability of firing a subsequent action potential. This entire process occurs in less than 1 ms. In

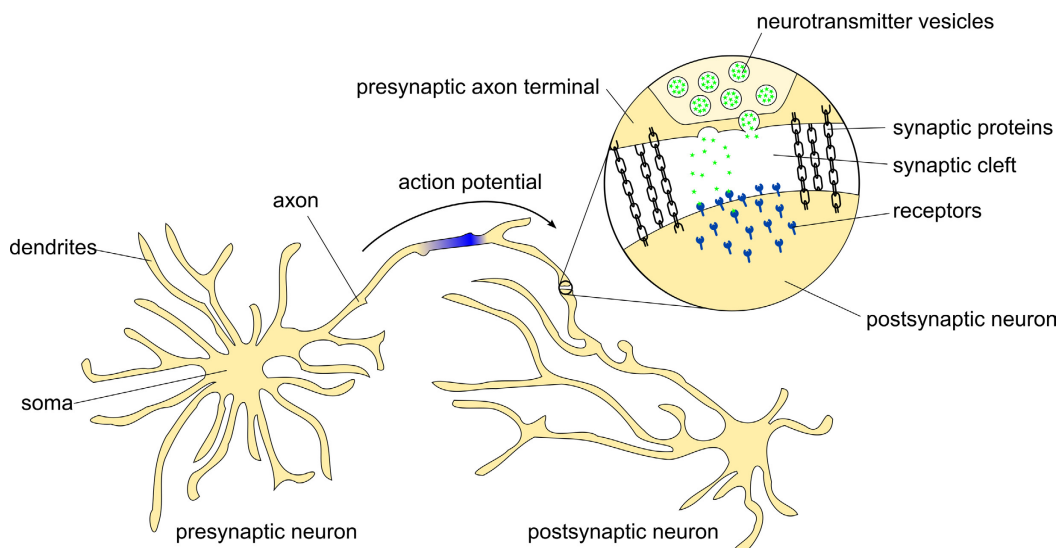


Figure 2.1 Signal propagation in neurons. Within neurons, information is integrated and transmitted as electrical signals such as action potentials. Between neurons, communication occurs by release of neurotransmitters at chemical synapses. In contrast to this simple example, real neurons form an average of 10^4 synapses.

most cases, a single synapse is insufficient to generate an action potential. Rather, firing of an action potential depends on integration of all of a neuron's inputs, which may include excitatory and inhibitory synapses. After neurotransmission, removal of neurotransmitter from the synaptic cleft occurs rapidly through reuptake by transporters, enzymatic degradation or other mechanisms.

After receptors recognize specific extracellular chemical signals, processing within a neuron occurs electrically. Neurons maintain electrical potentials across their membranes by control of simple ions (calcium, sodium, chloride) through ion channels and ion pumps. Control of the membrane potential enables integration of synaptic inputs and generation and propagation of action potentials.

In contrast, communication between neurons occurs by transmission of chemical signals¹ at synapses. Information propagation between neurons relies on exocytosis of neurotransmitters, producing localized extracellular chemical signals. More than 100 chemical neurotransmitters are known, which may have inhibitory or excitatory effects. The specific effects depend on the type and distribution of receptors on the postsynaptic neuron, so that the same neurotransmitter may cause both excitation and inhibition in different neurons. The most common neurotransmitters include acetylcholine, glutamate, γ -aminobutyric acid (GABA), and glycine. Although small molecule neurotransmitters are most commonly discussed, another class of neurotransmitters are neuropeptides, which are short peptides 3–36 amino acids in length. Before release, neurotransmitters are contained in individual ~ 50 nm vesicles in the presynaptic neuron. Individual vesicles are released during neurotransmission, giving a degree of quantization to this process. Single neurons can produce more than one type of neurotransmitter. Moreover, a single synapse can release vesicles containing different neurotransmitters. Vesicles containing different neurotransmitter can even be selectively released depending, for example, on firing rate. Further complications arise from the diversity of synaptic structures which may restrict neurotransmitters to within the synapse, or allow diffusion for activation of receptors outside of the synapse and volume transmission [3].

An upper limit on release rate can be determined from extreme examples. Vesicles in motor neurons contain 1000–40 000 molecules of acetylcholine [4]. Action potentials do not always cause vesicular release, and typically an action potential causes less than 0.5 vesicles to be released per active zone [5, 6]. Firing rates as high as 650 Hz have been observed [7], although this was driven by a depolarizing current and it is unlikely that vesicular release can match this rate. However, this provides a generous upper limit for release rates from an active zone. Synapses have areas of $1\text{--}1000\ \mu\text{m}^2$, and vesicle release occurs at active zones which are distributed with a density of $\sim 0.1\ \mu\text{m}^{-2}$ [8]. For an overestimated upper limit, assuming an active zone density of $1\ \mu\text{m}^{-2}$ gives a flux of $2 \times 10^{-17}\ \text{mol s}^{-1}\ \mu\text{m}^{-2}$. (A helpful comparison:

¹Neurons also communicate by electrical synapses, but these are a minority and will be neglected here.

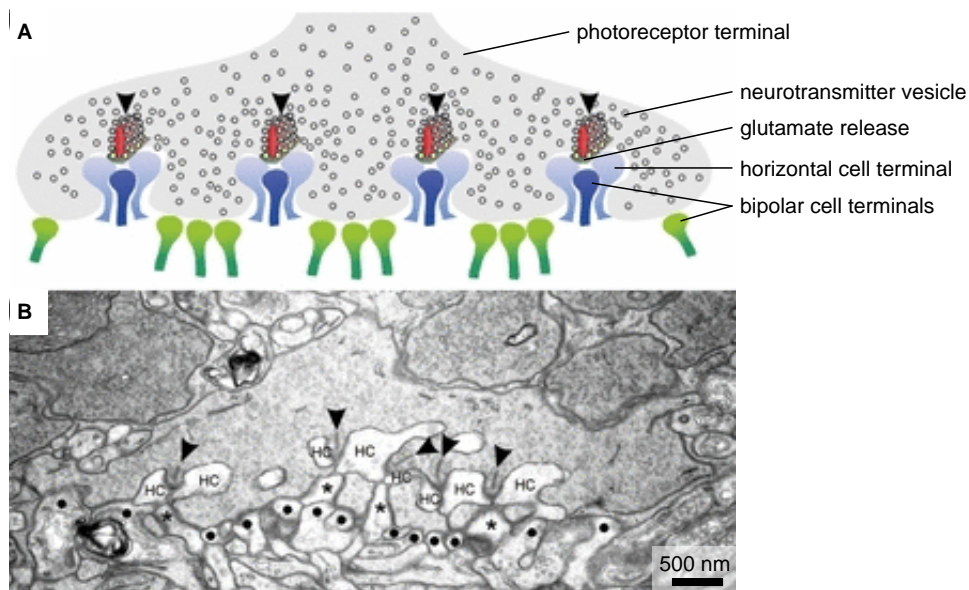


Figure 2.2 Structure of a photoreceptor terminal, adapted from [9]. This example illustrates the incredible complexity of biological synapses. Schematic illustration **A** and representative electron micrograph **B** of a cross-section of a photoreceptor cone terminal in a mouse retina. The presynaptic photoreceptor releases glutamate-containing vesicles at ribbon proteins (red, arrowheads). Postsynaptic neurons include bipolar cells (dark blue, asterisks; green, dots) and horizontal cells (light blue, HC), which form postsynaptic specializations at two locations, near (dark and light blue) and far (green) from the glutamate release sites. Adapted with permission from John Wiley & Sons, Inc. © 2011 H. Regus-Leidig, J. H. Brandstätter, *Acta Physiologica*, Scandinavian Physiological Society.

considering each molecule as an elementary charge, this would be a current of $2 \text{ pA } \mu\text{m}^{-2}$.) This rate would increase concentrations in the 20 nm synaptic cleft by $\sim 1 \text{ M s}^{-1}$.

Photoreceptor neurons provide an example of the potential complexity of synapses, as illustrated in Figure 2.2 [9]. This example is in stark contrast to the simple illustration of Figure 2.1. Photoreceptors enable perception of light intensity across more than ten orders of magnitude by continuous glutamate release, although the mechanisms which achieve this enormous dynamic range are not well understood. Glutamate release occurs at multiple locations in individual terminals, with each site releasing between 1 and 100 vesicles per second. For the terminal in Figure 2.2, this corresponds to a maximum release of $10^{-17} \text{ mol s}^{-1}$ over an area of $\sim 50 \mu\text{m}^2$, assuming 10^4 molecules per vesicle and a terminal diameter of $7 \mu\text{m}$. Parallel processing in the retina begins already at individual photoreceptor terminals, which have been observed to synapse onto at least 500 postsynaptic bipolar cell dendrites. Furthermore, three different synaptic specializations are known: two types of chemical synapse specializations with horizontal and bipolar cells, as well as electrical synapses to neighbouring photoreceptors. Glutamate release occurs directly at one of these chemical synapse specializations (blue cell terminals in Figure 2.2), while spill-over of glutamate is required to stimulate the second specialization (green bipolar cells). The activity of the downstream neurons reflects their proximity to glutamate release sites.

Neurodegenerative conditions such as retinitis pigmentosa cause degeneration of photoreceptors, destroying the synaptic connections with retinal circuitry described above. Neuroprostheses aim to replace functions lost to neurodegeneration. Artificial neurostimulation mechanisms will be discussed in section 2.2. It is clear that the current state of neuroprostheses does not approach the complexity observed in these biological systems. If the retinal circuitry is considered as an isolated system which receives a multitude of inputs from individual photoreceptor terminals, an ideal neuroprosthesis would replace these degenerated photoreceptors by providing chemical signals which mimic normal glutamate release. The exclusive use of electrical stimulation is far away from providing natural input to these cells.

2.2 Neurostimulation

Neuroprostheses have been used clinically since the 1980s. These fit within a broader category of active implantable biomedical devices, which includes the artificial cardiac pacemaker. The most widely used neuroprosthesis is the deep brain stimulator. As presented below, technology for interfacing with neuronal systems can be divided into three categories: electrical, optical, and chemical. Electrical interfacing is the most developed of these, with widespread neuroscience research driven by electrical recording of neuronal signals. Clinically approved neuroprostheses operate exclusively by electrical stimulation. Optical techniques may read out neuronal activity, as well as directly influence it through optogenetic or other techniques. Clinical use of optical techniques is being explored. Chemical application is well established as drug delivery, for example with intrathecal pumps, but has not been achieved as *functional* stimulation. Functional chemical stimulation could provide information to the nervous system, similar to the chemical communication between neurons, but this is currently prevented by a lack of suitable technology.

As early as 1985, it was recognized that electrical stimulation based on complex technology from the microelectronics industry was easier than chemical stimulation, but mechanisms at the cellular level were difficult to interpret [10]. In contrast, chemical stimulation produced well-defined effects at the cellular level, but applying chemical stimuli was difficult. This has not changed. Some efforts have been made towards artificial chemical stimulation, but technological limitations continue to constrain this technique.

An envisioned chemical neuroprosthesis would share many similarities with electrical devices. Although the fundamental technologies are different, the intended applications are the same and therefore the capabilities must be similar. The properties and capabilities of existing electrical neuroprostheses will be reviewed, and define the minimum requirements for a competitive chemical neuroprosthesis. A review of state-of-the-art chemical stimulation technologies reveals that enormous progress will be required before chemical stimulation can compete with electrical stimulation.

A vision for future chemical prostheses will be presented in chapter 3. Comparison with current fabrication techniques reveals what may be realistic in early prototypes of chemical prostheses, while comparison with biology will set goals for future prospects.

Optical stimulation methods will be briefly introduced, as they also have the potential to treat neurodegenerative diseases. Other modalities of neuromodulation, such as transcranial magnetic stimulation, cannot approach the capabilities of electrical, optical, or chemical stimulation and will not be discussed.

Related technology can record neural activity. Such devices are widely used in neuroscience research, and are being increasingly applied to clinical research and therapy. For example, recording of neural activity can help to identify target regions during insertion of deep brain stimulation electrodes [11]. Closed-loop stimulation with neurochemical feedback can improve therapy by monitoring responses to electrical stimulation [12]. However, this work focuses on a method for neurostimulation, and methods to record electrical or chemical neural activity will not be discussed in detail.

2.2.1 Electrical stimulation

Electrical neurostimulation has seen clinical application for more than two decades. The most well-known example is deep brain stimulation (DBS), most commonly used to treat Parkinson's disease and essential tremor, and more recently being applied to other neurological disorders including obsessive-compulsive disorder, chronic pain, depression, and Tourette syndrome [13]. Treatment of systemic neurodegenerative conditions including dementia and Alzheimer's disease has also been reported [14]. This treatment involves insertion of one or more stimulating electrodes into a specific area of the brain. Applying pulses of electrical current relieves symptoms of the neurological disorder. These electrodes do not require advanced technology. They do not target specific neurons, but rather modulate activity in dysfunctional regions of the brain based on undefined mechanisms.

In recent years, high-resolution electrical stimulation devices have been approved to locally stimulate neurons with arrays of microelectrodes. Several retinal neuroprostheses have been developed to treat blindness due to retinitis pigmentosa [15, 16] and until now, two companies have devices approved for

clinical use. The Argus II from Second Sight (Sylmar, CA, USA) stimulates the retina epiretinally with an array of 60 electrodes, with an image acquired from an external glasses-mounted camera. The Alpha IMS prosthesis from Retinal Implant AG (Reutlingen, Germany) stimulates the retina subretinally with 1500 electrodes, and acquires the image directly on the device. An updated version, the Alpha AMS, has 1600 electrodes [17]. The implants from Retinal Implant AG are currently the most advanced neuroprosthesis, and most likely to successfully treat blindness [18]. Recently, touch restoration in humans by stimulation of the somatosensory cortex with microelectrode arrays was reported [19].

Despite the impressive success of these devices, two main challenges limit further refinement of devices based on electrical stimulation: resolution and specificity.

The Alpha IMS prosthetic has electrode spacing of $70\ \mu\text{m}$, corresponding to a density of $200\ \text{mm}^{-2}$ over an area of several square millimetres. In clinical studies the best visual acuity demonstrated until now is 0.037 (Snellen acuity of 20/546), corresponding to a visual angle of 0.45° or a spatial resolution of $126\ \mu\text{m}$ on the retina [20]. This is equivalent to centimetre resolution at an arm's length away. In comparison, the density of photoreceptor cells in healthy retinas is three orders of magnitude higher ($100\ 000\text{--}324\ 000\ \text{mm}^{-2}$) [21].

The obvious solution of increasing electrode density to improve visual acuity is not so straightforward. Certainly, fabrication of smaller electrodes is not a challenge with modern fabrication processes. However, the current electrode spacing was designed based on preclinical studies, which predicted that electrical stimulation from planar microelectrodes has a fundamental resolution limit of $50\text{--}100\ \mu\text{m}$ [22]. This study examined the response of chicken retina to stimulation from planar microelectrodes, and found that higher resolution stimulation is prevented by spread of the applied electric field as well as the inherent structure and projections of neurons.

It is possible that more complex electrode arrangements or three-dimensional electrodes may improve upon the limits of current neuroprostheses [23, 24]. Patch clamp with micropipettes is able to stimulate single neurons, but is invasive and leads to cell death. Microfabricated electrodes which can enable large-scale integration of similar single-cell interfacing could provide a solution [25, 26].

The second challenge is specificity. Again, using the retina as an example [27], there are 5 types of neurons, each with several subtypes. These neurons use a variety of neurotransmitters, which have excitatory as well as inhibitory effects. Glutamate is the primary excitatory retinal neurotransmitter, while glycine and GABA are the main inhibitory ones. Several additional neurotransmitters are also used, including serotonin, dopamine, acetylcholine, and substance P. Moreover, individual neurotransmitters can activate multiple receptor types with different effects. Neurotransmission depends on the presence of these receptors, which are localized to specific structures of neurons.

In contrast, electrical stimulation is exclusively excitatory and can activate all neurons within a target region. Current injected into tissue by electrodes produces electric fields, which depolarize cell membranes without biological specificity. Some stimulation protocols have been studied which can provide some selectivity by varying parameters of the electrical stimulation [28, 29], but this does not approach the complexity which exists in normal neuronal communication. Other works have examined different electrode materials for improved stimulation [30].

Although it is common to treat neuronal communication as analogous to transmission of electrical signals, this is in fact an oversimplification. As discussed in section 2.1, signal propagation *within* neurons is an electrical phenomenon controlled by electrochemical potential established across the cell membrane. However, the communication between neurons, or between a neuron and the extracellular environment – the type of communication achieved by neuroprostheses – depends overwhelmingly on chemical signals. Although electrical stimulation can clearly affect neural activity, it cannot match the sensitivity of biological neurotransmission.

2.2.2 Chemical stimulation

The chemical basis of neurotransmission has inspired research into artificial chemical communication with neurons. The technological and biological aspects of a neurotransmitter-based retinal prostheses have been reviewed [27]. Many lessons can be learned with the current state of technology. Pipette-based experiments support the idea that artificial glutamate release could restore vision in retinal prostheses. Finlayson and Iezzi reported that “neurotransmitter-based retinal prostheses may more

closely mimic natural visual stimulation” [31]. Microfluidic devices have been proposed to achieve neurotransmitter-based neuroprostheses [32, 33]. Inayat et al. concluded that “it is feasible to achieve a neurotransmitter-based epiretinal prosthesis that might be developed using advanced microfabrication and microfluidics technology.” Rountree et al. concluded that “the concept of neurotransmitter-based subretinal stimulation [is] a feasible and potentially more effective alternative to electrical stimulation.” This work argues that nanofluidic technology will be required [34]. Chapter 3 presents a vision for such a prosthesis.

Technology for high-resolution chemical stimulation of cells remains primitive. While neuroelectronic devices have benefited from the translation of knowledge and expertise from the microelectronics industry, advanced technology which can manipulate chemical transport at the nanometre- or micrometre-scale is rare. Investigation of chemical signalling at the level of single cells was first enabled by the development of micropipettes [35]. The techniques of microiontophoresis and pressure ejection continue to rely on such pipettes [36]. More advanced techniques are summarized in Table 2.1 and Figure 2.3.

It is important to differentiate between drug delivery and functional chemical stimulation. Drug delivery is any process by which a pharmacological agent may be transported to cells upon which it causes a desired therapeutic effect. Local drug delivery can reduce systemic doses and associated side effects, and drug delivery devices can also bypass the blood–brain barrier to reach the nervous system and brain. Microfluidic devices have enabled investigation of many intercellular chemical signalling methods at the scale of subpopulations of cells [37]. Functional chemical stimulation, in contrast, refers to chemical release which is designed to convey information, mimicking neurotransmission between cells. Functional chemical stimulation would require control of chemical release at spatial dimensions relevant to the targeted biological structures. A fundamental requirement is absolute control of chemical release, capable of preventing any leakage by diffusion. Furthermore, useful stimulation from large numbers of chemical release sites will require parallelization.

Mimicking synaptic chemical release is possible with microiontophoresis, which can counteract diffusion by applying a retaining current. Precise positioning of a micropipette under microscopic observation can achieve high-resolution stimulation of single synapses [38]. The capabilities of microiontophoresis are discussed in more detail in section 2.4.5. Developments have enabled use in freely behaving animals [39] and some degree of automation in combination with scanning ion conductance microscopy systems [40]. A complex system with eight independent micropipettes has been demonstrated for electrical recording although not for chemical stimulation [41]. However, miniaturization or integration in a microfabricated system requires new technology.

Implantable drug delivery pumps have been clinically used for at least thirty years [42, 43] and are also available for use in animal models [44]. These devices slowly release a drug through a catheter to a targeted area. For example, the SynchroMed II (Medtronic Inc., Minneapolis, MN, USA) releases baclofen into the intrathecal volume of the spine [45]. This device uses pressures of up to 275 kPa [46] to continuously release controlled volumes of a drug, and can be refilled by injection through a septum.

Conceptually similar devices have been reported with improvements in performance, multiple local release sites, or design for specific applications. Microfluidic channels can be integrated with *in vivo* neural probes for simultaneous electrophysiological recording and chemical release. Channels have been buried in Si microelectrode arrays, and release of bicuculline through 10 μm openings caused elevated neural activity *in vivo* [47]. Channels in SU-8 with 50 μm openings have been produced to supplement Si microelectrode arrays, and response to glutamate and potassium release was measured *in vivo* [48]. Neural probes have also been produced with SU-8 as the base material, and included microfluidic channels with 40 μm outlets [49]. Altuna et al. reported expected responses to kainate and potassium *in vivo*. Localized *in vivo* drug delivery systems were reviewed in more detail by Sven Spieth in his dissertation [50].

Microfabricated devices for localized chemical release cannot yet mimic synaptic release, although several groups have developed devices intended for functional chemical stimulation (Table 2.1). These devices are better described as an extension of drug delivery devices to smaller dimensions. No technique to prevent constant leakage by diffusion has been reported which can sufficiently control high-resolution chemical release with the potential for *in vivo* use. Claims of “artificial synapses” must be critically examined when microfluidic release channels have dimensions larger than typical biological synapses by an order of magnitude or more, and no adequate means of controlling chemical release is

provided. Attempts to imitate synaptic release with microfabricated devices have focused on in vitro systems to avoid the complexity of in vivo experiments. Simple devices for local in vitro drug delivery have been produced from polydimethylsiloxane (PDMS) with channels of tens or hundreds of micrometres [51, 52]. A so-called “artificial synapse chip” reported by the Fishman group achieved release through 5 μm apertures and observed the response of PC12 cells to bradykinin stimulation by calcium imaging [53, 54]. No sufficient technique to prevent leakage by diffusion was reported, although the neurotoxicity of such leakage was recognized. The proposed solution of counteracting diffusion by constant withdrawal would not be practical for long-term use with many channels. Furthermore, the claim of mimicking synaptic release misrepresents the real potential for a device with micrometre-scale dimensions. Another group reported similar results with release from pores as small as 2 μm , and glutamate stimulation of cultured embryonic neurons was observed with calcium imaging [55, 56]. The Fishman group later reported functional neurostimulation from a single 25 μm aperture, with neurons stimulated by short glutamate pulses achieved by laminar control of the microfluidic channel [51]. Devices with 12 microfluidic channels and 20 μm apertures were used with brain slices to demonstrate local delivery of a fluorescent dye and stimulation of activity by potassium release [57]. Scott et al. also used their microfluidic channels as conductive paths to electrically record neural activity. The area of the 20 μm apertures was also reduced by bonding of membranes with 1 μm pores, typically with 5 pores per aperture. Mehenti et al. recognized that feasible functional stimulation devices would require developments to achieve physical gating with methods which can be scaled up and integrated. Probes with shuttered microfluidic channels prevented leakage. Shuttered openings 60 μm wide opened for pressure ejection, but no biological results were shown [58]. Sufficient miniaturization of this technique would not be possible. Stimulation by ejection of discrete droplets as small as 20 pl across an air gap addressed the challenge of diffusion and successfully stimulated TE671 cells with acetylcholine, and was demonstrated with 20 channels [59–61]. This technique was extended to picolitre dispensing [62], but the air gap prohibits its use in implantable devices. Diffusion has also been solved by solid barriers which can be electrochemically opened [63, 64]. The irreversibility of this gating makes it unsuitable for neurostimulation, but promising results for implantable drug delivery have been reported [65]. So-called U-tube channels have also achieved precise control of chemical release. Addressing release sites with U-tube channels allowed switching of the channel contents to turn release on and off. A design intended for in vivo neurostimulation was reported with switching speeds as fast as 5 s [66]. However, no biological results have been reported.

The above discussion focuses on microfluidic devices for chemical stimulation. Chemical transport by ionic transport through organic electronics has demonstrated neurotransmitter-based stimulation of cells [67–70]. Most recently, a device with six 20 μm sites capable of chemical release with 50 ms resolution was reported [71]. This technique can solve the problem of diffusion in microfluidic devices. However, release by driving ionic currents is limited to charged compounds, and may be complicated by transport of multiple ionic species.

This work is compared to these devices in Figure 2.3 and Table 2.1. None of the reported devices have demonstrated functional chemical neurostimulation at scales similar to single synapses. The results from this work are notable because of the improved number of channels beyond any previous works. More significantly, the ability to integrate chemical release sites with dimensions below 100 nm should enable new possibilities for high-resolution chemical stimulation.

2.2.3 Optical stimulation

Neurons may be optically stimulated by one of several methods. These methods require advanced optical systems to achieve high-resolution stimulation, and are limited by transmission of light in neural tissue. Focusing of light depends on optics, wavelengths of lights, and tissue properties. Implanted acute or chronic probes can have integrated optical fibres but localization of this light release has limitations [74]. In vitro devices have also been produced with arrays of light-emitting diodes for local light stimulation [75].

Optogenetic techniques have seen widespread adoption since the first report of a practical method in 2005 [76]. Optogenetics achieves remarkable results by genetic manipulation to express specific light-sensitive proteins in desired neurons. The prospects for restoring degenerated retinal function were

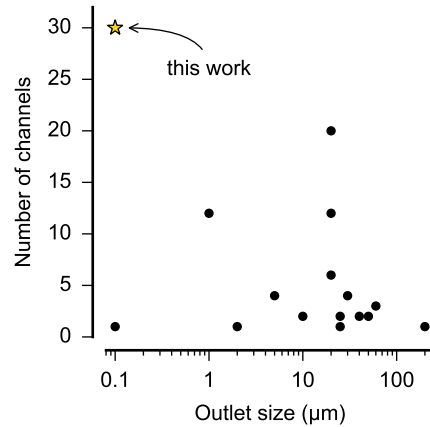


Figure 2.3 Comparison of microfluidic chemical stimulation techniques by outlet size and number of channels. Further details are in Table 2.1.

recently reviewed [77]. RetroSense Therapeutics (Ann Arbor, MI, USA) has begun a clinical trial for optogenetic treatment of retinitis pigmentosa [78]. Such techniques present unique ethical questions, as genetic modification of patients' cells is required [79].

Photochemical stimulation can function by uncaging [80] or photoisomerization [81]. Uncaging relies on chemicals which can cage specific neurotransmitters to disable their normal biological function. Photoisomerization similarly requires a compound which can exist in neuroactive and inactive states. These inactive compounds must be released broadly in the extracellular fluid. Exposure to specific wavelengths of light releases or activates the compounds, unlocking their normal biological activity. Photochemical techniques have been proposed as a solution to manage the leakage problem of microfluidic chemical release devices [27].

Table 2.1 Overview of microfluidic chemical stimulation techniques.

Method	Outlet size (μm)	Fluidic channels	Electrodes	Notes	References
Nanopipette	0.1	1	–	Not scalable	[38, 40]
U-tube channels	30	4	4	In vivo neural probe. Biological results not reported.	[66]
Micropores in SiN_x	5	4	–	In vitro	[53, 54]
Shuttered channels in Si	60	3	several	In vivo neural probe	[58]
Microapertures in PDMS	25	1	–	In vitro	[51]
Microaperture in Si	2	1	–	In vitro	[55, 56]
Droplet ejection across air gap	20	20	–	Not implantable	[59–61]
Channels in SU-8	50	2	–	Used with Si neural probes	[48]
Channels in Si neural probes (NeuroMedicator)	25	2	8	Wireless in vivo neural probe	[72, 73]
SU-8 neural probes	40	2	8	In vivo neural probe	[49]
Buried channels in Si neural probes	10	2	16	In vivo neural probe	[47]
PDMS microfluidic microelectrode array	20 (or 1)	12	12	In vitro brain slice experiments	[57]
Glass capillary in PDMS microfluidics	200	1	–	In vitro local drug delivery	[52]
Organic electronic ion pump	20	6	–	In vitro	[71]
Nanopores in SiN_x	<0.1	30	29	In vitro. No biological results.	This work

2.3 Argument for neuroprostheses

Development of technology for interaction with biological systems is challenging. Twenty years of development led to the approval of the Alpha IMS implant. Despite its complexity, its 1500 electrodes pale in comparison to the biological counterpart that they are intended to replace. Research into treatment by biological methods may provide better results. Optogenetic techniques may transfer degenerate functions to other neurons, for example by imbuing retinal ganglion cells with photosensitivity to replace degenerate photoreceptor cells. Cellular strategies are also promising, which could replace degenerate cells with new cells derived from stem cells [82]. It may be reasonable to expect that such biological methods will restore functions to a greater extent than artificial devices.

So, why should we continue developing neuroprostheses?

A central argument for prostheses is in fact the complexity of biological systems. Even a single disease such as retinitis pigmentosa has diverse causes and contributing factors, so that no single treatment will work for all patients [27]. Although retinal neuroprostheses do not restore normal vision, they can treat degeneration resulting from different causes. Another argument is that optogenetic or cellular treatments will cause permanent changes to patients' bodies [79]. In comparison, prostheses can be explanted if necessary.

In fact, both biological and technological methods to treat disorders of the brain should be pursued. It is likely that improved understanding of neurological disorders and their causes will lead to improved treatment or prevention in the future. Understanding of the brain is constantly improving, but much remains to be discovered. Many conditions could benefit from treatment with prostheses, and the rapid advances of nanotechnology suggest that development of artificial devices could provide feasible solutions in the near future.

2.4 Physics

This work involves fluidic structures with small structures at vastly different length scales. Nanopores, approximately cylindrical with diameters of 20–200 nm, and lengths of 100–1000 nm, have been produced and characterized towards the goal of fine control of chemical release. Microfluidic channels used to integrate networks of nanopores are rectangular with heights of 10 μm , widths of 10–50 μm , and lengths on the order of 30 mm. The microfluidic channels are integrated in-plane, while the nanopores are fabricated perpendicularly and allow chemical release from the microfluidic channels at single points.

This section will introduce concepts which are important for the fluid dynamics in these structures, to be referred to in later chapters. Because the relevant scales in this work vary by 10^6 , it is important to analyse the relevance and validity of various effects and their models. Several dimensionless numbers can estimate the importance of various physical phenomena. Nanofluidic transport mechanisms have been reviewed [83, 84] and the discussion here will focus on relevant effects for the application of chemical release. Concepts relevant for hydrophobic gating of nanopores will also be introduced.

Normally, the channels are filled with water with dissolved salts, usually in the form of phosphate-buffered saline (PBS) with total dissolved salts of 0.15 M. Chemical transport in the channels and nanopores relies on pressure-driven flow and diffusion, and electrokinetic effects will also be discussed.

2.4.1 Artificial nanopores

Solid-state nanopores are common systems for nanofluidic experiments. They are fabricated through thin membranes, in contrast to nanochannels which are fabricated as in-plane features. A vast literature has developed towards single molecule biosensing applications, for example towards protein analysis and DNA sequencing [85]. Biosensing nanopores have engineered dimensions corresponding to their target analytes, and surface properties to facilitate the passage of or interaction with analyte molecules. The setup for nanopore experiments consists of two liquid reservoirs connected solely by a single nanopore. In the simplest setup, illustrated in Figure 2.4, the membrane is an insulator with homogeneous surface properties extending through the nanopore. Measuring ionic currents through the nanopore driven by an applied voltage can elucidate its properties or enable analysis of single particles as they

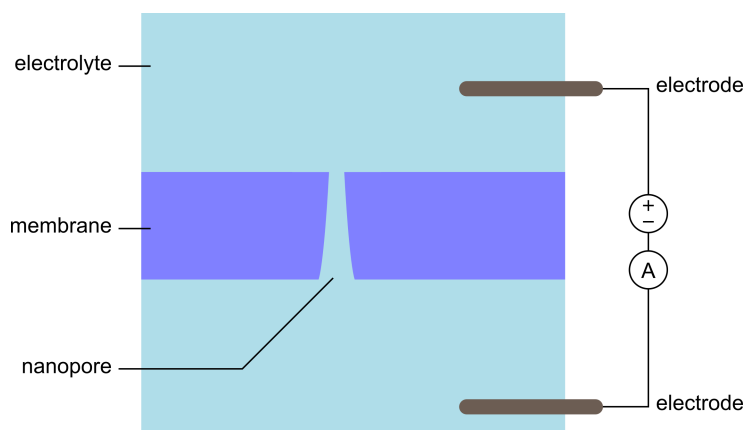


Figure 2.4 Schematic of nanopore measurements. The nanopore membrane is exposed on both sides to an electrolyte, which fills the nanopore. Electrodes are used to apply a voltage and measure the current response.

pass through the nanopore. More complex arrangements include electrodes for interrogation or control of the nanopore [86].

At the research scale, nanopores are fabricated by FIB or electron beam milling. Both are serial processes with limited reproducibility and low throughput. FIB milling most commonly uses a gallium beam, and can produce nanopores in membranes up to micrometres thick with minimum diameters of 20 nm. Helium FIB milling has also been used, producing nanopores below 4 nm [87]. Electron beam milling is limited to thinner membranes, which are beneficial for biosensing applications. Even for membranes only tens of nanometres thick, electron beam milling requires long times per nanopore [88]. Ion or electron beam sculpting can modify nanopores after milling to tune their dimensions, but further reduces throughput [89].

SiN_x is the most common material for nanopore membrane fabrication and is compatible with many microfabrication processes. Free-standing membranes are produced on silicon wafers. Deposition and patterning of low stress silicon-rich SiN_x is followed by etching of the Si to create free-standing SiN_x membranes. These membranes are commercially available with thicknesses of 30–1000 nm (Silson Ltd., Northampton, England).

Deposition of thin metal films by sputtering or evaporation has been done after nanopore fabrication [90]. Gold has been used with Ti or Cr adhesion layers. Atomic layer deposition can also shrink nanopores, and can produce defined dimensions by self-limiting processes [91]. Oxidation by piranha solution or oxygen plasma can clean the surfaces and prepare for chemical functionalization [85]. Modification with silanes on SiN_x or thiols on gold can add specific chemical properties, such as hydrophobic (alkyl-, perfluoroalkyl-) or other functionalities (e.g. amino-) [92, 93].

Interest in parallel methods has led to recent progress in reactive ion etching with best results producing 18 nm diameters in membranes with integrated electrode layers at the wafer scale [86]. Controlled dielectric breakdown has been demonstrated as a promising method for in situ formation of nanopores with nanometre-scale control of diameter in silicon nitride membranes thinner than 50 nm [94, 95], and also with integrated metal thin films [96]. This method requires high electric fields on the order of $10^3 \text{ V } \mu\text{m}^{-1}$.

Shrinking diameters of FIB-milled nanopores to below 20 nm by electrodeposition of platinum has been reported [97]. More recently, diameters below 10 nm were reported by gold electrodeposition [98]. However, the validity of these claimed dimensions is questionable. This diameter was extracted from ionic conductance based on a geometrical model. For the report of gold electrodeposition, important details including the length of the nanopore were not reported, the structure of deposited gold was not discussed, no electron microscopy was performed to validate these claims, and details of the electrodeposition such as voltage or electrolyte composition were withheld.

In this work, minimum diameters which can be feasibly produced will be assumed to be 20 nm. This sets a strict limit on the physical mechanisms which can be exploited in such nanopores. The following sections will introduce relevant physical concepts, which will be expanded upon in chapter 5. At

these minimum diameters, reproducibility of nanopore fabrication suffers, and many of the nanopores studied in this work were intentionally produced with larger dimensions.

2.4.2 Fluid dynamics at small dimensions

Fluid flow can exhibit different behaviours at smaller dimensions, due to the increased importance of forces or properties which may be negligible at larger dimensions. Estimates of expected behaviour can be derived from several dimensionless numbers.

Knudsen number

The Knudsen number estimates the validity of continuum physics by comparing the characteristic length scale of a system with the mean free path of particles [99]. In liquids, the lattice spacing can be used instead of the mean free path, and is defined for water as

$$\delta = \left(\frac{\text{molar volume}}{\text{Avogadro's number}} \right)^{1/3} = 0.3 \text{ nm.} \quad (2.1)$$

The Knudsen number then becomes

$$\text{Kn} = \frac{\delta}{L_s} \quad (2.2)$$

where L_s is the characteristic length scale of the system. Continuum physics such as the Navier–Stokes equations can be used when $\text{Kn} < 10^{-3}$ ($L_s > 300 \text{ nm}$). At smaller dimensions ($\text{Kn} < 10^{-1}$, $L_s > 3 \text{ nm}$), continuum models can be adjusted with a slip condition at solid interfaces. Beyond these limits ($\text{Kn} > 10^{-1}$, $L_s < 3 \text{ nm}$), continuum models break down and molecular dynamics must be considered [99].

Reynolds number

The Reynolds number relates to the stability of fluid flow, with low values indicating laminar flow. The Reynolds number is

$$\text{Re} = \frac{\text{inertial forces}}{\text{viscous forces}} = \frac{\rho v L}{\eta} \quad (2.3)$$

with density ρ and dynamic viscosity η , average velocity v , and characteristic length L . Pressure-driven laminar flow rates can be estimated by the Hagen–Poiseuille equation (2.8). The microfluidic channels and nanopores in this work exhibit $\text{Re} \ll 1$. Such low Reynolds numbers predict laminar flow.

Péclet number

The Péclet number describes the balance between chemical transport by advection and diffusion. It is defined as the product of the Reynolds number and Schmidt number, $\text{Sc} = \eta/\rho D$, so

$$\text{Pe} = \frac{\text{advection}}{\text{diffusion}} = \text{ReSc} = \frac{v D_H}{D} \quad (2.4)$$

with linear flow rate v , hydraulic diameter D_H , and diffusivity D . Solving for $\text{Pe} = 1$ can determine conditions at which advection and diffusion are balanced. As a function of pore diameter, the Péclet number for pressure driven flow is

$$\text{Pe} = \frac{4Q}{\pi D D_{\text{pore}}}. \quad (2.5)$$

From equation 2.8, the Péclet number can be calculated for pressure-driven flow through a nanopore (details in following section). For example, a 100 nm diameter, 500 nm long nanopore with a pressure difference of 100 kPa has $\text{Pe} = 7$, assuming $D = 10^{-9} \text{ m}^2 \text{ s}^{-1}$ and $\eta = 0.89 \text{ mPa}\cdot\text{s}$. With a diameter of 20 nm, Pe reduces to 0.06. These numbers indicate the unintuitive concept that advection and diffusion are competitive effects in nanopores.

Eötvös number

The Eötvös number describes the balance between surface tension and gravitational forces in a two-phase system, and is

$$Eo = \frac{\Delta\rho g L^2}{\gamma} \quad (2.6)$$

for the difference in density between phases $\Delta\rho$, gravitational acceleration g , characteristic length L , and surface tension γ . Surface tension dominates when $Eo < 1$. For air/water systems, this condition is met at $L < 2.7$ mm. In microfluidic channels and nanopores, surface tension strongly dominates.

Weber number

The Weber number describes the balance between surface tension and inertia in two-phase systems with flow, and is

$$We = \frac{\rho v^2 L}{\gamma} \quad (2.7)$$

with velocity v . Surface tension dominates when $We < 1$. With pressure-driven flow in a nanopore with a diameter of 100 nm and length of 500 nm, a pressure of 1 MPa may produce average velocities of 0.7 m s^{-1} , with a corresponding Weber number of 10^{-3} . Reaching $We > 1$ in micro- or nanofluidic systems requires extreme conditions.

2.4.3 Pressure-driven flow

The Hagen–Poiseuille equation describes the relationship between pressure and flow rate according to the hydrodynamic resistance of a channel. Requirements for validity of the equation include that flow remains laminar, and that channel length is longer than its diameter. The equation for flow rate Q in a cylindrical channel is

$$Q = \frac{\pi \Delta P D_{\text{channel}}^4}{128 \eta L} \quad (2.8)$$

with channel diameter D_{channel} and length L , dynamic viscosity η , and pressure difference ΔP .

The Hagen–Poiseuille equation can be expressed with the hydraulic resistance of channels of arbitrary cross-sections. This is analogous Ohm’s law for electrical circuits. The equation becomes

$$Q = \frac{\Delta P}{R_H} \quad (2.9)$$

for hydraulic resistance R_H , which for a cylindrical channel is $R_H = 128 \eta L / \pi D_{\text{channel}}^4$. This can be extended to allow calculations, for example, of rectangular channels. Although a closed analytical solution for the hydraulic resistance has not been found [100], an approximation for rectangular channels is

$$R_H \approx \frac{12 \eta L}{w h^3 (1 - 0.63 h/w)} \quad (2.10)$$

with width w and height h . This is accurate to better than 0.2% when $h < 0.5w$, and to about 13% for the worst case when $h \approx w$ [100].

Equation 2.9 can be extended for calculations of fluidic networks with multiple elements in parallel or series [101]. A major difference with respect to electrical circuits is the scaling of resistance with dimensions. Resistance of electrical resistors increases proportionally with a decrease in cross-sectional area. That is, a cylindrical resistor of diameter D has resistance proportional to D^{-2} . In comparison, hydraulic resistance scales with D^{-4} . This leads to dramatically reduced flow rates at smaller dimensions.

As an illustration, a cylindrical microfluidic channel with a diameter of $10 \mu\text{m}$ has the same cross-sectional area as an array of 10^4 channels with 100 nm diameter. However, the single larger channel will flow 10^4 times more fluid than the array of smaller channels, under the same pressure. Achieving the

same flow rate with the 100 nm channels would require 10^8 channels, with total area equivalent to a single 1 mm channel.

As mentioned in the above discussion of the Knudsen number, corrections to continuum models may be needed in channels with dimensions between 3 and 300 nm. The Hagen–Poiseuille equation can be modified to include a slip length λ [102]:

$$Q = \frac{\pi \Delta P D_{\text{channel}}^4}{128 \eta L} \left(1 + \frac{8\lambda}{D_{\text{channel}}} \right). \quad (2.11)$$

This can provide useful results, although the physical validity of this correction continues to be disputed. Hydrophilic surfaces exhibit no slip, but hydrophobic surfaces have slip lengths of ~ 20 nm [102]. Extreme examples include flow through carbon nanotubes, with measured flow rates three orders of magnitude higher than predicted by equation 2.8, corresponding to slip lengths of 140–1400 nm [103].

2.4.4 Diffusion

Diffusion is a ubiquitous effect by which dissolved species are transported in liquid systems, caused by the random movement of particles towards states of higher entropy. To achieve sensitive chemical release, diffusion can be a limiting factor. Elimination of diffusion requires interrupting the liquid path by an immiscible phase, such as a solid or vapour barrier. Diffusion cannot be eliminated as long as a continuous solvent pathway exists. Furthermore, it is an isotropic and unselective process, so that chemical species diffuse in all directions.

Extracellular propagation of chemical signals after release occurs primarily by diffusion. Fast and efficient chemical signal transmission necessitates a small distance between the chemical source and target. Larger distances lead to the dilution and exponentially increasing timescales, which has been referred to as the proximity effect [27].

Diffusion is described by Fick's first and second laws:

$$\begin{aligned} J_{\text{diff}} &= -D \nabla c \\ \frac{\partial c}{\partial t} &= D \nabla^2 c \end{aligned} \quad (2.12)$$

with diffusive flux J_{diff} depending on the diffusivity D (typically on the order of $10^{-9} \text{ m}^2 \text{ s}^{-1}$ for small molecules) and gradient of the concentration c . The second law describes the evolution of concentration with time, as a function of the second spatial derivative of concentration.

A useful tool for estimation of diffusion is the diffusion length,

$$L_{\text{diff}} = \sqrt{2nDt} \quad (2.13)$$

which approximates the distance over which a near-linear concentration gradient will be formed after an elapsed time t in an n -dimensional system. Conversely, the time to form a linear gradient over a determined distance can be determined. This is a critical factor for propagation of chemical signals, which relies on diffusion. Chemical signals can be transmitted over a micrometre within 1 ms, but longer distances require quadratic increases in time.

Analytical expressions have been derived for simple situations of diffusion [104]. After instantaneous release of a quantity N from a point source at $t = 0$, the concentration at any distance r and time $t > 0$ is

$$c(r, t) = \frac{N}{8(\pi Dt)^{3/2}} \exp \frac{-r^2}{4Dt}. \quad (2.14)$$

An analytical solution for constant diffusion from a point source is

$$c(r, t) = \frac{\dot{N}}{4\pi Dr} \operatorname{erfc} \left(\frac{r}{2\sqrt{Dt}} \right) \quad (2.15)$$

with a constant chemical release \dot{N} in mol s^{-1} at $t > 0$, and the complementary error function erfc . A limit exists for maximum concentration at any point:

$$\lim_{t \rightarrow \infty} c(r, t) = \frac{\dot{N}}{4\pi D r} \quad (2.16)$$

In biological applications, diffusion is affected by the tortuosity of cells and the limited fraction of the extracellular volume. Although specific nanometre- or micrometre-scale features must be considered for exact solutions, these properties can be approximated at larger scales by using a reduced diffusivity $D^* = D/\lambda^2$, with tortuosity λ , and including the volume fraction α [105]. With these additions, equation 2.15 becomes

$$c(r, t) = \frac{\dot{N}\lambda^2}{4\pi D r \alpha} \text{erfc}\left(\frac{r\lambda}{2\sqrt{Dt}}\right). \quad (2.17)$$

Combined electrochemical measurements with chemical injection at a point source in tissues can determine the tortuosity and extracellular volume fraction [105].

2.4.5 Electrokinetic effects

The electric double layer is an important characteristic of micro- and nanofluidic systems. Solid surfaces in contact with a liquid have fixed charges due to their chemical nature and the properties of the liquid such as pH. Counter ions accumulate near surfaces to balance these charges, creating a region with electrical potential and concentration deviations. This region is limited to a distance from the surface characterized by the Debye length,

$$\lambda_D = \sqrt{\frac{\varepsilon_r \varepsilon_0 k_B T}{\sum_{j=1}^N c_j z_j^2}} \quad (2.18)$$

with relative permittivity ε_r , electric constant ε_0 , Boltzmann constant k_B , temperature T , and N charged species with concentrations c_j and valence z_j [106]. A useful approximation is obtained at 25 °C for a monovalent electrolyte, for which the Debye length in nanometres is

$$\lambda_D = \frac{0.3 \text{ nm}}{\sqrt{c}}, \quad (2.19)$$

with the concentration c in M. A concentration of 1 M has a Debye length of 0.3 nm, while at 1 mM the length is 10 nm. In nanoscale channels, the electric double layer from opposing surfaces can overlap, leading to accumulation of counterions and depletion of coions.

Electrophoresis is the movement of charged particles in solution due to an applied electric field. This is used, for example, to control movement of ions, to separate ions based on their charge and mobility, or to deliver ions. In applications of chemical release, the terms iontophoresis and microiontophoresis describe the application of electric fields to drive ionic currents. Microiontophoresis delivers charged species by ejection of an ionic current from a micropipette. Quantification of delivery by iontophoresis is challenging, and is normally estimated by an empirically derived transport number which is specific for different ionic species, and depends on the properties and dimensions of the micropipette [107].

Electroosmosis is the effect by which an electric field acts on ions in the electric double layer, causing their electrophoretic movement while also dragging along solvent molecules. The movement of ions and solvent along the walls causes bulk movement of solvent across the entire channel. Slip length strongly affects electroosmosis [108].

Electrophoretic and electroosmotic effects can be controlled by selecting concentration and surface charges [109]. Detailed models and experimental validations of these electrokinetic effects have been demonstrated [106, 110]. Other electrofluidic effects including streaming potential and ion current rectification have been reviewed [84].

The challenges of electrokinetic transport can be seen in microiontophoresis. Typically, currents of nanoamperes are applied to expel charged species from a micropipette. Both electrophoretic and electroosmotic effects must be considered, which can lead to counterintuitive effects [107]. For example,

electroosmosis can supplement electrophoresis, even contributing a majority of chemical flux. In other cases, electroosmosis may work against and even prevent electrophoretic release. These effects have also been studied in nanopores [109]. The actual quantity of released chemical can be estimated by an empirical transport number, which describes the ratio of applied current to delivered chemical. The challenge of quantifying iontophoretic release makes direct measurement preferable [39].

2.4.6 Electrostatic gating in nanopores

Electrostatic effects rely on the attraction and repulsion between charged interfaces and dissolved ions or suspended particles. The electric charge of surfaces in contact with water leads to accumulation of counterions and depletion of coions. This ionic imbalance is confined to the electrical double layer, characterized by the Debye length (2.18). As an example, the Debye length is 2 nm in a symmetric monovalent electrolyte, isotonic with extracellular fluid (150 mM).

By manipulating surface charges, electrolytes in nanopores can be doped with counterions, leading to effects similar to semiconductor physics. Nanopores can be designed to exhibit diode-like rectification [111], transistor-like behaviour [112], and even logic gates [113].

However, for the goal of precise chemical release, these electrostatic effects provide insufficient control of chemical release. These effects do not provide absolute prevention of chemical release. This is a challenge for microiontophoresis, which requires a retaining current to avoid leakage and stimulation by diffusion. Moreover, electrostatic effects are nonspecific, so that all similarly charged ions may be transported. Among other challenges, this is complicated by interdependent effects of electroosmosis, electrophoresis, and advection.

An illustrative example considers an ideal nanopore with a length of 1 μm and a diameter of 50 nm. This nanopore connects a source reservoir, filled with an electrolyte, to a target reservoir, filled with a stimulant solution; both have concentrations of 150 mM and conductivities of 1.5 S m^{-1} . Ideal electrostatic gating allows only water and the charged stimulant molecule to pass through the nanopore. An applied voltage of 100 mV will drive a current² of 300 pA, which is equivalent to a flux of 3 fmol s^{-1} if considering only electrophoresis of the stimulant. In comparison, an applied pressure of 100 kPa will push an advective flow³ of 17 fl s^{-1} , with a flux of 3 fmol s^{-1} . Diffusion⁴ will release the stimulant at 0.3 fmol s^{-1} , a small but significant contribution. Voltage and pressure can be controlled, but the absence of a barrier prevents any control of diffusion.

2.4.7 Hydrophobic gating in nanopores

Absolute blockage of chemical release requires a physical barrier to disrupt the aqueous phase. As discussed in section 2.2.2, this has not been demonstrated in any device suitable for chemical neurostimulation at sufficiently small dimensions. Microfluidics valves as small as 6 μm have been reliably achieved across large areas, but require in-plane integration in multilayer structures for pneumatic control [114]. Mechanical stability of such valves makes further miniaturization challenging. A similar concept has been proposed in single carbon nanotubes [115], but practical fabrication and integration is not currently possible. Single use barriers are simpler. Drug delivery devices release discrete doses by electrochemical dissolution of metal barriers [63], but without any possibility for reversible gating as the chemical constituents of the barrier diffuse away.

Hydrophobic gating in nanopores is a mechanism which could achieve a physical barrier for precise control of chemical release, in contrast to the electrostatic effects discussed in section 2.4.6. This is an ingenious mechanism by which nanopores can use water vapour as a barrier. Not only does vapour block chemical transport across the nanopore, but the ubiquity of water solves the challenge of re-establishing the barrier.

The discovery of a liquid–vapour transitions in nanometre-scale carbon nanotubes was first reported in 2001 [116]. Hydrophobic gating based on a close equilibrium between liquid and vapour phases of water in hydrophobic biological pores was soon verified by molecular dynamics simulations [117] and

²With ohmic behaviour, $R = 4L_{\text{pore}}/D_{\text{pore}}^2\sigma$

³According to equation 2.8.

⁴For linear diffusion, $\dot{N} = c_0\pi DD_{\text{pore}}^2/4L_{\text{pore}}$.

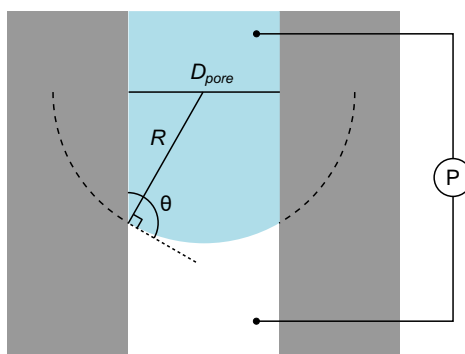


Figure 2.5 The Young–Laplace equation describes the pressure across a curved meniscus, illustrated here for a cylindrical channel.

experiments [118]. These pores exhibit complete blockage despite their lumen remaining physically open with diameters larger than water molecules. In small hydrophobic nanopores, electric fields due to the membrane potential are sufficient to contribute to gating behaviour [119, 120]. It is now accepted that hydrophobic gating is a common phenomenon in the gating of biological pores [121].

The mechanisms of hydrophobic gating in biological nanopores and other small nanopores are limited to dimensions of a few nanometres, which will be discussed in section 5.1.2. However, two papers published in 2011 demonstrated similar effects in larger nanopores in response to applied electric fields [122, 123]. Control with applied voltages is experimentally straightforward, which makes this hydrophobic gating mechanism promising for practical applications. These reports provided the basis for the research presented in chapter 5, which pursued the goal of robust, reversible hydrophobic gating in large nanopores with diameters above 20 nm.

2.4.8 Liquid–vapour fluid dynamics

Hydrophobic gating depends on mechanisms of two-phase fluid dynamics. The presence of vapour is often challenging, leading to bubbles trapped in microfluidic devices [124] or in nanopores [125].

A curved interface between fluids is described by the Young–Laplace equation,

$$\Delta P = \gamma \left(\frac{1}{R_1} + \frac{1}{R_2} \right) \quad (2.20)$$

which defines the pressure ΔP across the interface with surface tension γ (near 72 mN m^{-1} for water) and principle radii of curvature R_1 and R_2 . One application of this equation is in studying droplets or bubbles. Small air bubbles in water contain high pressures. A bubble with a diameter of $1 \mu\text{m}$, for example, will have an internal pressure of almost 300 kPa.

Equation 2.20 also describes the liquid–vapour boundary in channels. The Young–Laplace equation in a cylindrical pore with diameter D_{pore} , illustrated in Figure 2.5, is

$$\Delta P = \frac{4\gamma \cos \theta}{D_{\text{pore}}} \quad (2.21)$$

for contact angle θ with the channel walls (discussed in section 2.4.9). The Young–Laplace equation has been verified in nanopores as small as 2.6 nm [126], with pressures approaching 100 MPa. The Young–Laplace equation in a rectangular channel [127] is

$$\Delta P = 2\gamma \cos \theta \left(\frac{1}{h} + \frac{1}{w} \right) \quad (2.22)$$

with channel height h and width w . In microfluidic channels, the Young–Laplace equation can be exploited to control filling of microfluidic networks by engineering of capillary stop valves [127].

Capillary action is the commonly experienced effect by which water is drawn spontaneously into narrow spaces between surfaces (as long as the surfaces are hydrophilic). The opposite effect occurs on hydrophobic surfaces, and can be illustrated by hydrophobic capillaries dipped into water (Figure 2.6).

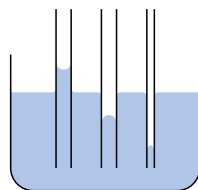


Figure 2.6 Behaviour of water in narrow capillaries depends on surface energy. In a hydrophilic capillary, water rises against gravity (left). In a hydrophobic capillary, intrusion is hindered and the reverse effect is seen (centre). The pressure required for intrusion scales inversely with diameter (right).

The meniscus in a capillary will be forced below the surface to a distance depending on its diameter and contact angle. A hydrophobic capillary with a diameter of $100\ \mu\text{m}$ with $\theta = 100^\circ$, for example, might force the meniscus 5 cm down.

Capillary action may lead to spontaneous filling of hydrophilic channels, while channels with hydrophobic walls will resist filling. Capillary action may also hinder complete filling, if the liquid flows spontaneously around features and traps bubbles.

The same models used for filling of channels can also apply to emptying of channels. Microfluidic channels can be emptied by injection of air to displace liquids, and requires pressures according to the Young–Laplace equation. This is more challenging in smaller dimension. For example, a wetted hydrophilic nanopore would require a high pressure to expel water. With a contact angle of 30° and diameter of $50\ \text{nm}$, a water meniscus could resist an applied air pressure of 5 MPa across the nanopore.

Similarly, the Young–Laplace equation predicts that hydrophobic channels will expel water. However, the Young–Laplace equation does not apply to fully wetted channels which lack a liquid–vapour interface. In small nanoscale channels, spontaneous evaporation can produce a vapour phase. This behaviour will be fully discussed in chapter 5.

2.4.9 Contact angle

A macroscopic measurement of surface properties is obtained by placing a droplet of liquid on a planar substrate and observing the angle at the liquid/solid/vapour contact line. For droplets of water in air, hydrophilic substrates exhibit contact angles below 90° . Hydrophobic contact angles are above 90° , and for smooth substrates are limited to approaching 120° . Higher contact angles above 120° depend on surface roughness, which allows larger apparent contact angles although the local microscopic contact angle may not be so high.

Measurements of contact angle should include both advancing (θ_a) and receding (θ_r) angles. These angles, and the contact angle hysteresis ($\Delta\theta = \theta_a - \theta_r$), can provide important information about the surface energy and homogeneity of a surface. Single measurements of contact angle only provide limited information, as they may indicate any value between the advancing and receding angles.

Despite widespread acceptance, the well-known models of Young, Wenzel, Cassie and Baxter do not consider contact angle hysteresis. I recommend reading “Wetting 101” [128] for an excellent advice for contact angle measurements, along with widely repeated misconceptions. Contact angle hysteresis is expected to be critical in hydrophobic nanopores.

Despite the macroscopic nature of contact angle measurements, it provides valid results even in nanometre-scale nanopores [126]. However, in nanopores additional care must be taken to ensure that models are correctly applied. For example, superhydrophobicity is a macroscopic effect caused by microscopic surface roughness. Considering superhydrophobic contact angles at the nanoscale would be mathematically possible, but physically invalid.

2.4.10 Electrowetting

Electrowetting is the effect by which the apparent contact angle⁵ of liquid on a solid surface can be modulated by applying a voltage between the liquid and solid. It is “arguably the most flexible method to actively control the wetting behaviour of conductive liquids on partially wetting surfaces,” capable of

⁵This common definition will be clarified extensively. Electrowetting does not reduce the local contact angle.

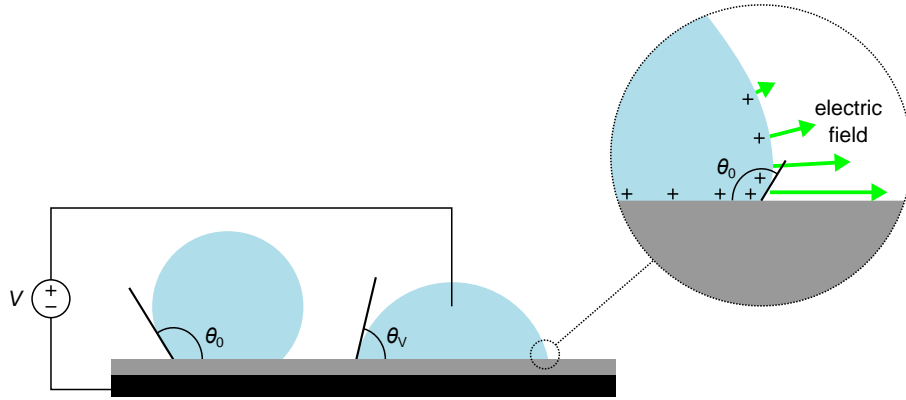


Figure 2.7 Electrowetting. A voltage applied between an insulated electrode and a liquid droplet reduces the apparent contact angle. The reduction in apparent contact angle results from electric fields near the contact line generating Maxwell stress, which distorts the droplet's surface, although the local contact angle remains unchanged. Adapted from Figure 1 of [129].

large changes in apparent contact angle over hundreds of thousands of actuation cycles, with response times of milliseconds or better [129].

The underlying physics of electrowetting are explained by the so-called electromechanical model (Figure 2.7) [129]. A simpler explanation (the electrochemical model) is often used but has been shown to be invalid.

An applied voltage produces electric fringe fields near the liquid–vapour–solid contact line. The electric field generates a Maxwell stress at the liquid–vapour surface, which modifies the Young–Laplace equation (2.20) to include a contribution from the electric field:

$$\Delta P = \gamma \left(\frac{1}{R_1} + \frac{1}{R_2} \right) - \frac{1}{2} \varepsilon_r \varepsilon_0 E_n^2 \quad (2.23)$$

with relative permittivity of vapour ε_r , electric constant ε_0 , and the normal component E_n of the local electric field. This expression has been verified by direct observation of liquid gold droplets in a transmission electron microscope [130].

Electrowetting experiments often use the electrowetting-on-dielectric (EWOD) format, illustrated in Figure 2.7, in which a voltage is applied across an insulating layer separating a planar electrode and a conductive liquid droplet. Most EWOD applications have characteristic liquid dimensions of 100 μm to 1 mm, and insulators less than several micrometres thick [129]. At these dimensions, behaviour correlates with the macroscopic apparent contact angle; microscopic effects are rarely considered. For such applications, the well-known electrowetting equation describes how an applied voltage changes the apparent contact angle θ_{app} from its initial value θ_0 :

$$\cos \theta_{\text{app}} = \cos \theta_0 + \frac{C}{2\gamma} V^2 \quad (2.24)$$

with the liquid–vapour surface energy γ and the applied voltage V [129, 131]. The specific capacitance C comprises series contributions from the insulator and the Helmholtz capacitance of the solid–liquid interface. The Helmholtz capacitance may have a significant effect with insulating layers only a few nanometres thick. In most cases, the Helmholtz capacitance can be neglected, so that

$$C = \frac{\varepsilon_r \varepsilon_0}{d} \quad (2.25)$$

with the thickness d and relative permittivity ε_r of the insulator.

Equation 2.24 is valid at low voltages, but the effect saturates to finite contact angles at increasing voltages. The range of validity for the low voltage approximation is limited by the onset of saturation, which has been estimated as [132]

$$V_{\text{sat}} = \sqrt{\frac{2(\gamma_C - \gamma \cos \theta_0)}{C}} \quad (2.26)$$

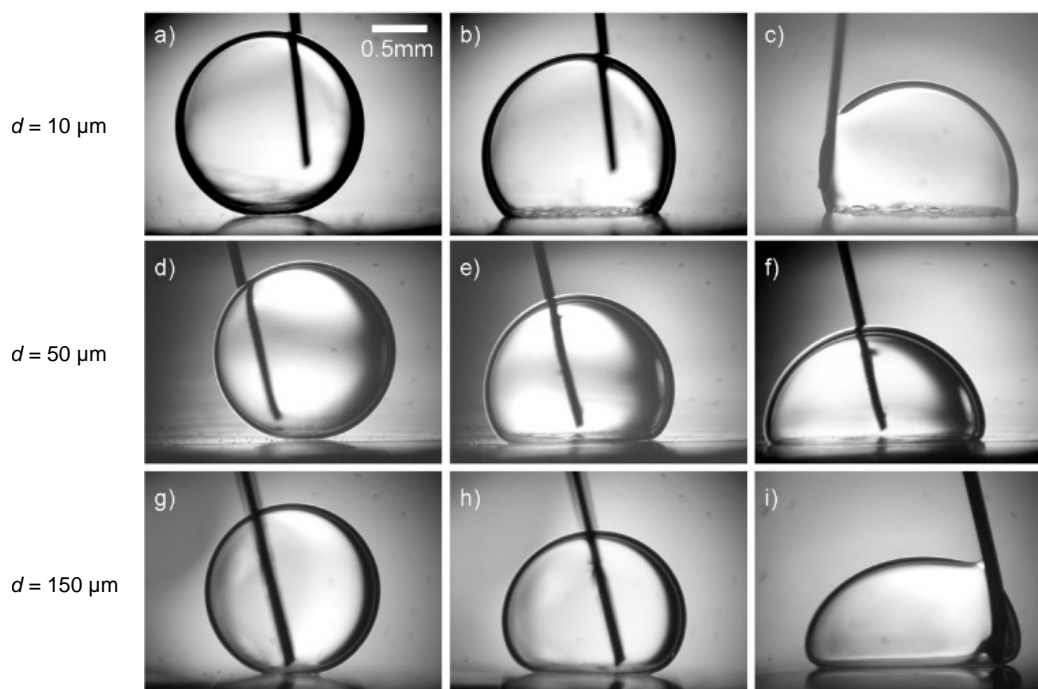


Figure 2.8 Failure of the electrochemical model of electrowetting. Electrowetting with drops of an aqueous salt solution in silicone oil, with increasing insulator thickness (10, 50 and 150 μm , from top to bottom) and increasing electrowetting number $CV^2/2\gamma$ (0, 0.5, and 1, from left to right). The contact angle near the contact line remains constant; this is more evident with thicker insulators. © 2007 IOP Publishing Ltd. Reproduced with permission from “Equilibrium drop surface profiles in electric fields” by F. Mugele and J. Buehrle [142].

depending on the critical surface energy of wetting for the solid surface γ_c . Notably, the electromechanical model does not explain contact angle saturation. Contact angle saturation may be caused by charge ejection from the liquid, as demonstrated by molecular dynamics simulations [133] and observed experimentally [134, 135].

As mentioned above, electrowetting is commonly explained⁶ by the electrochemical model. This interpretation claims that an applied electric field modulates either the contact angle or the surface energy of a liquid–solid interface. The effect may be attributed to electrochemical effects such as ion accumulation at the interface. Arguments have been made for [139] or against [140] this model. Although it can be a useful simplification, no plausible mechanisms change the contact angle or surface energy in response to an applied electric field.⁷ Experiments have shown that neither the liquid–solid surface energy nor the local contact angle change with an applied voltage [141, 142]. Figure 2.8 illustrates a clear breakdown of the electrochemical model, as demonstrated by Mugele and Buehrle. The reduction in contact angle is only apparent at a distance similar to the thickness of the insulator, while the local contact angle remains unchanged.

The difference between the electrochemical and electromechanical interpretations is clarified by T.B. Jones [143]. He recognized that many authors erroneously attribute the motion of liquids to the change in apparent contact angle. In contrast, motion of liquids arises from a force derived from the Maxwell stress tensor, and the change in contact angle is a side effect.

At the scale of many electrowetting applications, liquid behaviour can be visually observed and the

⁶Misleading discussions of electrowetting are common, as in a recent review [136]. First, the effect was falsely attributed to a change in surface energy: “electric field-induced charge accumulation at the solid–liquid interface [...] decreases the associated interfacial tension (energy).” Later, the electromechanical interpretation was presented, almost as an alternative explanation. The challenges of solving the electromechanical equations are emphasized more than their physical validity. Such explanations mislead readers. Many publications simply repeat the electrochemical model. For example, “[electrowetting] controls surface wettability [...] by an applied electric field” [137]. The best review of the physics of electrowetting that I have found until now is by Mugele, 2009. Many publications by T.B. Jones also clearly describe fundamentals of electrowetting, including a lecture [138].

⁷Of course, electrochemical reactions will change the surface energy, but electrowetting should be reversible and should not involve faradaic currents.

electrochemical model agrees well with experimental results. In fact, with characteristic dimensions larger than the insulator thickness, both the electromechanical and electrochemical models can be simplified to describe a force acting on the contact line [129]. This may be described as a contact-angle-driven interpretation. Although useful due to its simplicity, this interpretation is incorrect and is known to be invalid in small geometries. T.B. Jones expressed this clearly: “Do not attribute translational displacements and motions to contact angle changes” [138]. While the electromechanical model can be solved numerically, it is more challenging than the simple contact-angle-driven interpretation [142, 144, 145]. Chapter 5 delves deeper into the challenge of applying these models.

Simulations of electrowetting predict that its behaviour extends to nanometre-scale dimensions [133] but may be complicated when confinement in nanopores results in electric fields diverging from the perpendicular orientation expected across the insulator [146]. Electrowetting in nanopores with molecular dimensions requires molecular dynamics simulations [147]. Models for electrowetting based on continuum equations in larger nanopores will be introduced in chapter 5.

Reversible electrowetting requires prevention of damage by dielectric breakdown or other mechanisms. Typical insulator layers have a thickness of several micrometres, and can withstand the voltages of tens to hundreds of volts required to obtain appreciable effects. Insulating layers with nanometre-scale thickness should allow electrowetting at low voltages of only a few volts. However, such layers have limited stability. For example, electrowetting with self-assembled monolayers of thiols on gold can only achieve small changes in apparent contact angle at safe voltages [148].

Dielectric breakdown or electrochemical reactions must be avoided to ensure reversibility of electrowetting. For example, electrochemical desorption of hydrophobic self-assembled monolayers on gold electrodes has been demonstrated, which was reversible due to the confinement of the desorbed thiols in a small liquid drop [149]. Plasma generation and droplet ejection has also been observed [134, 135], and will be discussed further in section 5.3.6.

3 Vision

An ideal neuroprosthesis would interact naturally with the nervous system, so that target neurons would be incapable of distinguishing between artificial and biological signals. Such a device would form synapses with neurons, imitating synaptic transmission, and would do this over a sufficiently large area (or even a three-dimensional volume) with enough neurons to provide a useful input to the nervous system. Simultaneous readout and processing of electrophysiological or neurochemical signals would be required for appropriate feedback.

However, the idea that such artificial structures could be designed and fabricated remains science fiction. I would instead describe a future neuroprosthesis, which is also currently unachievable but may be possible in the coming years with continued technological development.

This device would integrate an array of synthetic synapses, each capable of forming intimate biochemical contact with target neurons. A first requirement would be that each synthetic synapse can produce relevant signals by controlled release of a desired neurotransmitter. A second requirement is intimate proximity between the chemical release site and neurons, which is necessary to transmit signals with useful speed. Biochemical functionalization of the external surfaces of the device would promote acceptance by the neurons. In combination with release of neurotrophic factors and neurotransmitters, neurons may extend dendrites to interface with such a device. Close proximity will be necessary as chemical signals propagate by diffusion, such that dose and transmission speed decay prohibitively with increasing distance.

The density of synthetic synapses in a chemical neuroprosthesis must be significantly higher than the capabilities of electrical prostheses to justify the additional complexity. For example, the Alpha IMS implant from Retina Implant AG has 1500 electrodes with a density of 200 mm^{-2} (pitch of $70\text{ }\mu\text{m}$). In contrast, photoreceptor density in healthy retinas is three orders of magnitude higher (on the order of 10^5 mm^{-2} , or pitch of $2\text{ }\mu\text{m}$). Synthetic synapses with a density of $10^3\text{--}10^4\text{ mm}^{-2}$ would reduce spacing to $10\text{--}30\text{ }\mu\text{m}$. Such features sizes are in the range of high density CMOS electrode arrays, which use complex integrated circuits to address each electrode.

Realization of this vision would require research to develop novel technology. Many challenges remain before the feasibility of implantable chemical neuroprostheses may even be evaluated. Several technological hurdles must yet be overcome before a model of a chemical neuroprosthesis can be fabricated. This includes development of new technologies for the precise control of chemical release and large scale integration of chemical release sites. Furthermore, integration with chemical reservoirs and electronic systems for control, telemetry, and power will be necessary; these peripheral systems have proven challenging in current neuroprostheses. These challenges are compounded by the need for neuroprostheses to be implantable, and to function flawlessly for periods of years or decades. At best, any failure would require surgery to remove or replace the implant. At worst, failure could result in loss of neurological function and death.

In this thesis, I will describe the concrete steps that I have taken towards an *in vitro* platform to achieve chemical stimulation of neurons, presented in chapter 6. This platform integrates 30 nanopores over an area of 2 mm^2 , each of which is addressed by a microfluidic channel and electrode. This platform is based on the well-established microelectrode arrays developed over the past twenty years at the NMI [150], and can be used with standard electrophysiological recording platforms (MCS Multi Channel Systems GmbH). It is compatible with established biological preparations of neural cultures and tissues.

Furthermore, I have undertaken experiments towards novel gated nanopores, which may provide the mechanism for synaptic-like chemical release. A key challenge to overcome is diffusive leakage, which is critical in micro- and nanofluidic systems. Continued research is needed to achieve reversible gating, which must also be sufficiently robust to survive under biological conditions. Developments towards this goal are presented in chapter 5. Future gated nanopores may be integrated to control chemical release from the nanopore array platform.

If the current technological challenges can be overcome, and the technology can be proven to function reliably, many years of testing will be necessary before any application towards clinical use in humans can be examined. Further development of nanofluidic technology is required to evaluate if chemical neuroprostheses will present a practical solution in comparison to other methods. However, the anticipated benefits of such devices make continued technological development of the concept worthwhile. Furthermore, research towards this goal will necessarily produce novel tools for investigations of neurochemistry and neurophysiology, as well as for the broader field of lab-on-a-chip devices.

4 Nanopores enable local, high-resolution chemical release

Integration of nanopores in chemical stimulation devices will enable control and precision of chemical release which has not been possible in microfluidic devices.¹ This chapter will establish the mechanisms of chemical release through nanopores to justify why these smaller channels will enable new possibilities. The primary mechanisms which must be considered are diffusion and pressure-driven advection. Electrokinetic flow will be briefly considered for comparison with results of microiontophoresis, but its use in future applications is not recommended (see section 2.4.5).

This chapter will determine the chemical flux which can be released through a nanopore, and will illustrate how the chemical signals will be dispersed in the target volume. The chemical release parameters determined here will be compared to the discussion of biological synaptic release from section 2.1. As introduced in section 2.4.7, hydrophobic gating may be an ideal mechanism to control nanopores. This chapter will consider ideal gating which can turn nanopores on and off as desired (Figure 4.1). Chapter 5 presents experimental work towards such gating.

Figure 4.1A illustrates the system before any release occurs. A membrane containing a single nanopore separates a target reservoir from the source reservoir, containing a chemical stimulant. The target reservoir is intended to contain neurons or other biological tissue which will be the target of the chemical release. For simplicity, the current discussion will consider the target reservoir which contains only an aqueous solution.

The discussion begins by considering transport of a dissolved chemical through a single wetted nanopore and its release into a target reservoir, as illustrated in Figure 4.1B. The mechanisms by which such release occurs are diffusion, pressure ejection, and electrokinetic effects. Equally important is the spread of the chemical signal into the target reservoir. This can be estimated from analytical solutions to the diffusion equation. Calculations will consider properties of water at 25 °C and other parameters as listed in Table 4.1.

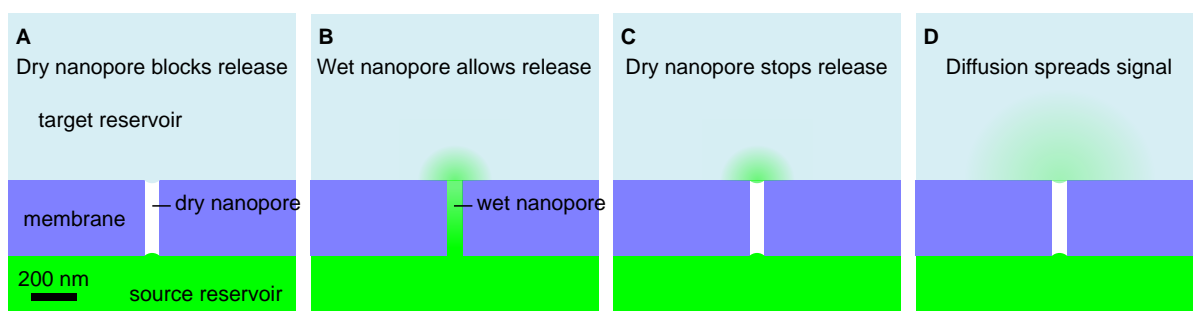


Figure 4.1 Schematic of chemical release from a nanopore. **A** The dry nanopore prevents transport of a chemical (green) from the source to the target reservoir. **B** The wet nanopore allows release of the chemical, for example by diffusion and advection, which then spreads in the target reservoir by diffusion. **C** Release stops when the nanopore returns to its dry state. **D** Diffusion continues to spread and dilute the chemical signal.

In anticipated applications, release driven by pressure or diffusion alone is preferable. Electrically driven release could interfere with the electrical actuation of the hydrophobic barrier. Furthermore, electrokinetic effects must consider specific features of a given system, such as surface charges, pH, and concentration. A simple analysis of electrically driven release will be presented for comparison, but more complete descriptions of electrokinetic effects are in section 2.4.5 and the references therein. Total

¹A version of some of the discussion in this section was published [34]. This section contains additional discussion which did not fit in the scope of the publication.

Table 4.1 Parameters for chemical release calculations.

Property	Symbol	Value ^a	Units
Surface tension ^b	γ	72.0	mN m ⁻¹
Dynamic viscosity ^c	η	0.89	mPa s
Density ^d	ρ	1.00	g ml ⁻¹
Vapour pressure ^e	P_{vap}	3.17	kPa
Reservoir concentration	c_0	0–1	M
Diffusivity ^f	D	10 ⁻⁹	m ² s ⁻¹
Pressure ^g	ΔP	0–300	kPa
Slip length ^h	λ	20	nm
Nanopore length	L_{pore}	500	nm
Nanopore diameter	D_{pore}	10–100	nm

^aAt 25 °C. ^bInternational Association for the Properties of Water and Steam. *Revised Release on Surface Tension of Ordinary Water Substance*. (2014). ^cInternational Association for the Properties of Water and Steam. *Revised Supplementary Release on Properties of Liquid Water at 0.1 MPa*. (2011). ^dLange's Handbook of Chemistry, 10th ed., p1199. ^eLange's Handbook of Chemistry, 10th ed., p1436. ^fDiffusivity of ions and small molecules is near this value [151]. ^gApplied pressures of up to 300 kPa are regularly applied in implantable devices [46]. ^hSlip lengths of 20 nm have been measured on hydrophobic surfaces, and slip is not observed on hydrophilic surfaces [102].

concentrations of dissolved species should be isotonic with biological fluids, and therefore the negligibly small Debye length allows for the neglect of ion accumulation or depletion. The transport mechanisms in this section will apply similarly to wetted hydrophilic or wetted hydrophobic nanopores. Pressure-driven flow will vary depending on the hydrophobicity of the nanopore walls, so both slip and non-slip conditions will be discussed.

Diffusion begins immediately, and initially a sharp concentration gradient exists. Diffusion is calculated by equations 2.12, which simplify in one-dimensional systems such as nanopores² to

$$\begin{aligned} J_{\text{diff}}(z) &= -D \frac{\partial c}{\partial z} \\ \frac{\partial c}{\partial t} &= D \frac{\partial^2 c}{\partial z^2}. \end{aligned} \quad (4.1)$$

The time constant of diffusion along the nanopore length from equation 2.13 is 125 μs , after which a linear gradient will be formed and diffusive release will reach a steady state. For the current analysis, this initial period is neglected, although it should be considered if target structures are within 1 μm of the nanopore and fast switching is being investigated. Assuming that the majority of the concentration gradient falls across the nanopore ($\partial c / \partial z = c_0 / L_{\text{pore}}$), the diffusive release calculated from the diffusive flux J_{diff} and the nanopore's area is

$$\dot{N}_{\text{diff}} = \frac{\pi c_0 D D_{\text{pore}}^2}{4 L_{\text{pore}}}. \quad (4.2)$$

This release rate will decrease as the target concentration increases. However, calculations of the concentration near the nanopore exit show that most of the concentration gradient remains along the length of the nanopore. This assumption is sufficient in these calculations, but should be reconsidered if improved accuracy is needed, for example if propagation is restricted by cells.

Pressure ejection follows equation 2.11 for pressure driven flow. Multiplying by the reservoir concentration gives the release rate of

$$\dot{N}_{\text{pressure}} = \frac{\pi c_0 \Delta P D_{\text{pore}}^4}{128 \eta L_{\text{pore}}} \left(1 + \frac{8 \lambda}{D_{\text{channel}}} \right). \quad (4.3)$$

²The timescale for diffusion across the diameter of a nanopore is on the order of 1 μs or less.

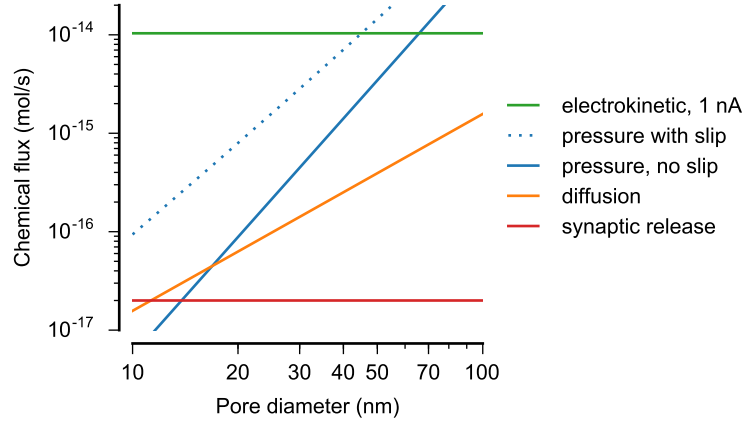


Figure 4.2 Chemical release rates through a single nanopore. Reservoir concentration was 0.1 M. Pressure was 100 kPa.

Release by electrokinetic flow can be estimated by a transport number, similar to microiontophoresis [152]. An applied current I delivers a rate of

$$\dot{N}_{\text{EK}} = \frac{nI}{zF} \quad (4.4)$$

with transport number n , valence z , and Faraday constant $F = 96\,485 \text{ C mol}^{-1}$. Considering a current of 1 nA with a monovalent species and a transport number $n = 1$, the electrokinetic release is $\sim 10^{-14} \text{ mol s}^{-1}$.

Equations 4.2 and 4.3 are graphed in Figure 4.2 for a range of nanopore diameters with the parameters given in Table 4.1. Release is directly proportional to the reservoir concentration, which has been chosen to be 0.1 M. Pressure-driven release was calculated for a pressure of 100 kPa. Calculations considered a no-slip condition ($\lambda = 0$) expected for hydrophilic nanopores as well as with a slip length of 20 nm for hydrophobic nanopores. The estimated release from a 1 nA current is also included for comparison. For synaptic release at a single active zone in a biological synapse, an upper limit of $2 \times 10^{-17} \text{ mol s}^{-1}$ was estimated in section 2.1. The estimated release from a 1 nA current is three orders of magnitude above the estimated upper limit of synaptic release. At diameters below 20 nm, the pressure-driven flow and diffusive release are similar, but they increase rapidly with nanopore diameter. Scaling of the release rates could be accomplished by choosing a different reservoir concentration, or modification of parameters such as the nanopore length. However, these rates are sufficient for the current discussion.

Another possibility to modulate the release rate is through gating of the nanopores. If an ideal hydrophobic gating mechanism can be achieved as illustrated in Figure 4.1, then a reduction would be readily achieved by pulsatile release. In reality, hydrophobic gating has limitations for its switching speed. In biological nanopores, this switching can be observed at nanosecond times [121]. Slower switching is expected in larger nanopores but cannot yet be predicted.

As a chemical is released from a nanopore, it will spread into the target reservoir. Propagation of the chemical signal to larger distances is limited by diffusion. At increasing distances, the speed of signal transmission decreases prohibitively, and dilution limits the maximum concentration that can be reached. Analytical solutions of the diffusion equation can estimate concentration in the target reservoir. Equations 2.14 and 2.15 must be doubled to account for absence of diffusion into the planar substrate. The onset of the chemical signal, illustrated schematically in Figure 4.1A–B can be described by

$$c(r, t) = \frac{\dot{N}}{2\pi Dr} \operatorname{erfc}\left(\frac{r}{2\sqrt{Dt}}\right) \quad (4.5)$$

with the origin $r = 0$ placed at the exit of the nanopore and sustained release initiated at $t = 0$. For the release rate \dot{N} , values calculated from the above equations for diffusion or pressure-driven release can be used. This expression has been examined experimentally and should be valid for the release rates and most dimensions considered here [153].

Solutions to equation 4.5 are shown in Figure 4.3. Release by diffusion alone was considered, from a 50 nm-diameter nanopore. The calculated results were normalized with respect to the reservoir concen-

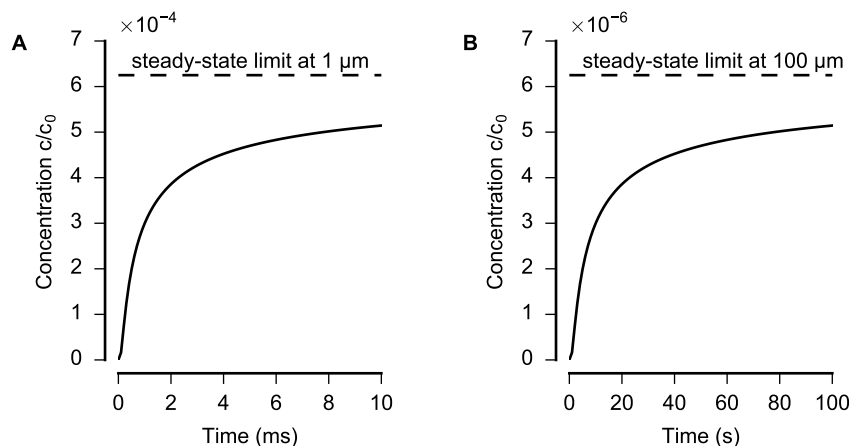


Figure 4.3 Spread of a chemical signal released from a nanopore into a target reservoir. The release rate was calculated with equation 4.2 for a 50 nm-diameter, 500 nm-long nanopore. Concentration distribution after release begins at $t = 0$ was calculated with equation 4.5. Concentrations were normalized to the source reservoir. **A** At a distance of 1 μm , the concentration approaches its steady-state limit of within 10 ms. The steady-state limit is below 0.1% of the reservoir concentration. **B** At 100 μm , tens of seconds are required before the concentration begins to approach its steady state, which is diluted by 10^5 from the reservoir concentration. Note the differences in axes and units in **A** and **B**.

tration. It is evident that the concentration reaches its maximum value rapidly at micrometre-scale distances, but at larger distance much longer times are required. The dilution of the reservoir concentration is also evident. At 1 μm , the concentration is diluted already by 10^3 . Clearly, a high source concentration would be required to produce useful concentrations in the target reservoir, and the chemical signal will remain localized near the nanopore. Similar results would be obtained for pressure-driven release, but could produce higher concentrations corresponding to the higher release rates seen in 4.2.

Applications will need to consider required concentrations as well as the proximity between nanopores and target structures. For example, synaptic concentrations of glutamate have been reported to reach 1.1 mM [154]. A more recent review suggests a range of 0.5–11 mM is necessary for stimulation [27]. Assuming a source concentration of 1 M, Figure 4.3 shows that a concentration of 1 mM would only be reached within 1 μm of the nanopore. However, this concentration would be attained within 1 ms. These factors must be carefully considered for future applications or specific chemical stimulation experiments.

Application of pressure-driven flow could deviate from equation 4.5 due to the added volume. However, this effect should be negligible. The injected volume driven by a pressure of 100 kPa through a 100 nm nanopore under slip conditions is 1.4 pl s^{-1} . Diffusion will quickly spread the chemical signal into a volume which is orders of magnitude larger. However, this volume could perturb cells or tissues in future applications.

It is clear that chemical release from a nanopore can rapidly establish a local chemical signal. The decay of this signal can be estimated from equation 2.14. This equation describes the concentration distribution after instantaneous release of an amount of chemical at a single point. For release from a nanopore in a planar substrate, the equation must be doubled to account for lack of diffusion into the substrate:

$$c(r, t) = \frac{N}{4(\pi Dt)^{3/2}} \exp \frac{-r^2}{4Dt}. \quad (4.6)$$

Instantaneous release and sustained release are illustrated in Figure 4.4. Instantaneous release of 10^6 molecules was calculated according to equation 4.6. The concentration 1 μm from the nanopore rises and falls by orders of magnitudes within milliseconds. Sustained release was calculated with equations 4.2 and 4.5 for a 50 nm-diameter, 500 nm-long nanopore, with diffusion from a 100 mM reservoir and a diffusion constant of $10^{-9} \text{ m}^2 \text{ s}^{-1}$. The concentrations at larger distances approach an increasingly diluted steady state. The release rate from equation 4.2 was $4 \times 10^{-16} \text{ mol s}^{-1}$, or $2.4 \times 10^8 \text{ molecules s}^{-1}$. At this rate, the instantaneous release of 10^6 molecules would have actually

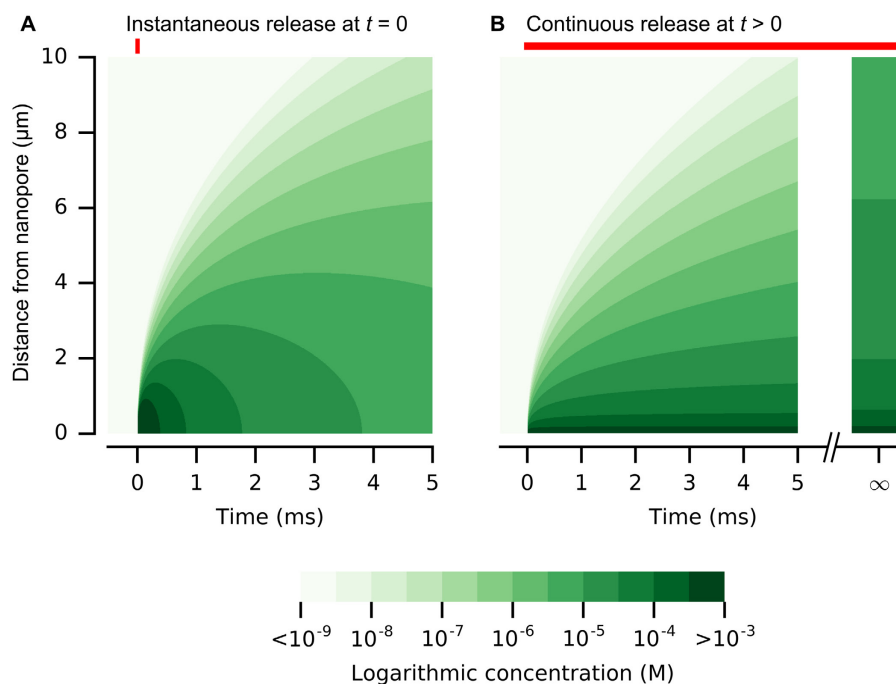


Figure 4.4 Release and spread of chemical signals by diffusion. **A** Propagation of an instantaneous chemical impulse of 10^6 molecules at $t = 0$, calculated with equation 4.6. **B** Propagation of sustained release by diffusion, calculated with equation 4.5. The release rate was calculated with equation 4.2 for diffusion from a 50 nm-diameter, 500 nm-long nanopore, and a reservoir concentration of 100 mM. The colour scale is logarithmic and shown in discrete steps for clarity. Reproduced with permission [34].

taken 4 ms.

Release from a nanopore may also be compared to single vesicle release. As introduced in section 2.1, single vesicles may contain 40 000 molecules. Applying this amount in equation 4.6 calculates the expected concentration distribution of this release from a planar substrate, shown in Figure 4.5 for a distance of 200 nm from the release site. From equation 4.2, the release of the same amount from a 50 nm nanopore with a source concentration of 0.1 M would be achieved in 0.2 ms by diffusion. Such a short time would require closer consideration of the diffusion profile even along the nanopore's length. Furthermore, such a small amount only produces a concentration necessary for stimulation within a small volume. Even at a distance of 500 nm, equation 4.6 predicts a peak below 100 µM. When considering these small dimensions, the specific release mechanism will cause deviation from the prediction of equation 4.6. For example, fluid dynamics of the solvent will be different for a 50 nm vesicle and a 50 nm nanopore, and this effect is not considered in Figure 4.5.

It is also helpful to consider an array of nanopores to predict what resolution could be achieved with chemical stimulation. Predicted chemical release from an array of nanopores spaced at 10 µm is shown in Figure 4.6, calculated from equation 4.5 and assuming release from each nanopore is unaffected by its neighbours. Concentrations are shown on a logarithmic scale over the range from 1 nM to 1 mM. For comparison, glutamate is present in the extracellular fluid at background concentrations of 3 µM, while synaptic concentrations during neurotransmission reach 1 mM [154, 155].

At a distance of 0.5 µm above the nanopores, chemical signals are transmitted faster than 1 ms and can be individually discerned. At 10 µm, signal propagation requires longer times, and the signals from individual nanopores cannot be distinguished. These results reiterate that rapid, high-resolution chemical signalling will require intimate contact between the nanopores and their targets.

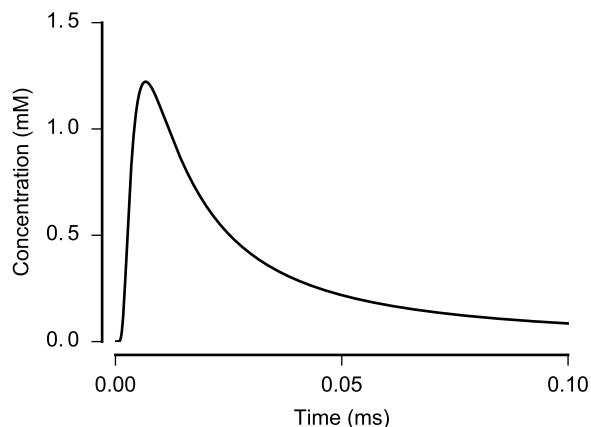


Figure 4.5 Rise and decay of vesicular chemical release. Concentration at a distance of 200 nm was calculated from equation 4.6 for instantaneous release of 40 000 molecules at $t = 0$, corresponding to a single synaptic vesicle.

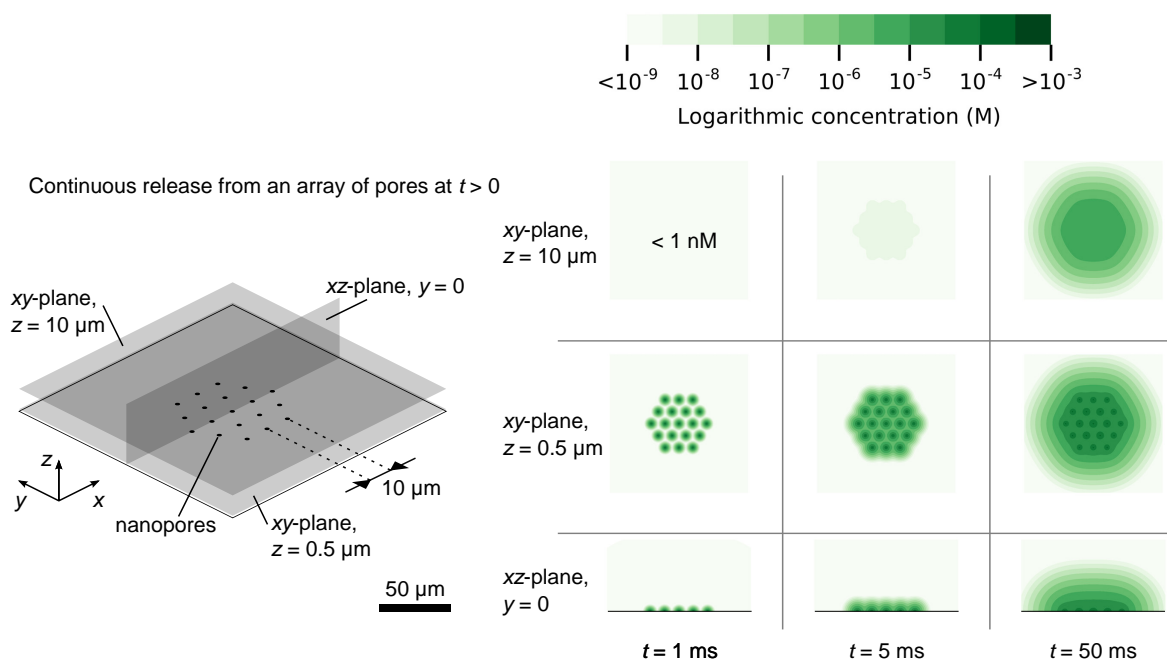


Figure 4.6 Chemical release from an array of nanopores. Concentrations were calculated from equation 4.5 with parameters from Table 4.1. Nanopores have diameters of 50 nm, lengths of 500 nm, and are spaced 10 μm apart. The source concentration is 0.1 M. Snapshots at increasing times are shown from left to right. The bottom snapshots are vertical cross-sections, and the plane of the nanopores is shown as a black line. The snapshots above show horizontal cross-sections at specified distances above the plane of the nanopores. The colour scale is logarithmic and shown in discrete steps for clarity. Reproduced with permission [34].

5 Nanovalves

A primary goal of my work has been to develop gated nanopores to control chemical release with precision and robustness similar to biological synapses. The novelty of this goal is that no controllable artificial nanoscale valves exist which can reliably and reversibly switch between on and off states. Towards this goal, I have undertaken a variety of experiments exploring hydrophobic effects in solid-state nanopores, focusing on producing novel liquid–vapour behaviour to construct reversible hydrophobic nanovalves. The concept of hydrophobic gating is illustrated in Figure 4.1.

The previous chapter established that chemical release from nanopores, driven by diffusion or applied pressures, can match and surpass the rates observed in biological synapses. However, uncontrolled nanopores will always allow diffusion, which would not be acceptable for the envisioned application of high-resolution chemical neurostimulation. A mechanism is required to turn nanopores on and off, with absolute prevention of leakage in the off state. The mechanism should allow switching with millisecond resolution, similar to neurotransmission.

Focusing on hydrophobic gating in nanopores, I will discuss the relevant physics and comment on the current state of understanding in the published literature. I will explain that clear distinctions exist between the hydrophobic gating observed in artificial nanopores and the phenomenon of the same name found in biological nanopores. Electric field–induced reversible hydrophobic gating of nanopores has been previously reported in SiN_x nanopores [122] and track-etched nanopores [123]. Despite these experimental results, a satisfactory understanding of nanofluidic electrowetting has not been reported.

A primary challenge of these results is their reproducibility, which I will explain arises from an inherent lack of control in their fabrication methods. Limited understanding of nanoscale electrowetting and challenging characterization also hinder both the interpretation of nanopore electrowetting and rational experimental design.

Towards an improved understanding of hydrophobic gating, I will present experimental results in SiN_x nanopores and gold nanopores modified with thiol self-assembled monolayers (SAMs). Insight into the mechanisms by which electrowetting of nanopore occurs will be discussed. Reliable and reproducible gating has not been achieved, but an improved understanding of hydrophobic interactions in nanopores has allowed the design of structures which should enable reversible hydrophobic gating. Improvement of fabrication methods is required to produce these structures with sufficient precision.

Furthermore, I have developed models to predict electrowetting in hydrophobic nanopores. Limitations arising from the use of the simplified contact-angle-driven interpretation of electrowetting are discussed. These models describe the common configuration of transmembrane voltage application, as well as a new configuration with integrated electrodes coated with a thin insulator. Integrated electrodes could control nanopores individually. The model is extended to predict controlled trapping of bubbles within nanopores, which may allow reversible hydrophobic gating. Experimental realization of this model will require materials with better electrochemical stability than thiol SAMs. If the model is demonstrated to be valid, rational design of nanopores should achieve reversible electrowetting.

5.1 Literature review

Hydrophobic gating has been reported in different types of nanopores, including biological nanopores [121], carbon nanotubes [116, 156], and artificial nanopores in SiN_x membranes [122] or track-etched polymer membranes [123]. The diameters of these nanopores vary from channels smaller than 1 nm in biological proteins to tens or hundreds of nanometres for FIB-milled SiN_x nanopores. Their lengths also vary from a few nanometres to the 12 μm -thick track-etched membranes.

Due to the inability to directly observe hydrophobic gating, indirect measurements may only be understood through appropriate physical models. Understanding the limitations of such models is necessary to affirm their validity in nanopores with certain dimensions. Below, reports of hydrophobic

gating will be reviewed to demonstrate that behaviours described as hydrophobic gating rely on different physical mechanisms depending on nanopore dimensions. Therefore, understanding hydrophobic gating in artificial nanopores requires new models.

Of course, such models are challenging. Hydrophobic gating by electrowetting requires consideration of electrical and chemical effects coupled to fluidic dynamics. Behaviour of these systems cannot be directly observed, but requires examination by indirect methods. After the review in this section, following sections propose new nanopore designs, formulate physical models, and present new experimental results.

5.1.1 Previous experimental observations of hydrophobic gating

Hydrophobic gating depends on the possibility of a nanopore to exist in and switch between two states: on and off. Terminology to describe these states can be misleading. The two states are labelled as *dry* (or *off*) and *wet* (or *on*) to avoid confusion. Considering the nanopore as a fluidic valve, these dry and wet states could be correctly called *closed* and *open*, respectively. In contrast, if the nanopore is considered as a switch in an electric circuit, the *closed* and *open* states would indicate the switch is conductive (wet) or insulating (dry), respectively. To avoid this contradiction, I use the terms *dry* (or *off*) and *wet* (or *on*) exclusively.

A challenge identified in previous reports of reversible hydrophobic gating is the reproducibility of the effect [122, 123]. This problem arises from the limited control of surface chemistry in the reported methods. Smirnov et al. reported results of 40 nanopores fabricated by FIB milling with diameters of 60–600 nm in 300 nm-thick SiN_x membranes. The nanopores were oxidized with piranha solution and oxygen plasma, and silanized with either hexadecyltrimethoxysilane or 1H,1H,2H,2H-perfluorodecyltrimethoxysilane. The research group has previously reported that such nanopores have intrinsic conductance due to ionic transport in the silane layer [157]. The non-zero conductance even in the dry state required arbitrary choices of off-state nanopore conductance (defined by measured currents at 0.5 V) and critical wetting voltage (defined as producing a current of 5 nA), which partially obscure the measurements of wetting. Initial measurements showed that 16 of 40 nanopores were not conducting. Wetting (assumed by currents above 5 nA) in non-conducting nanopores was observed at transmembrane voltages of 0.5–8 V. Nanopores modified with the fluorinated silane were not observed to wet even up to 20 V.

Control of silane modification of surfaces is difficult [158]. Surface polymerization and deposition of oligomers is difficult to control, but can be reduced by using monofunctional silanes with two protected groups [159]. However, the protected groups cause steric effects which can reduce packing density. Silane-modified surfaces often have a large contact angle hysteresis, indicating high defect density. Smirnov et al. used trifunctional silanes, neglected to discuss the challenge of silane chemistry, and did not discuss any measures taken to control the silane reaction. Control of atmospheric humidity and water content in solvents is critical in silane chemistry, and no information regarding these factors was discussed. The claim of the silane reaction producing a “loosely packed self-assembled monolayer of hydrophobic molecules” [122] is not supported by evidence, and would be remarkable for a trifunctional silane. The silane layers are likely thicker than single monolayers. Furthermore, ultrasonic cleaning to remove excess silane shatters nanopore membranes and cannot be used. It is plausible that the absence of wetting in fluorinated nanopores up to 20 V is caused by complete blockage rather than the moderate increase in contact angle in comparison to alkyl silanes.

Electrowetting in track-etched membranes has also been demonstrated [123]. Reversible wetting was observed in nanopores with minimum diameters between 4 and 30 nm. The nanopores were made hydrophobic by functionalization which was shown to produce heterogeneous surface chemistry, with hydrophilic and hydrophobic regions and a macroscopic contact angle below 90°. Degassing of electrolytes was observed to have no effect, which confirmed that the gating is explained by water vapour blockages. I have previously reported similar results in track-etched membranes without specific functionalization [160]. Understanding of these results is limited by the difficulty of characterizing the geometry of track-etched nanopores, which can have sub-20 nm tip diameters and lengths above 10 μm.

In both SiN_x nanopores and track-etched nanopores, results showed that dewetting must be caused by nanobubbles within the nanopores. When these bubbles were removed by wetting with solvents or

higher voltages, wetting became irreversible.

The effects reported by Smirnov et al. and Powell et al. remain poorly understood. Several mechanisms discussed by Smirnov et al. require significantly higher voltages, and none sufficiently explain the observed effects. Powell et al. referred to a “threshold value” for applied electric fields, in reference to Smirnov et al. and a molecular dynamics study [146], but did not discuss mechanisms or the physical meaning of threshold voltage in their experiments. Powell et al. also implied (although avoided explicitly stating) that dewetting may have been made accessible with diameters up to 20 nm due to the length of their nanopores. However, the length should have minor effects; dewetting has been studied in long, narrow nanopores with no influence from their length [126]. Moreover, their track-etched nanopores had narrow tips but widened to 500 nm.

From these reports of hydrophobic gating, it is clear that hydrophobic nanopores resist spontaneous wetting, but can be wetted by applied transmembrane voltages. Reversibility could be explained by nanobubbles trapped in the nanopores, but no means to control these bubbles was suggested. These bubbles were always necessary but not always sufficient to ensure reversibility. It is clear that reliable fabrication is a primary challenge.

Similar effects of vapour blockages in nanopores have been studied in which bubbles are actively generated. Joule heating from high ionic currents can produce bubbles [161, 162] but requires high voltages and produces high temperatures. Bubbles have also been generated by laser irradiation of plasmonic structures around nanopores [163] or electrochemically generated by integrated electrodes [164]. Such effects could be useful, but require added complexity which could be avoided by electrowetting and spontaneous dewetting.

5.1.2 Biological hydrophobic gating is a separate phenomenon

Biological nanopores provide inspiration with their impressive gating abilities and the atomic precision of their structures. The mechanism of hydrophobic gating in these nanopores cannot be realistically achieved with top-down nanofabrication methods. Proposals and simulations of similar artificial nanopores can be made [115, 165], but fabrication and practical integration remain unreachable. Impressively, gating has been observed in carbon nanotubes (CNTs) incorporated in lipid bilayers and cell membranes [156], which suggests that integration in functional devices could be possible. For now, these nanopores must serve as conceptual inspiration in the search for alternative mechanisms compatible with achievable dimensions.

These systems exploit a physical phenomenon which is only accessible in nanopores with diameters below a few nanometres. Dewetting requires nucleation and growth of vapour bubbles which span the cross-section of the nanopore and sever the water channel. The kinetics of this process restrict its applicability to nanopores only a few nanometres in diameter [126, 166]. As described by Guillemot et al., dewetting by spontaneous nucleation follows the Arrhenius equation, with the nucleation rate v shrinking exponentially with an energy barrier $\Delta\Omega$:

$$v = k \exp \frac{-\Delta\Omega}{k_{\text{B}}T} \quad (5.1)$$

with the leading coefficient k and the energy barrier depending on the dimensions and properties of the system, and the Boltzmann constant k_{B} and temperature T . Lefevre et al. and Guillemot et al. found that dewetting occurred in nanopores with diameters as large as 4.6 nm, with $\Delta\Omega \approx 40k_{\text{B}}T$. This barrier increases proportionally to the third power of diameter, which compounds the exponential factor in equation 5.1. For example, Lefevre et al. did not observe dewetting in nanopores with diameters of 11.2 nm. Molecular dynamics simulations have also confirmed the dimensions required for reversible wetting of nanopores, with recent results specifically examining electrowetting [147].

Extreme sensitivity to structural and chemical variations is illustrated by the effects that sub-nanometre changes in dimensions or single amino acid residue substitutions have on the gating behaviour of these nanopores [167–169]. This is not surprising, as the nanopore lumen has a width equivalent to only a few atoms. Biological nanopores offer precision of both size and chemical composition, achieved by their impressive bottom-up assembly. These facts are crucial to comprehend when studying or designing larger nanopores (> 5 nm diameter).

Similar effects of reversible hydrophobic gating observed in large artificial nanopores [122, 123, 160] cannot be caused by the mechanism discussed above. Smirnov et al. estimate the barrier to dewetting even in 15 nm nanopores at $1500k_B T$. From equation 5.1, it is clear that dewetting is impossible in such nanopores (with its rate decreased by a factor of 10^{634} in comparison to the accessible barrier of $40k_B T$). A better explanation for this observed reversibility is bubble-assisted dewetting. The lack of spontaneous dewetting in fully wetted nanopores will be justified in more detail in the following section.

5.1.3 Fully wet, hydrophobic nanopores remain wet

A large, hydrophobic tube filled with pure water will not spontaneously form bubbles of water vapour. Any such bubbles would collapse under atmospheric pressure. However, the previous section discussed how water in nanometre-sized hydrophobic pores can switch between liquid and vapour states. But when is a nanopore small enough to easily switch between liquid and vapour states? This question is critical for the design of artificial hydrophobic gating.

Thermodynamic calculations provide potentially misleading results. The dry state of large nanopores is thermodynamically preferable yet wetting of such nanopores is not spontaneously reversible [126]. Analysis of the mechanism of spontaneous dewetting and its kinetics proved that spontaneous evaporation is prevented by insurmountable energy barriers at dimensions larger than a few nanometres [126].

Further confusion is introduced by experimental results of reversibility in large nanopores [122, 123]. The authors of these publications identified that nanobubbles must contribute to this reversibility. However, Smirnov et al. made the generous claim that nanopores with diameters larger than 20 nm will not spontaneously dewet. Although not strictly wrong, a more reasonable limit is somewhere in the range of 2 to 5 nm [126, 166]. This difference has enormous implications for achieving gating based on spontaneous liquid–vapour fluctuations. Top-down nanofabrication can readily produce 20 nm structures with reasonable precision, but not features below 5 nm.

Many molecular dynamics simulations examine spontaneous evaporation in hydrophobic confinement. Such methods are limited to small spatial dimensions and time scales. Implications for behaviour at attainable dimensions and experimental time scales are not always obvious. However, these simulations also make it clear that spontaneous evaporation will not occur with dimensions above a few nanometres [147].

Elegant experiments have studied this mechanism in nanoporous silica, which can be produced as a bulk material with homogenous nanopores at the single-nanometre scale [126, 166]. These experiments confirmed that pressure-driven wetting according to the Young–Laplace equation is not reversible after complete wetting. The Laplace pressure requires a liquid–vapour interface, which does not exist in fully wetted nanopores. Rather, an additional mechanism is required to first generate a liquid–vapour interface in the form of a bubble. Specifically, dewetting required nucleation and growth of bubbles to form two disconnected menisci. This was observed in nanopores as large as 4.6 nm, but not with diameters of 11.2 nm [126].

To reiterate this point, I consider two model hydrophobic nanopores, with diameters of 3 nm and 50 nm and internal surfaces having contact angles of 110° with water. According to equation 2.21, the Laplace pressure is nearly 2 MPa for the larger nanopore and 33 MPa for the small nanopore. In contact with water, the small volumes of the nanopores will equilibrate rapidly with the vapour pressure of water and any dissolved gases. The nanopores can be filled with liquid water by applying high pressures to the reservoirs. Any vapour in the nanopore will be dissolved into the liquid. Now, upon removal of the high pressure, the behaviour of these two nanopores diverges. In the small nanopore, spontaneous bubble formation will restore the dry state. The large nanopore will remain wet indefinitely.

The inaccessibility of spontaneous bubble nucleation at dimensions above 5 nm forces another explanation to be found for the experimentally observed reversibility of gating in large nanopores [122, 123]. The necessity of trapped bubbles to assist in dewetting in these nanopores will be discussed further in the following section.

5.1.4 Trapped bubbles allow drying

The accepted explanation for dewetting of large hydrophobic nanopores is that bubbles are trapped during wetting. Bubbles in artificial nanopores were first reported in 2006 [125]. Such bubbles caused noise and conductance changes during current recordings. In pressure-induced wetting of arrays of hydrophobic nanopores, trapped bubbles were also necessary to ensure reversibility [170]. Pressure-driven intrusion into tapered nanopores with decreasing diameters was electrically monitored, and showed that incomplete filling allowed reversibility, while complete intrusion was irreversible. The reversibility of electrowetting in nanopores has been similarly explained by trapped bubbles [122, 123].

The study of nanobubbles is challenging even on planar substrates, and has been controversial in recent years [171]. Despite observation of nanobubbles on planar surfaces, theories predicted that they should not exist. Observation by scanning probe microscopy was demonstrated as early as 2001 [172], but later experiments showed an absence of bubbles [173], and were even highlighted in an editorial in *Nature* [174]. Since then, the existence of nanobubbles has been widely accepted [171, 175] and a recent special issue of *Langmuir* focused on the topic [176].

The mechanism by which bubbles cause dewetting should be similar to that for spontaneous bubble nucleation [126, 166]. In large nanopores, single or multiple trapped bubbles must somehow span across the nanopore. Bubbles trapped against nanopore walls may grow or join together, leading to a critical bubble size which can span across the nanopore, cleaving the water channel into two separate menisci. These menisci will experience large Laplace pressures and will be rapidly expelled from the nanopore.

Trapping of bubbles will depend on physical and chemical structures on the nanopore walls. Heterogeneous surface chemistry, for example, may enable capillary action along hydrophilic surfaces to enclose bubbles around hydrophobic regions. Similarly, the movement of the meniscus into the nanopore could trap bubbles against rough topography on the nanopore walls. Previously reported results of nanopores with rough surfaces and heterogeneous surface energies could be explained by such mechanisms [122, 123, 160]. The high current noise and fluctuations measured in these nanopores is also expected with trapped bubbles [125].

5.2 New nanopore designs

This work explores several distinct configurations for nanopores (Figure 5.1), which can be split into two distinct classes regarding their electrowetting behaviour (top/bottom row), and two distinct classes regarding their drying behaviour (left/right column). Specific designs using these configurations were investigated as summarized in Table 5.1.

Electrowetting of hydrophobic nanopores has been previously demonstrated by applying a transmembrane voltage (Figure 5.1, top left) [122, 123, 160] but mechanisms of this behaviour have not been satisfactorily explained. Physical models are discussed in section 5.3 and new experimental results are presented in section 5.4. These results follow the conventional experimental setup for the majority of nanopore research, in which an insulating nanopore membrane separates opposing electrolyte reservoirs, each containing a large Ag/AgCl electrode. A limitation of this configuration is that all nanopores in a membrane are addressed by the applied voltage; individual addressing would require fluidic and electrical insulation.

A new configuration explored in this work integrates gate electrodes (in analogy to transistor gate electrodes) in the membrane to address nanopores individually (Figure 5.1, bottom left). The integrated electrodes may be insulated to prevent electrochemical reactions. Electrodes in the electrolyte reservoirs remain for measuring ionic currents through the nanopore. The physics of this configuration are described in section 5.3.3. Section 5.4.6 presents early inconclusive results.

A second distinction is in the physical structure of the nanopores. Most nanopores used for biosensing have smooth walls and a tapered or hourglass profile to achieve a sensing region as thin and narrow as possible. Smooth walls are produced by common fabrication methods (Figure 5.1, left column). Roughness or heterogeneity of surface energy may be introduced by chemical functionalization, but is difficult to control. A bubble trap could achieve spontaneous dewetting of electrowetted nanopores, as presented in section 5.3.5. This could apply to nanopores wetted by a transmembrane voltage (Figure 5.1, top right) or by integrated gate electrodes (Figure 5.1, bottom right). Because complete wetting of nano-

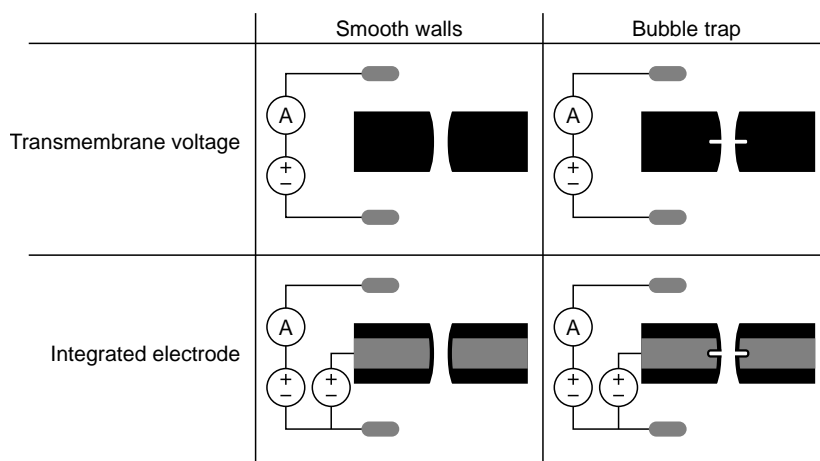


Figure 5.1 Nanopore configurations. Electrowetting may be achieved by applying a voltage across the membrane (top row) or to an integrated gate electrode (bottom row). Nanopores usually have smooth walls (left column). A bubble trap could enable spontaneous dewetting (right column).

pores is irreversible, the rationale for a bubble trap is that maintaining a liquid–vapour interface should allow dewetting. Narrow cavities in nanopore walls should allow controlled trapping of bubbles, and therefore reversible wetting of nanopores.

Specific nanopore designs are summarized in Table 5.1. Early experiments with Design 0 (hydrophobic SiN_x nanopores) used the transmembrane configuration and exploited unspecific hydrocarbon deposition in the SEM for their hydrophobic behaviour. After obtaining results similar to the hydrophobic gating reported by Smirnov et al., I planned experiments to further investigate the effect.

As discussed above in section 5.1, sufficient control of silane chemistry is challenging. Silanes with multiple reactive groups may polymerize, forming a three-dimensional silane network rather than a monolayer. This issue likely contributed to the variability reported by Smirnov et al., so improved control of hydrophobic modification would be necessary for more reproducible results. A straightforward solution would be to use monofunctional silanes, such as ODMCS. Monofunctional silanes ensure at most monolayer functionalization. However, packing density is limited due to steric hindrance from the protecting groups (two methyl groups for ODMCS).

An alternate method for easy hydrophobic modification is thiol functionalization of gold. Thiols reliably form dense self-assembled monolayers. Many thiols are commercially available and have been studied in more detail than monofunctional silanes. Furthermore, gold allows local electrical control of the nanopore, which was promising for extending any results to arrays of individually-addressed nanopores. Even for electrowetting with transmembrane voltages, integration of an insulated, conducting layer within a nanopore may reduce necessary voltages, as electrowetting will depend on the voltage across the insulator at each end of the pore, rather than the voltage across the entire membrane.

Thiols also have advantages with regard to their wetting behaviour. Thiol SAMs may have smaller contact angle hysteresis compared to silanes. For hydrophobic silanes, contact angle hysteresis of $5\text{--}10^\circ$ is commonly reported, even for monofunctional silanes [177]. In comparison, contact angle hysteresis for hydrophobic thiols has been reported as low as 2° [178]. Contact angle hysteresis reflects nanometre-scale roughness [179], which should contribute to bubble trapping and the unpredictable reversibility of hydrophobic gating seen in the silane-modified nanopores of Smirnov et al. Although bubbles are necessary for reversibility of hydrophobic gating, use of silane chemistry may make controlled bubble trapping more challenging. Thiol layers on gold should be smoother, reducing the random trapping of bubbles in comparison to silane surfaces. Then, intentional integration of bubble-trapping structures in the nanopores should allow control of reversibility.

Thiol SAMs can modify certain metal surfaces with a variety of functionalities [180]. Alkyl and fluorinated alkyl thiols produce hydrophobic SAMs. Fluorinated SAMs exhibit higher hydrophobicity and oleophobicity, which may reduce fouling of nanopore surfaces. Fluorinated SAMs also have higher thermal and chemical stability [181]. Many thiols are commercially available and well-studied in the scientific literature. The well-studied 1H,1H,2H,2H-perfluorodecanethiol (PFDT) was chosen, which is

hydrophobic with a contact angle of 115° [148].

Designs 1, 2, and 3 were produced with gold layers on SiN_x membranes, and were modified by PFDT to be hydrophobic. Details of these designs are summarized in Table 5.1. Fabrication methods are described in section 8. Experiments were carried out with the goal of elucidating the underlying physics. Unfortunately, this goal was hindered by experimental complications of stability of the metal structures and PFDT. Design 1 was produced by sputtering Ti and gold on the SiN_x membranes. Sputtering necessitated a thick 30 nm Ti adhesion layer; this layer was etched from within the nanopore during piranha cleaning, which caused challenges of reproducibility. Design 2 used metal evaporation to precisely control layer thicknesses. An 8 nm Cr adhesion layer showed improved resistance against piranha etching, and a sacrificial Ti layer was integrated within the gold to produce bubble traps by wet etching. Common etchants did not etch the Ti layer as expected. Piranha etched the Ti layer but also damaged the gold layers. Design 3 was developed to improve upon these results by replacing the single Ti layer with multiple thin Ti/gold layers. Wet etching of these layers produced a marbled porous layer for trapping of bubbles. A primary disadvantage for all gold–thiol nanopores was the low stability of thiol SAMs. Thiol stability has been studied in culture medium, and critical damage due to oxidation was found after three weeks [182]. Thermal degradation begins at temperatures approaching 100°C , although this can be improved for fluorinated thiols. Electrochemical stability is limited, which is a crucial weakness in this work and is discussed further in the experimental discussion below. In comparison, silane layers are stable at high temperatures and in aggressive chemicals (fluorinated silane layers survived and retained their hydrophobicity after piranha etching).

After encountering difficulties obtaining reproducible results in gold–thiol nanopores, and consequently difficulties in their interpretation, the use of thiols was abandoned in favour of SiN_x nanopores with monofunctional silane functionalization (Design 4). Retrospectively, Design 4 would have been a more prudent option than beginning experiments with gold–thiol nanopores. SiN_x can be cleaned with piranha without concern for damaging the nanopores [183]. Silane-modified surfaces are stable to high temperatures and are not sensitive to oxidation. Experiments with SiN_x –silane nanopores can be carried out with fewer concerns that their structure or surface chemistry will be damaged. In turn, this simplifies interpretation of experimental results.

Design 0 nanopores were milled in 500 nm-thick SiN_x membranes. Experiments were performed by Dr. Birgit Schröppel to test limits of nanopore milling in these membranes using a gallium FIB (Figure 5.2). Well-controlled milling could achieve minimum diameters as small as 30 nm with 2 pA beam currents, although measuring such dimensions required destructive FIB tomography of the nanopores.

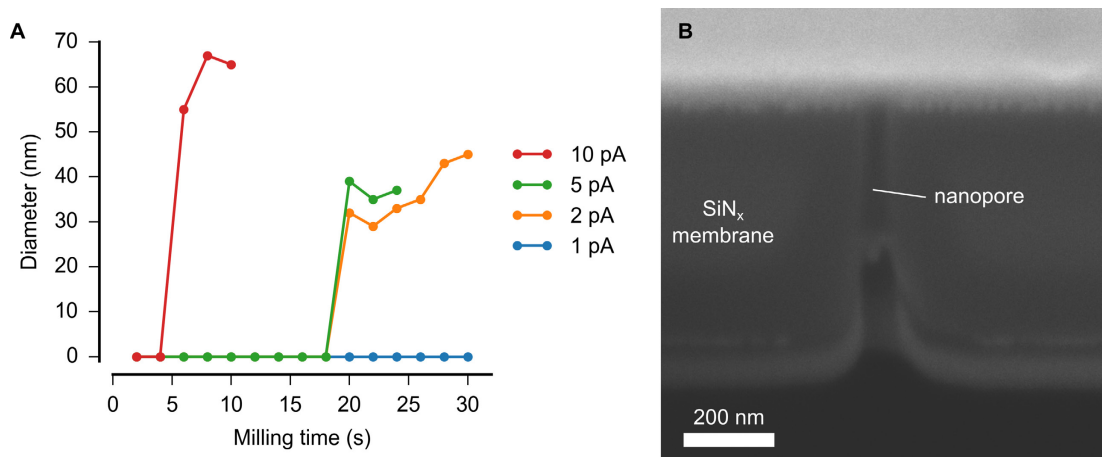


Figure 5.2 Nanopore diameters obtained by FIB milling. **A** Minimum diameters were achieved just after breakthrough and depended on beam currents. Diameters of 0 indicate that nanopore breakthrough was not observed. One pore was measured per data point. Lines are shown as a visual guide. **B** An example FIB cross-section of a nanopore milled for 22 s with a current of 2 pA, which had a diameter of 35 nm. Before cross-sectioning, the nanopore was protected by electron-beam-induced deposition (visible within the nanopore).

Design 1 nanopores were approximately cylindrical (Figure 5.3). Gold layers with Ti adhesion layers were sputtered on SiN_x membranes. Nanopores were produced by FIB milling, cleaned in piranha

Table 5.1 Designs for hydrophobic nanopores, ordered chronologically.

Design	Structure	Metal deposition	Hydrophobic treatment	Presented results
Design 0 SiN _x nanopores	500 nm SiN _x	—	Unspecific hydrocarbons	Models: 5.3.1, 5.3.2, 5.3.6 Results: 5.4.5
Design 1 Hydrophobic gold–thiol nanopores	340 nm gold 30 nm Ti 470 nm SiN _x	Sputtering	PFDT	Models: 5.3.1–5.3.3 Results: 5.4.3, 5.4.4, 5.4.6
Design 2 Gold–thiol nanopores with bubble traps	130 nm gold 15 nm Ti 130 nm gold ~8 nm Cr 480 nm SiN _x	Evaporation	PFDT	Models: 5.3.1–5.3.3 Results: 5.4.3, 5.4.4, 5.4.6
Design 3 Gold–thiol nanopores with improved bubble traps	90 nm gold 90 nm Ti/gold 90 nm gold ~8 nm Cr 500 nm SiN _x	Evaporation	PFDT	Models: 5.3.1–5.3.3 Results: 5.4.6
Design 4 SiN _x –silane	100–500 nm SiN _x	—	ODMCS	Models: 5.3.1, 5.3.2, 5.3.6 Results: 5.4.3, 5.4.5

solution, and hydrophobicized by immersion in PFDT solution. This design confirmed the phenomenon of vapour blockages in hydrophobic nanopores and was used to explore the electrowetting models introduced in section 5.3. No reversibility of gating was expected for this model. Results for these nanopores revealed diverse behaviours: irreversible electrowetting was observed in some nanopores (section 5.4.6), with the dry state only restored by drying of the nanopore chip. Other nanopores were not wetted by applied voltages (section 5.4.6), while others were spontaneously wetted (section 5.4.4). The best explanation for these diverse results is that cleaning in piranha solution changes the structure of the gold segment of the nanopores, as illustrated in Figure 5.3.

Design 2 was developed to investigate the integration of nanostructures in the nanopore walls (Figure 5.4). As introduced in section 5.1.4, trapping of bubbles is necessary for reversible gating. The possibility to fabricate circumferential bubble traps was investigated by wet etching of a thin Ti layer within the gold layer. The expected mechanism by which these nanopores should trap bubbles for reversible gating is presented in section 5.3.5. Results of the fabrication process and measurements are presented in section 5.4.6.

Design 3 is a refinement of Design 2, to improve the integrated bubble-trapping structures (Figure 5.5). The trap layer consisted of alternating 7 nm layers of Ti and gold. This method produced promising structures within the nanopores, and section 5.4.6 discusses their implications for reversibility.

As a first set of experiments with Design 4, twenty-four nanopores with lengths of 100, 200 or 500 nm were produced. The goal of these experiments was to analyse if similar effects would be observed in nanopores with different lengths. Such results could, for example, show a dependence on voltage or electric field. Due to challenging handling during experiments, results with four of these nanopores were obtained after hydrophobicization. These results are presented in section 5.4.5.

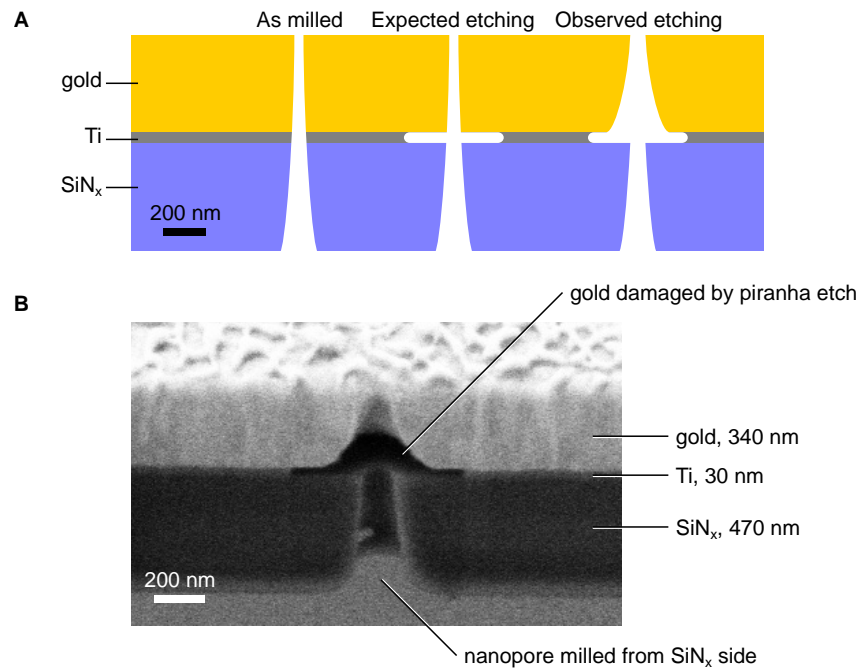


Figure 5.3 Nanopore Design 1. **A** Schematic cross-sections of nanopores after milling, and the expected and observed results of wet etching. The Ti layer was included for adhesion of gold on SiN_x, and minor etching of this layer was expected during piranha cleaning. Damage to the gold layer was also observed, and may explain the apparent diversity of observed wetting behaviours. **B** SEM image of a cross-section of a nanopore after piranha etching. Preparation of the cross-section by FIB milling revealed that piranha cleaning etched the Ti adhesion layer and also damaged the gold layer. The nanopore was milled for 30 s with a current of 10 pA and cleaned in piranha for 10 min before coating with PFDT. This nanopore was from an array of 25 nanopores which had a hydrophilic conductance of 676 nS. Based on the cylindrical model, each nanopore had an average diameter of 139 nm.

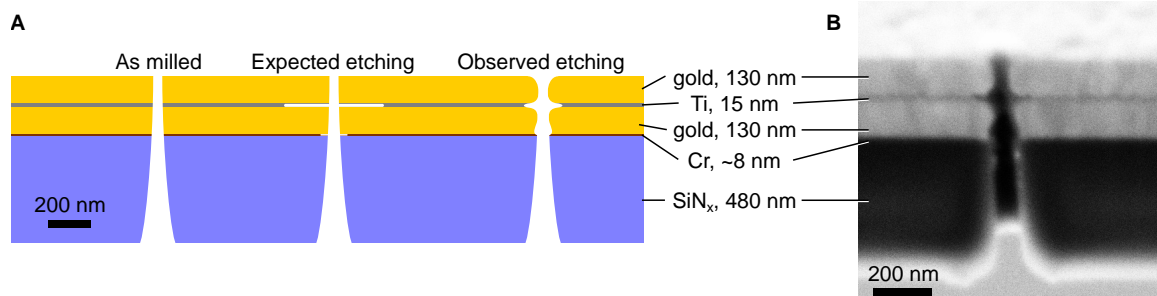


Figure 5.4 Nanopore Design 2. **A** Schematic cross-sections of nanopores with a 15 nm-thick Ti layer integrated to allow wet etching of a bubble trap. **B** The observed traps were wider than expected due to deformation of the gold layers during etching.

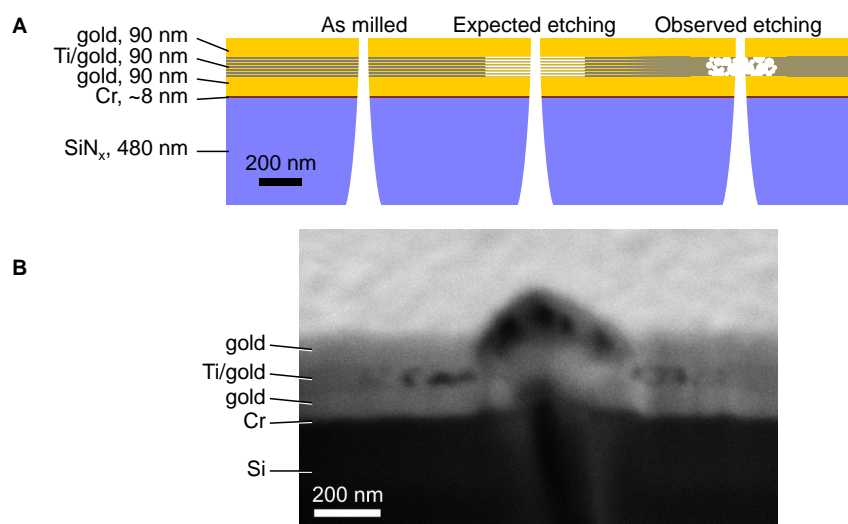


Figure 5.5 Nanopore Design 3. **A** Schematic cross-sections showing the expected nanopores before and after wet etching, and the structure observed after wet etching. Alternating 7 nm layers of Ti and gold were sandwiched between two 90 nm gold layers to produce bubble traps by wet etching. **B** Piranha etching produced marbled cavities in the Ti/gold layer. SEM resolution was insufficient to confirm whether distinct Ti/gold layers remained. Here, the metal layers were deposited on a Si substrate rather than a SiN_x membrane. Nanopores were therefore milled from the metal side and were larger than typical results when milled through a membrane from the SiN_x side. The marbled structure may be caused by aggressive piranha etching or the distinct layers may be mixed due to solid-state diffusion between the gold and Ti layers.

5.3 Theories of hydrophobic gating in nanopores

This section derives models to understand and predict electrowetting behaviour of the nanopore designs presented above. The models presented here were derived from established models for electrowetting and for liquid–vapour dynamics in hydrophobic confinement, and are formulated for nanopores with transmembrane electric fields or integrated electrodes (Figure 5.6). These models are helpful to understand the experiments included later in the chapter, and will provide a foundation for future experiments. As reviewed in section 5.1.1, no satisfactory understanding of electrowetting in hydrophobic nanopores exists in the literature. This section focuses on reversible electrowetting effects, as introduced in section 2.4.10, but also introduces other mechanisms in sections 5.3.6 and 5.3.7.

First, the electromechanical electrowetting mechanism is discussed in the context of nanopores. The model is challenging to apply, and the requirement for numerical solutions has prevented its solution in nanopores. Retrospectively, developing numerical solutions of the electromechanical model would have been prudent to guide and understand experiments. Instead, models were developed according to the contact-angle-driven interpretation.¹ This interpretation will become invalid in nanofluidic electrowetting at distances smaller than the insulator’s thickness. However, it may provide preliminary estimates to be compared to experimental results and more refined models.

Some experimental results presented in section 5.4 could not be explained by reversible electrowetting. Therefore, additional phenomena which may occur when voltages are applied to liquid systems will be discussed in section 5.3.6. These include electric field emission, which could cause irreversible effects if sufficient energies are reached. Any reversible electrowetting system must avoid such effects.

Finally, section 5.3.7 introduces phenomena which may be related to nanofluidic hydrophobic gating, and may share underlying physical mechanisms. Improved understanding of these various phenomena may be gained by new experimental or theoretical results.

¹ The contact-angle-driven interpretation is applied despite its limitations, and against the recommendation to “not attribute translational displacements and motions to contact angle changes” [138]. Further discussion is in section 2.4.10.

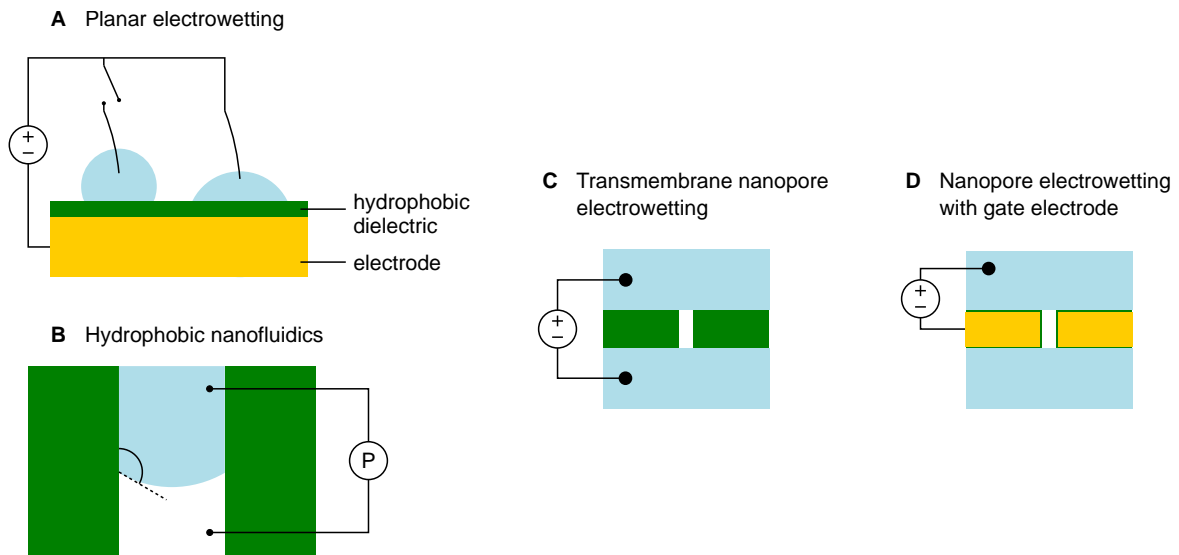


Figure 5.6 Models of nanopore electrowetting combine planar electrowetting with the Young–Laplace equation. **A** Electrowetting reduces the apparent contact angle by application of a potential between an insulated electrode and a liquid. **B** Intrusion of water into hydrophobic nanostructures usually requires high pressures. **C** Nanopores can be wetted by applying a voltage between opposing reservoirs. **D** Nanopores with integrated gate electrodes may enable electrowetting-based control of individual nanopores.

5.3.1 Electromechanical models of nanopore electrowetting

According to the electromechanical model of electrowetting, the combination of Laplace pressure and Maxwell stress defines the shape of the liquid–vapour surface, which itself determines the electrical field distribution, as expressed in equation 2.23. This model is accepted as the most physically valid explanation of electrowetting, but requires numerical solution and is therefore infrequently applied [129]. At dimensions larger than the thickness of the insulator in an electrowetting system, the apparent contact angle may be solved by both the electromechanical and electrochemical models of electrowetting according to equation 2.24.

The electromechanical model has been considered for a capillary [143]. This model was limited to capillaries much wider than the insulator layer. With relatively wide capillaries, the shape of the meniscus did not affect the predicted results. When characteristic dimensions are much larger than the insulator thickness, “the Maxwell stress can be reduced to a net force per unit length that pulls on the three-phase contact line and therefore reduces the apparent contact angle” [145]. This defines the contact-angle-driven interpretation, which ignores the shape of the liquid–vapour interface.

The configurations which must be solved are illustrated in Figure 5.7, with reference to the limitations of the classical electrowetting equation 2.24. The electrowetting effect derives entirely by the Maxwell stress generated at by the electric field across the liquid–vapour surface. Notably, the electric field at the solid–liquid boundary (red lines in Figure 5.7) has no effect. For nanopores in insulating membranes (A), the entire system is within the membrane, so the electrowetting equation is expected to be invalid. In nanopores with integrated electrodes (B), the electrowetting equation will become invalid if the diameter is similar to the thickness of the insulator. Applying a transmembrane voltage when the nanopore has an integrated electrode will be complicated (C). Solving these configurations numerically should provide better estimates for electrowetting behaviour than the following sections, which use the contact-angle-driven interpretation described by the classical electrowetting equation.

The group of Prof. Dr. Frieder Mugele has solved electrowetting near the contact line in two dimensions with MATLAB [142, 144] and three dimensions using OpenFOAM [145]. Using OpenFOAM necessitated developing new solvers to combine capillary and electrical phenomena. Their technique allows construction of arbitrary geometries and specification of parameters including contact angles, pressures, flow rates, and voltages. In addition to publishing their model [145], Ivo Roghair discussed the solvers in a forum (username Ivo00) [184] and provided code and test cases².

²The code and test cases are no longer available at the link given by Ivo Roghair. I have archived these files for future use.

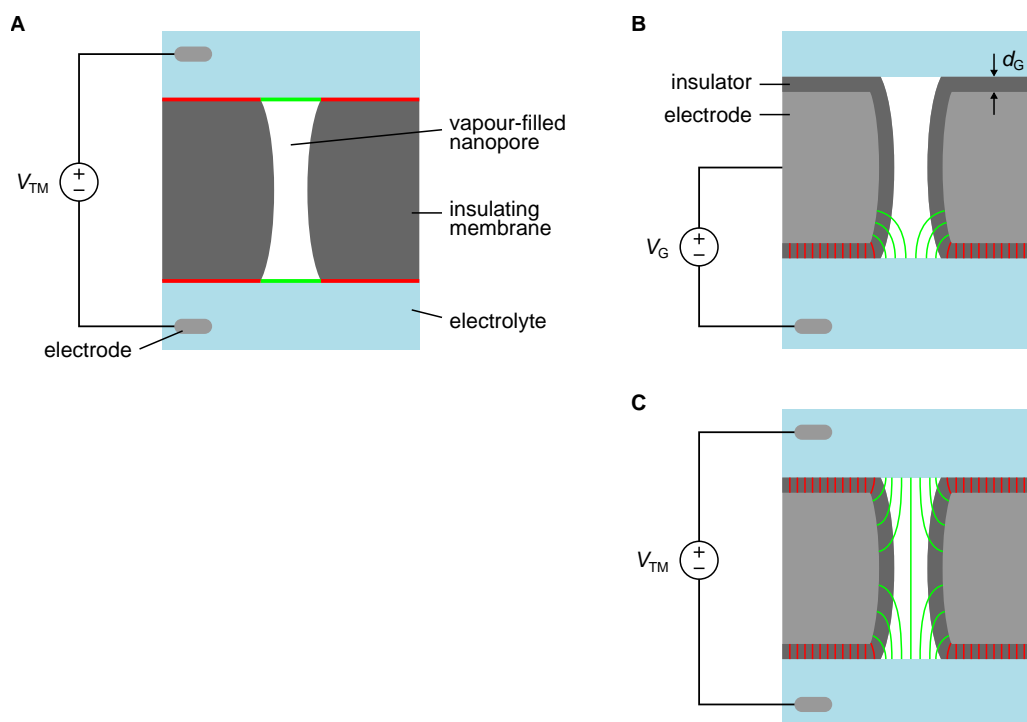


Figure 5.7 Electrowetting occurs due to the electric field across the liquid–vapour interface. **A** In the transmembrane configuration, electric fields act on both menisci (green). The electric field at the liquid–solid interface does not contribute to electrowetting. **B** Schematic illustration of electric field lines in a nanopore with a gate electrode. Lines are sketched to contrast the field across the insulator (red) with the fringe field across the liquid–vapour surface, vapour, and insulator (green). **C** Transmembrane voltages with integrated electrodes may partially drop across the insulator. Curvature of the menisci is not depicted. Dimensions and field lines are for illustration only.

These numerical simulations are limited to electrohydrodynamic phenomena, and do not consider effects such as electrochemical damage to the insulator or electric field emission. However, electric fields required for nanopore wetting will be solved, and may suggest which other phenomena may occur. As an example, a voltage drop of 1 V or more across a 2 nm-thick gate insulator would damage the insulator. It will also be interesting to see the extent to which the meniscus is distorted, and whether ejection of droplets occurs. Such phenomena are discussed in section 5.3.6.

5.3.2 Nanopore electrowetting by a transmembrane voltage across an insulating membrane

The contact-angle-driven interpretation of electrowetting can be formulated for dry hydrophobic nanopores, with voltage applied between the electrolytes on opposing sides of the membrane (Figure 5.8). This discussion focuses on nanopore in insulating membranes; the following section considers nanopores in membranes with integrated electrodes. Hydrophobic contact angles will prevent wetting according to the Young–Laplace equation 2.21. If the contact angle drops below 90° , capillary action will wet the nanopore, with the small volume of gas within the nanopore dissolving into the liquid. Achieving an apparent contact angle below 90° with the electrowetting equation 2.24³ requires a transmembrane voltage,

$$V_{\text{TM}} > \sqrt{-\frac{2\gamma \cos \theta_0}{C_M}}, \quad (5.2)$$

with membrane capacitance $C_M = \epsilon_r \epsilon_0 / L$. The contact angle is determined by the surface chemistry of the nanopore. With an initial contact angle θ_0 of 115° , water surface energy γ of 72 mN m^{-1} , and a

³Although most commonly used for metal–insulator–electrolyte systems, the electrowetting equation applies equally to electrolyte–insulator–electrolyte systems.

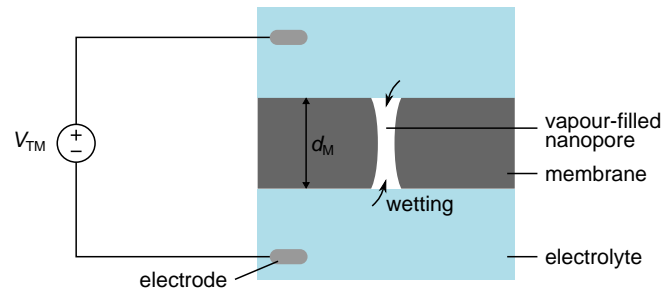


Figure 5.8 Contact-angle-driven electrowetting in a hydrophobic nanopore with a transmembrane voltage.

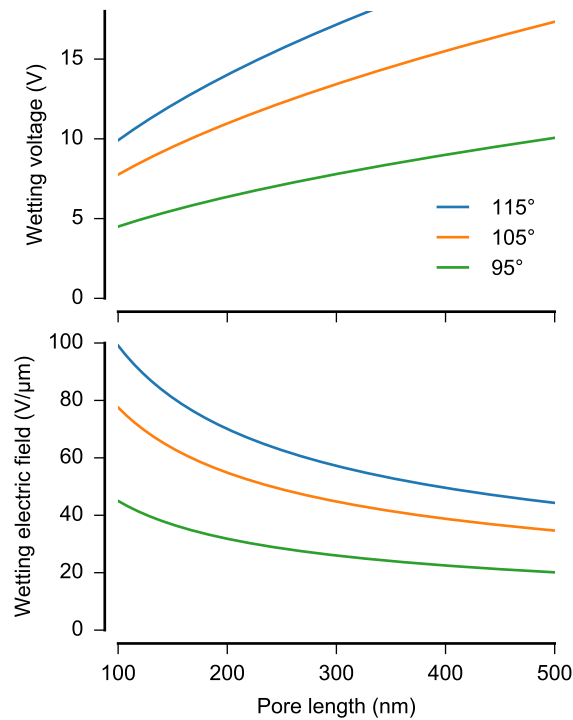


Figure 5.9 Electroswetting of hydrophobic nanopores according to the contact-angle-driven interpretation. The voltages and electric fields predicted to wet hydrophobic nanopores according to equation 5.2 are graphed for nanopore lengths of 100–500 nm and contact angles of 95–115°.

relative permittivity ϵ_r for SiN_x of 7 [185], voltages of 10, 14 or 22 V would be needed for membrane thickness L (nanopore length) of 100, 200 or 500 nm. Results for contact angles of 95°, 105°, and 115° are shown in Figure 5.9. As intrusion proceeds, the dry nanopore length (and necessary voltage) would decrease. Contributions from atmospheric pressure would reduce the wetting voltage (dependent on pore diameter) but are neglected in this simple model.

Figure 5.8 also illustrates the challenge that the contact-angle-driven interpretation, and specifically the electrochemical model, has with movement of the contact line. According to this model, the electric field across the membrane should reduce the liquid–solid surface energy. Before wetting, the internal nanopore walls are not in contact with the liquid; they should remain hydrophobic. How, then, will the liquid advance from the presumably reduced-surface-energy liquid–solid surface to regions of the dry and hydrophobic nanopore walls? What force is moving the contact line?

Of course, the contact-angle-driven interpretation does not describe local behaviour near the liquid–solid boundary or the contact line. This behaviour can only be solved by the electromechanical model, in which electric fields across the liquid–vapour interface generate Maxwell stress. In contrast to the electric fields which pull the edges of a droplet outwards (Figure 2.7), the electric fields in a nanopore will be aligned between opposing electrolytes. This contact-angle-driven interpretation may therefore

overestimate the threshold voltage for nanopore electrowetting.

Smirnov et al. described a similar estimation, but derived it as an electrostatic pressure between opposing menisci [122, equation 4]. Their estimation used the capacitance of the vapour-filled nanopore, which resulted in higher voltages due to its lower permittivity.

5.3.3 Nanopore electrowetting with gate electrodes

The contact-angle-driven interpretation can also be formulated for nanopores with integrated gate electrodes (Figure 5.10). As in the previous section, this formulation ignores the limitations of this interpretation of electrowetting. A voltage is applied between the gate electrode and the reservoir on one side of the membrane. The gate electrode is coated by a thin insulating layer.

Here, a voltage is applied between the electrolyte and integrated gate electrode. Additionally, the derivation here could apply to use of a transmembrane voltage applied between the two electrolyte reservoirs (see Figure 5.7C). By polarizing the gate electrode, the transmembrane voltage could be focused across the insulator at both ends of the nanopore. The situation would be similar to Figure 5.10, but with an additional voltage applied between the gate electrode and upper reservoir. The division of the transmembrane voltage between two interfaces separating the gate electrode from each reservoir would depend on the specific dimensions of the nanopore.

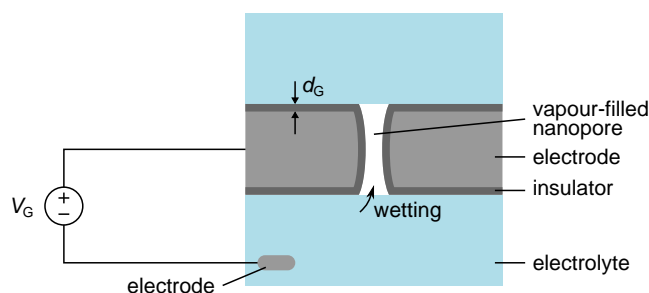


Figure 5.10 Contact-angle-driven electrowetting in a hydrophobic nanopore with an integrated gate electrode.

The conditions for wetting can be predicted as in the previous section. The voltage applied between the gate and reservoir electrodes required to reduce the apparent contact angle below 90° is

$$V_G > \sqrt{-\frac{2\gamma \cos \theta_0}{C_G}}, \quad (5.3)$$

with the specific gate capacitance in C m^{-2} comprising series contributions from the insulator (equation 2.25) and Helmholtz capacitance C_H ,

$$C_G = \left(\frac{d_G}{\epsilon_r \epsilon_0} + C_H^{-1} \right)^{-1}. \quad (5.4)$$

The specific capacitance of a PFDT SAM is $2 \mu\text{F cm}^{-2}$ [186]. With an initial contact angle θ_0 of 115° [148] and water surface energy γ of 72 mN m^{-1} , this model predicts that a gate voltage of 1.7 V would allow intrusion of water into a nanopore. A similar SAM with a contact angle of 95° would allow wetting with a gate voltage of 0.8 V .

For application of a transmembrane voltage rather than a gate voltage, the voltages between the gate electrode and each reservoir must sum to the total applied voltage: $V_{\text{TM}} = V_{G,1} + V_{G,2}$. Wetting could be predicted at each meniscus according to equation 5.3. In a symmetrical nanopore as illustrated in Figure 5.10, these gate voltages may be equal, such that $V_G = V_{\text{TM}}/2$. In an asymmetrical nanopore, the gate electrode could be biased more towards one of the electrolyte reservoirs. A higher voltage would be found between the gate electrode and the opposite reservoir, with $V_G \approx V_{\text{TM}}$. Quantitative estimates could be made by measuring the gate potential.

The limitations of this model must again be emphasized. The contact-angle-driven interpretation correctly predicts macroscopic apparent contact angles in simple geometries. With a 2 nm -thin insulator,

this apparent contact angle may be valid at distances greater than a few nanometres from the surface, but will be invalid near the surface. Within the confined geometry of a nanopore, the liquid–vapour interface and the electric field will distort and electrowetting behaviour may deviate from these predictions. More accurate predictions will require numerical solutions as discussed in section 5.3.1.

This model further assumes ideal insulation of the gate electrode by a molecularly thin film. No roughness or heterogeneity of surface chemistry is considered. This assumption may be sufficient for SAMs on gold, although additional challenges such as electrochemical stability as discussed in section 5.2 must be considered. Real application of thiol-based SAMs will be limited by their low stability. SAMs oxidize when exposed to atmospheric oxygen. Desorption of PFDT SAMs begins already at voltages of +0.6 V [187].

5.3.4 Nanopore electrowetting at high pressures

The previous sections predict that electrowetting of nanopores will occur when the apparent contact angle drops below 90°. In fact, substitution of the electrowetting equation into the Young–Laplace equation predicts that a combination of pressure and voltage will cause wetting of hydrophobic nanopores. Here, a nanopore with a gate electrode is considered with increased pressure across the liquid–vapour surface (Figure 5.11). As in the previous section, this analysis could be extended to transmembrane potentials, which would be divided between the two electrolyte–membrane interfaces.

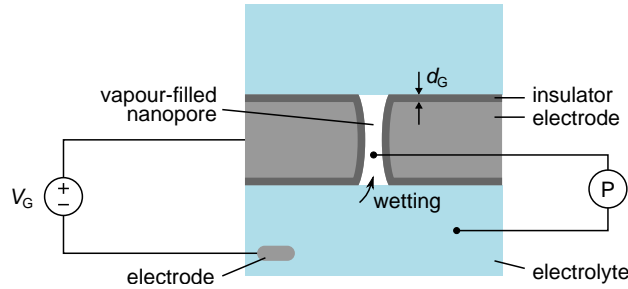


Figure 5.11 Contact-angle-driven electrowetting in a hydrophobic nanopore with an integrated gate electrode, considering additionally pressure between the liquid and vapour phases.

The conditions for wetting can be predicted by the combination of equations 2.21 and 2.24, giving

$$\Delta P = \frac{-(4\gamma \cos \theta_0 + 2C_G V_G^2)}{D_{\text{pore}}}, \quad (5.5)$$

with pressure ΔP , gate capacitance C_G , gate voltage V_G , and diameter of the nanopore D_{pore} . Wetting should occur below the hydrophilic threshold voltage due to the pressure contribution. The intrusion voltage,

$$V_{G,\text{intrusion}} = \sqrt{-\frac{D_{\text{pore}}\Delta P + 4\gamma \cos \theta_0}{2C_G}}, \quad (5.6)$$

describes the conditions for electrowetting of a nanopore at a pressure ΔP between the liquid reservoir and vapour in the nanopore. The small volume of the nanopore ensures that its vapour contents will equilibrate rapidly with dissolved gases in the liquid, reducing this pressure to zero. If the liquid is perfectly degassed, the meniscus would experience the difference between ambient pressure (near 100 kPa) and the vapour pressure of water – for example, 2.3 kPa at 20 °C [188]. However, measurement of this pressure would be unfeasible. An easier method to control this pressure may be to differentially pressurize the two liquid reservoirs, with the electrified reservoir (bottom in Figure 5.11) at a higher pressure.

Solutions to equation 5.6 are graphed in Figure 5.12 for PFDT, with a specific capacitance of $2 \mu\text{F cm}^{-2}$ [186], a contact angle of 115° [148], and pressures of 100, 500 and 1000 kPa. Internal nanopore pressure was neglected. The predicted hydrophilic limit is 1.7 V, as discussed in the previous

section. Thiol SAMs become unstable at potentials as low as 0.6 V [148] and are not well-suited for electrowetting. An optimistic electrochemical voltage limit of 1 V is also graphed. Electrowetting at 100 kPa remains inaccessible even for large pores with diameters of 500 nm. Such large pores would inhibit dewetting or may spontaneously wet [189].

Electrowetting is predicted to become possible at accessible voltages if the ambient pressure is increased. For example, a 100 nm-diameter nanopore at 1000 kPa is predicted to wet at 0.74 V. Practical realization of such experiments should be possible with thin nanopore membranes, which can withstand high pressure differences [183], especially if small membrane windows are used. Carrying out these experiments could help to understand fundamental phenomena of hydrophobicity and electrowetting, while applications could be envisioned for nanopore release from pressurized reservoirs.

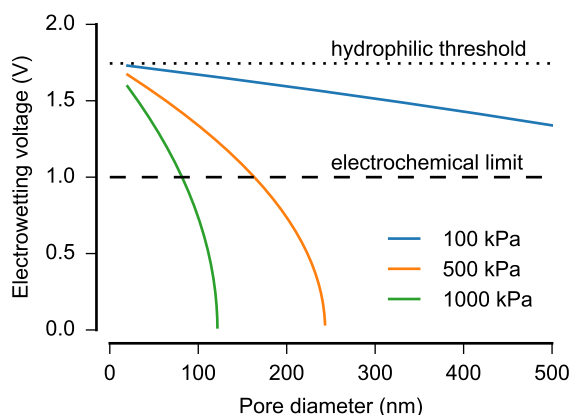


Figure 5.12 Predicted electrowetting gate voltages for gold-thiol nanopores, calculated from equation 5.6 with $\theta_0 = 115^\circ$, $C = 2 \mu\text{F cm}^{-2}$, ΔP of 100–1000 kPa, and $\gamma = 72 \text{ mN m}^{-1}$. An approximate electrochemical limit is shown at 1 V.

5.3.5 Bubble traps will enable dewetting of nanopores

This section considers nanopores with bubble traps, in the form of thin cavities extending radially within the nanopore lumen. Contact-angle-driven electrowetting is applied; the dimensions of the bubble trap challenge the validity of this interpretation, and predictions here should be validated with numerical solutions of the electromechanical model. The bubble trap structure, illustrated in 5.13, is a radial planar capillary with a thickness of L_{trap} and an outer diameter sufficiently large to be neglected. With ideal geometry, the cylindrical nanopore wall meets the plane of the trap at an edge with radius of curvature⁴ a . This model considers nanopores in the wetted state illustrated in 5.13, and does not consider how water intrudes into the nanopores. The wetting mechanism is discussed below. The low electrochemical resistance of thiol SAMs limits the evaluation of this model, although it was tested within safe voltage limits in section 5.4.6.

The Young–Laplace equation can be formulated for the meniscus spanning across the trap based on its radii of curvature, similar to the derivation for capillary stop valves in microfluidics [127]. Ideally, this liquid bridge will form an axially symmetric minimal surface of constant curvature [190]. This surface can be approximated by revolution of a circular arc around the axis of the nanopore [191], as is illustrated in 5.13. The contact line will move to achieve its equilibrium contact angle, with its position expressed by the contact line angle α . Due to this movement, the contact angle with respect to the nanopore axis may vary between the equilibrium contact angle on the walls of the nanopore and the trap. Outside of this range, the position of the contact line is not stable and will move.

The first radius of curvature is $R_1 = D_{\text{pore}}/2 + a(1 - \cos \alpha)$ and can be approximated by $R_1 \approx D_{\text{pore}}/2 +$

⁴The exact value of a has little influence as long as it is similar to or smaller than the gap thickness. Controlling the curvature or sharpness of the trap edge will be a nanofabrication challenge.

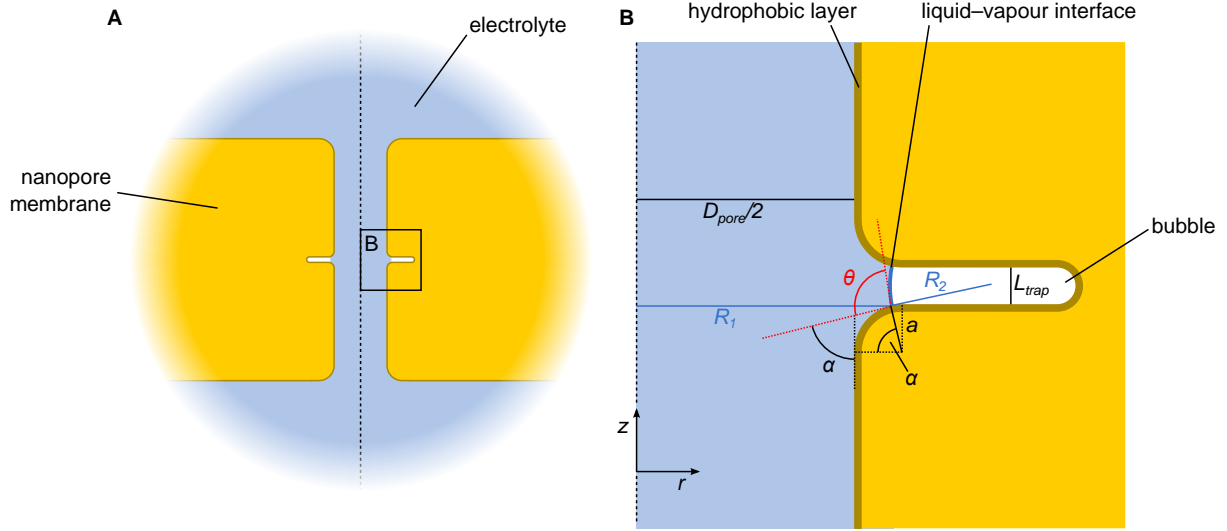


Figure 5.13 Geometry of the bubble trap in the nanopore wall. **A** A single nanopore with a circumferential cavity. **B** Magnification showing the geometry of the trap and the liquid–vapour interface. The liquid–vapour interface is approximated by revolving a circular arc of radius R_2 around the axis at R_1 .

a. The second radius of curvature depends on the thickness of the trap and is

$$R_2 = \frac{L_{\text{trap}} + 2a(1 - \sin \alpha)}{2 \sin \theta_{\text{ax}}}, \quad (5.7)$$

with the contact angle with respect to the nanopore axis $\theta_{\text{ax}} = \theta + \alpha$. R_2 extends out of the liquid phase and must be negative, so the Young–Laplace equation is

$$\Delta P = \gamma \left(\frac{1}{D_{\text{pore}}/2 + a} - \frac{2 \sin \theta_{\text{ax}}}{L_{\text{trap}} + 2a(1 - \sin \alpha)} \right). \quad (5.8)$$

Some assumptions can be applied to simplify this equation. In the wet state, $\alpha \approx 90^\circ$ such that $2a(1 - \sin \alpha) \approx 0$ and $\sin \theta_{\text{ax}} \approx \cos \theta$. Now,

$$\Delta P = \gamma \left(\frac{1}{D_{\text{pore}}/2 + a} - \frac{2 \cos \theta}{L_{\text{trap}}} \right). \quad (5.9)$$

By substitution of $\cos \theta$ into equation 2.24, the voltage at which the trap will wet is

$$V_{\text{trap}} = \sqrt{\frac{1}{C} \left(\frac{\gamma L_{\text{trap}}}{D_{\text{pore}}/2 + a} - \Delta P L_{\text{trap}} - 2\gamma \cos \theta_0 \right)}. \quad (5.10)$$

This exceeds the hydrophilic voltage limit from equation 5.3 at moderate pressures. Expected behaviour for hydrophilic capillaries would be complete wetting. This counterintuitive result predicts that the bubble trap will resist wetting even with a hydrophilic contact angle. Similar behaviour has been reported with hydrophilic materials which exhibit superhydrophobic contact angles due to three-dimensional structures on their surfaces [192] or resist wetting even by low-energy fluorinated liquids [193]. While its small height allows the hydrophobic bubble trap to resist wetting, the critical contribution to wetting resistance even with hydrophilic contact angles comes from the radius of curvature R_1 , which does not depend on contact with a solid surface.

The height of the bubble trap should be small to resist wetting, while large enough to be fabricated by practical methods. Evaporation can produce thin sacrificial layers with nanometre accuracy. The thickness of the trap must also consider the addition of a hydrophobic layer. For example, a 10 nm trap could be produced by wet etching of a 14 nm-thick layer, followed by SAM formation with a thickness of 2 nm.

Figure 5.14 shows the predicted operating voltages for hydrophobic nanopores with a 10 nm-thick bubble trap, with equation 5.6 for intrusion of water into the nanopore, equation 5.10 for intrusion of water into the trap, and the hydrophilic limit from equation 5.3. Vapour pressure of water or other gases inside the nanopore was neglected. The calculations considered the electrowetting behaviour of an ideal stable PFDT-like hydrophobic coating.

At atmospheric pressure (Figure 5.14A), a nanopore with a diameter of 100 nm would be wetted upon application of 1.7 V between the electrode and electrolyte. At this voltage, the bubble trap will resist wetting, and will remain dry even above the hydrophilic limit. A voltage up to 1.9 V may be applied before the meniscus intrudes further and wets the trap. Above this limit, the trap would wet and the reversibility of gating would be compromised by the removal of the bubble. The high wetting voltage may damage the insulator, and is only separated from irreversible wetting by a narrow margin.

At an elevated pressure of 1000 kPa (Figure 5.14B), the same nanopore would wet at 0.7 V, and should be reversible up to 1.8 V. This lower voltage may be possible without electrochemical damage, and a broad margin separates thresholds for wetting of the nanopore and the bubble trap.

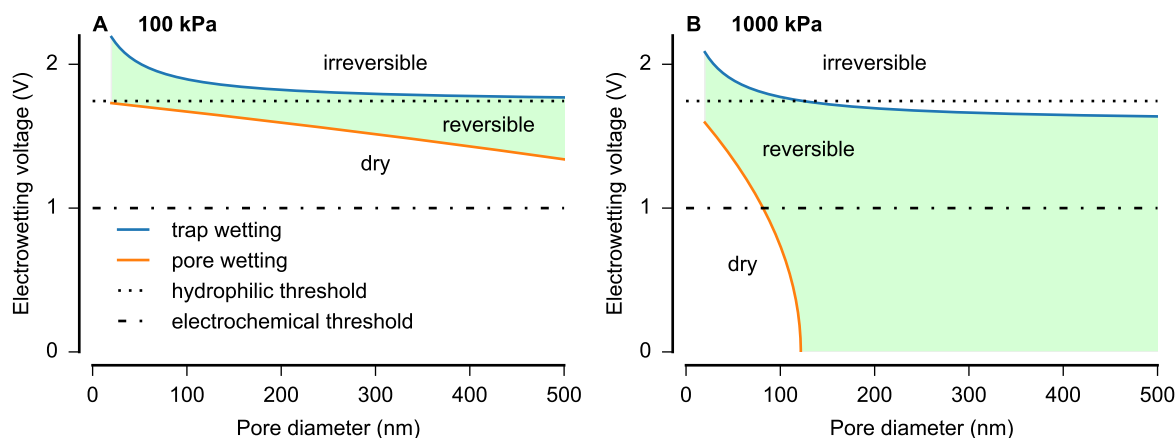


Figure 5.14 Predicted contact-angle-driven electrowetting conditions for a nanopore with a 10 nm bubble trap, for $\Delta P = 100$ kPa (A) and $\Delta P = 1000$ kPa (B). Calculations used electrowetting parameters for PFDT-coated gold, with $\theta_0 = 115^\circ$ and $C = 2 \mu\text{F cm}^{-2}$. Other parameters were $\gamma = 72 \text{ mN m}^{-1}$ and $a = 10 \text{ nm}$. An optimistic threshold for electrochemical damage to PFDT is shown.

Due to its derivation from the contact-angle-driven interpretation of electrowetting, this model ignores the underlying electromechanical mechanism of Maxwell stress acting on the liquid surface. An interesting difference between the contact-angle-driven interpretation and Maxwell stress tensor can be found by inspecting the intrusion of water into a nanopore with a circumferential vapour trap. If driven by a reduction in contact angle, the contact line pulls the meniscus into the nanopore. The meniscus may stop at the edges of the vapour trap due to capillary stop valve behaviour. If wetting proceeds from one end of the nanopore, it is not clear how the meniscus will cross the vapour trap. If wetting proceeds from both nanopore ends, it is not clear how the opposing menisci would connect, as their curvature alone will not suffice to make contact.

When explained by Maxwell stress on the meniscus, applied voltages produces stray electric fields across the meniscus, which pulls water into the nanopore against the constant contact angle. Maxwell stress deforms the meniscus, and numerical solution of the meniscus should reveal its behaviour at the vapour trap.

Although the model presented here does not reflect the underlying mechanism of electrowetting, its prediction that a circumferential cavity will trap a bubble should hold for the electromechanical interpretation, and presents an alternative to relying on random entrapment of bubbles on rough hydrophobic surfaces. After removal of the electrowetting voltage, the presence of liquid water will be unfavourable and dewetting should then be achieved as the Laplace pressure expels water from the nanopore. Optimization of layer thickness or integration of multiple layers could be investigated to ensure that dewetting is not kinetically inhibited. Numerical simulations may help to determine optimal geometry.

This model may even be extended to allow for complete wetting.⁵ Fabrication of sufficiently thin trap layers could make spontaneous evaporation kinetically accessible, by enabling nucleation of trap-spanning bubbles which could expand to circumferential bubbles and drive dewetting. This would require precise control of the trap layer, and could provide a unique method to evaluate relevant molecular dynamics simulations [147]. Fabrication of planar channels with atomic precision has recently been demonstrated [195]. Similar fabrication with hydrophobic materials could explore nucleation of vapour bubbles.

This geometry may allow trapping of bubbles in a transmembrane electrowetting configuration. An initial concept for fabrication of traps in gold–thiol nanopores was developed based on wet etching of a Ti layer (Figure 5.4) and preliminary results are presented in section 5.4.6.

5.3.6 Field emission

Some measurements of hydrophobic nanopores presented in section 5.4 can be convincingly explained as electrowetting, although such effects were observed at lower voltages than those predicted by the contact-angle-driven interpretation. However, distinct characteristics of other measurements required an alternative explanation.

These distinct measurements challenged the expectation that currents measured in nanopores indicate dissolved ions as charge carriers. Broader questions were required: What charge carriers could carry current in a nanopore? Could charged water droplets be ejected and transported through the nanopore? Could charges be transported along the pore walls? Are ions or electrons ejected from the water and transported through the vapour-filled nanopore?

In fact, two related phenomena have been observed in electrowetting experiments. In electrowetting-on-dielectric experiments, both ejection of droplets and plasma generation have been observed [134, 135]. Despite these observations, Vallet et al. also subscribed to the electrochemical interpretation of electrowetting, stating that “the principle of electrowetting is that charges are adsorbed in the conducting liquid at the liquid–solid interface” [135]. Droplet ejection was observed when using deionized water, while plasma was observed with a salt solution. In both cases, the effect coincided with saturation of contact angle when voltage was further increased. This suggests that voltage across the liquid–vapour interface approaches a limit, and any additional voltage drops across the vapour surrounding the droplet.

In the case of droplet ejection, Vallet et al. proposed that the contact line develops instabilities with large applied voltages. Droplet ejection was observed with ultrapure water, which could be explained by the ultrapure water prohibiting ionic currents necessary to sustain plasma. Droplet ejection should not occur in nanopores, as the necessary deformation of the meniscus would require radii of curvature smaller than the nanopore radius and therefore extremely high local Laplace pressures. Movement of the contact line along the nanopore walls would already occur at lower pressures.

The case of plasma generation can be explained by field emission from water. The colour of visible light observed in the gas phase around the droplet depended on the gas, demonstrating that energies of emitted particles were sufficient to produce a plasma. With a 50 μm insulator, emission was visible beginning at 500 V, corresponding to an electric field of $10 \text{ V } \mu\text{m}^{-1}$ across the insulator. The same electric field would be produced by 5 V applied across a 500 nm membrane. Notably, plasma modified the hydrophobic surface outside of the droplet boundary to be hydrophilic, while the surface wetted by the droplet remained hydrophobic. This change occurred after a single voltage cycle of several minutes.

These results suggest that moderate voltages applied across a hydrophobic nanopore may be sufficient to cause field emission. However, the length of the nanopores and the magnitude of applied voltages are insufficient to produce ionizing collisions, as particle energies will remain below ionization energies of molecules in the nanopore. Therefore, emission of light as observed by Vallet et al. would not be expected in nanopores. It is not clear what effects charged particles could have on the internal pore surfaces. Charged particles may not have enough energy to cause chemical reactions, but perhaps electrons could charge surfaces and lead to wetting.

In hydrophobic nanopores, field emission would rely on the local meniscus geometry and properties of the electrolyte. Notably, for a given configuration, voltages should be proportional to nanopore

⁵This concept was recently described for textured planar surfaces [194].

length. In contrast, section 5.3.2 predicted that electrowetting voltages scale with the square root of nanopore length. Field emission may therefore occur at lower voltages than electrowetting in shorter nanopores, while in longer nanopores the order may be reversed.

5.3.7 Related electrohydrodynamic effects

Studies or knowledge of other electrohydrodynamic effects may help advance the understanding of nanopore electrowetting. A few effects are briefly described here.

Electrospraying is a common electrohydrodynamic phenomenon, by which a high voltage drives ejection of a liquid. Electrosprayed droplets typically have diameters of micrometres or larger [196], so it is not clear whether knowledge of this effect may be applied to nanopores.

Formation of macroscopic liquid bridges by an applied voltage is an effect that is qualitatively similar to the goal of hydrophobic gating. This effect involves forming free-standing liquid channels across millimetre distances, in response to applied kilovolt potentials [197]. The magnitude of the electric field required for formation of these bridges is similar to that observed for electrowetting, but the spatial dimensions are several orders of magnitude larger. The mechanism of formation and the stability of these bridges remain poorly understood.

Closer to the scale of nanopores, liquid bridges can form between atomic force microscope tips and surfaces [198]. Formation of liquid bridges in scanning probe microscopy can be assisted by electric fields [199]. However, this effect is observed at higher voltages and at smaller dimensions in comparison to the lengths of nanopores.

5.4 Experimental explorations

This section describes experiments with electrowetting of hydrophobic nanopores. Inspiration for these experiments came from previous reports [122, 123]. Initial challenges included reliable fabrication and characterization of nanopores. Understanding of experimental results relied on characterization by ionic current measurements and destructive focused ion beam tomography. Interpretation of nanopore measurements suggests that previously unreported mechanisms contribute to the results. Insights gained during the analysis of the results allow me to suggest directions for future experiments.

Track-etched nanopores were investigated and similar results to Powell et al. were previously reported [160]. This work was not pursued due to complex fabrication (requiring particle accelerator facilities) which limited prospects for integration with common microfabrication processes.

5.4.1 Characterization of nanopores

A central challenge in nanofluidics – and specifically in nanopores – is characterization. Scanning electron microscopy (SEM) is challenged by the high aspect ratio which obscures the nanopores' internal structures. FIB cross-sectioning is destructive and requires high vacuum. Transmission electron microscopy (TEM) is limited to nanopores in thin membranes, with reduced feasibility for thicknesses above 100 nm. TEM could enable high-resolution imaging of cross-sections prepared by FIB milling, but would again be destructive.

Surface chemistry within nanopores is also difficult to determine. Methods such as atomic force microscopy, tip-enhanced Raman spectroscopy, and other scanning probe microscopies cannot access the nanopore lumen. Other methods, including x-ray photoelectron spectroscopy (XPS) and energy-dispersive x-ray spectroscopy (EDX) are limited to larger features. Internal properties of nanopores must therefore be estimated from measurements on planar substrates. Methods should be used which can be reasonably expected to give similar results within nanopores. For surface energy characterization, contact angle measurement on planar substrates is suitable.

Upon filling the nanopores with water, direct observation becomes impractical and the behaviour of the nanopore must be measured to infer details about its structures. Most commonly, measurements of ionic current are used to interrogate nanopores. Direct imaging of liquid behaviour within the nanopores is not possible. However, complex liquid behaviour has been observed directly in carbon nanotubes [200, 201] and graphene liquid cells [202], showing that formation of droplets, bubbles,

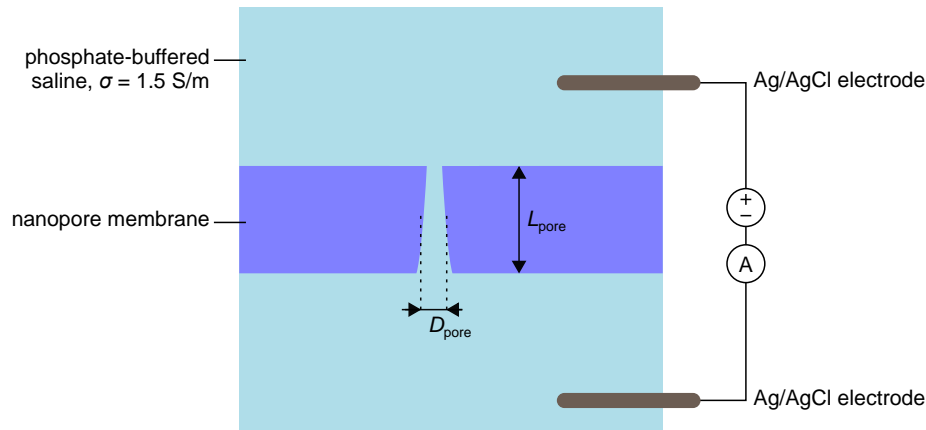


Figure 5.15 Schematic of nanopore measurements.

and menisci occur in nanoscale confinement. These complex structures illustrate the challenge of interpreting behaviour from a simple method such as ionic current recording. Practical challenges of these measurements are discussed in the following section.

Ionic current measurements are commonly used to quantify dimensions of nanopores (Figure 5.15). This requires measurement of stable, ohmic currents in fully wetted nanopores. Hydrophilic nanopores spontaneously wet by capillary action, with any vapour in the nanopore readily dissolving in water. The conductance measured at low voltages can be fit to geometric models based on some knowledge of the shape of the nanopore. A first approximation is obtained by considering a nanopore as an ohmic resistor, so that its conductance is

$$G \approx \frac{\pi \sigma D_{\text{pore}}^2}{4L_{\text{pore}}} \quad (5.11)$$

based on the conductivity σ of the electrolyte. The diameter of the nanopore can then be estimated as

$$D_{\text{pore}} \approx \sqrt{\frac{4GL_{\text{pore}}}{\pi\sigma}}. \quad (5.12)$$

This provides only a rough estimate of nanopore dimensions. At high voltages, or in small nanopores with diameters similar to the Debye length, ionic currents become rectified and this model does not apply. Milled nanopores are not uniformly cylindrical, with widening of one end due to spreading of the FIB. The cylindrical model will therefore overestimate minimum diameters. Further complexity arises from wet etching of nanopores. Models which reflect observed nanopore shapes could provide improved estimates [203]. However, the cylindrical model provided first-order estimates of nanopore dimensions in agreement with SEM images.

Nanopore systems may have large capacitances, which interfere with electrical measurements. Large contributions arise from contact between the electrolyte and the nanopore chip, either across the SiN_x film or in direct contact with Si surfaces.⁶ Integration of metal layers further increases the capacitance. Many experiments apply fixed voltages, and allow capacitive currents to decay before recording constant current. This is used in resistive pulse measurements, which measure brief changes to a constant current caused by passage of single molecules through the nanopore [93]. Current measurements at a series of stepped voltages can reveal the dependence of nanopore behaviour on electric fields [123], with capacitive currents allowed to decay at each step.

A similar method is to apply triangular voltage waves with a low scan rate (Figure 5.16). Decreasing the scan rate can reduce capacitive currents to acceptable levels. In contrast, higher scan rates reduce experiment time when scanning to higher voltages, but produce measurable capacitive currents. A separate method is impedance spectroscopy, which determines complex impedance by measuring the current response to an alternating voltage at different frequencies (Figure 5.17). The impedance spectrum

⁶Measured capacitances of a nanopore membrane chip varied due to different wetted surfaces/areas. For example, the capacitance depended on how tight the fluidic cell was assembled and the hydrophilicity of the chip.

shows a high capacitance, which was typical for nanopore membranes with integrated metal layers. Impedance spectroscopy provides information about components of the system. For example, it can validate proper filling of the fluidic cell and properly wetting of the nanopore membrane. This knowledge provides confidence that measurements probe the behaviour of the nanopore rather than other components.

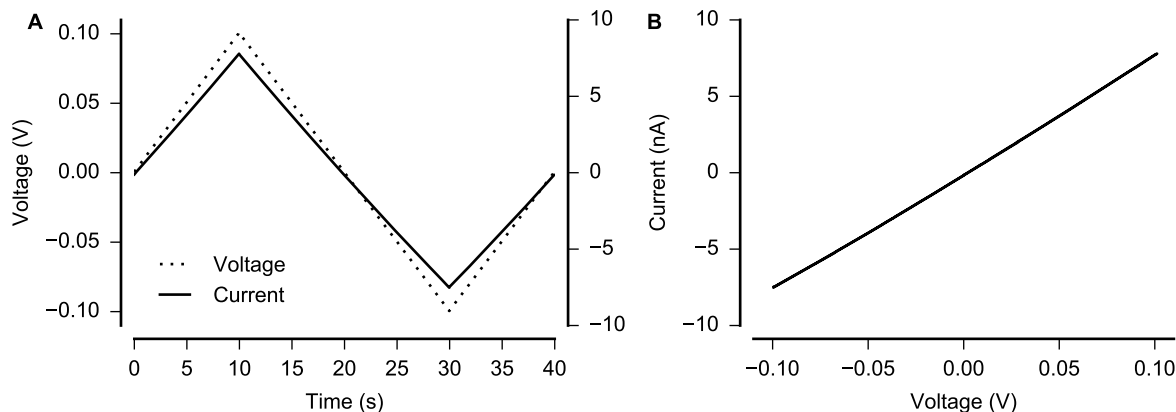


Figure 5.16 Voltage scan of a hydrophilic nanopore in a SiN_x membrane. The same measurement is displayed versus time (A) and with current versus voltage (B). Current–voltage characteristics are ohmic at low voltages. The conductance can be used to estimate nanopore dimensions. Here, the 200 nm-long nanopore had a conductance of 76 nS and an estimated nanopore diameter of 114 nm. No capacitive currents were measured due to the low scan rate of 10 mV s^{-1} .

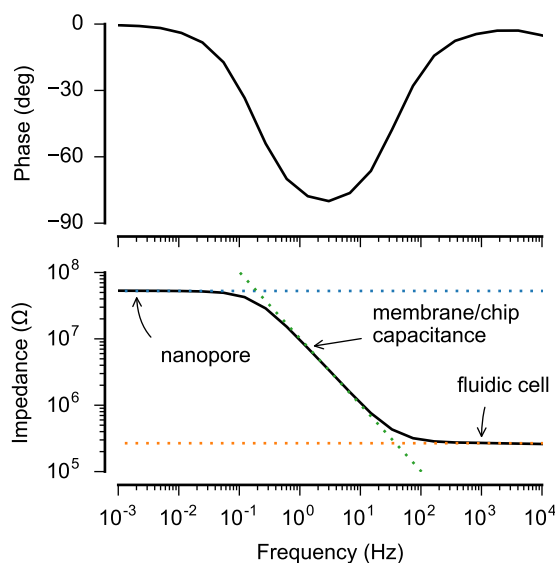


Figure 5.17 Impedance spectroscopy reveals the elements of the system. This gold/ SiN_x nanopore had an impedance of $53 \text{ M}\Omega$ (estimated diameter of 57 nm), the chip had a capacitance of 16 nF, and the fluidic cell had an impedance of $270 \text{ k}\Omega$. The high capacitance necessitated measurement of nanopore impedance at low frequency. Here, the nanopore impedance is seen at $f < 0.1 \text{ Hz}$.

Ionic current measurements also reveal information about the behaviour of a nanopore. Equation 5.11 is valid for a nanopore when it is completely filled with a conductive solution (Figure 5.15). Hydrophobic nanopores, however, may not be completely filled. If a section of the nanopore is filled with a bubble (Figure 5.18A–B), the conductance will be lower and equation 5.11 will not apply. If liquid contact across the nanopore is entirely severed, the conductance will drop to zero (Figure 5.18C–D). Knowledge about the surface chemistry of the nanopore is critical to correctly interpret conductance measurements.

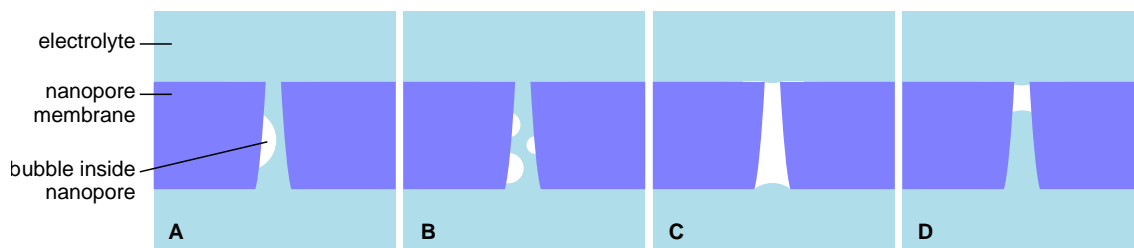


Figure 5.18 Hydrophobic nanopores may contain bubbles which may reduce the nanopore conductance (A, B) or may block the entire nanopore (C, D).

5.4.2 Nanopore fluidic cell

Ionic current recording requires mounting the nanopore chip in a fluidic cell in which the nanopore provides the only conductive path between opposite reservoirs, conceptually illustrated in Figure 5.15. Such fluidic cells are most often custom-built in individual laboratories, for example as described by Beamish et al. [204]. Figure 5.19 shows a fluidic cell used in this work, which was the final and reliable result after several generations of development. Fluidic cells consisted of two polymer blocks containing liquid reservoirs. Nanopore chips were mounted with elastomer gaskets between the blocks. The reservoirs were filled with an electrolyte, and electrodes were inserted for measurements. Unless otherwise noted, the electrolyte was phosphate-buffered saline (PBS) with a conductivity of 1.5 S m^{-1} at 21°C .

Filling of the fluidic cell with electrolyte must avoid trapping bubbles at the surface of the nanopore chip. As most researchers exclusively study wetted nanopores, bubbles are avoided by hydrophilization of the chip by piranha solution or oxygen plasma, or by priming the cell with a low surface tension liquid like ethanol followed by rinsing with the intended electrolyte.

In studying hydrophobic nanopores, it is more challenging to avoid bubbles (in fact, trapping bubbles is my goal—albeit only within the nanopore). If the nanopore chip is hydrophobic, capillary effects can often wick the electrolyte around the chip, trapping bubbles at the membrane. It can be especially challenging if the Si side of the nanopore chip is hydrophobic, as the small cavity easily traps bubbles (Figure 5.21). Priming with ethanol is impractical as it could cause irreversible wetting of the nanopore. This complicates measurements of hydrophobically blocked nanopores, which should exhibit zero conductance. Blockage by macroscopic bubbles would also give zero conductance, and must therefore be avoided.

Furthermore, confident measurements of hydrophobically blocked nanopores require elimination of leakage currents. I have observed leakage currents from picoamperes up to microamperes during nanopore measurements. Incomplete sealing or wet external surfaces of the fluidic cell lead to high leakage currents. Lower currents may arise from thin water films, for example on the gaskets. In some cases, leakage could be resolved by drying of the assembled fluidic cell with paper tissues or nitrogen. Otherwise, disassembly, thorough rinsing of all parts with isopropanol, and reassembly helped.

Two Ag/AgCl wires are most often used for nanopore measurements. Pt or gold wires have unstable potentials and should be avoided. I also evaluated three- or four-electrode configurations to separate the voltage-sensing and current-carrying electrodes, but results were indistinguishable from the two-electrode configuration. The ability of Ag/AgCl electrodes to pass currents of nanoamperes while accurately measuring voltages has also been established in patch clamp recordings [205]. Measurements were performed with a low current potentiostat (VMP3, Bio-Logic Science Instruments SAS, Claix, France).

Additionally, electrical addressing of the nanopore chip is desired to control membrane-integrated electrodes. This required making electrical connections within the fluidic cell, while avoiding disturbance of the sealing of the nanopore chip or ionic measurements of the nanopore.

The final fluidic cell design is shown in Figure 5.19, and was developed through several iterations. It consists of two polycarbonate blocks with fluidic channels, a third piece for alignment of the nanopore chip with the channels, and two elastomer gaskets for sealing. Polycarbonate pieces were produced by CNC milling. Elastomers were laser-cut from a Viton sheet and cleaned by sonication in isopropanol and water. The cell is sealed by four screws. Electrodes to contact the membrane can be included in ei-

ther side through holes in the polycarbonate blocks. The fluidic channel accepts male Luer connections at each end for direct connection by syringes. Syringes with integrated Ag/AgCl electrodes were produced by sealing Ag wire at the syringe tip with silicone. Syringe surfaces were first treated with corona discharge plasma to ensure bonding with the silicone and to prevent leakage. The Ag wires were chloridized by oxidation in a chloride solution (potassium chloride or phosphate-buffered saline) with repetitions of long pulses at +1 V and short reverse pulses at -1 V versus another Ag/AgCl wire. Excellent sealing of the fluidic cell was validated by measurement with a pristine SiN_x membrane (Figure 5.20). With intact membranes or hydrophobically blocked nanopores, leakage currents were typically below 0.06 nS, and could be reduced by meticulous cleaning of the fluidic cell.

In addition to visual inspection to avoid bubbles, impedance spectroscopy can be used to determine if the fluidic cell is properly filled and the membrane is wetted. Figure 5.17 shows an impedance spectrum for a gold-coated SiN_x nanopore chip. If a bubble is in the fluidic cell (Figure 5.21), the impedance spectrum will be affected. Figure 5.22 shows impedance spectra for a SiN_x membrane without a nanopore. Initially, the impedance spectrum (blue) showed that the fluidic cell was properly filled. Subsequent measurements (after ~6 h, orange) showed an increase in impedance above 10 Hz, which was caused by growth of a bubble in the microfluidic channel (Figure 5.21B), constricting the fluid path and leading to an increase in resistance. Further bubble growth severed the fluidic connection completely (Figure 5.22, green). If care was taken to avoid introducing bubbles during filling, and the opposite end of the channels were sealed, this problem could be avoided and continuous measurement for days was possible.

5.4.3 Hydrophobic nanopores stay dry

Resistance to wetting is often encountered in artificial nanopores, but is unwanted in most applications. Although SiN_x is hydrophilic with a native contact angle of 20°–60° [206], nanopores produced by FIB milling are coated with unspecific hydrocarbon contamination from the SEM environment [183]. Cleaning in piranha solution or oxygen plasma removes such hydrophobic contamination, and generates a hydrophilic oxidized SiN_x surface, enabling recording of reliable, low noise ionic currents [207].

I have studied various hydrophobic nanopores: SiN_x nanopores with native hydrocarbon hydrophobicity, SiN_x-silane nanopores, and gold-thiol nanopores. Nanopores in this work with diameters of 20–150 nm and contact angles above 110° would require pressures of 300–2500 kPa to be wetted (equation 2.21). At atmospheric pressure (~100 kPa), these nanopores should resist intrusion of water even if filled with a pure vacuum.

When hydrophobic nanopores are dry, they do not conduct ionic currents. This can be determined by measurements of ionic currents or impedance spectroscopy. Figure 5.23 shows measurements of a 100 nm-thick membrane containing a single hydrophobic SiN_x-silane nanopore. The nanopore (Design 4) was milled with a 10 pA FIB current for 30 s. The nanopore chip was cleaned for 30 min in 1:3 piranha solution, prepared by adding 1 part 30 % H₂O₂ to 3 parts 96 % H₂SO₄, preheated to 100 °C. The conductance of the hydrophilic nanopore was 82 nS in PBS, with an estimated diameter of 84 nm. The nanopore was rendered hydrophobic by immersion in a 1 % v/v ODMCS solution in toluene. Impedance spectroscopy revealed capacitive behaviour of the hydrophobic nanopore chip (Figure 5.23A), with a capacitance of 1 nF. Negligible conductance of 0.06 nS was measured, which was indistinguishable from measurements of an intact membrane. For comparison, the nanopore's hydrophilic conductance is shown in the steep dotted line in Figure 5.23B. Electrowetting was achieved at higher voltages, as presented in section 5.4.5 (Figure 5.30).

Gold nanopores with hydrophobic PFDT SAMs also formed effective hydrophobic blockages. An example of a hydrophobically blocked nanopore is shown in Figure 5.24. A nanopore (Design 1) was produced by milling with a 10 pA FIB current for 60 s from the SiN_x side. The nanopore had a diamond shape due to imperfect focus of the FIB. SEM observation of the opening on the milled side showed a length of 240 nm and width of 120 nm (Figure 5.24D). The nanopore chip was cleaned for 10 min in 1:50 piranha solution, prepared by adding 100 µl 30 % H₂O₂ to 5 ml 96 % H₂SO₄, preheated to 100 °C. The conductance of the hydrophilic nanopore was 35 nS in PBS (Figure 5.24B). Approximation as a cylinder by equation 5.12 gives a diameter of 153 nm. Approximation as an ellipse with an aspect ratio of 2 estimates the short and long axes⁷ as 111 nm and 222 nm, in close agreement with the observed

⁷Ellipse axes were estimated analogous to equation 5.11 with $G \approx \pi \sigma D_{\text{short}} D_{\text{long}} / 4L_{\text{pore}}$ for a given aspect ratio.

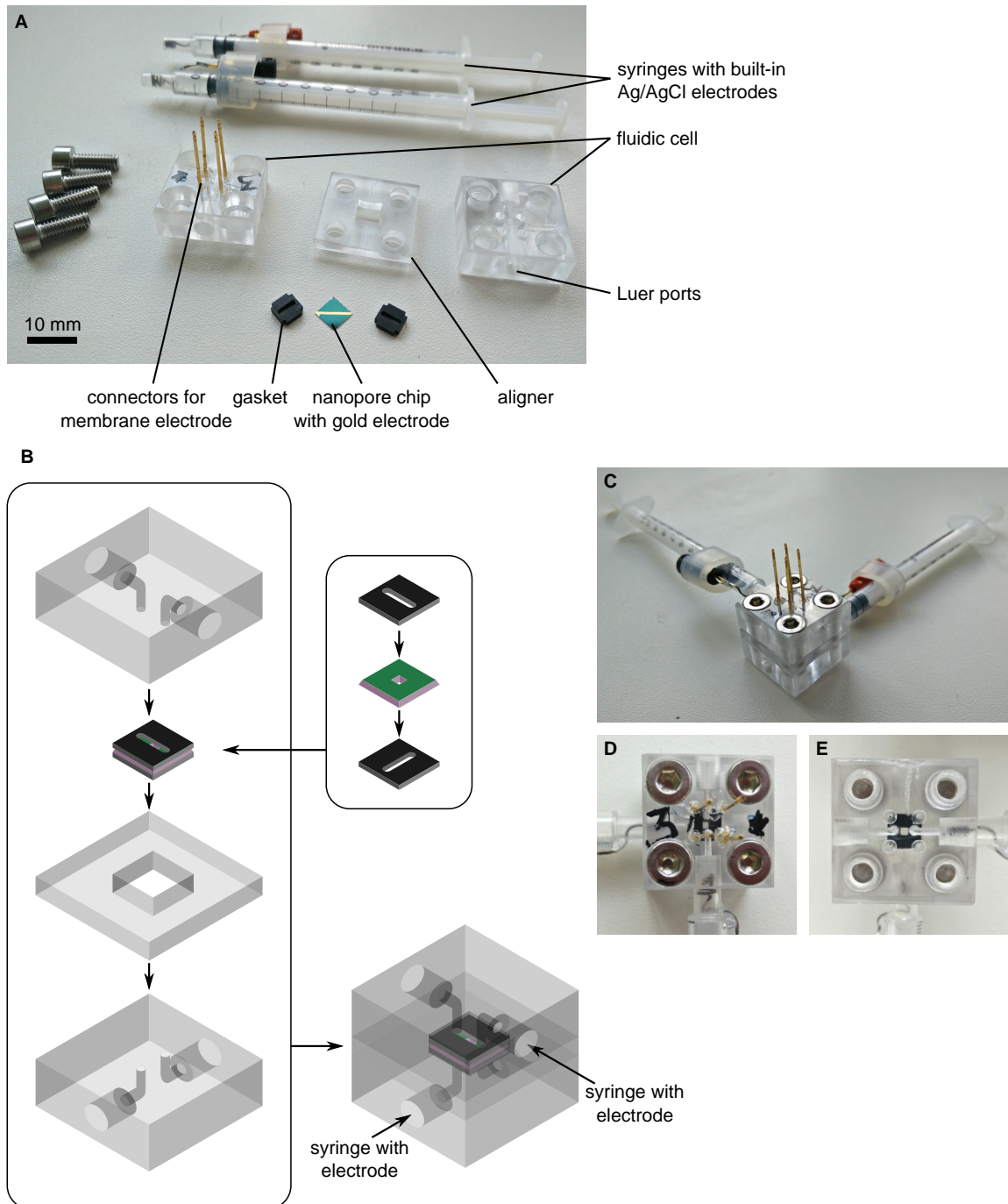


Figure 5.19 Nanopore fluidic cell. **A** Disassembled. **B** Assembly instructions. Screws, electrical connections and syringes are not shown. **C** Assembled. **D**, **E** Top and bottom view of the fluidic cell. Mounted nanopore chips can be observed to ensure proper wetting without bubbles.

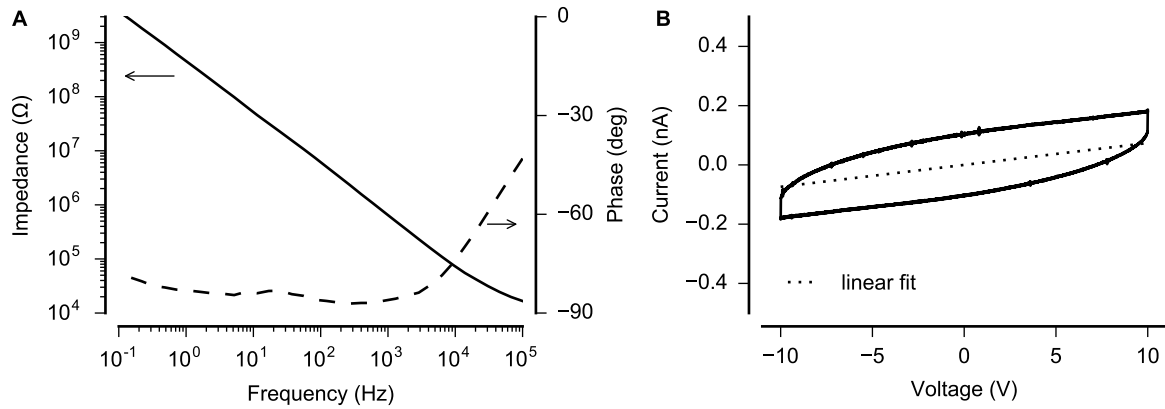


Figure 5.20 Nanopore fluidic cell validation with a pristine 500 nm-thick SiN_x membrane chip. **A** Impedance spectroscopy shows the expected capacitance of the chip and no leakage. **B** Scanning over ± 10 V shows expected capacitive currents (capacitance \times scan rate). A low leakage of 0.007 nS obtained by linear fitting is shown as a dashed line. Leakage was typically below 0.06 nS.

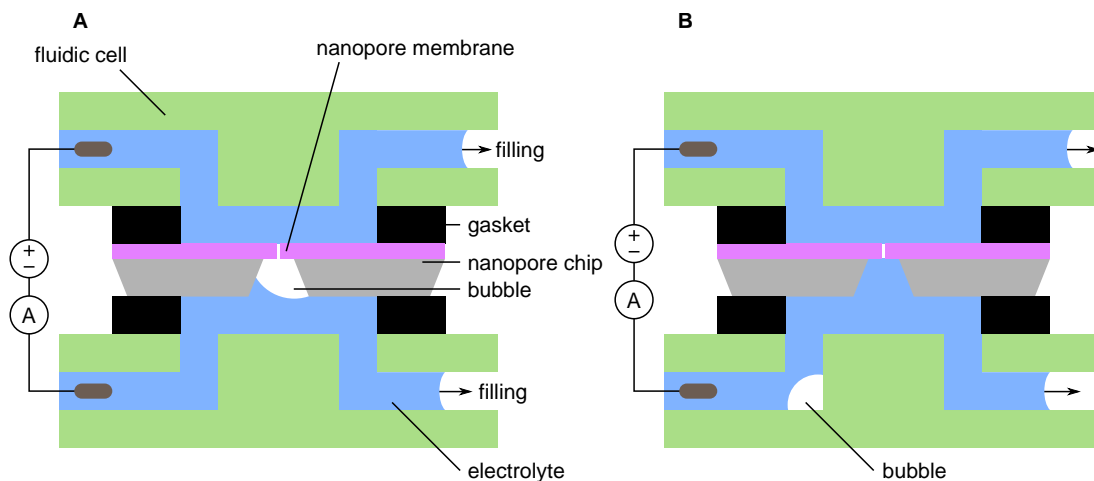


Figure 5.21 Filling of the fluidic cell can trap bubbles. **A** A bubble trapped at the nanopore membrane prevents measurement of the nanopore. **B** A bubble trapped in the fluidic cell can move or grow and create an open circuit.

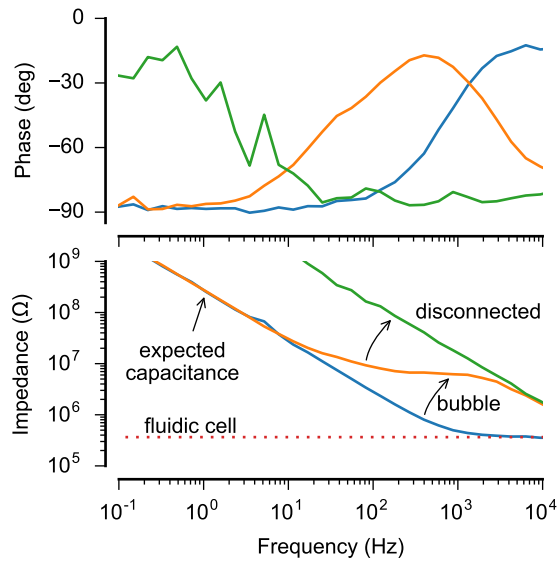


Figure 5.22 Spectra showing bubble growth in the fluidic cell. Impedance spectroscopy revealed frequency-dependent impedance contributions. Fluidic cell impedance of $350 \text{ k}\Omega$ agreed with the estimated value. A bubble in the fluidic channel caused a measurable increase in high frequency impedance after 6 h (orange), causing eventual disconnection of the conductive path (green). The apparent increase in phase at low frequencies (green) was due to limitations of measuring with a 10 mV amplitude.

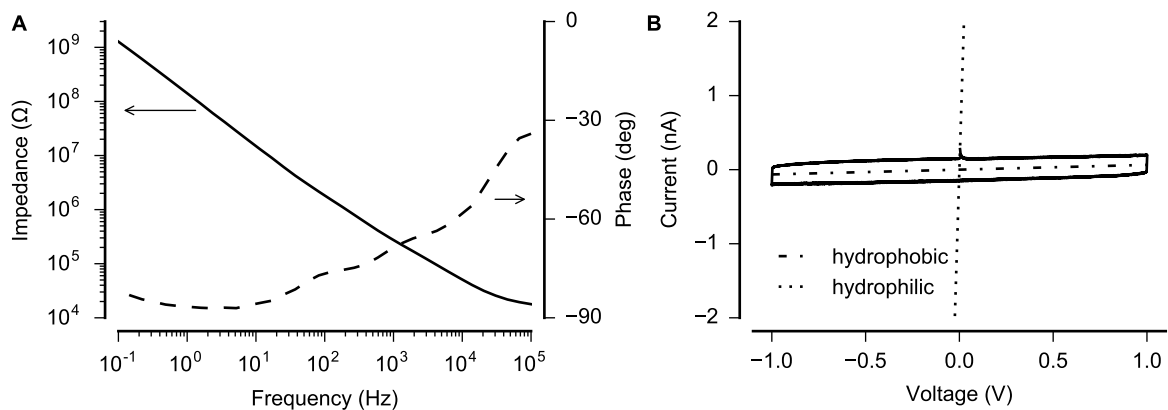


Figure 5.23 Electrical measurements of a hydrophobic SiN_x -silane nanopore verifies its dry state by negligible conductance. **A** Impedance spectrum showing capacitive behaviour of the hydrophobically blocked nanopore. **B** Scanning over $\pm 1 \text{ V}$ at 100 mV s^{-1} shows a capacitive current corresponding to the total system capacitance of 1 nF . A linear fit shows a negligible slope of 0.06 nS (dash-dot). For comparison, the dotted line shows the hydrophilic conductance of 82 nS . Electrowetting of this pore is presented in section 5.4.5 (SiN_x -3, Figure 5.30).

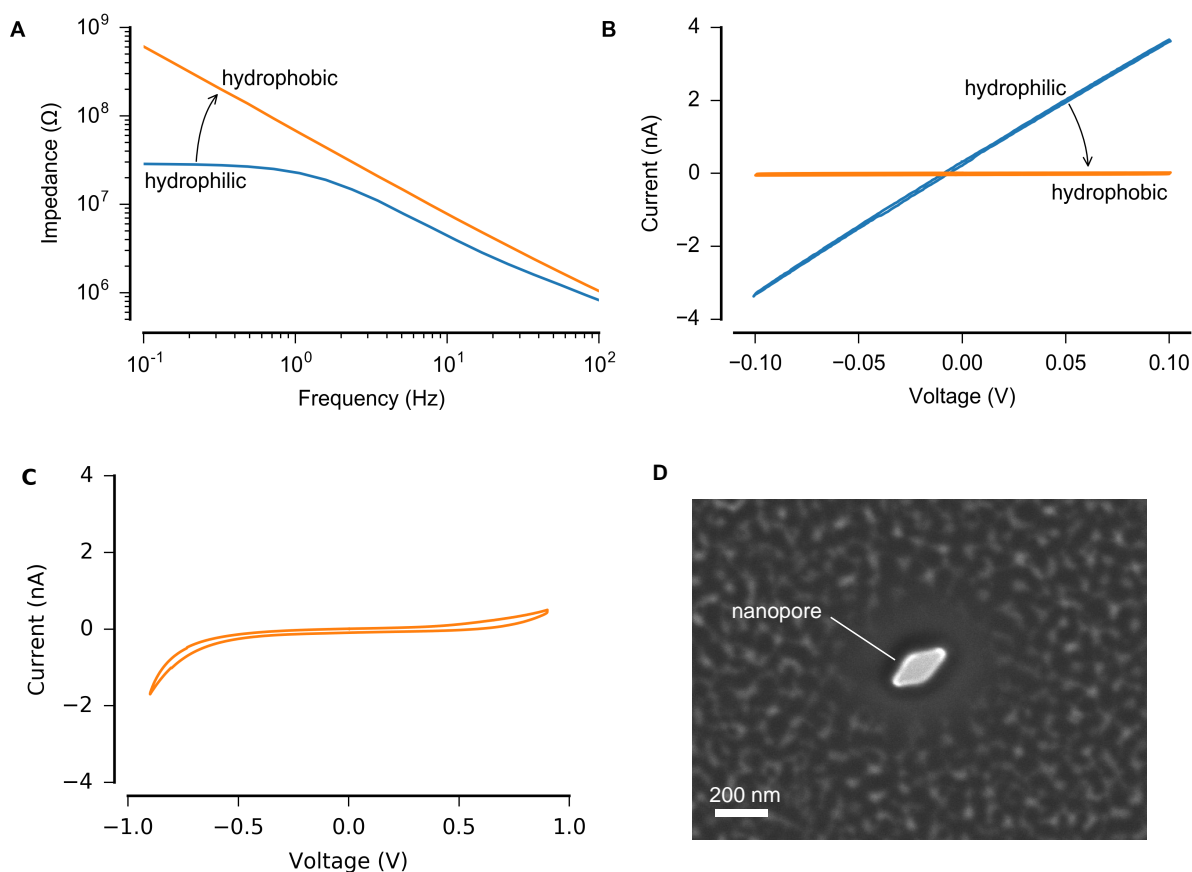


Figure 5.24 A gold–thiol nanopore forms a hydrophobic barrier. **A** The hydrophilic nanopore had a conductance of 35 nS, and was blocked after modification with hydrophobic PFDT. Impedance spectroscopy showed that the membrane was properly wetted on both sides, so that the absence of conductivity was not caused by a bubble trapped against the membrane. The increase in capacitive impedance (visible as the upwards shift of the hydrophobic impedance spectrum) can be attributed to the SAM, and to a smaller wetted area of the hydrophobic nanopore chip. **B** The hydrophilic nanopore exhibited linear conductance. Modification with PFDT blocked the nanopore. **C** The hydrophobic barrier was stable at least up to ± 0.9 V. At higher voltages, the measured current results from the metal layer acting as a bipolar electrode. **D** SEM image of the nanopore directly after milling into the SiN_x side of the membrane. The short and long axes were 120 nm and 240 nm, which agree with the measured conductance.

dimensions. The nanopore was modified with PFDT by immersion in a 1 mM solution in ethanol for 48 h, resulting in a hydrophobic surface on the gold section of the nanopore. Measurements of ionic current showed that the nanopore was blocked (Figure 5.24A,B). Voltages of up to ± 0.9 V were applied across the nanopore, and no wetting was observed (Figure 5.24C). Small currents seen at higher voltages likely bypassed the vapour barrier through the metal layer, which acted as a bipolar electrode. This effect is discussed in more detail in section 5.4.6.

5.4.4 Some hydrophobic nanopores are spontaneously wet

Hydrophobic nanopores resist wetting as explained in the previous section, and ideally will exhibit zero conductance. Because modification with ODMCS on SiN_x or PFDT on gold reliably produced hydrophobic contact angles, all hydrophobic nanopores should have formed a hydrophobic barrier. However, some nanopores were measured to be conductive after hydrophobic treatment. Two experimental weaknesses likely caused this effect. Avoiding these problems in future experiments should allow reliable production of hydrophobically blocked nanopores.

During assembly and filling of the fluidic cell, electrostatic charge may accumulate in opposing chambers, producing sufficient voltage across the membrane to electrowet the nanopores. This effect has been shown to damage 10 nm SiN_x membranes by producing voltages of up to at least 12 V [208]. A simple

solution demonstrated by Matsui et al. is to short-circuit the electrolyte chambers during filling. I had not anticipated this possibility before reading the work of Matsui et al., so this short-circuit bypass method was not used for any results presented in this work. It would be prudent to use it in all future experiments of hydrophobic gating.

In nanopores with metal layers, this problem could be caused by damage to the nanopore structures from piranha etching after FIB milling, as illustrated in Figure 5.3A. Examples of this behaviour are given below, and an SEM image of the piranha-induced damage is shown in Figure 5.3B.

This effect was studied by producing arrays of 25 nanopores (Design 1 from Table 5.1) in a grid with 15 μm pitch. Typical results are shown in Figure 5.25, with most nanopores blocked, and Figure 5.26, in which many nanopores remained wet. Individual nanopores were milled for 30 s with a current of 10 pA. The membranes were cleaned in 1:50 piranha solution for 10 min.

For the hydrophilic nanopore array in Figure 5.25, the total conductance was 859 nS, for an average of 34 nS per nanopore and estimated diameters of 157 nm (Figure 5.25A). After SAM formation for 17 h, the membrane was measured again, showing that most nanopores were hydrophobically blocked. Initially, the conductance was 61 nS, corresponding to two nanopores with diameters of 148 nm. The membrane was blown dry with nitrogen in an attempt to dry these two nanopores. Repeated rinsing and drying of the chip resulted in measurements which distinctly showed one, two, or no nanopores (Figure 5.25A), without intermediate values. This supports the interpretation that these discrete conductance steps indicate individual nanopores. After repeated measurements, a stable conductance of 32 nS (one nanopore) emerged. This state was stable with an applied voltage up to +1 V (Figure 5.25B).

In this example, conductance of individual nanopores was lower than expected from the measurement of the entire nanopore array. One explanation is that the PFDT SAM is 2 nm thick and reduces the diameter of the gold segment of each nanopore by 4 nm. However, the SAM also changes the surface charge in these nanopores, which can distort the simple cylindrical model used here. Furthermore, the structure of each nanopore will vary, as piranha etching damaged the nanopores as seen in Figure 5.3. Individual nanopores may vary due to inherent variability in the nanopore fabrication.

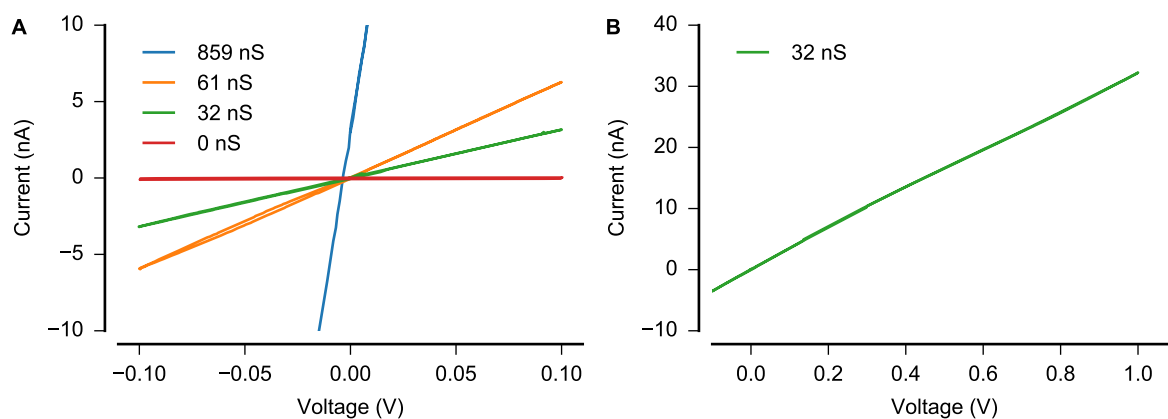


Figure 5.25 Most of twenty-five nanopores were dry after modification with a hydrophobic SAM. **A** The hydrophilic array had a conductance of 859 nS, or 34 nS per nanopore. After SAM formation, the hydrophobic array showed discrete conductance levels corresponding to zero, one, or two nanopores. **B** A stable conductance of 1 nanopore was not changed by voltages up to 1 V.

Figure 5.26 shows an example in which about half of the nanopores were wet after hydrophobic SAM formation. The 25 nanopores were milled for 30 s each with a current of 10 pA. After 10 min piranha etching, a total conductance of 676 nS was measured, corresponding to 27 nS per nanopore for an estimated diameter of 139 nm. After modification with PFDT, a stable conductance of 325 nS was measured, corresponding to 12 wetted nanopores. This conductance was stable despite blow drying with nitrogen, and measured for more than 20 min. Further results with this nanopore array are presented in section 5.4.5, showing electrowetting of the dry nanopores.

Uncontrolled wetting of SAM-modified nanopores may have resulted from damage to the gold layer during piranha etching or electrostatic effects during filling of the fluidic cell. After FIB-SEM analysis

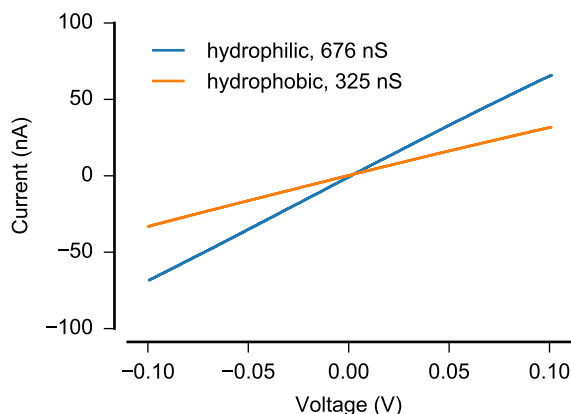


Figure 5.26 Some of twenty-five nanopores were dry after modification with a hydrophobic SAM. The hydrophilic array had a conductance of 676 nS. After SAM formation, the conductance of 325 nS corresponds to 12 wet nanopores.

showed that piranha cleaning damaged the gold layer in addition to expected etching of the Ti adhesion layer (Figure 5.3), piranha cleaning was minimized. The nanopore arrays above were etched for 10 min, which was sufficient to observe stable, ohmic conductance. Shorter cleaning of 5 min resulted in unstable, non-ohmic conductance, which may result from bubbles trapped at remaining hydrophobic regions. If damage to the gold layer produced shorter, wider nanopores, wetting may be thermodynamically favourable, with more conservative conditions than the Young–Laplace equation required to prevent wetting [189]. Lee and Karnik formulated an expression for the thermodynamic limit in ideal cylindrical pores, but emphasized that the behaviour of menisci in short nanopores is not known and transitions to thermodynamically favourable states could remain kinetically prohibited.

Variability of etching of different nanopore chips would justify why the nanopore array in Figure 5.26 had 12 wetted nanopores, while the array in Figure 5.25 showed only 1 or 2 wet nanopores. The reactivity of piranha is sensitive to its preparation and temperature. Although piranha solution was always freshly prepared, its reactivity could change quickly and variability in etching with similar preparations was observed.

Designs 2 and 3 used a sub-10 nm Cr layer for adhesion, which was more stable against piranha. However, etching of the integrated Ti layers still required piranha. Section 5.4.6 will present results on this issue.

In addition to the effects of piranha etching and variability of FIB focus, inherent material variability could also play a role. The gold layer consists of many crystallites, and thiol SAM formation varies on different crystal facets. Perfect SAM formation is not expected in the nanopores. Even on planar surfaces, SAMs will include defects, flaws at grain boundaries, and regions of reduced density or laying down molecules [209]. The well-known images of perfect crystallized SAMs are in fact only expected under ideal conditions on large Au (111) facets. Small grain sizes form incomplete SAMs [210] and similar results would be reasonable in the confined interior of a nanopore. It is also not known whether SAM formation could be affected by gallium implantation during FIB milling. If sufficiently hydrophobic SAMs do form in the nanopores, these factors could still reduce SAM stability compared to planar substrates. Therefore, nanopores here were measured as soon as possible after SAM formation, and always stored under inert conditions away from light. It will be important to study the stability of SAMs in nanopores to determine suitability for future applications.

5.4.5 Electrowetting of hydrophobic SiN_x nanopores

Results of five hydrophobic SiN_x nanopores are presented in this section: SiN_x-1 to SiN_x-5. My first experiments with SiN_x nanopores (Design 0) produced results similar to previous reports [122], including the nanopore SiN_x-1 (Figure 5.28). I moved on to study gold–thiol nanopores, as introduced in section 5.2, and obtained results presented later in this chapter. However, challenging fabrication and stability of gold–thiol nanopores led to difficulties in interpreting their results. I returned to SiN_x nanopores in

an effort to elucidate the mechanisms of nanopore electrowetting. Therefore, nanopores SiN_x-2 to SiN_x-5 (Design 4) were investigated chronologically after the gold-thiol nanopores.

The results presented here point to two putative mechanisms: electrowetting, and field emission leading to wetting. Electrowetting may occur as discussed in sections 5.3.1 and 5.3.2. The results of nanopores SiN_x-2 and -5 may be best explained by this mechanism – that is, electric-field-induced Maxwell stress across the liquid–vapour interface. Field emission in nanopores was discussed in section 5.3.6. Evidence for such a mechanism was observed in nanopores SiN_x-1, -3, and -4. A distinct current profile was measured in these nanopores, which does not fit expectations for transport of dissolved ions.

Key results are summarized in Table 5.2. Preparation and characterization of nanopores proceeded as follows, unless otherwise noted. Nanopores were produced in SiN_x membranes by FIB milling with beam currents of 2–20 pA and sufficient milling times to reliably mill through the membranes (typically 10–60 s). SEM images of the nanopores immediately after milling are shown in Figure 5.27. Membranes with thicknesses of 100, 200, or 500 nm were used. Nanopores were cleaned with piranha solution, prepared by adding 1 part 30 % H₂O₂ to 3 parts 96 % H₂SO₄, preheated to 100 °C. Hydrophilic conductance was measured by voltage scans over ±0.1 V to determine nanopore size. The electrolyte was PBS with a conductivity of 1.5 S m⁻¹ unless noted otherwise. Piranha cleaning was repeated immediately before silanization. Toluene solutions of 1 % ODMCS were prepared in a nitrogen glovebox, and nanopore chips were immersed in individual glass vials at least overnight. Nanopore chips were rinsed with fresh toluene and immersed in fresh toluene for at least 30 min, then dried and baked in an oven at 120 °C for 30 min. Voltage scans over ±0.1 V verified hydrophobic blockage. Voltage range was increased until interesting effects were observed.

An early nanopore which showed interesting behaviour was SiN_x-1 (Design 0, Figure 5.28). This nanopore was characterized before I had established reliable experimental methods.⁸ Similar behaviour was also observed in another similarly prepared nanopore. SiN_x-1 was milled in a 500 nm SiN_x membrane for 25 s at 2 pA. A first attempt to clean the nanopore with piranha solution was unsuccessful,⁹ and the nanopore remained hydrophobic due to hydrocarbon adsorption from the SEM [183]. The measurements in Figure 5.28 were obtained with this hydrophobic state. Although the nanopore was 500 nm long, the length which remained hydrophobic was unknown. Another difference was that the measurements used 150 mM KCl, rather than PBS. The nanopore's wetted conductance was eventually measured to be 13 nS, which corresponded to a diameter of 70 nm.

Initially, SiN_x-1 was insulating at low voltages. Measurements with picoampere resolution showed zero conductance through the nanopore¹⁰ below 3 V, in contrast to the silane-coated nanopores studied by Smirnov et al. Ramping to positive voltages showed no effect up +5 V, while field emission currents were observed beginning near -3 V. Currents disappeared again at low voltages, and were observed for several cycles. After multiple cycles, electrolyte currents were observed. The nanopore began to exhibit a finite conductance with stochastic fluctuations at positive voltages, and then higher currents after many cycles. These results may be explained by partial wetting with incomplete dewetting.

These results resembled those reported by Smirnov et al. in SiN_x-silane nanopores, and demonstrated that hydrophobic gating in nanopores could be achieved by other hydrophobic materials. Notably, putative field emission currents were not reported by Smirnov et al. My first interpretation of these measurements did not consider the possibility of field emission. As in the work of Smirnov et al., this gating was poorly reproducibility, with uncontrolled stochastic fluctuations and substantial changes in behaviour after tens of cycles. These factors supported the development of improved materials for hydrophobically gated nanopores.

The remaining four nanopores¹¹ (Design 4) listed in Table 5.2 were made hydrophobic with ODMCS.

⁸For example, I did not have a reliable fluidic cell, and extraordinary care was required to avoid electrolyte leakage and associated currents.

⁹Approximately 5 ml of piranha was prepared in a small beaker by mixing a 1:3 mixture of 30 % H₂O₂ and 96 % H₂SO₄. Both components were at room temperature, and the small volume allowed heat to dissipate so that the mixture's reactivity was low. Proper cleaning of nanopores required hot, reactive piranha, which can be reliably prepared by preheating the H₂SO₄ to 100 °C.

¹⁰A constant capacitive current of ±70 pA was measured, depending only on the voltage scan rate and capacitance of the nanopore chip, but without any slope which would indicate current through the membrane.

¹¹Twenty-four nanopores were produced as part of a student's internship. Due to challenging handling and a steep learning curve for experiments, useful results were obtained from four nanopores. Nanopore chips are easily damaged during handling (piranha cleaning, rinsing, mounting in the fluidic cell, and silanization).

Advancing and receding contact angles of 102° and 94° have been reported for ODMCS [177]. Three nanopores (SiN_x -2, Figure 5.29; SiN_x -4, Figure 5.31; SiN_x -5, Figure 5.32) were 200 nm long. One nanopore (SiN_x -3) was 100 nm long. SiN_x -3 was cleaned and silanized twice (first results Figure 5.30A–C and second results in Figure 5.30D). The nanopores were hydrophobically blocked at low voltages, and currents were measured through the nanopores at voltages beginning at 2.4–5.2 V. Behaviour of these nanopores is summarized in Table 5.2, and may be explained by electrowetting or field emission leading to wetting. Further detail is given below, in reference to specific measurements. The small number of nanopores and limited reproducibility between consecutive scans and between nanopores prevent strong statements about these effects. The transmembrane electrowetting voltages predicted by the contact-angle-driven interpretation (section 5.3.2) for a contact angle of 102° are 7, 10, and 16 V for 100, 200, and 500 nm-long nanopores, which are higher than those observed. In fact, current onset was observed at a wide range of voltages, in different nanopores and even in the same pore. More experiments could reveal variability arising from surface chemistry, nanopore diameter, or other factors.

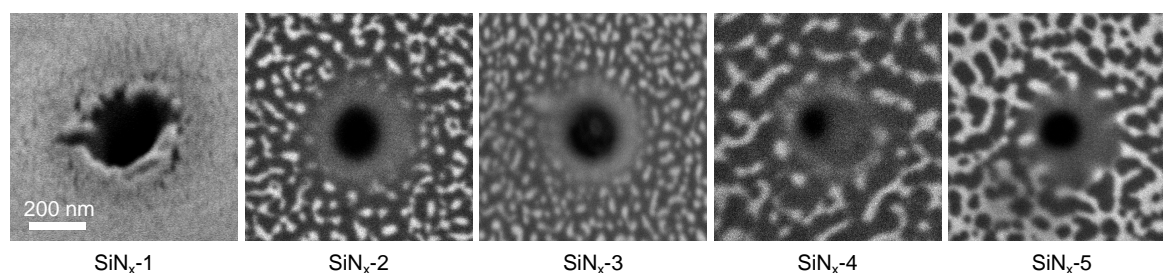


Figure 5.27 SEM of SiN_x nanopores after milling. The bright structures around the pore result from AuPd sputtered for conductivity. Nanopores SiN_x -4 and SiN_x -5 were milled for 60 s and showed evidence of beam drift. The scale bar applies to all images.

In these nanopores, hydrophobic blockage prevented the conductive electrolyte from entering the nanopore, shown by no conductance at low voltages. At higher voltages, measured currents show two distinct profiles (Figure 5.33). In all five nanopores, putative electrolyte currents were measured. In nanopores SiN_x -1, SiN_x -3, and SiN_x -4, putative field emission currents preceded the electrolyte currents, while no such currents were observed in SiN_x -2 and SiN_x -5.

Two putative mechanisms may have caused the observed wetting. The first is electrowetting, by which the menisci restrained at the ends of the nanopores experience Maxwell stress due to applied electric fields. The second mechanism is theorized to be field emission. Emitted particles may charge the nanopore walls, leading to wetting.

No consistent relationship between pore dimensions and onset voltages was observed for electrolyte or field emission currents. Onset was observed with estimated electric fields of some tens of volts per micrometre, as summarized in Table 5.2. These electric fields were estimated by the voltage and nanopore membrane thickness, and would be valid only for flat menisci separated by the full length of the nanopore. Local electric fields across real menisci will depend on their local curvature and any intrusion into the nanopore. Possible meniscus shapes illustrated in Figure 5.34 would produce greater local electric fields than the estimated values, and could facilitate both field emission and electrowetting.

Electrolyte currents occur when water partially or completely fills a nanopore, providing a path for dissolved ions. Most nanopore research uses fully wetted nanopores with stable electrolyte conductances. However, nanobubbles within nanopores reduce conductance and add current fluctuations [125]. Smeets et al. observed flickering currents and sharp transitions between multiple conductance states. The electrolyte currents observed here fit well with their results. While Smeets et al. manipulated nanobubbles with a laser, nanopores here were affected by large voltages and resulting electrohydrodynamic forces and flow.

Several features support the interpretation of the currents as occurring in the electrolyte. The currents began as a fraction of the hydrophilic conductance, which could be explained as an electrolyte path along part of the nanopore wall. In Figure 5.31L, the conductance of 4 nS at ± 0.1 V could correspond to a semicylindrical channel with a radius of 18 nm on the wall of the 69 nm-diameter nanopore (although an irregular shape would be expected). Early scans sometimes returned to zero conductance at low

Table 5.2 Summary of SiN_x nanopore results.

Pore, design, diameter, ^a length	Preparation	Hydrophobic behaviour
SiN _x -1 Design 0 <i>D</i> = 70 nm <i>L</i> = 500 nm	Milled with 2 pA for 25 s. Hydrophobic from unspecific hydrocarbons. Unknown hydrophobic length. Hydrophilic conductance ^b was 13 nS.	Figure 5.28. Field emission leading to wetting. First sharp current at -3.1 V (B). The electric field ^c was at least 6.2 V μm ⁻¹ , but the hydrophobic length within the pore was not known. Field emission (B–C), led to partially wetted electrolyte currents (D–P) with flickering (e.g. J), and eventually near-fully wetted current (Q).
SiN _x -2 Design 4 <i>D</i> = 113 nm <i>L</i> = 200 nm	Milled with 10 pA for 15 s. Piranha cleaned (hydrophilic conductance of 75 nS). Silanized with ODMCS.	Figure 5.29. Electrowetting. Hydrophobic blockage maintained after many cycles ±4 V. First currents at +5.2 V and -6 V (26–30 V μm ⁻¹). No field emission observed. Electrowetting produced flickering electrolyte currents, which returned to zero current near 0 V (G, H). Later cycles maintained conductance at low voltage (I), and approached the hydrophilic conductance (J).
SiN _x -3 Design 4 <i>D</i> = 84 nm <i>L</i> = 100 nm	Milled with 10 pA for 10 s. Piranha cleaned (hydrophilic conductance of 82 nS). Silanized with ODMCS.	Figure 5.30A–C. Field emission leading to wetting. Hydrophobic blockage maintained during cycles at ±2 V (E). Field emission first observed at negative voltages with onset between -3 and -4 V (30–40 V μm ⁻¹) (F, G), then also at positive voltages above 5.5 V (55 V μm ⁻¹) (H). After a transition at +7.3 V (I) the nanopore remained conductive at low voltages, and approached its hydrophilic conductance over subsequent scans (I–K).
	Cleaned with piranha and silanized. Similar conductance after second cleaning (85 nS).	Figure 5.30D. Hydrophobic blockage maintained over ±4 V. Field emission observed with an initial onset of +4.9 V (49 V μm ⁻¹).
SiN _x -4 Design 4 <i>D</i> = 69 nm <i>L</i> = 200 nm	Milled with 2 pA for 60 s. Piranha cleaned (hydrophilic conductance of 28 nS). Silanized with ODMCS.	Figure 5.31. Field emission leading to wetting. Field emission with initial onset at +4.4 V (22 V μm ⁻¹) (C). The onset voltage progressively increased (D–J). After a distinct transition at -6.9 V (K), partially wetted electrolyte currents were measured, and non-zero conductance remained even at low voltages (L). Another distinct transition (M) restored the nanopore's hydrophilic conductance (N).
SiN _x -5 Design 4 <i>D</i> = 70 nm <i>L</i> = 200 nm	Milled with 2 pA for 60 s. Piranha cleaned (hydrophilic conductance of 29 nS). Silanized with ODMCS.	Figure 5.32. Electrowetting. Most scans at ±4 V were hydrophobically blocked (A, E), although some sporadic currents were measured at negative voltage with onset at -2.4 to -2.8 V (12–14 V μm ⁻¹) (D, F). Scans at ±5 V measured increasing flickering currents at negative and positive voltages, returning to zero conductance (G–I), and later maintaining non-zero conductance at low voltages (J, K). The nanopore approached its hydrophilic conductance with decreasing rectification (L–M).

^aNanopore diameters were calculated with the cylindrical assumption and equation 5.12. ^bMeasured with 150 mM KCl (1.75 S m⁻¹). All other measurements used 150 mM PBS (1.5 S m⁻¹). ^cElectric fields were estimated based on the nanopore membrane thickness.

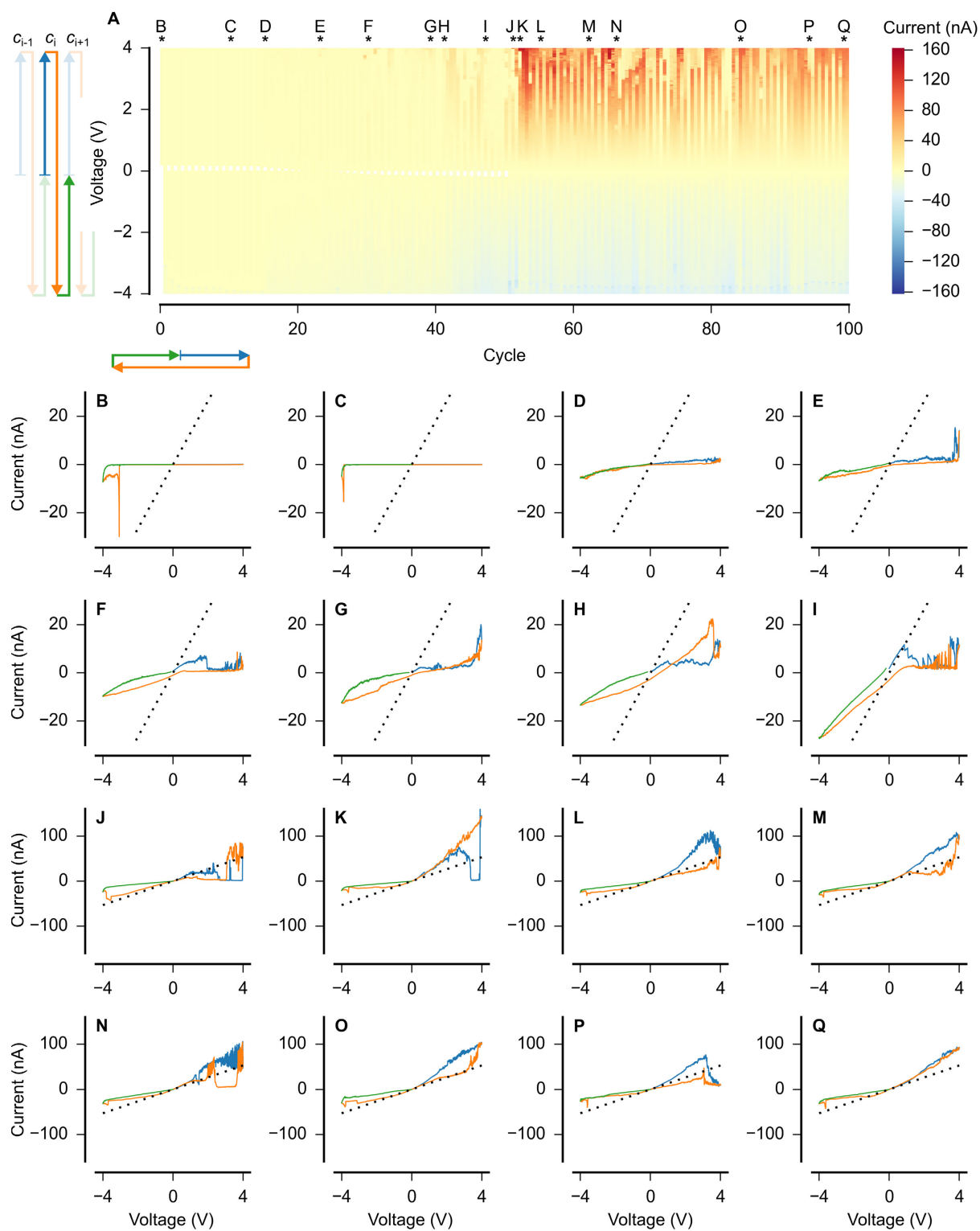


Figure 5.28 Electrowetting of a hydrophobic nanopore, SiN_x-1 (70 nm diameter, 500 nm length). Additional details are given in Table 5.2. **A** Voltage scans of the hydrophobic nanopore revealed a transition from hydrophobic blockage to wetted conductance. **B, C** Field emission currents, characterized by sharp onsets returning to zero conductance on reverse scans. **D–Q** Electrolyte currents due to partial wetting and dewetting were characterized by non-zero conductance, flickering transitions, becoming more stable over many cycles. Some cycles continued to show simultaneous field emission currents (negative peaks between -3 and -4 V, **J–Q**). The dotted line in all plots shows the hydrophilic conductance of 13 nS.

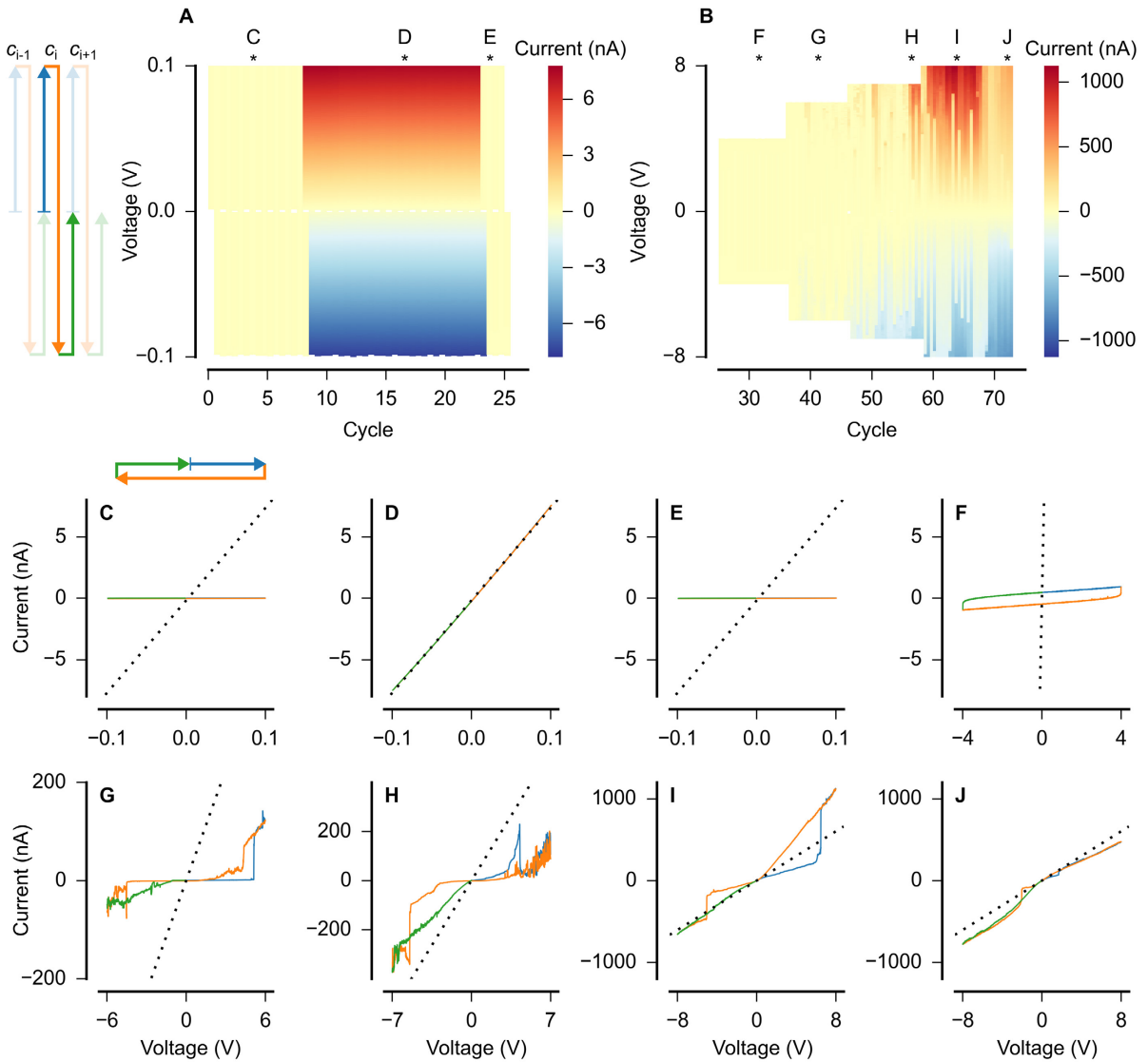


Figure 5.29 Electrowetting of a hydrophobic nanopore, SiN_x -2 (113 nm diameter, 200 nm length). Additional details are given in Table 5.2. **A** Low-voltage scans before nanopore milling (cycles 1–8), after milling and piranha cleaning (cycles 9–23), and after hydrophobization with ODMCS (cycles 24–26). The hydrophobically blocked nanopore was indistinguishable from the intact membrane. **B** High voltage scans of the hydrophobic nanopore showed no current up to ± 4 V. Currents were observed at increasing voltage ranges. **C** Intact membrane. **D** Hydrophilic nanopore (shown as a dotted line in all plots). **E, F** Nonconductive hydrophobic nanopore. Capacitive currents in **F** resulted from the scan rate of 200 mV s^{-1} , compared to 10 mV s^{-1} for the ± 0.1 V measurements. **G, H** Early scans had sharp current jumps, rapid flickering, and hysteresis. Conductance returned to zero at low voltages. **I, J** Later scans had fewer sharp transitions and maintained non-zero conductance at low voltages, approaching 75 nS.

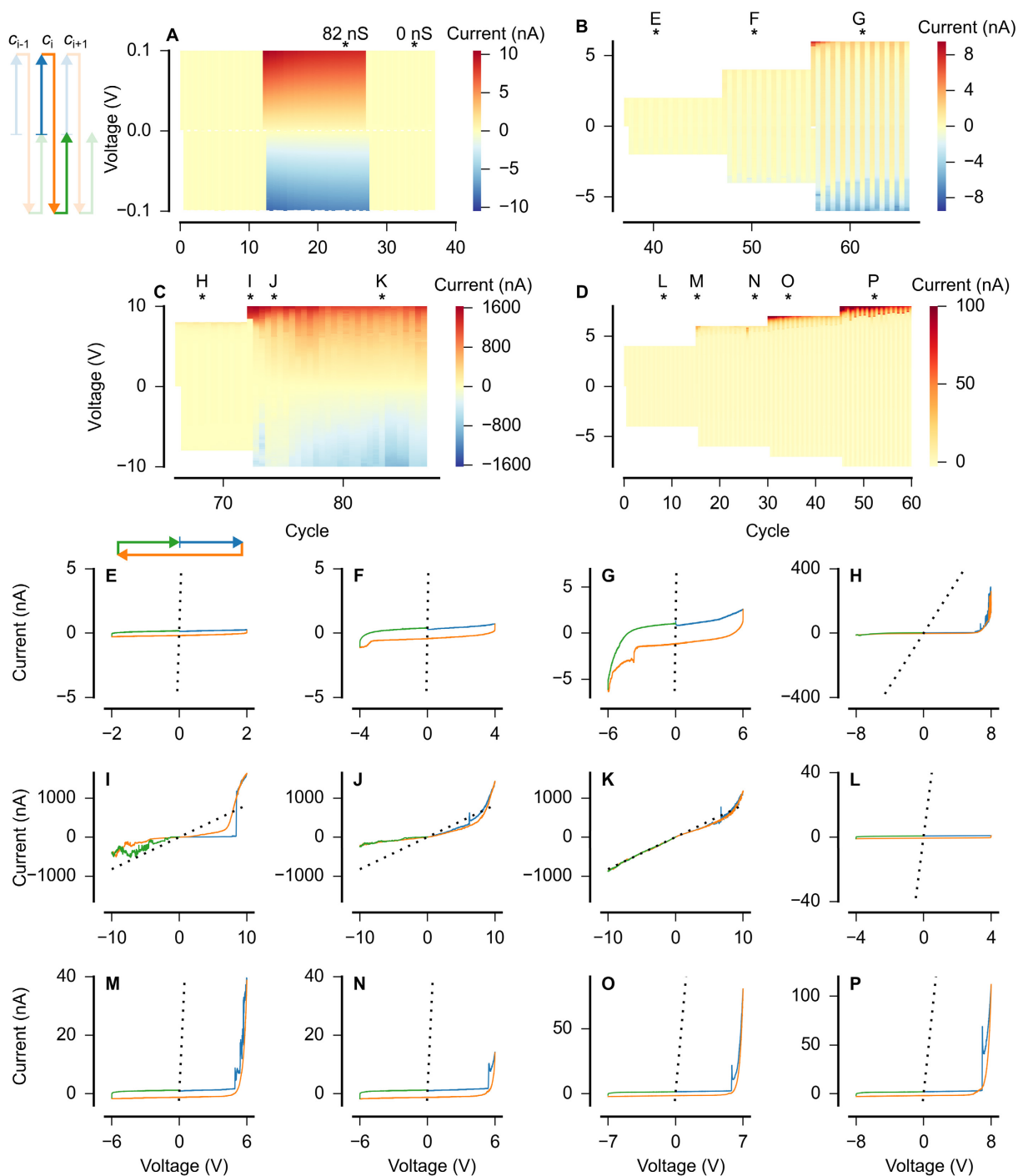


Figure 5.30 Electrowetting of a hydrophobic nanopore, SiN_x -3 (84 nm diameter, 100 nm length). Additional details are given in Table 5.2. **A** Low-voltage scans before nanopore formation (cycles 1–12), after nanopore milling and piranha cleaning (cycles 13–27), and after hydrophobicization with ODMCS (cycles 28–37). **B** High voltage scans of the hydrophobic nanopore, showed no current up to ± 2 V. Field emission currents were observed at increasing voltage ranges, beginning between -3 and -4 V. **C** After an abrupt transition (**I**), partially wetted electrolyte currents were observed. **D** After cleaning and a second silanization, hydrophobic blockage (cycles 1–15) and field emission (16–60) were again observed. Negative currents were not observed and are neglected in the colour scale. **E** Nonconductive hydrophobic nanopore. **F–H** Field emission. Conductance returned to zero at low voltages. **I–K** Partially wetted electrolyte currents began after an abrupt transition in **I**. Later scans had fewer sharp transitions, less rectification, and approached a conductance of 82 nS near 0 V. **L** Hydrophobic blockage was restored by silanization. **M–P** Field emission. The dotted line in all plots shows the hydrophilic conductance of 82 nS.

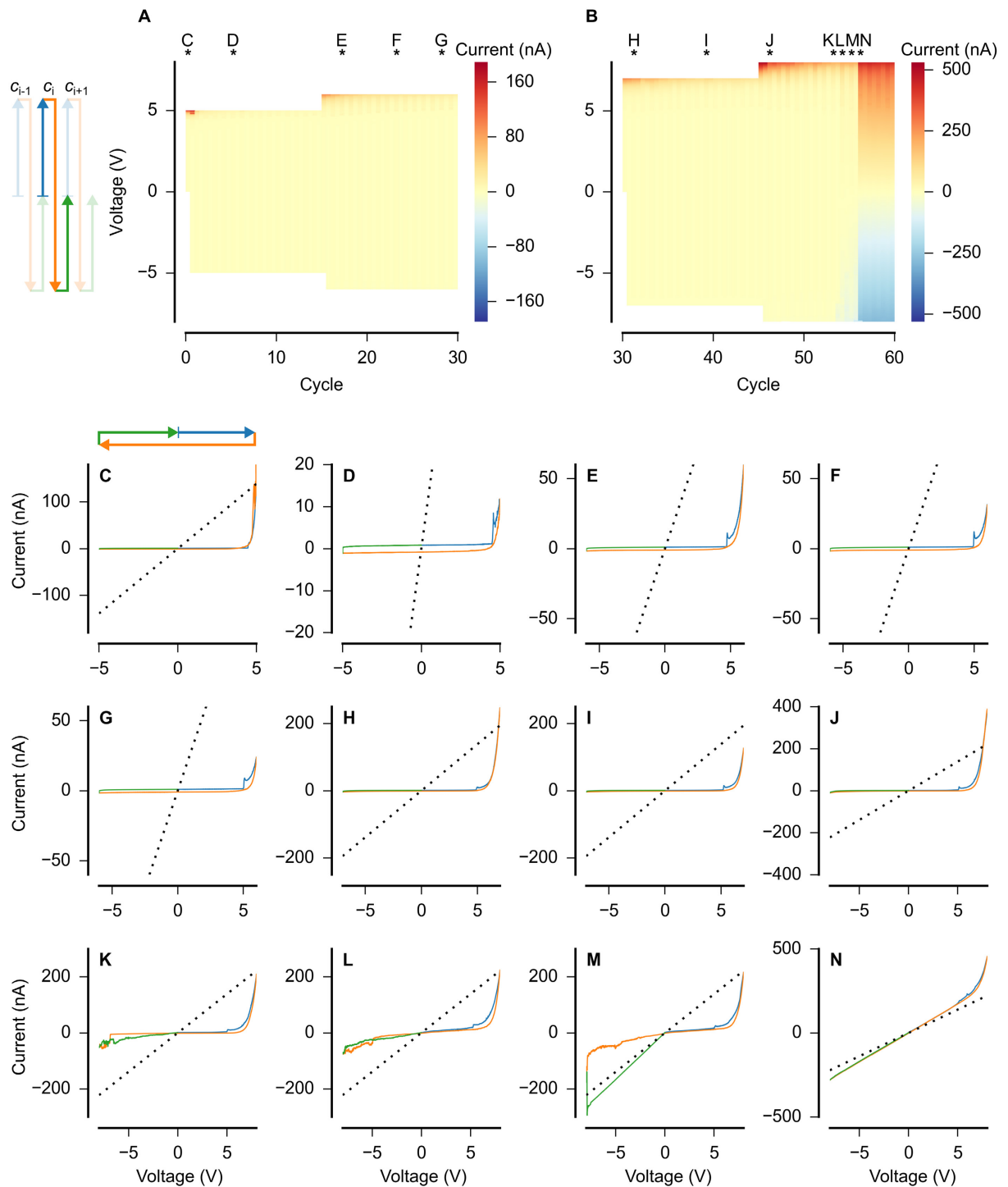


Figure 5.31 Electrowetting of a hydrophobic nanopore, SiN_x -4 (69 nm diameter, 200 nm length). Additional details are given in Table 5.2. **A, B** High voltage scans after hydrophobicization with ODMCS. Field emission currents were observed with increasing onset voltages. Electrolyte currents were observed starting at cycle 54. **C–J** Field emission. Conductance returned to zero at low voltages. **K, L** After a transition at -6.9 V, conductance remained small but non-zero at low voltage. **M, N** After another transition (near -8 V in **M**), conductance was near its hydrophilic value. The dotted line in all plots shows the hydrophilic conductance of 28 nS.

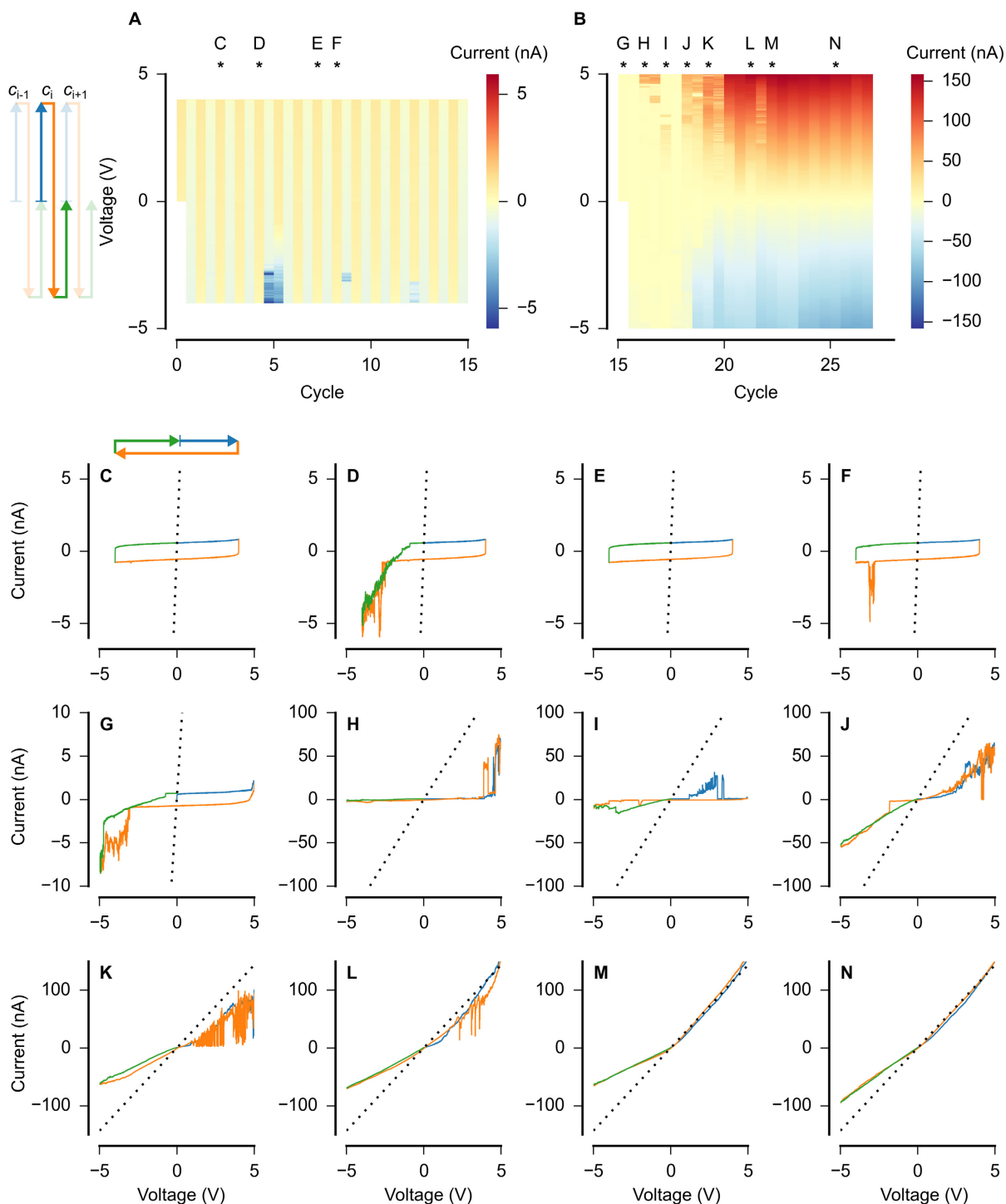


Figure 5.32 Electrowetting of a hydrophobic nanopore, SiN_x-5 (70 nm diameter, 200 nm length). Additional details are given in Table 5.2. **A, B** High voltage scans after hydrophobicization with ODMCS. **C–F** First scans showed both hydrophobic blockage and current pulses at negative voltages. **G–I** Electrolyte currents were observed and returned to zero conductance at low voltages. **J–N** In later cycles, conductance was maintained at low voltages. Flickering behaviour and sharp transitions reduced, and the nanopore approached its hydrophilic conductance. The dotted line in all plots shows the hydrophilic conductance of 29 nS.

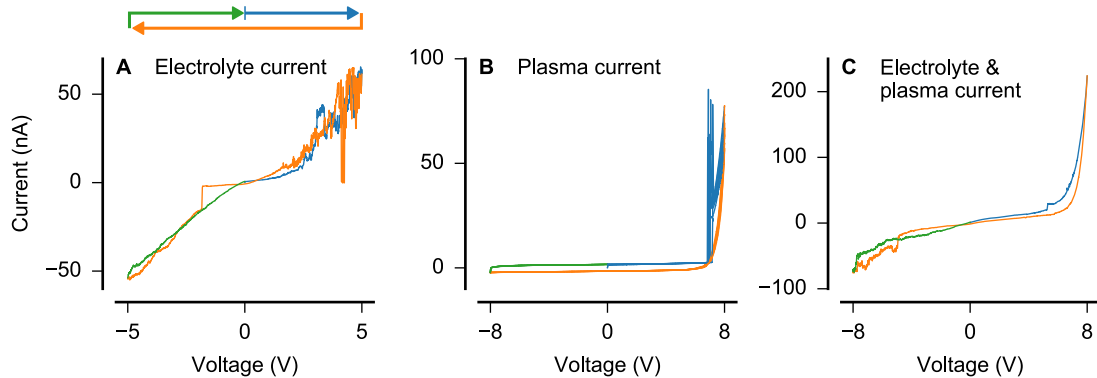


Figure 5.33 Hydrophobic nanopores may pass electrolyte or field emission currents. **A** A single voltage cycle showing electrolyte current. Reproduced from Figure 5.32J. **B** Field emission current. Eight cycles are plotted to show the reproducibility of the observed current. One cycle reproduced from Figure 5.30P. **C** A cycle showing both electrolyte currents (flickering currents at negative voltages and non-zero conductance at 0 V) and field emission current above +5.3 V. The conductance at ± 0.1 V was 16% of its hydrophilic value, suggesting that a majority of the pore's volume contained gas. Reproduced from Figure 5.31L.

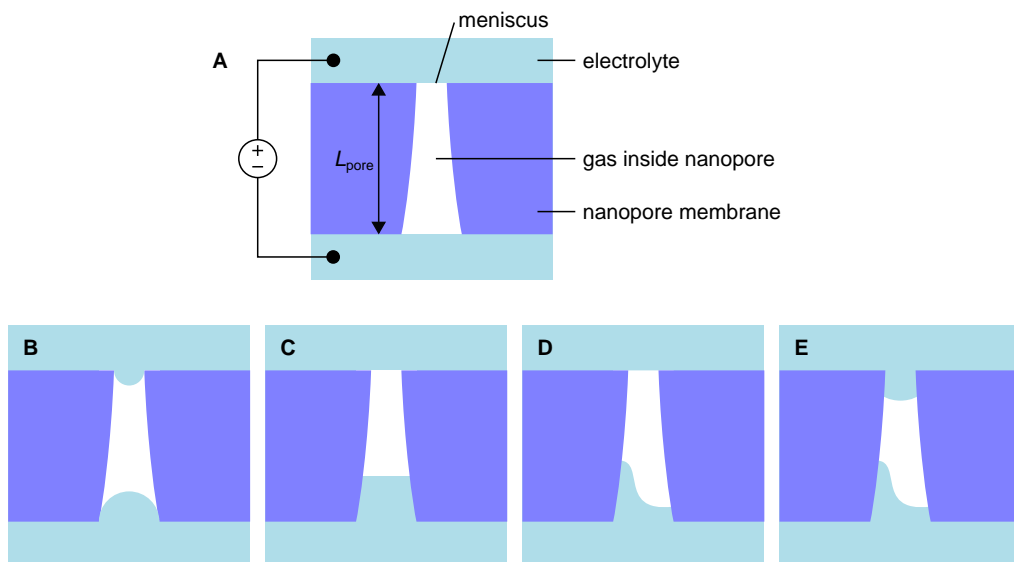


Figure 5.34 Local electric fields may be increased depending on the conformation of menisci within a nanopore. **A** Dividing voltage by the length of the nanopore gives a minimal estimate of electric fields. **B** Curved menisci would produce higher local electric fields. **C** Partial intrusion would increase electric fields. **D** Defects in a nanopore could allow asymmetrical intrusion. **E** These factors could compound to decrease voltages necessary for wetting or field emission. The illustrations here are schematic and not intended to represent real dimensions or contact angles.

voltages (Figure 5.29G); depending on geometry and surface energy of the nanopore walls, a thin electrolyte path could sever. Electrolyte remaining in the nanopore could facilitate reconnection of the path. Rectification is often observed in early scans (Figure 5.28K, Figure 5.30J) which is expected in narrow electrolyte channels under high electric fields [84]. Subsequent scans exhibit reductions in rectification (Figure 5.30J→K, Figure 5.32L→N), indicating increased wetting and broadening of the narrow electrolyte channels. Low-voltage conductance in all nanopores approached the values measured in their fully wetted, hydrophilic states. Furthermore, low voltage conductances never surpassed their expected fully wet values (higher currents at high voltages in rectified nanopores were expected from models of ionic current rectification).

Reports of plasma generation in electrowetting experiments of water droplets were introduced in section 5.3.6 [134, 135]. The voltages applied across small distances in nanopores should not be sufficient to generate plasma. However, putative field emission currents in nanopores began at field strengths of $6\text{--}30\text{ V }\mu\text{m}^{-1}$, similar to the $10\text{ V }\mu\text{m}^{-1}$ which produced plasma around an electrowetted droplet. In nanopores, these currents began with a sharp onset. After onset, the currents increased and decreased smoothly, unlike the flickering transitions observed for electrolyte currents. After an initial decrease following onset, currents increased rapidly with voltage; this nonlinear increase was larger than any observed ionic rectification in nanopores. After reversal of the scan direction, currents decreased smoothly, with hysteresis which would not be expected in electrolyte currents, and decayed to zero below the onset voltage. Consecutive cycles showed a strong reproducibility of these field emission currents (eight consecutive cycles overlap in Figure 5.33B), in contrast to the unpredictable electrolyte currents. However, subsequent cycles showed steadily increasing onset voltages, decreasing onset peak heights, and decreasing current magnitudes, as shown in Figure 5.30D and Figure 5.31A–B; the cause of these changes is unknown.

Support for the interpretation of these currents as field emission comes from Fowler–Nordheim plots of the measurements (Figure 5.35). Fowler–Nordheim equations describe field emission of electrons from metals based on tunneling through a potential barrier. The Fowler–Nordheim equation for a triangular barrier has the form [211]

$$I = Aa\phi^{-1}E^2 \exp\left(-b\phi^{3/2}/E\right) \quad (5.13)$$

with current I , emitting area A , work function ϕ , universal constants a and b . The electric field E may be assumed to be V/L_{pore} in a nanopore. The linearised form to produce Fowler–Nordheim plots is

$$\ln \frac{I}{V^2} = -\frac{bL_{\text{pore}}\phi^{3/2}}{V} - \frac{L_{\text{pore}}^2\phi}{aA} \quad (5.14)$$

so that a plot of $\ln(I/V^2)$ vs. $1/V$ should be linear with a slope of $-bL_{\text{pore}}\phi^{3/2}$ and an intercept of $-L_{\text{pore}}^2\phi/aA$. The linear section of Figure 5.35 therefore supports a field emission mechanism. The peak in the forward scan indicates the involvement of another mechanism. For example, a change in the shape of the water meniscus could result if field emission from water modifies its surface energy. Further details of these mechanisms can only be speculated.

Charge transport between liquid and plasma or gas phases can include electrons, ionized species or radicals of hydrogen, oxygen, water, or any dissolved chemicals (H^+ , OH^- , Cl^- , K^+ , Na^+ , PO_4^-) [212]. To the best of my knowledge, no field emission between two liquid water electrodes or in nanopores has been reported. Microplasmas between metal electrodes and liquid have been studied [213] but it is unknown how such results may be transferable to nanopores.

Field emission currently is the most plausible explanation for the observed currents. Further experiments are required to better understand and confirm this effect.

Electrolyte currents in nanopores $\text{SiN}_x\text{-2}$ and $\text{SiN}_x\text{-5}$ began without observed field emission currents. These results may result from electrowetting, but this interpretation must still be confirmed. After initial wetting, currents returned to zero conductance at low voltages, or flickered between conductive and non-conductive states. This behaviour could demonstrate wetting and dewetting along hydrophobic walls. In comparison, nanopores wetted after field emission currents maintained low conductances even at low voltages, which could be explained by a narrow electrolyte path forming along a charged wall of the nanopore.

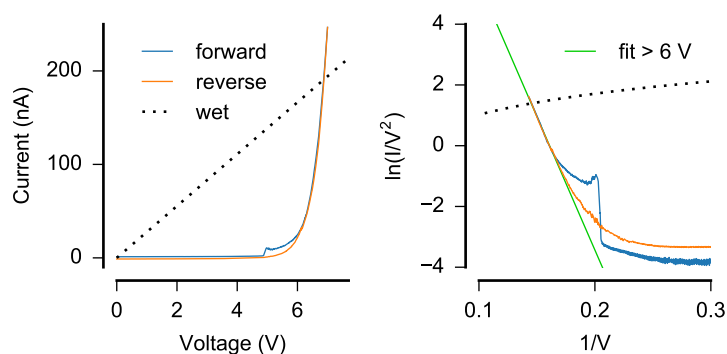


Figure 5.35 Fowler–Nordheim plot. Here, a measurement of SiN_x-4 (from Figure 5.31H) is graphed as I vs. V (left) and $\ln(I/V^2)$ vs. $1/V$ (right). The linear fit at $V > 6$ V supports the interpretation of field emission. The peak in the forward scan indicates the contribution of an unknown mechanism, which could be speculated to reflect a change in the shape of the water meniscus.

The contact-angle-driven electrowetting model predicted a wetting voltage of 10 V in these 200 nm-long nanopores assuming a contact angle of 102°. Currents were observed beginning at 2.4 V (SiN_x-5) and 5.2 V (SiN_x-2). The validity of the contact-angle-driven interpretation is questionable in these nanopores. However, even these two nanopores did not exhibit similar voltages. Lower wetting voltages may have resulted from defects in the hydrophobic modification. Hydrophilic defects could allow intrusion of water and reduction of the length of the hydrophobic blockage. Lower contact angles would reduce the required voltage. For example, the contact-angle-driven model predicts that 4.5 V would wet a 100 nm-long nanopore with a contact angle of 95°. More data with better reproducibility are needed to make strong statements.

One confounding result is that the nanopores remained wet after disassembly of the fluidic cell and manual drying. This suggests that the nanopores became hydrophilic. However, possibilities such as electrostatic discharge (section 5.4.4) during reassembly and filling of the fluidic cell cannot be ruled out.

Some cycles also showed typical characteristics of both electrolyte and field emission currents (Figure 5.33C). Such cases followed cycles of field emission current alone. The electrolyte current measured at low voltages was a small fraction of the pore's hydrophilic conductance, so the majority of the pore's volume should have contained gas. The concurrent measurement of electrolyte currents suggests that field emission may occur even in partially wetted nanopores.

5.4.6 Electrowetting of hydrophobic gold–thiol nanopores

This section presents results of gold nanopores modified with hydrophobic PFDT SAMs. Gold–thiol nanopores were investigated due to anticipated benefits introduced in section 5.2. Hydrophobic thiols form monolayers, rather than thicker layers commonly obtained with trifunctional silanes, and have lower contact angle hysteresis than monofunctional silanes, indicating smoother surfaces. The ability to hydrophobically modify electrically conductive materials also opens new possibilities for control of nanopores with gate electrodes. Finally, nanopores with a conductive, insulated layer may wet at lower transmembrane voltages as electrowetting will depend on electric fields across the thiol SAM, rather than the lower electric fields produced across the entire thickness of an insulating membrane.

Results are presented for the three gold–thiol nanopore designs introduced in Table 5.1. Fabrication challenges limited the reproducibility of these results, and made their interpretation more challenging. After nanopore milling, piranha was used to clean hydrocarbon contamination from the nanopore surfaces and obtain hydrophilic nanopores. Piranha etches neither SiN_x nor gold. However, the adhesion metal was etched. A dilute piranha recipe was used, and cleaning time was minimized, yet titanium etching was significant and resulted in damage to the gold segment of the nanopores. Use of chromium minimized this issue. Thiol chemistry presented another challenge. Thiols are sensitive to oxidation, thermal degradation, and electrochemical damage. In comparison, silane-modified SiN_x surfaces withstand high temperatures and aggressive chemistry. Some experiments were unsuccessful due to pre-

sumed damage to the thiol. Although thiols produce molecular insulating layers on metal electrodes even with fine nanometre-scale structures, electrowetting on PFDT enables only minor modulation of apparent contact angle within safe voltage limits [148].

Preliminary evidence suggests that gold–thiol nanopores have smoother surfaces than SiN_x–silane nanopores. The possibility for currents to bypass the hydrophobic nanopore by passing through the conductive membrane was encountered, which limits the voltages that may be applied across the nanopores. Electrowetting by using the gold layer as a gate electrode was attempted, but inconclusive results were obtained. Integration of multiple materials for Designs 2 and 3 produced nanopores with bubble trap structures in their walls.

Although interesting results were obtained and allowed the refinement and improvement of fabrication processes, the challenges of gold–thiol nanopores limited their use in investigating underlying electrowetting mechanisms. Further investigation of gold–thiol nanopores was suspended, and efforts to elucidate these mechanisms concentrated on the Design 4 SiN_x nanopores modified with monofunctional silanes presented in the previous section.

Gold nanopores with Ti adhesion layers were damaged and showed inconsistent results

Electrowetting of gold–thiol nanopores (Design 1) was observed at lower voltages (Figure 5.36) than in SiN_x nanopores. These lower voltages in comparison to SiN_x nanopores matched trends predicted in section 5.3, although quantitative agreement between models and experimental results was not observed. Notably, the structure of these nanopores was not well controlled. Etching of the Ti adhesion layer and damage of the gold layer occurred during piranha cleaning, resulting in widening and thinning of the gold layer at the nanopore. The transmembrane voltage was limited to ± 1 V to avoid damage to the SAM or the metal layers. This behaviour appears to be an intermediate between the results discussed in sections 5.4.3 and 5.4.4, which were always blocked and never blocked, respectively. The effect is described below for an array of hydrophobic nanopores. Arrays of nanopores were measured to examine the variability observed in single nanopore chips.

An array of 25 nanopores was milled with a FIB current of 10 pA and 25 s per nanopore. The nanopore chip was cleaned for 10 min in dilute piranha, prepared by adding 100 μ l 30 % H₂O₂ to 5 ml 96 % H₂SO₄, preheated to 100 °C. After cleaning, the hydrophilic array had a conductance of 793 nS (Figure 5.36A), corresponding to an average conductance and diameter of 32 nS and 150 nm, respectively. The array was modified with a hydrophobic SAM by immersion in a 1 mM PFDT solution in ethanol for 20 h. A conductance of 29 nS was measured for the hydrophobic nanopore array, suggesting that 1 nanopore was spontaneously wetted (as discussed in section 5.4.4). This was confirmed with repeated cycling between -0.1 and $+0.1$ V. The positive voltage limit was slowly increased, until a jump in conductance was seen above $+0.8$ V (Figure 5.36B). The upper limit was kept at $+0.9$ V and cycling continued for 2 h. Over this time, 19 individual jumps in conductance were seen, at voltages as indicated at the top of Figure 5.36B. On average, jumps were observed at $+0.84 \pm 0.08$ V. Two examples of voltage cycles illustrate the nature of these jumps. The first two jumps were almost simultaneous, and followed shortly by a third (Figure 5.36C). The measured conductances before and after these transitions supports the assertion that these jumps reflect wetting of individual nanopores. After these three jumps, the conductance corresponded to four nanopores with 32 nS per nanopore. Similar results in Figure 5.36D show the wetting of three more nanopores, evident as three distinct jumps resulting in a conductance of 32 nS per nanopore for seven nanopores. As measurements continued, nanopores continued to wet (Figure 5.36B). A maximum conductance of 558 nS was measured and no further increases were measured. This conductance should correspond to 17 or 18 nanopores, although some drift in the conductance was also observed. The drift may have been caused by changes in the structure or chemistry of the nanopore surfaces. For example, changes in the structure of SiN_x nanopores have been observed [214] or polarization of gold surfaces can affect conductance [215].

Spontaneous dewetting of these nanopores was not observed. After the conductance of 558 nS was reached, the nanopore chip was rinsed, dried, and returned to the fluidic cell. The conductance after drying was 111 nS (Figure 5.36A). This suggests that two additional nanopores were spontaneously wet, which may have been caused by changes during the 2 h of cycling. However, most of the wetted nanopores returned to the dry state, confirming that most nanopores were undamaged.

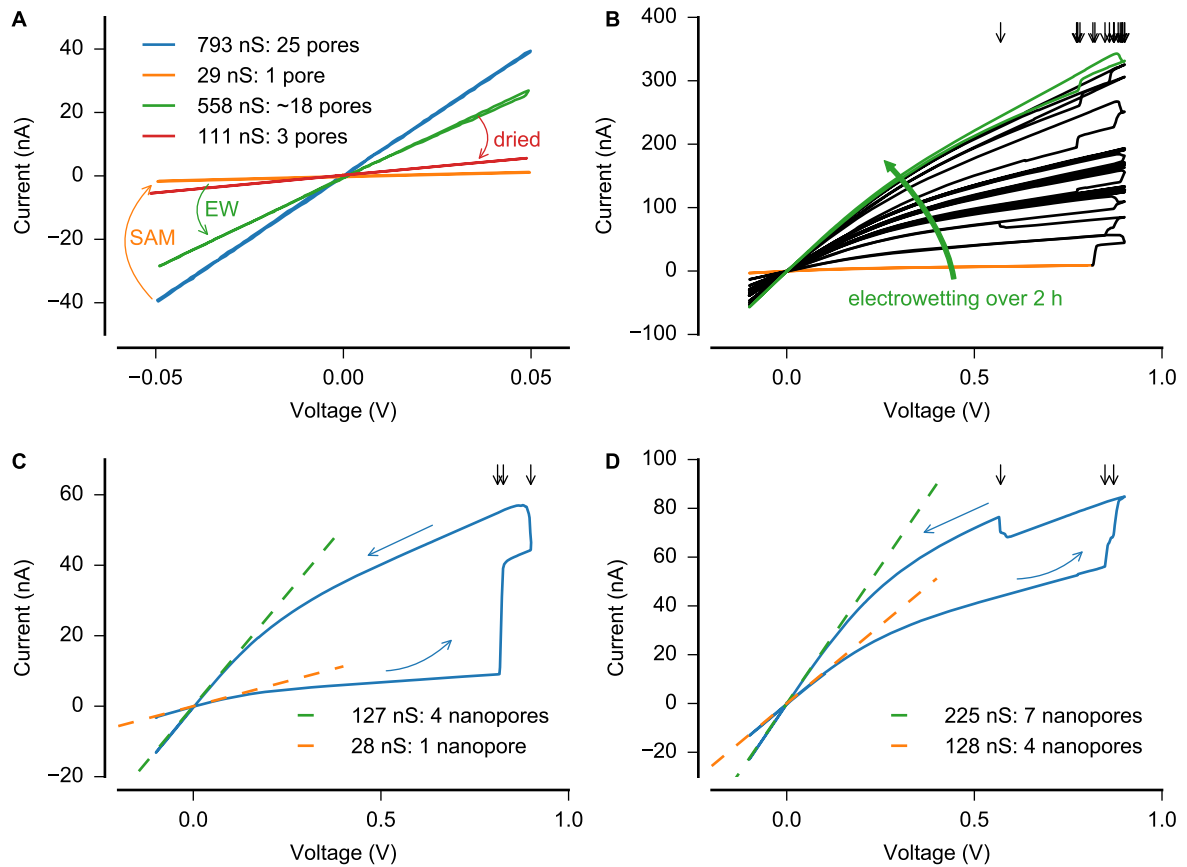


Figure 5.36 Electrowetting of a gold-thiol nanopore array. **A** After piranha cleaning, the array had a conductance of 793 nS for an average conductance of 32 nS per nanopore. After coating with PFDT, one nanopore remained wet with a conductance of 29 nS. Electrowetting caused the conductance to increase in discrete jumps to a maximum of 558 nS. **B** Electrowetting was observed during cycling up to 0.9 V over 2 h (scan rate 10 mV s^{-1}). Individual jumps in conductance were observed and are identified above the plot. **C, D** Examples of voltage cycles during which wetting of nanopores was observed.

These results of electrowetting illustrate different behaviour than the absence of gating in section 5.4.3 or the spontaneous wetting in section 5.4.4. One contribution to spontaneous wetting may have been damage and thinning of the gold section of the nanopores by piranha cleaning. However, it is also not known why many voltage cycles could occur before wetting occurs. For example, the measurements shown in Figure 5.36 were performed over ~ 2 h. Some nanopores wetted in the first scan to higher voltages, but others remained dry for many cycles. Wetting by Maxwell stress on the liquid–vapour interface would have been expected to wet the nanopores on the first cycle above the threshold voltage. Field emission is not expected to have contributed to wetting, or was at least not observed similar to in SiN_x nanopores. Furthermore, rinsing and drying restored the dry state of most nanopores (Figure 5.36A), suggesting that wetting was not caused by changes to their structure or surfaces. However, there is a possibility that the nanopores were damaged, resulting in wetting, and then recovered their hydrophobicity when dried. Examples of movement of thiolates on gold have been reported [180].

In comparison to behaviour in SiN_x nanopores, wetting of individual gold–thiol nanopores occurred as single distinct events. No flickering between conductance states or evidence of partial wetting was observed in the results in Figure 5.36. This observation may indicate that the hydrophobic surfaces of PFDT on gold are smoother than the silane-modified SiN_x surfaces. Smoother surfaces could allow the menisci to smoothly intrude into the nanopores, whereas rough surfaces would be expected to pin the contact line and trap bubbles [128]. Better control of the structure of nanopores and more reproducible results will be necessary to investigate the behaviour of gold–thiol nanopores.

Conductive membranes pass current as bipolar electrodes

Experiments with gold–thiol nanopores showed that current may bypass hydrophobically blocked nanopores, passing instead through the metal. In such cases, the metal layers act as a bipolar electrode: “an electrically conductive material that promotes electrochemical reactions at its extremities (poles) even in the absence of a direct ohmic contact” [216]. The voltage applied across the electrolyte–metal–electrolyte system drives redox reactions across each electrolyte–metal interface, as illustrated in Figure 5.37.

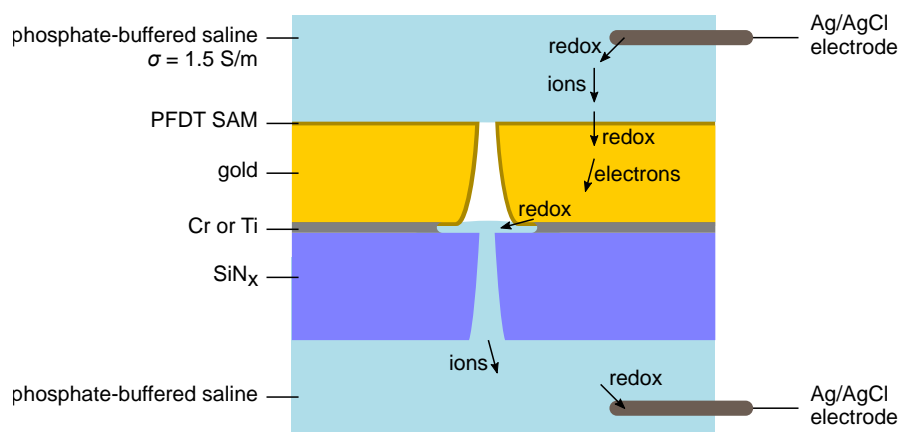


Figure 5.37 Conductive membranes act as bipolar electrodes. The conductive membrane is in contact with opposing electrolyte reservoirs. Applied voltages can drive redox reactions, providing an alternate route for current which bypasses a vapour blockage in a hydrophobic nanopore.

Current through the metallized membrane would show characteristics of the wetted SiN_x segment of the nanopore, as well as the redox reactions at the electrolyte–gold interface. These reactions will depend on the chemical species in the electrolyte and electrode material. Redox reactions have specific potentials at which the reaction rate increases steeply, resulting in nonlinear voltage dependence of faradaic electrochemical currents. Such currents contrast with ionic currents through nanopores, which are ohmic at low voltages. Reactions would also be influenced by functionalization of the electrode, for example with PFDT as shown in Figure 5.37. Current could pass through inherent defects in the SAM or through defects produced by electrochemical desorption.

Figure 5.24 in section 5.4.3 showed measurements with a gold–thiol nanopore (Design 1). Its hydrophilic conductance was 35 nS. After functionalization with PFDT, its low voltage conductance was 0 nS, showing that it was hydrophobically blocked. Bipolar electrode behaviour became evident at higher voltages, shown in Figure 5.24C. The measured currents increased nonlinearly, as expected for electrochemical currents, while the conductance at low voltages remained small. The difference between positive and negative voltages can be explained by different accessible electrochemical reactions, limited by the small area of the electrode–electrolyte interface within the nanopore.

Current passing through the bipolar membrane electrode may limit the possible voltages that can be applied across nanopores in conducting membranes in a transmembrane configuration. This alternative current route allows voltage to drop along an unintended path in the system, such that voltage across the liquid–vapour interface will be less than the total applied voltage. Furthermore, electrochemical reactions may damage the nanopore, change local pH or chemical concentrations, or produce bubbles. Such effects have been studied with unipolar Pt electrodes recessed within nanopores [164].

Attempts at electrowetting with gate electrodes

Electrowetting of nanopores with integrated gate electrodes was attempted, to test the model presented in section 5.3.3. The model predicts that PFDT-coated gold nanopores will require 1.7 V to be wetted (Figure 5.12), which is higher than the electrochemical stability of PFDT. Here, the model was tested experimentally, to explore if any effects could be observed within the electrochemical limits of PFDT. However, applied potentials up to ± 1 V had no effect. Higher voltages were not tested, as damage to the PFDT or gold was expected.

The experimental setup is illustrated in Figure 5.38A with a single nanopore (design 1). Shared counter and reference electrodes in the top reservoir were connected with a potentiostat to two independently controlled working electrodes, addressing the gold electrode integrated on the membrane and a Ag/AgCl electrode in the bottom reservoir. Representative results are presented in Figure 5.38, measured with the nanopore array also presented in Figure 5.36. The nanopore array had 3 or 4 nanopores which were spontaneously wetted (as explained previously in section 5.4.4), measured as a conductance of 130 nS. Pulses of various amplitudes up to ± 1 V vs. Ag/AgCl were applied to the membrane for several seconds, over a period of 20 min. Two example pulses are shown in Figure 5.38B. Between pulses, ionic currents through the nanopores were measured over ± 50 mV to monitor changes in conductance. Figure 5.38C shows the nanopore conductance initially and after 20 min of attempted electrowetting. The minor changes in conductance were likely caused by changes of surface charge in the wetted nanopores [215]. However, no wetting of additional nanopores was observed.

No established materials provide the capability to insulate this type of nanopore electrode with a thin, conformal layer with sufficient dielectric strength. Polymers commonly used as insulators in electrowetting have insufficient dielectric strength in thin layers [131] and cannot be coated inside nanopores. Materials produced by atomic layer deposition could enable the necessary conformal coating of nanopores, can have sufficient dielectric strength [217], and could be modified by hydrophobic silane chemistry [218]. Further possibilities include using a material with a large relative permittivity to reduce required voltages [131].

Fabrication of circumferential bubble traps

Nanopores with vapour traps were produced by evaporation of several metal layers, FIB milling, and wet etching (Figure 5.39). Fine control of layer thickness required evaporation rather than sputtering. A thin Cr adhesion layer was evaporated, followed by two gold layers separated by a Ti sacrificial layer. Nanopores were fabricated by FIB milling (Figure 5.39A). To create the bubble trap, etching of the Ti layer in HF was attempted. Wetting small structures with HF can be difficult, so the nanopore chips were treated on both sides with oxygen plasma, wetted with isopropanol, and while still wet, immersed in a 1 % HF solution for 5 min. The etch rate¹² of planar sputtered Ti in 1 % HF is expected to be 250 nm min⁻¹, although a reduction in the confinement of the nanopore was expected. FIB cross-sections revealed no etching of the Ti layer (Figure 5.39B). Piranha etching was then used. H₂SO₄ (20 ml, 96 %)

¹²The etch rate of sputtered Ti in 4.5 % HF is 1100 nm min⁻¹, and decreases linearly with concentration [219].

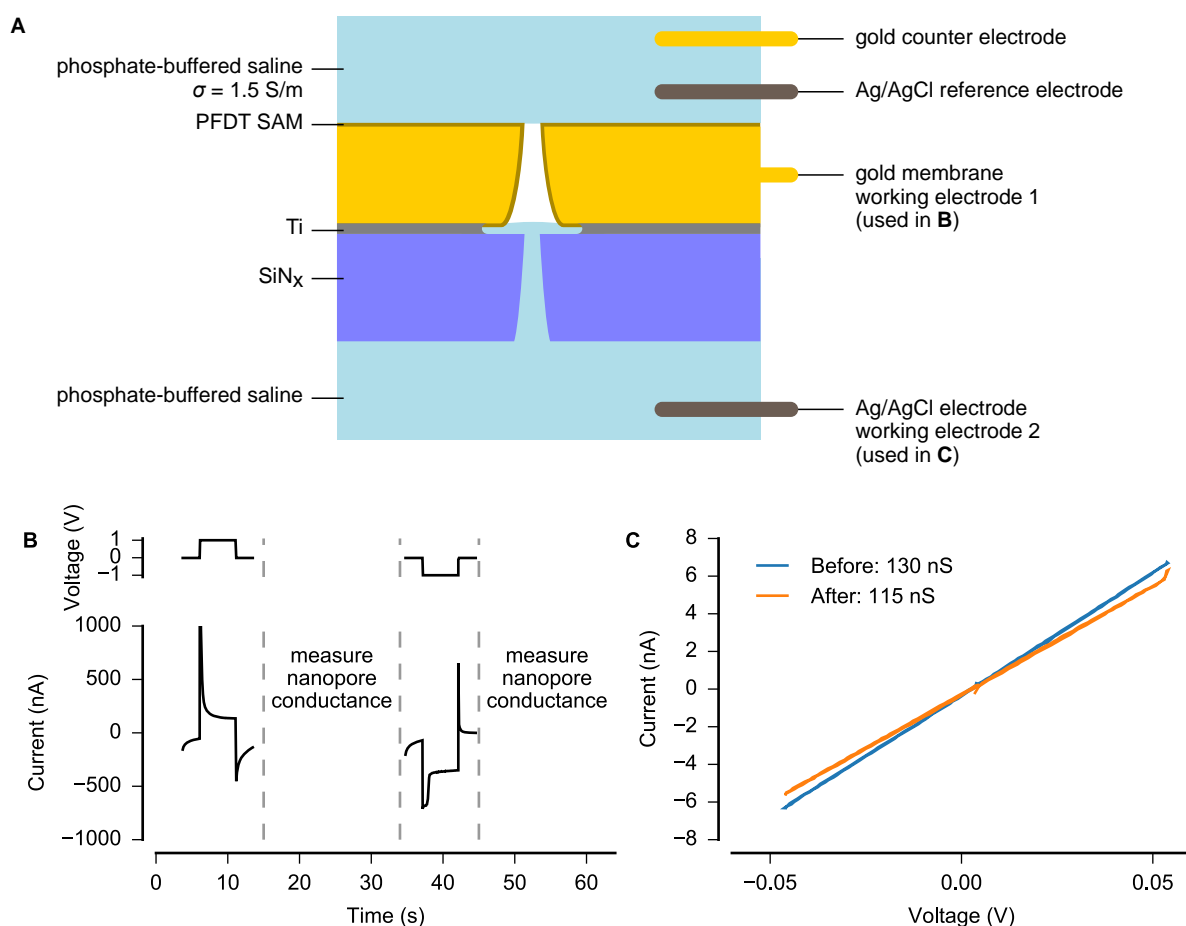


Figure 5.38 Attempted gate-electrode-controlled electro-wetting of an array of 25 nanopores. **A** Schematic of experimental setup. Electro-wetting and conductance measurements were performed by independent working electrodes and shared counter (gold) and Ag/AgCl reference electrodes in the top reservoir. The working electrodes were the gold membrane (working electrode 1) for electro-wetting (**B**) and the Ag/AgCl electrode (bottom reservoir) for conductance (**C**). **B** Example pulses at +1 V and -1 V vs. Ag/AgCl. A variety of pulses up to ± 1 V vs. Ag/AgCl were applied for 20 min, alternating with measurements of the nanopore conductance. **C** Electro-wetting was not observed. Four of the 25 nanopores were wet at the start of the experiment (see text and Figure 5.36) and no additional nanopores wetted. The small reduction in conductance may reflect changes in surface charge.

was preheated to 100 °C. H_2O_2 (400 μl , 30 %) was added while stirring. An etch rate of 240 nm min^{-1} is expected on planar substrates [219], and should be reduced in the nanopore. The nanopore chip was immersed for a prescribed time, then rinsed with water and dried. The results of etching for 3 min are shown in Figure 5.39C, with a visible bubble trap structure. Piranha etching deformed the gold layers, causing enlargement of the trap beyond the thickness of the Ti layer.

Milling of single nanopores with a 10 pA current was tested, and minimum times to breakthrough were 18 s. Single nanopores were milled at 10 pA for 36 s to guarantee breakthrough. Nanopores were etched in piranha for 8 min to produce larger bubble traps compared to Figure 5.39C, and then modified with PFDT (1 mM in ethanol for 52 h). Some nanopores remained dry after treatment with the SAM, in agreement with section 5.4.3.

Other nanopores were electro-wetted, but not reversibly. A transmembrane voltage was applied, as wetting with the gate electrode was not observed. Although these nanopores contained bubble traps, their specific structures were not known, and the traps may have been too large to successfully trap bubbles, as seen in the enlarged etched structure of Figure 5.39C. Large cavities would easily wet, rather than trapping bubbles as intended. Figure 5.40 shows wetting of one of these nanopores. After coating with the PFDT SAM, the nanopore was dry (Figure 5.40A). Currents measured during voltage scans indicated that wetting of the nanopore occurred (Figure 5.40B–D). In B, the wetting transition was ob-

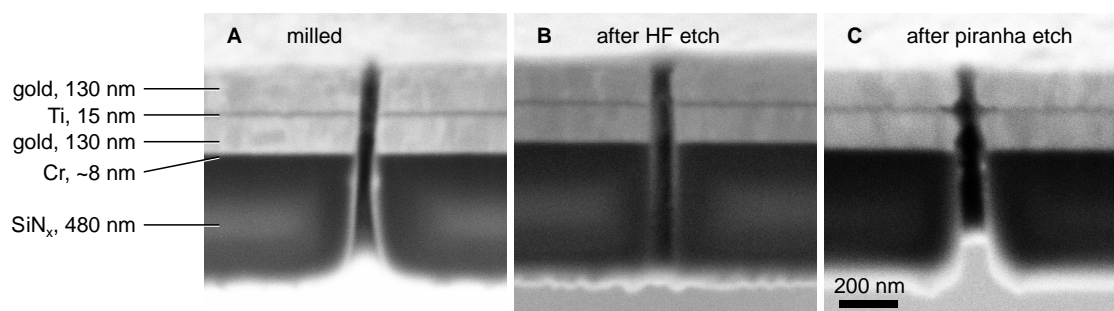


Figure 5.39 Fabrication of nanopores with bubble traps. A Milled nanopores had an approximately cylindrical shape, and the sacrificial Ti layer is visible. B No etching of Ti was observed after 5 min in 1 % HF. C Etching was achieved with piranha solution. Scale bar applies to all images.

served during the second scan at ± 0.6 V. Wetting was irreversible upon returning to low voltages, but the dry state was restored by manual drying of the nanopore chip by blowing with nitrogen. In C, wetting was observed in the first scan to $+0.8$ V. The blocked state was again restored by drying. In D, wetting was observed during the first scan to $+0.9$ V. These results are similar to those presented in section 5.4.5. However, wetting occurred here in the first or second scan. Variability in wetting voltage may have been caused by variation of the liquid–vapour interface at the nanopore entrances prior to wetting or changes to the nanopore structure. Another possibility is that wetting was time-dependent. In B, wetting was observed during the second scan. The scan rate was 10 mV s^{-1} , so that scanning to $+0.6$ V and back to zero took 120 s. In C and D, where wetting was observed in the first scan in both cases, each scan was much longer due to the reduced scan rate of 1 mV s^{-1} .

The results of one nanopore with partially reversible wetting are shown in Figure 5.41. The hydrophobic nanopore was initially blocked (Figure 5.41A) but wetted under a transmembrane voltage above 0.7 V (Figure 5.41B). Conductance dropped during the reverse voltage ramp. Repeated voltage scans showed finite conductance and transitions between discrete conductance states (Figure 5.41C,D) with their stable characteristics measured by scanning at low voltages (Figure 5.41A). It must be emphasized that these results are from a single nanopore. Its structure should be similar to Figure 5.39C, but it was etched for a longer time in piranha, and its specific structure is not known. These results show that partial dewetting is possible but not yet controllable.

These results can be explained by the ability of a water channel within the hydrophobic nanopore to form discrete metastable configurations in combination with gas (Figure 5.42). In contrast, similar transitions in nanopores without bubble traps were never observed. The measured currents indicate incomplete wetting of the channel, with conductance an order of magnitude lower than its fully wetted value. The metastable states observed here contrast with the unstable flickering signals measured in SiN_x nanopores (for example, Figure 5.32). This suggests that the SiN_x nanopores with rough hydrophobic surfaces trap complex arrangements of bubbles, similar to those seen on planar silane-modified surfaces [172].

Although these results do not demonstrate fully reversible or controllable transitions, they support the concept that integration of bubble traps within hydrophobic nanopores can enable control of nanopore wetting. Improved control of the discrete configurations of the water channel must be achieved by refinement of design and fabrication of the bubble trap. Improvements could include traps which are thinner and etched deeper into the nanopore walls, and multiple traps; first steps are described below.

The design of the bubble trap layer was refined in Design 3 (Figure 5.5) This was produced similarly to Design 2, with the outer gold layers reduced to 90 nm, and the single Ti layer replaced with alternating 7 nm layers of Ti and gold (seven layers of Ti with six layers of gold). HF etching was attempted, again without success. Additionally, etching with 1.1 M oxalic acid was attempted for 70 h; no etching was observed. Piranha etching was again employed, with rough etching of the Ti/gold layers expected based on the results of Design 2. The etching produced marbled structures in the trap layer. If layered structures remained, no indication of them could be observed with the resolution of the SEM. Figure 5.5B shows nanopores milled in metal structures on a Si substrate, for evaluation before fabrication on membranes. Diameters were enlarged, as nanopores were milled from the metal side rather

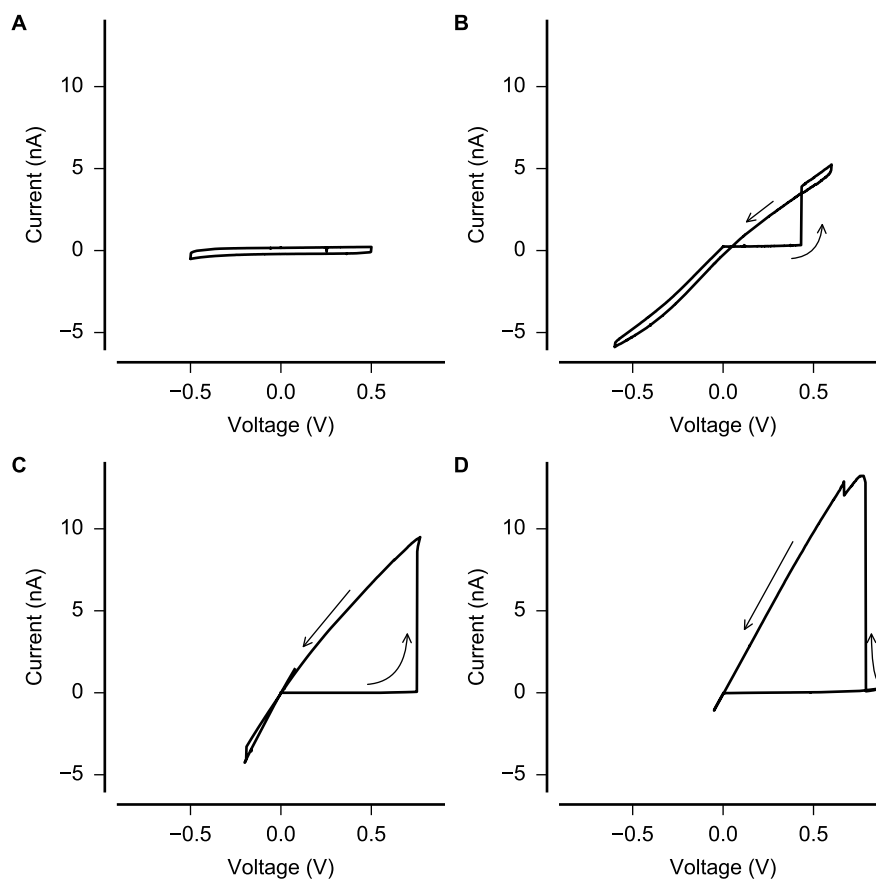


Figure 5.40 Electrowetting of a single hydrophobic nanopore (Design 2). **A** After mounting the nanopore chip in the fluidic cell and filling with PBS, voltage scans revealed no conductance through the nanopore. The scan rate of 10 mV s^{-1} produced measurable capacitive current. **B** During one scan, the nanopore wetted at $+0.43 \text{ V}$. No dewetting was observed. **C** The nanopore chip was manually dried and remounted in the fluidic cell to recover its dry state. Wetting was observed again, this time at $+0.75 \text{ V}$. Again, no dewetting was observed. The reverse scan showed an additional jump in conductance at -0.19 V . In **C** and **D**, capacitive currents were reduced by using a scan rate of 1 mV s^{-1} . **D** The nanopore chip was again manually dried, recovering its blocked state. Wetting was observed just after scan reversal at $+0.79 \text{ V}$, with an additional small increase at $+0.67 \text{ V}$. No dewetting was observed.

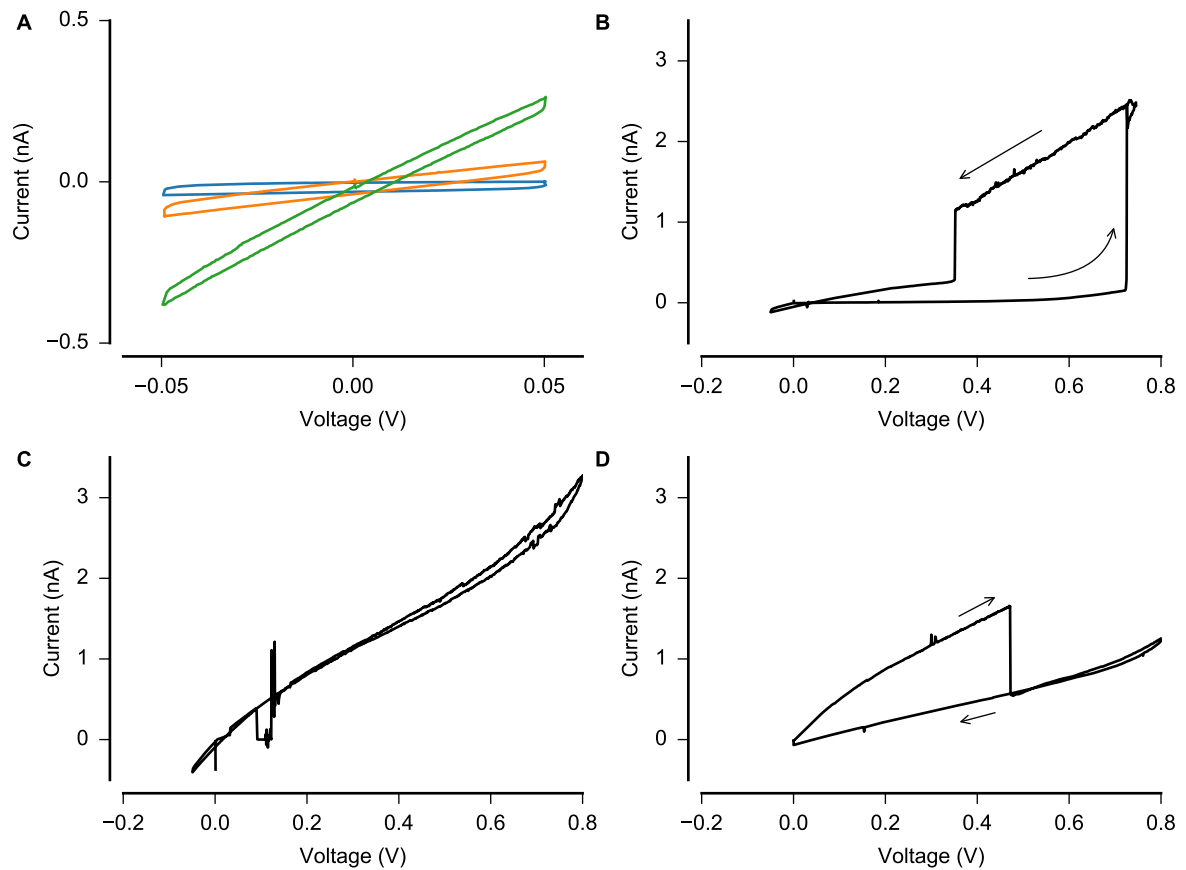


Figure 5.41 Behaviour of a single hydrophobic nanopore with a bubble trap. **A** The nanopore was initially blocked but discrete conducting states were observed after voltage cycling. Conductance was measured at low voltage without affecting the conductance state. **B–D** Scanning at higher voltages revealed transitions between metastable conductance states. In **B**, the dry nanopore wetted above 0.7 V, although the conductance was an order of magnitude lower than expected for complete wetting. Partial dewetting was observed during the reverse scan, and again during the forward scan in **D**. These changes in conductance likely reflect different conformations of the water channel within the nanopore. It is not clear what causes these transitions, as these are singular measurements and the transitions occurred intermittently over the course of several voltage cycles. Further experiments in more controlled geometry are required to understand these effects.

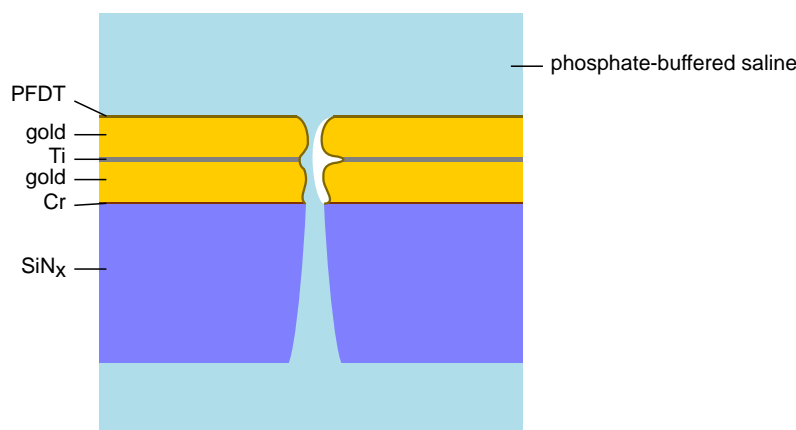


Figure 5.42 Discrete conductance levels observed in nanopores with vapour traps could be explained by the coexistence of metastable configurations of the water channel and trapped bubbles.

than the SiN_x side of the membrane as usual. Measurements of Design 3 nanopores have until now not achieved useful results.¹³

Unsuccessful etching with HF and oxalic acid, both of which are well-known Ti etchants, may be due to interactions between the gold and Ti layers. Solid-state diffusion is known to occur between Ti and gold [220] and the mixing of these layers may explain why etching was not observed with these common etchants. Diffusion would occur more readily in the thinner layer of Design 3. An estimate of the diffusion coefficient at room temperature [220] suggests diffusion could occur over a few nanometres as the Design 3 samples were stored for 7 months between evaporation of the layers and nanopore fabrication. Future designs should examine alternative sacrificial layers which would prevent diffusion and allow use of less aggressive etchants than piranha. For example, titanium nitride (TiN) does not diffuse with gold [220] and can be selectively wet etched by a mixture of ammonium hydroxide, hydrogen peroxide, and water [221].

Although the results presented suggest that refinement of these bubble traps may enable reversible electrowetting, the mechanism still relies on a transmembrane voltage rather than control by gate electrodes according to the model presented in sections 5.3.3 and 5.3.5. The transmembrane voltage addresses all nanopores which connect the two reservoirs, as in Figure 5.36. Future work should investigate materials with electrochemical stability sufficient to apply the model for nanopore electrowetting with a gate electrode, to enable individual nanopore control with integrated electrodes.

5.5 Conclusions and outlook

The goal of reversible hydrophobic gating remains to be achieved, but investigations with SiN_x -silane nanopores and gold-thiol nanopores have led to an improved understanding of how hydrophobic gating may be rationally developed. Reversible hydrophobic gating in agreement with Smirnov et al. and Powell et al. has been observed in hydrophobic SiN_x nanopores, but not in nanopores with engineered structures. Results of gold-thiol nanopores suggest that rational design of hydrophobic gating should be possible, but is currently hindered by damage due to cleaning with piranha solution and low stability of thiol SAMs. Diverse results were explained by widening and thinning of the metal structures during piranha cleaning, shrinking the narrow nanopore region which remains dry. After encountering these complications, further experiments investigated SiN_x -silane nanopores to focus on the physical mechanisms of nanopore electrowetting. Wetting of SiN_x -silane nanopores was observed at higher voltages, although lower than predicted by available models.

The reversibility observed in SiN_x nanopores with hydrophobic hydrocarbon or silane-modified surfaces may appear closer to the goal of reversible electrowetting than the irreversible results of gold-thiol nanopores. However, this behaviour suggests uncontrolled roughness, which will impede further opti-

¹³Milling may not have achieved breakthrough; nanopores could not be measured after piranha cleaning.

mization. In comparison, flickering currents were not observed in gold–thiol nanopores, and partial reversibility was observed in only one nanopore, suggesting an absence of uncontrolled bubble trapping. This supports the prediction that thiol SAMs provide better control of surface chemistry, producing smooth hydrophobic surfaces. Together with the proposed bubble-trapping concept, improved control of surface roughness and chemistry may achieve reversible hydrophobic gating.

Unusual current observed in SiN_x nanopores provided evidence for field emission. Although undesirable in reversible electrowetting applications, this phenomenon could be scientifically interesting or have unanticipated applications.

Models of electrowetting in nanopores were developed, but are currently limited by reliance on the contact-angle-driven interpretation of electrowetting. The validity of the transmembrane model is especially questionable. The model for electrowetting with a gate electrode is attractive for its lower voltages and ability to control individual nanopores. However, electrochemical stability of gold and thiols prevented testing of this model. Comparison of these contact-angle-driven models with numerical solutions of the electromechanical formulation and future experimental results will be interesting.

Furthermore, a concept for achieving reversible electrowetting in large nanopores has been developed based on the design of bubble-trapping cavities in the nanopore walls. This concept should be testable without the need for atomic precision of nanopore fabrication. Nanopores with integrated bubble traps were produced towards testing this concept. The current fabrication of bubble traps was limited by the aggressive etching of piranha. Reversible gating was not observed in these nanopores, although partial dewetting in one nanopore hints at future possibilities. A second design with multiple thin layers of Ti and gold was produced which resulted in a marbled bubble-trapping layer between two thicker gold layers. The electrowetting behaviour of such nanopores remains to be evaluated. Suggestions for these experiments and further investigations of hydrophobic gating are proposed in chapter 7.

6 Nanopore arrays for chemical stimulation

This chapter describes the development of a nanopore/microelectrode array (NPMEA). This device integrates an array of individually-addressable nanopores for chemical stimulation of neurons. The concept of a nanopore array is analogous to microelectrode arrays, but with the intention of local chemical, rather than electrical, stimulation (Figure 6.1).

This work focused on *in vitro* chemical neurostimulation, a necessary step for fundamental technological advances before *in vivo* developments. With the goal of local chemical stimulation, devices integrated nanopore arrays (NPAs) with each nanopore independently supplied with a chemical for release into a culture chamber. Electrodes in each channel may enable control of chemical release and nanopore characterization. The work described in this chapter was undertaken with the future goal of integrating controllable nanopores, similar to those presented in the previous chapter.

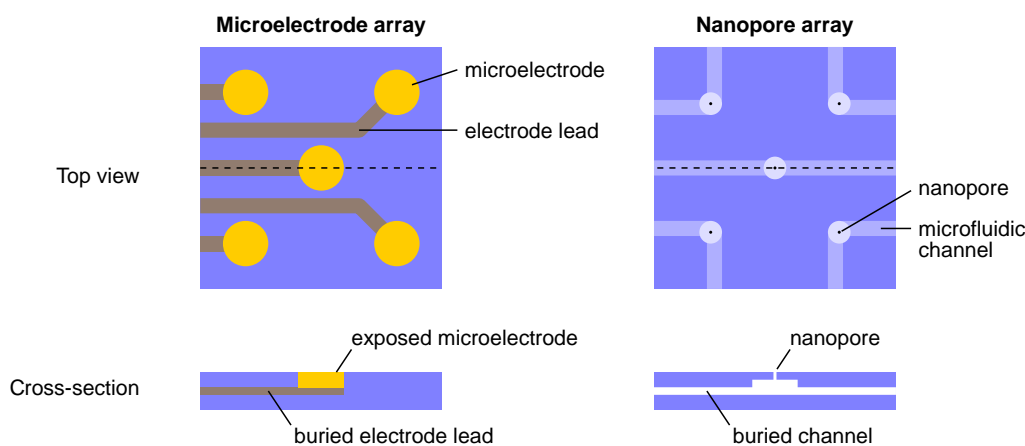


Figure 6.1 Concept of a nanopore array for chemical stimulation, compared to a microelectrode array. In a microelectrode array (left), exposed electrodes are addressed by leads. In a nanopore array (right) the nanopores are addressed by microfluidic channels. In contrast to the electrode leads, the microfluidic channels must be fabricated as empty structures. For delivery of desired chemical solutions the channel must allow flow from an inlet, past the nanopore, to an outlet. This contrasts with the electrode leads, which end at the microelectrodes.

Technical challenges are evident already from the spatial dimensions of the necessary technology. Nanopores require fabrication by FIB or other methods which can achieve nanometre-scale precision. Microfluidics must integrate these nanopores with micrometre-scale accuracy over tens of millimetres. Technology for microfluidic interfacing is measured with dimensions of millimetres, while peripheral devices including electronic and fluidic control systems are on the centimetre scale and larger. Overall, this work considers techniques for fabrication across 7 orders of magnitude – roughly equivalent to the difference between a thin stream of water from a tap, and the length of Lake Constance.

The interaction of artificial devices with biological matter places stringent requirements which must be met. I recall a scientist describing joining technology and biology as similar to throwing a computer into the sea, and retrieving it later with the expectation that it still works. This comparison is especially true for implantable devices, although the *in vitro* environment can be similarly aggressive. Devices must be stable at elevated temperatures, in long term contact with cell culture medium containing dissolved salts, small molecules, proteins, and enzymes. Under these conditions, microfluidic structures must resist pressures of several hundred kilopascals, as will be discussed below. Compatibility with standard procedures including sterilization with plasma or ultraviolet (UV) light and resistance against common solvents and chemicals is necessary.

Of course, the technology must be biocompatible to ensure the healthy survival of biological samples, including acute tissue preparations (several hours) as well as long-term cell cultures (several weeks

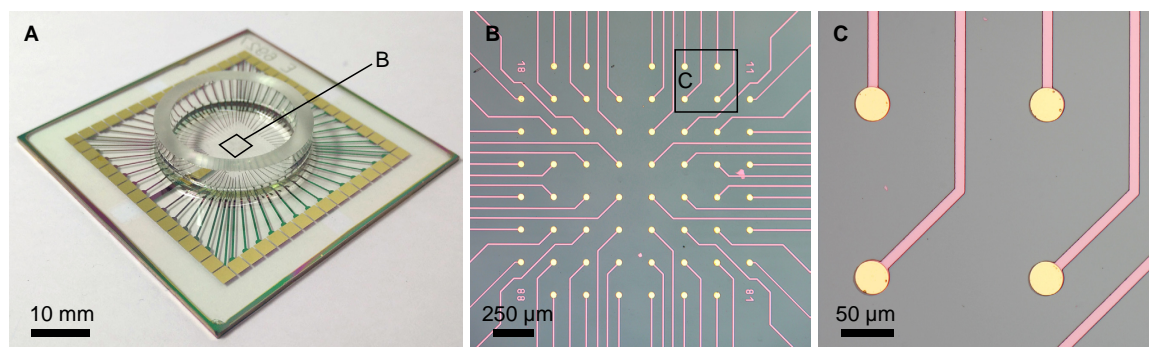


Figure 6.2 A microelectrode array from NMI TT GmbH. **A** The MEA is produced on a 1 mm-thick, $49 \times 49 \text{ mm}^2$ glass substrate. **B** An array of microelectrodes is exposed in the centre of the substrate. **C** Here, the electrodes are gold with a $30 \mu\text{m}$ diameter.

in culture medium at 37°C). It is helpful if devices allow use of established biological methods for preparing cell or tissue culture. Interrogation of cellular activity in response to chemical stimulation must be possible, by integration of microelectrodes for electrophysiology and ensuring transparency for microscopy.

Commercial *in vitro* MEAs are established tools for neuroscience research and provide an ideal starting point for the new development of nanopore/microelectrode arrays (NPMEAs). Compatibility with cell culture and the ability to measure electrophysiological response of neurons are proven, and modifications to these MEAs must only maintain these properties. MEAs can be ordered with confidence in their quality, and are made of well-characterized materials by reliable microfabrication processes. Additional flexibility could be gained from custom MEAs but should wait until proof of this new concept is achieved; first steps should build on standard layouts. Furthermore, building on MEAs enables exploitation of the commercially available systems for neuronal recording, imaging, and cultivation. The wealth of experience in performing biological experiments on MEAs will be accessible and comparable to future chemical stimulation experiments. For example, MEAs previously provided early validation for electrical retinal prostheses [222], which have since received clinical approval. This supports the idea that an *in vitro* chemical stimulation model could provide valuable information for future work towards *in vivo* technology.

In this work, MEAs were obtained from NMI Technologie Transfer GmbH (Reutlingen, Germany) and MCS Multi Channel Systems GmbH (Reutlingen, Germany). Several electrode materials are available, and various designs as well as custom layouts can be purchased. This work was built on a layout with sixty $30 \mu\text{m}$ -diameter electrodes with a pitch of $200 \mu\text{m}$ (Figure 6.2). One electrode in the array is replaced by a large internal reference electrode.

The first section in this chapter describes the development of microfluidic networks integrated on MEAs capable of controlling fluidic and electrical access to individual nanopores. The main challenge was to produce high-resolution microfluidic channels in a thin film format, suitable for bonding with a nanopore membrane.

The second step is the fabrication and integration of the nanopore array itself, based on commercially available SiN_x membranes. A new method was developed to achieve robust bonding between the membrane and the microfluidic networks.

After producing these devices, an additional challenge is their connection to peripheral systems. The task of reliably connecting a large number of tubes to a small device, and achieving useful control over the microfluidics, is not as straightforward as might be expected.

At this point, no suitable method for nanopore gating exists. Therefore, methods presented here were designed to accommodate future nanopore designs, so that gated nanopores may be easily integrated. At the present, external control of individual microfluidic channels is necessary to modulate release from nanopores. Chemical release from hydrophilic nanopores will be considered based on chapter 4. Protocols for achieving biological relevant chemical signals in the current system will be presented.

Finally, the preparation for biological experiments is discussed, and limited results from first biological experiments are presented along with a discussion of what is needed to achieve useful biological

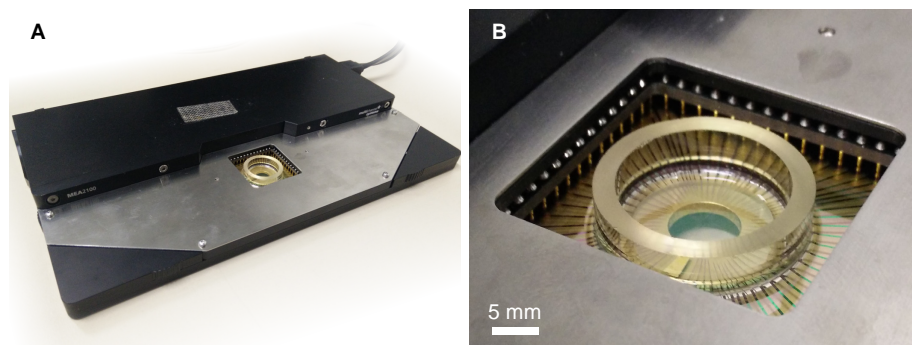


Figure 6.3 MEA in recording setup. **A** The recording setup (MEA2100 from MCS, Reutlingen, Germany) contains amplifiers for all channels on the MEA and connects to a computer by USB. **B** Close-up of a MEA mounted in the recording system. An area of $33 \times 33 \text{ mm}^2$ is exposed within the electrical contact pads. A glass ring defines the normal cell culture area, but may be modified or removed.

results.

6.1 Design constraints with commercial MEAs and SiN_x membranes

Standard MEAs are produced on 1 mm-thick glass and measure 49 mm on each side. In a standard design, 60 electrodes are arranged in a 1.5 mm square in the centre, and are addressed by pads near the edge of the MEA. The pads enclose a square slightly more than 33 mm wide. Typically, a ring around the electrodes defines the culture dish, but this can be modified. MEAs connect to electrophysiological recording devices as seen in Figure 6.3. Microfluidic interfacing must fit within this system without interfering with biological experiments.

Commercial SiN_x membranes are produced on Si wafers, and opened by through-wafer wet etching. Individual chips are commonly 5 mm wide and 200 μm thick with thin SiN_x membranes in sizes up to 2 mm (Silson Ltd., Northampton, England). To produce nanopore arrays on the MEA, 2 mm wide membranes are sufficient to cover the 1.5 mm electrode field while maximizing physical robustness.

In integrating fluidic structures on the MEA, the available area is limited to the 33 mm square within the electrode pads. Additionally, the area available for interfacing with the microfluidic channels is defined by the culture area needed around the electrode array. This area typically has a diameter of 20 mm but can be reduced.

Materials commonly used for the electrode surfaces include gold, Pt, titanium nitride (TiN), iridium oxide, poly(3,4-ethylenedioxythiophene) (PEDOT), and a PEDOT-carbon nanotube (CNT) composite. Electrode quality is evaluated by impedance measured at 1 kHz, which is a relevant frequency for capturing neuronal signals. PEDOT and PEDOT-CNT are preferred as they exhibit the lowest impedances of these [223], but would be affected by the fabrication processes in the following sections. Gold electrodes are preferred for this work, as it is a noble metal and can be cleaned in case of contamination. Furthermore, it is the preferred base electrode for PEDOT [224], which can be electrodeposited after integration of microfluidics and nanopores. In this work, TiN and gold MEAs were used. As explained in section 6.2, electrodeposition of PEDOT was used after NPMEA fabrication to improve electrode properties.

6.2 Development of thin film microfluidic networks

A microfluidic network for connecting nanopores on a MEA can most simply be realized as planar channels, bounded on the bottom by the MEA and the top by a cover foil. Figure 6.4 illustrates a two-dimensional schematic of this concept. The aperture layer encloses the channels, and defines the channel inlets and outlets and apertures over which nanopore membranes can be bonded. Similar devices have been produced for microfluidic chemical stimulation, as reviewed in section 2.2.2 and summarized in Table 2.1. The integration of nanopores substantially increases the challenge of fabrication. While the

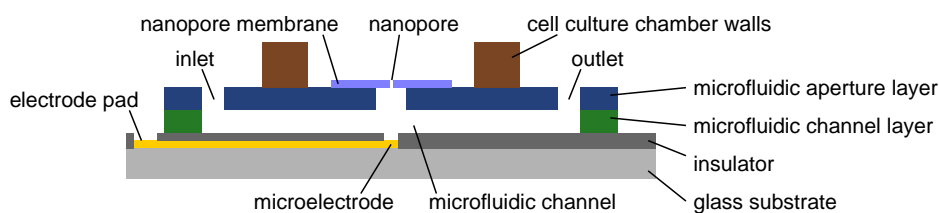


Figure 6.4 Schematic of a single nanopore addressed by a single buried microfluidic channel integrated in a microelectrode array. Dimensions are not to scale. The microfluidic channels require patterning of two layers on the MEA. The bottom layer defines the channels. The top layer encloses the channels and provides openings for an inlet, outlet, and a nanopore membrane.

microfluidic features can be readily produced by UV photolithography, the fabrication of nanofluidic features and their integration with microfluidic systems remain novel.

On a sixty electrode MEA, microfluidic channels were designed to individually address half of the electrodes. This design is illustrated in Figure 6.5, and includes minimum channel widths of $10\ \mu\text{m}$ with minimum spacing between channels of $40\ \mu\text{m}$. These dimensions were necessary to contact 30 electrodes in the given array layout, and were feasible for photolithographic fabrication. These electrodes may be used to control nanopores, although currently only uncontrolled hydrophilic nanopores have been integrated. The design also exposed the remaining 29 electrodes and the reference electrode, to maintain electrophysiological capabilities of the MEA.¹

The severe restriction of flow through a nanopore, as defined by equation 2.11, necessitated that they were addressed by flow-by channels, each requiring an inlet and outlet in addition to the nanopore aperture. Flow-by channels were necessary for filling, rinsing, or changing solutions. As the available area for inlets and outlets would allow more than 150 connections with 2 mm spacing, these did not restrict the design. Each of the thirty channels had an inlet and an outlet, organized along two sides of the 33 mm square bounded by the electrode pads. Making these 60 connections is covered in section 6.4.

Channel widths were maximized to reduce hydraulic resistance according to equation 2.10. Channels were widened from the $10\ \mu\text{m}$ width at the electrode array to a maximum width of $50\ \mu\text{m}$ at the inlets and outlets. Wider channels were avoided to prevent collapse of the cover layer. Channel heights of $10\ \mu\text{m}$ were chosen to simplify the lithography of the network of $10\ \mu\text{m}$ -wide channels. The estimated hydraulic resistance for the channels was $16\text{--}19\ \text{kPa}\ \text{s}\ \text{nl}^{-1}$ at $25\ ^\circ\text{C}$. Experimental hydraulic resistances were calculated from flow rate measurements to be $13\text{--}15\ \text{kPa}\ \text{s}\ \text{nl}^{-1}$, in reasonable agreement with the prediction. Further reduction in resistance could be gained by an increase in channel height, but this could reduce the reproducibility of the small microfluidic features. In contrast, increased density of channels and nanopores could be fabricated, but would increasingly impede control of liquids in the microfluidic channels. Flow control in the microfluidic channels will be discussed in section 6.5.

The thickness of the cover layer, to enclose the channels, is limited by the aspect ratio of the apertures for the nanopore membranes as well as resolution limits. Large aspect ratios would trap bubbles, prohibiting solutions in the channels from reaching the nanopore. The design allowed for aperture dimensions of approximately $50\ \mu\text{m}$ (Figure 6.5), and the aspect ratio should be less than one. The thickness of this layer must be sufficient to avoid mechanical deformation due to pressures applied to the microfluidic channels.

Materials for fabricating these structures must resist water, solvents, and pressures required to drive flow through the microfluidic channels. The materials must enable bonding of nanopore membranes, which can be achieved with liquid adhesives or by dry methods. Liquid adhesives are challenging because they can easily fill the channels or nanopores. Dry methods require compatible surface chemistries, and often elevated temperatures and pressures. Section 6.3 will cover this extensively.

The challenges presented here are illustrated by considering fabrication with polydimethylsiloxane (PDMS), the most common material in microfluidic research. A negative master for soft lithography of PDMS would be produced by two steps of SU-8 photolithography (more details below) to define the channels and the apertures. PDMS structures are normally several millimetres thick and any connec-

¹Minimal effect of recessing the electrodes within the substrate was expected. For example, acute retina preparations would lay across the recesses, the $30\ \mu\text{m}$ distance to the electrodes would add $\sim 20\ \text{k}\Omega$ of resistance to the typical electrode impedances of $50\text{--}100\ \text{k}\Omega$ at $1\ \text{kHz}$.

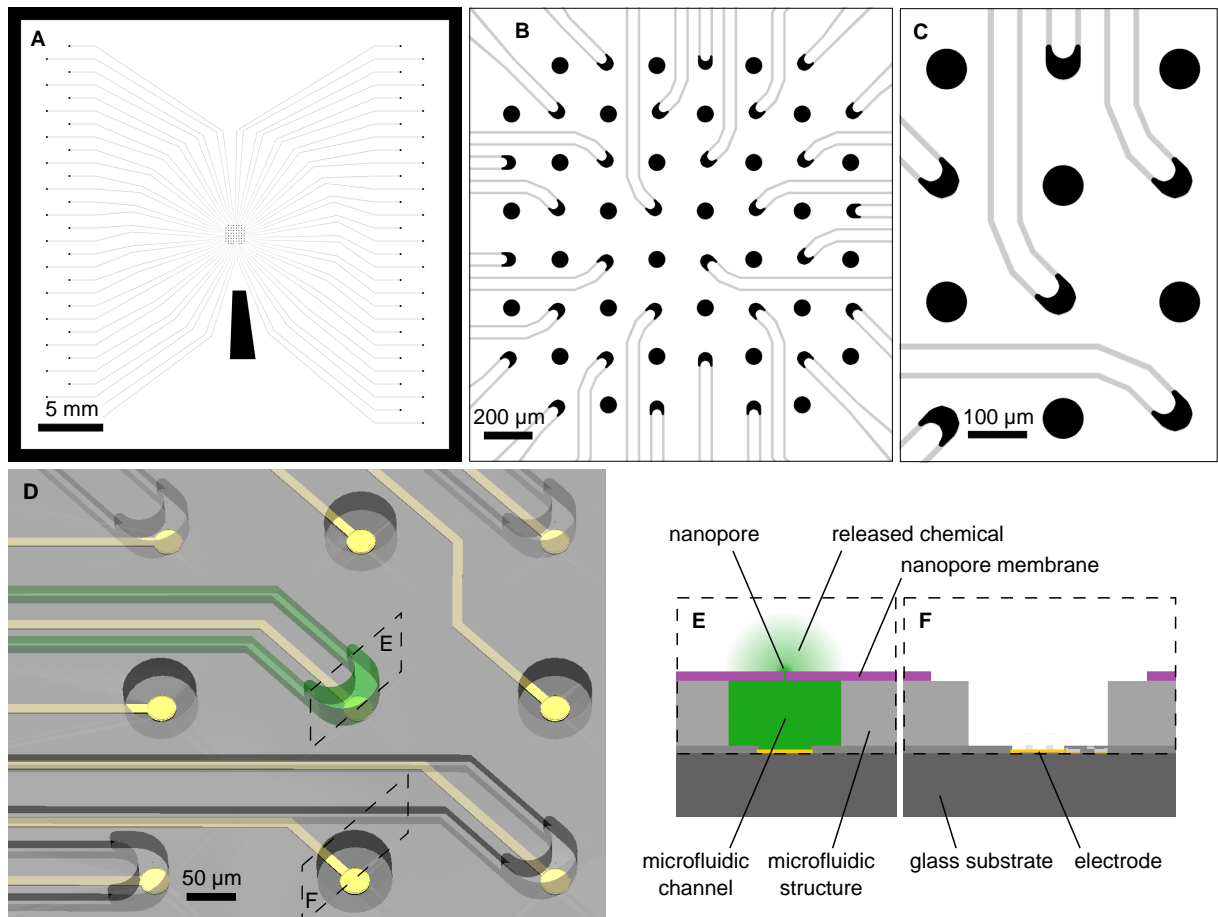


Figure 6.5 Design of the NPMEA. **A** The design covers the $33 \times 33 \text{ mm}^2$ area within the electrode pads. **B, C** Magnification of the microfluidic network. Channels are in grey, and apertures are in black. **D** An oblique illustration of the microfluidic structures on a MEA, showing enclosed channels (one filled with a green solution). The crescent-shaped apertures are enclosed by a nanopore membrane. The round apertures expose the electrodes for electrophysiology. **E, F** Cross-sections of the NPMEA at a nanopore and an exposed electrode, respectively.

tions are made by punching millimetre-scale holes. Forming the aperture array would require forcing a top cover against the master to produce a thin PDMS structure. After curing, the delicate and flexible PDMS film would require alignment and bonding on the MEA (without distortion), and finally bonding of the NPA. Further problems would include its low modulus and strength, so the channels would deform and burst when filled with moderate pressures. Vapour permeability would allow evaporation of water or formation of bubbles, soft hydrophobic surfaces would attract dust and contamination and absorb hydrophobic molecules. PDMS is unsuitable for this challenging application.

To address this challenge, I attempted to fabricate these structures from OSTE+, a new material for microfluidics with many promising characteristics. Although this material provides unique capabilities, further development would have been needed to meet the requirements. A second method based on well-established SU-8 epoxy photoresist and the chemically similar ADEX dry film resist was developed, and was ultimately successful.

6.2.1 Off-stoichiometry thiol-ene-epoxy

Off-stoichiometry thiol-ene-epoxy (OSTE+) is a negative photoresist belonging to the family of off-stoichiometry thiol-enes (OSTE). These polymers have been developed specifically for microfluidics since 2011 [225] at the Royal Institute of Technology in Sweden and are available from Mercene Labs AB (Stockholm, Sweden).

Novel properties of OSTE polymers include their two-step curing. The first step is exposure to UV light, and transforms the viscous liquid precursor to a soft polymer similar to cured PDMS. In this compliant state, transfer and noncovalent adhesion to other materials is easy. The second step is thermal curing, which produces a hard material with a modulus of 1.2 GPa [226]. OSTE+ additionally includes an epoxy (denoted by the '+'), which can bond with many materials during the thermal cure. Information about biocompatibility of OSTE+ is limited, although specific formulations of OSTE are biocompatible [227], and resistance against common solvents is good [225].

OSTE+ structures can be formed by soft lithography from a negative master. It can be patterned with UV photolithography and dry bonded to various substrates including silicon [226]. Combining these methods can provide additional capabilities [228].

The concept for fabrication involved producing a single layer of OSTE+, using soft lithography for the microfluidic channels and photolithography for the apertures. Transfer of this layer to the MEA and subsequent alignment of the NPA would create the final device. This process (Figure 6.6, described in more detail below) would simplify fabrication if successful.

Before trying the full process, several preliminary tests were done. Bonding between OSTE+ and SiN_x was evaluated. OSTE+ precursors were mixed and exposed to UV light. The soft intermediate material was placed in contact with SiN_x -coated Si pieces and baked with part of the OSTE+ overhanging the edge. The bond was strong enough that attempting to remove the OSTE+ by lifting up on the overhanging part resulted in fracture of the OSTE+ before breaking the bond.

Soft lithography of microfluidic channels was validated with a low resolution master. A positive master produced by milling 100 μm channels was used to form a negative PDMS master. This negative master was functionalized with 1H,1H,2H,2H-perfluorooctyltrichlorosilane (PFOTCS) to reduce adhesion, and coated with mixed OSTE+ precursors. The OSTE+ was exposed and the structure was transferred and bonded to a MEA. Filling of the microfluidic channels with a fluorescent solution verified that bonding without leakage was possible (Figure 6.7).

Bonding of SiN_x membranes was also evaluated. A planar OSTE+ piece was produced and a hole was punched with a needle. A 500 nm-thick SiN_x membrane was bonded over the hole (Figure 6.7). Conformal contact with the OSTE+ structure achieved bonding without fracturing the thin membrane.

With these capabilities proven, the feasibility of the entire process (Figure 6.6) could be evaluated. A critical challenge was discovered during developing of the OSTE+ structures, and will be described below.

OSTE+ structures with channels and apertures were produced by an alignment-free combined UV and soft lithography process. The photomask defined apertures and inlets and was integrated under a soft lithography negative master defining the channels (Figure 6.8A). The mask was produced by sputtering Ti on glass and patterning with S1818 photoresist and HF etching. SiN_x was deposited by

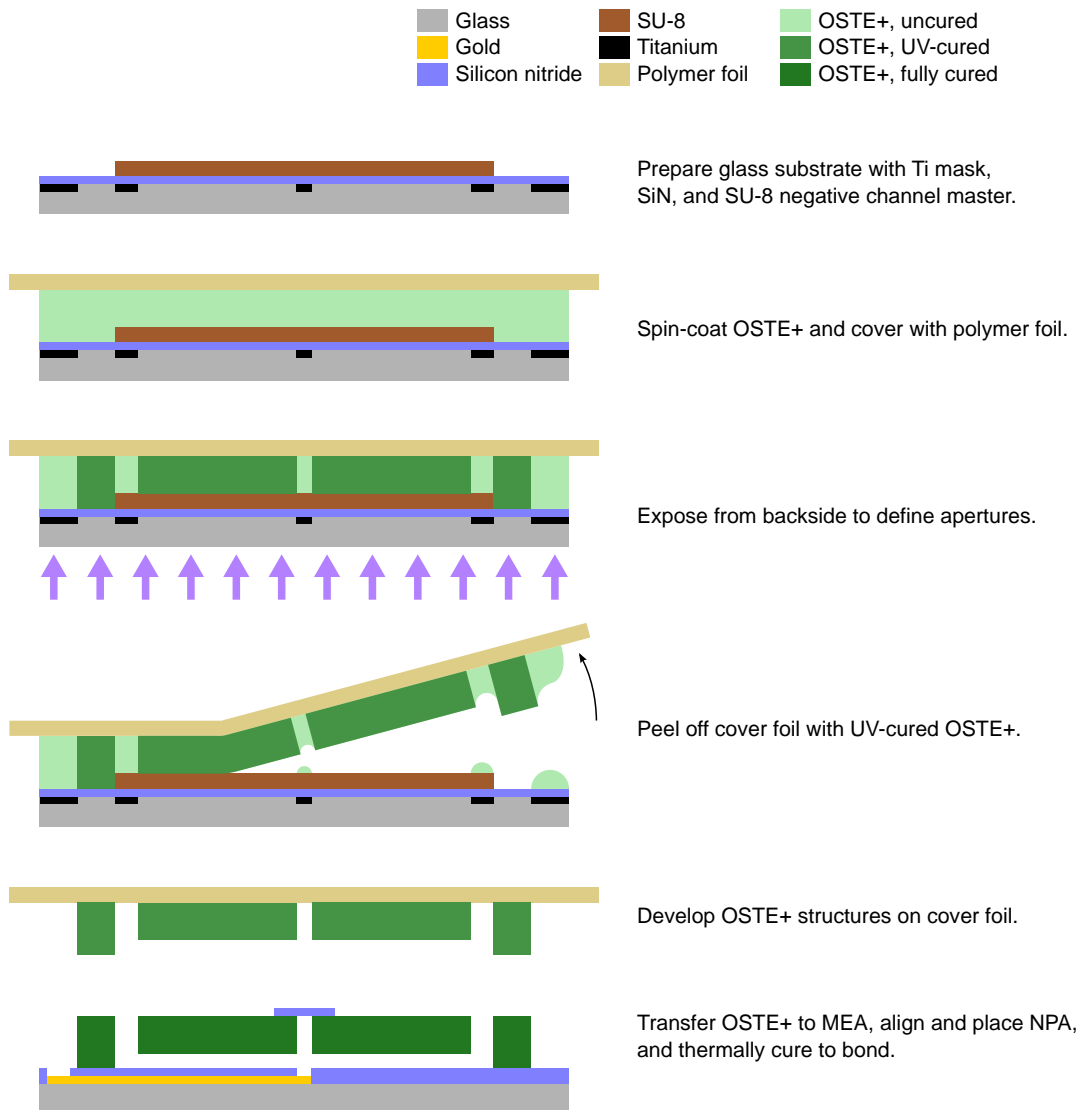


Figure 6.6 Process for NPMEA fabrication with OSTE+.

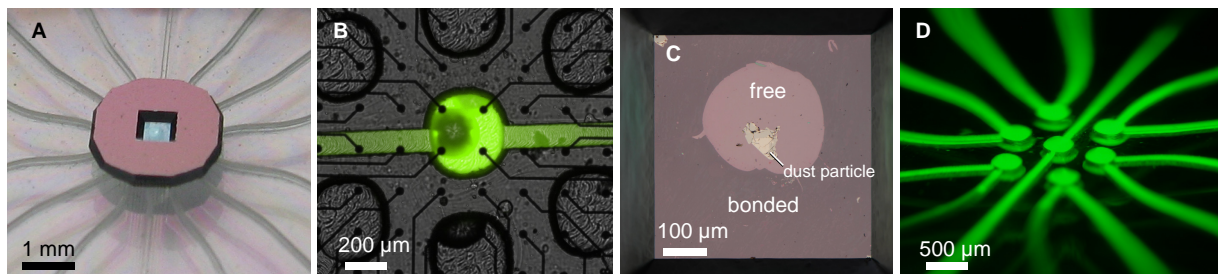


Figure 6.7 Low resolution verification of OSTE+ bonding to both the MEA and the NPA. **A** Photograph of OSTE+ microfluidics (with visible channels) bonded to a MEA (below) and a SiN_x membrane (above). **B** Channels could be filled with a fluorescent solution, showing robust leak-free bonding. **C** The free-standing region of the SiN_x membrane appeared bright, while the bonded regions were darker due to reduced reflectance. **D** Several channels in close proximity could be independently filled, shown in an oblique fluorescent micrograph.

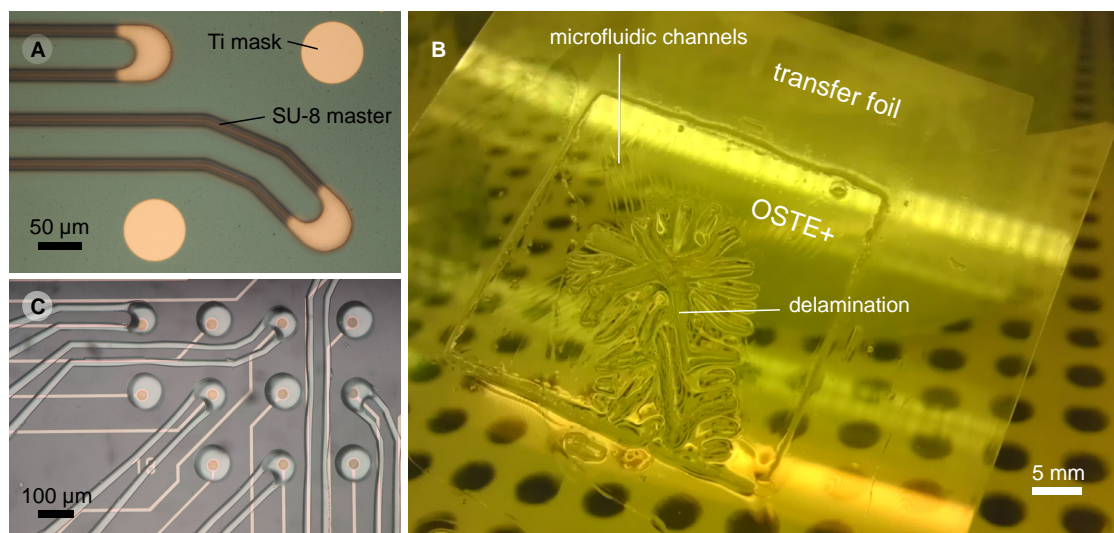


Figure 6.8 OSTE+ fabrication failed due to delamination of the microfluidic structure during developing. **A** SU-8 master with integrated Ti mask. **B** Solvent flowed between the OSTE+ structures and the transfer foil during developing, causing delamination and blistering of the OSTE+ structures. This critical issue caused this method to be abandoned. **C** Some OSTE+ structures could be salvaged and transferred to a MEA, but were deformed by delamination.

PECVD to improve subsequent adhesion of SU-8. SU-8 channel negatives were patterned according to the method in section 6.2.2. To prevent adhesion with OSTE+, the masters were modified with PFOTCS.

Spin-coating of OSTE+ produced a thick liquid film across the master/mask, and this liquid precursor was covered with a polymer foil for handling. The master was exposed to UV light from the backside through the integrated mask. After exposure, the cover foil and adhered OSTE+ structures were peeled from the master. Adhesion of the exposed OSTE+ to the cover foil was sufficient to reliably remove the OSTE+ from the fluorinated master. The cover foil then held the OSTE+ structures for development, and was used to transfer the final structure to the MEA, followed by bonding of the NPA.

Here, the process was limited by appropriate adhesion between OSTE+ and the cover foil. During developing in the recommended developer (mr-Dev 600, micro resist technology GmbH, Berlin, Germany), the OSTE+ layer consistently delaminated from the cover foil. This was visible as a blistering effect underneath the soft OSTE+ layer (Figure 6.8B). Improved adhesion of OSTE+ on the cover foil would be necessary to transfer the structure to a MEA. In some cases, the delaminated OSTE+ could be flattened again on the foil and transferred to a glass substrate or MEA, but this always resulted in damage and distortion of the layer (Figure 6.8C).

Significant effort was expended to investigate different foils or modifications to the foil. Attempts to solve this problem included using foils of cyclic olefin copolymer (COC) and several grades of commercial polyethylene terephthalate (PET) with different surface properties. Plasma treatment of COC increased adhesion, but even 1 s of plasma resulted in an irreversible bond with OSTE+. Other polymer foils or modifications of surface chemistry could be attempted. However, significant investigation would be involved with an unknown likelihood of finding a solution.

Further investigation of fabrication of OSTE+ structures was abandoned in favour of a process based on SU-8, which is presented in the following section.

6.2.2 SU-8 and ADEX film

SU-8 is a common material for microfluidic fabrication, often used to produce negative masters for soft lithography. It has also been used for direct fabrication of microfluidic structures. It has been reported as biocompatible [229], although proper processing is necessary to avoid cytotoxicity [230]. SU-8 has previously been used for microfluidic devices for *in vitro* experiments with neurons [231] as well as *in vivo* probes for chemical delivery in the brain [48, 49, 232]. Its biocompatibility is also supported by its use as an insulating material in commercially available MEAs (EcoMEAs from MCS, Reutlingen, Germany).

The primary rationale for the OSTE+ process in the previous section was to facilitate bonding of the nanopore membrane. The final step for SU-8 fabrication is a hard bake, after which SU-8 is chemically inert. Furthermore, adhesive bonding is difficult because liquid adhesives easily fill microfluidic structures. However, suitable adhesive bonding methods have been demonstrated, which can bond planar surfaces by rolling on a thin liquid film [233]. Dry bonding has also been accomplished with unreacted epoxy groups prior to hard baking [234]. A further complication is the delicate nature of the nanopore membrane. The next section describes how these challenges were solved.

SU-8 thin films are produced by spin-coating, which fills any features on the substrate with the liquid polymer. Enclosed structures can be produced by laminating chemically similar films such as ADEX and SUEX (DJ MicroLaminates, Sudbury, MA, USA). The processes for structuring SU-8 and ADEX are similar. The fabrication process for the microfluidic structures is illustrated in Figure 6.9 and typical results of the final process before NPA bonding are shown in Figure 6.10.

The channel layer was produced by spin-coating SU-8 3005 on dehydrated substrates to a thickness of 10 μm (10 s at 500 rpm and 30 s at 1000 rpm), followed by a soft bake for 3 min at 95 $^{\circ}\text{C}$. The substrate was exposed with an i-line filter and a dose of 430 mJ cm^{-2} . A post-exposure bake at 100 $^{\circ}\text{C}$ for 5 min was followed by a rest period of at least 20 min. Substrates were developed in mr-Dev 600 for 1 min, then rinsed with isopropanol and dried with nitrogen. A hard bake at 150 $^{\circ}\text{C}$ for at least 1 h prepared the substrates for the next step. Without this hard bake, damage to the SU-8 layer was observed during development of the subsequent ADEX layer.

The aperture layer was produced by laminating ADEX A20 using a heated laminator at temperatures of $\sim 80^{\circ}\text{C}$ and a speed of 3 mm s^{-1} . The substrate was exposed with an i-line filter and a dose of 1000 mJ cm^{-2} . Exposed substrates were baked at 65 $^{\circ}\text{C}$ for 1 min, 85 $^{\circ}\text{C}$ for 10 min, and 65 $^{\circ}\text{C}$ for 1 min, and then allowed to rest for 2 h. Substrates were developed in cyclohexanone for 3 min, then were sprayed with fresh cyclohexanone, rinsed with isopropanol, and blown dry with nitrogen. Aiming the nitrogen at the aperture array in the centre of the substrate cleared solvents from the channels, which could be visually observed by the reflectance of the empty channels. Dry bonding as described in the following section must be performed before the final hard bake which improves cross-linking for increased stability.

For SiN_x substrates, cleaning by piranha or oxygen plasma and dehydration before SU-8 spin-coating were critical to ensure adhesion. For adhesion of ADEX on the SU-8 layer, oxygen plasma was detrimental, but dehydration was helpful. Although benefits were not readily apparent during processing, avoiding these steps led to delamination and failure of devices at later times. Dehydration by baking substrates at 150 $^{\circ}\text{C}$ for 3 h produced good results. In contrast, baking at 120 $^{\circ}\text{C}$ for 30 min resulted in delamination. Higher temperatures may allow for shorter baking times and produce better results, but this was not studied. Substrates should be coated soon after removal from the oven to prevent problems from ambient moisture, although must be allowed to cool to room temperature to achieve expected thickness after spin-coating.

One issue discovered for patterning of ADEX on SU-8 channels was the potential for ADEX to reflow into the channels during the post-exposure bake (Figure 6.11). This could be observed microscopically (Figure 6.11D). In some cases, the channels became irreversibly blocked. Empirically, I found that sufficient rest time after the post-exposure bake and before developing was necessary for good results. This effect is perplexing: as reflow occurs during the post-exposure bake, the effect of resting after baking is not clear. With short rest times of 10–20 min, reflowed ADEX was not removed during developing and blocked the microfluidic channels. However, if substrates rested for 2 h or longer before developing, reflowed ADEX was reliably removed during developing. Additional effort to understand this effect was not expended, as the process provided satisfactory results.

In both layers, other parameters were optimized beyond manufacturers' recommendations. Exposure of 1000 mJ cm^{-2} was necessary to prevent collapse of the ADEX layer into the channels. This was several times the recommended dose of 175 mJ cm^{-2} [235]. Even at 700 mJ cm^{-2} , the ADEX collapsed during the post-exposure bake. The hard bake at 150 $^{\circ}\text{C}$ before the ADEX layer was necessary to avoid damage to the SU-8 structures during ADEX development in cyclohexanone. The hard bake can be longer if convenient.

Complete cross-linking and good adhesion of SU-8 on SiN_x requires a final hard bake at 150–200 $^{\circ}\text{C}$ [236] which must be performed after bonding of nanopore membranes as discussed in sec-

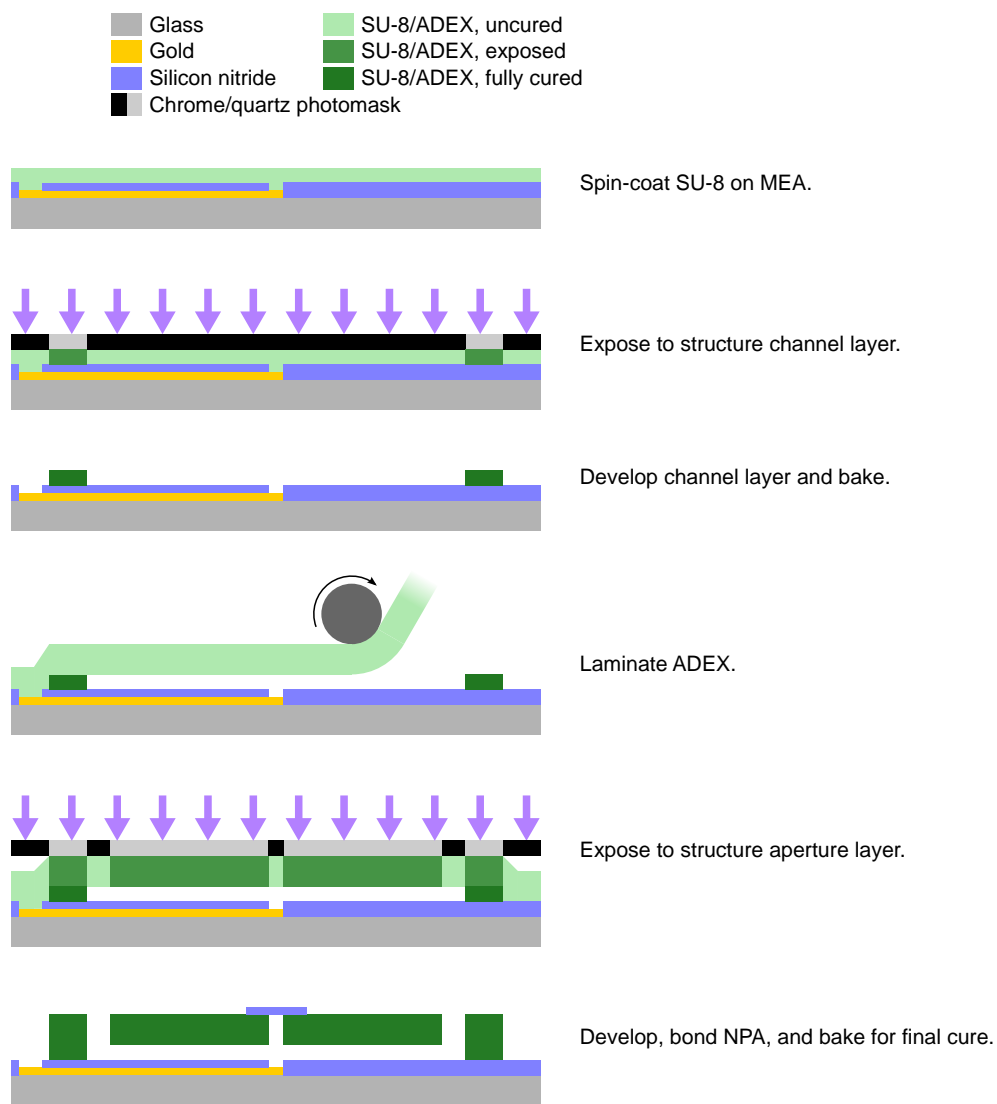


Figure 6.9 Process for NPMEA fabrication with SU-8 and ADEX.

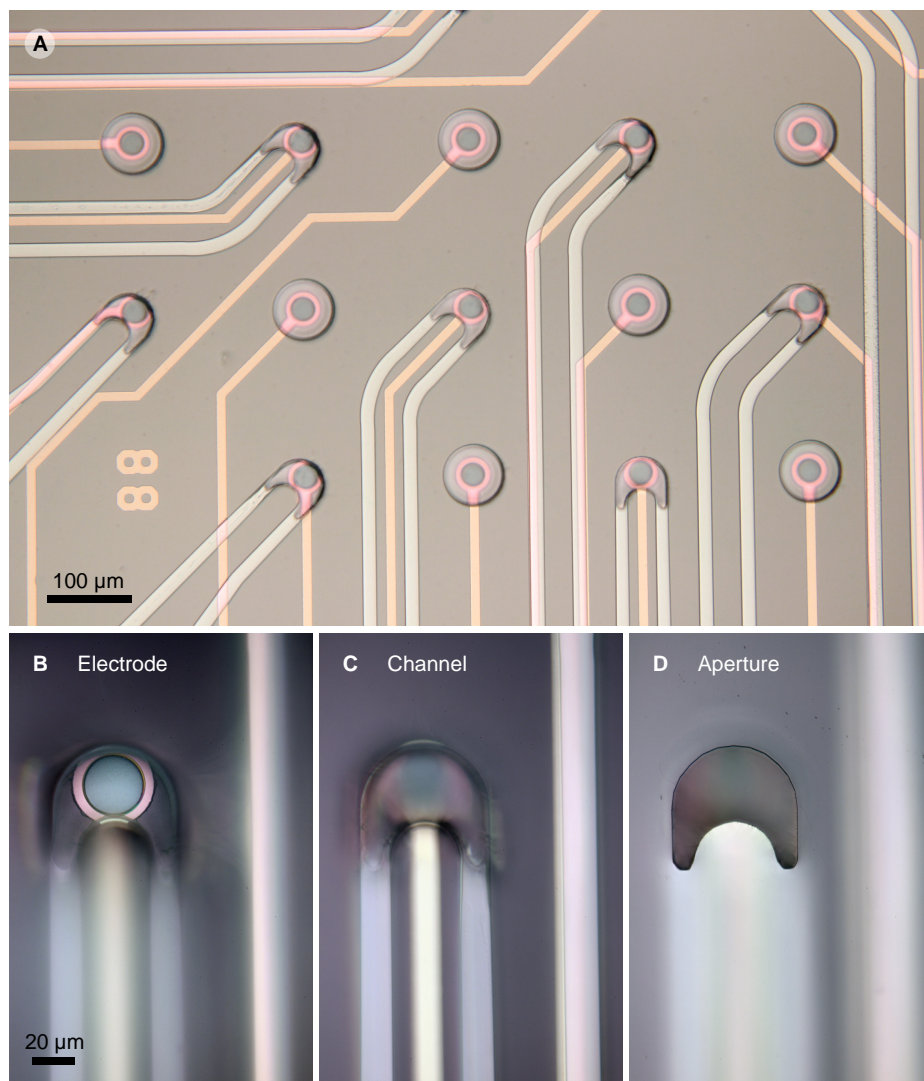


Figure 6.10 Microfluidics produced with SU-8 and ADEX. **A** Channels and apertures were reliably produced on MEAs. **B–D** Optical microscopy reveals individual features at different planes of focus. **B** Electrode at $z = 0$. **C** Channel at $z = +10 \mu\text{m}$. **D** Aperture at $z = +30 \mu\text{m}$.

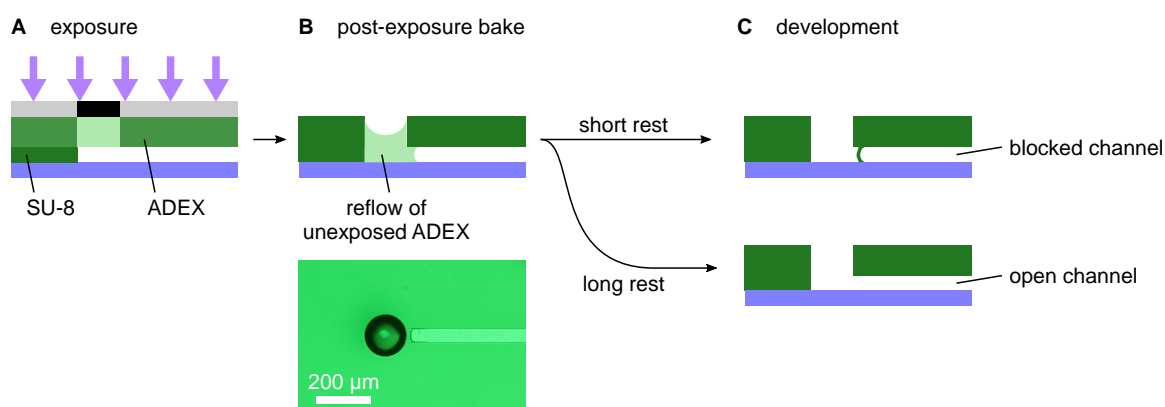


Figure 6.11 Reflow of ADEX into SU-8 channels. Blocked channels were observed with a short rest time between the post-exposure bake and development. With a longer rest time, channels were open.

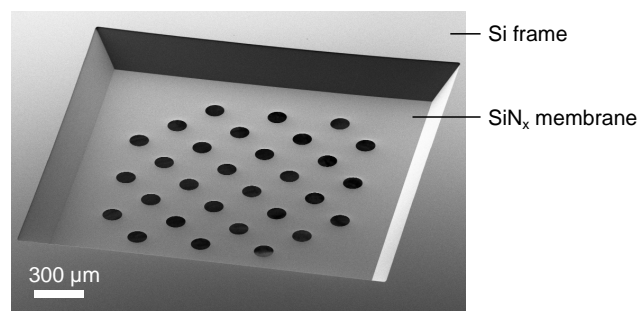


Figure 6.12 Oblique SEM of a nanopore array membrane. The membrane is 2 mm wide, and has thirty 120 μm holes to expose electrodes on the MEA. Nanopores (not visible) were milled between the larger holes.

tion 6.3.2. Substrates were placed in an oven at room temperature, the oven was heated to the desired temperature and maintained for several hours or overnight, and the oven was turned off and allowed to cool before removing the substrates. Early NPMEAs were baked at 150 $^{\circ}\text{C}$, but several days of exposure to water, either by filling the microfluidic channels or immersion, resulted in delamination between the SU-8 and SiN_x . Increasing the baking temperature to 200 $^{\circ}\text{C}$ resolved this issue, and no delamination of SU-8 was observed in devices baked at this higher temperature. Devices were immersed in deionized water at room temperature for 70 days with no delamination. Bonded nanopore membranes survived this hard bake. The hotter bake changed the colour of the microfluidic structures from mostly transparent to a yellow-brown and increased their autofluorescence. Optimizing the baking temperature between 150 $^{\circ}\text{C}$ and 200 $^{\circ}\text{C}$ may enable sufficient adhesion while minimizing the colour change and autofluorescence.

The first MEAs that were modified with this process had 30 μm TiN electrodes with impedances of <100 k Ω at 1 kHz [237]. After fabrication of the SU-8 and ADEX layers, the electrodes had increased impedances of 500–1000 k Ω , such that no recording of neuronal signals would have been possible. Cleaning with air plasma for up to 10 min did not help. This issue was remedied by electrodeposition of gold and PEDOT [223]. After PEDOT deposition, coated electrodes exhibited acceptable impedances of 60–80 k Ω at 1 kHz, although PEDOT/gold was observed to fall off some TiN electrodes. Later devices were produced starting with gold MEAs, and were coated with PEDOT after microfluidic fabrication and nanopore membrane bonding.

6.3 Bonding nanopore arrays to microfluidic networks

Nanopore arrays (NPAs) were produced by FIB milling in SiN_x membranes, similar to the nanopore membranes presented in chapter 5. Custom SiN_x membranes (Silson Ltd.) with a membrane size of $2 \times 2 \text{ mm}^2$ on $5 \times 5 \text{ mm}^2$ Si chips contained an array of photolithographically-defined 120 μm holes to expose 29 electrodes on the MEA (Figure 6.12). After sputtering with 20 s AuPd ($\sim 5 \text{ nm}$; SCD 040, Balzers Union) for conductivity, the membranes were manually aligned in the FIB-SEM, and nanopores were milled with a gallium FIB with currents of 10 pA and times of 20–60 s for apparent diameters of 100–200 nm. After milling, membranes were cleaned in freshly prepared piranha (1 part 30% H_2O_2 added to 3 parts 96% H_2SO_4 preheated to 100 $^{\circ}\text{C}$) to hydrophilize their surfaces; this cleaning also removed the sputtered AuPd.

A process to bond these membranes to the microfluidic network was necessary. Although nanopores are usually investigated in isolation, integration of nanopore arrays is an active research area. This is critical to increasing throughput of nanopore-based sensing methods, according to a recent discussion of nanopore-based DNA sequencing [238]. Recent methods include integration of single nanopores in PDMS microfluidics [239], and SiN_x membrane integration with a network of 5 PDMS channels followed by in situ nanopore fabrication [94] which was recently extended with integrated microfluidic control valves [240]. Until now, all reported methods contact the nanopore membranes from both sides, so that chemical bonding is additionally physically supported. Here, one side must be free for cell culture. Furthermore, PDMS is not suitable in this work, as discussed in section 6.2.

The methods presented here were developed to achieve robust bonding with simple SiN_x membranes, with the intention for future compatibility with other or more complex nanofluidic membranes. For process flexibility, bonding should be possible after separate fabrication of nanopores and microfluidic structures. Bonding after simple nanopore milling was necessary, as milling requires sputtering a thin conductive layer on the membranes (which was removed by the piranha cleaning). The bonding technique should also be suitable, for example, when reliable methods of nanopore gating are developed.

The process must avoid blocking both the microfluidic channels and the nanopores. It must withstand pressures applied to the microfluidic channels. It should also be electrically insulating and optically transparent. Finally, the method must consider the delicate nature of the membranes, and the necessity to align the NPA and MEA with micrometre-scale precision.

To enable biological experiments, the bond must be unaffected by exposure to water and cell culture medium at 37°C for weeks. It must be resistant against common solvents, and capable of sterilization by methods such as UV or plasma exposure.

Bonding of SiN_x membranes to OSTE+ was demonstrated, as discussed in section 6.2.1. The compliant nature of UV-cured OSTE+ and its included epoxy make dry bonding easy, and it was achieved without special processing of the SiN_x membrane. The soft material conforms to the substrate without high pressures. Unfortunately, the challenge of suitable adhesion to a foil for development and transfer prevented use of this method in this application. Solving this challenge would make this bonding method attractive.

Adhesive bonding and dry bonding were investigated for microfluidic networks produced with SU-8 and ADEX. Alignment and bonding were performed with a FINEPLACER® bonder (Finetech GmbH & Co. KG, Berlin, Germany). Microscopic alignment enabled precision of $\sim 10\ \mu\text{m}$. Substrates were manually brought into contact, and bonding force could be controlled by a weighted arm. Adhesive bonding had poor resistance against water exposure, and avoiding blockage of the microfluidic channels was challenging. Dry bonding achieved robust adhesion, even after extended exposure to culture medium at 37°C . The development and results of these methods are discussed in more detail below.

6.3.1 Adhesive bonding

First attempts to bond nanopore membranes to SU-8 microfluidics, used a liquid adhesive method [233]. For this method, both the membrane and the microfluidic structures were treated with air plasma to improve wetting of the liquid adhesive and produce reactive groups for covalent bonding. The membrane was carefully picked up with a PDMS manipulator by van der Waals forces. The MEA was coated with a thin micrometre-scale film of liquid UV adhesive (Vitalit 1655) by passing it through adhesive-coated rollers of a laminator. The coated microfluidics and NPA were aligned and the NPA was lowered to contact the microfluidics. The adhesive was cured by exposure to a UV lamp and allowed to cure for at least 24 h. The NPA could be bonded with accuracy on the order of $10\ \mu\text{m}$ (Figure 6.13A).

Care was required to avoid unwanted filling of the microfluidics. The method could successfully coat $30\ \mu\text{m}$ -thick, $33\ \text{mm}$ -wide SU-8 structures, without filling $70\ \mu\text{m}$ -wide holes. However, coating often filled some of the microfluidic channels, and had to be rinsed with isopropanol and recoated. Sometimes, the adhesive covered the exposed nanopore membranes, blocking the nanopores.

Finally, this method was rejected when the adhesive failed after several days in contact with water. This caused delamination and the movement of water underneath the membrane (Figure 6.14). A surprising consequence of this was the dissolution of Ti electrode leads. This did not happen simply due to the presence of water at electrodes, but rather only occurred when electrodes were exposed to water which had flowed under the delaminated membrane (Figure 6.14A). This suggests that that water picked up some chemical from the delaminated epoxy which then reacted with Ti on the MEA. Small carboxylic acids are known to etch Ti. However, these details are presented as a curiosity and this etching process was not further investigated.

Although this process failed due to insufficient water resistance, it demonstrates an advanced method for adhesive bonding of microstructures. Other applications which do not require water exposure could use this method. Microfluidic applications could be enabled by an adhesive with improved tolerance to water, although would require specific testing as the results here do not reflect the reported water resistance of Vitalit 1655 [241]. Prospects for using this method at smaller scales are limited (see the

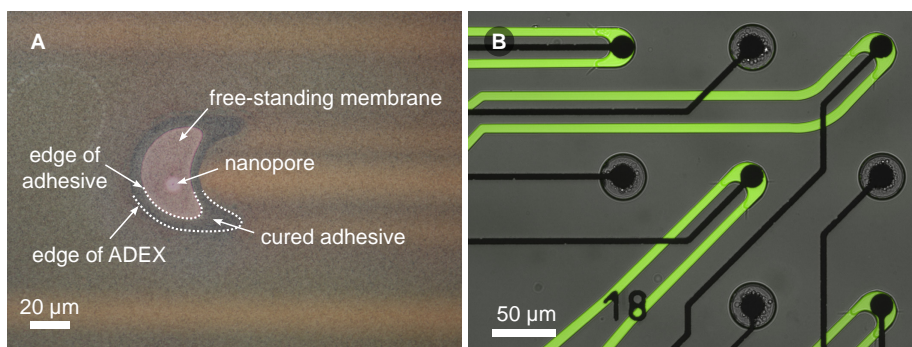


Figure 6.13 NPAs were successfully bonded to microfluidic structures by a liquid adhesive. **A** An artefact of FIB milling shows the location of a nanopore in the SiN_x membrane covering the microfluidic aperture. During bonding, the adhesive forms a meniscus around the edge of the aperture, visible as the dark rim of the crescent. **B** Microfluidic channels could be filled, shown here with a carboxyfluorescein solution.

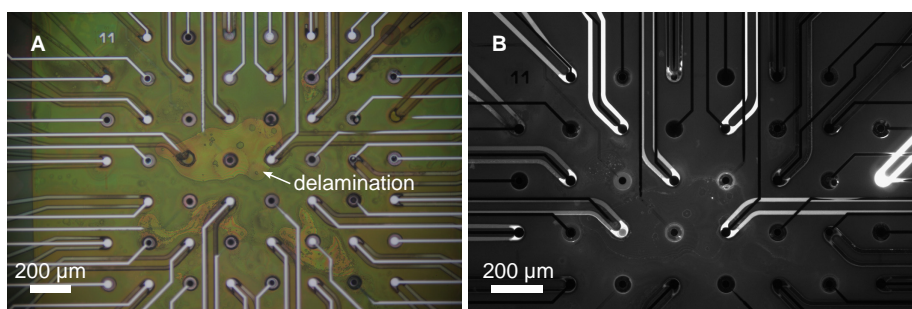


Figure 6.14 Adhesive bonding failed after several days in contact with water. **A** Delamination of the membrane was visible. Some Ti electrode leads are dissolved where water has moved under the membrane. **B** A single channel was filled with carboxyfluorescein solution, which spread under the delaminated membrane to other channels.

cured adhesive meniscus in Figure 6.13A).

6.3.2 Dry bonding

Dry bonding joins two surfaces chemically without an added adhesive. Such methods depend on compatible surface chemistries, and contact with appropriate pressure and temperature. A robust method to bond SiN_x nanopore membranes with ADEX microfluidics was developed based on complementary amino- and epoxysilanes.

Methods for dry bonding of PDMS and SU-8 have been demonstrated [234, 242, 243]. These methods used unreacted epoxy groups which remained after developing SU-8 structures. The complementary PDMS surfaces were modified to possess primary amine groups. By bringing the surfaces in contact, the amine and epoxy groups react to form strong covalent bonds. According to Zhang et al. “As long as the functional groups on the two surfaces are sufficient, and one of the materials is soft enough, a strong bonding should be achieved between two solid materials.” Bonding in their methods was facilitated by the flexibility of elastomeric PDMS and the robustness of SU-8. Forming tight contact between these materials was achieved by applying pressure without any need to be concerned about damage.

In contrast, bonding of NPAs requires extreme care to avoid shattering the SiN_x membranes. Although SiN_x is a rigid crystal, thin layers have some flexibility. However, pressing against a rigid structure often caused the delicate membrane to fracture. Bonding relied on the flexibility of the SiN_x , but also depended on softening of the ADEX structures at increased temperatures to form good contact.

The bonding reaction is illustrated in Figure 6.15. NPAs were modified by silane chemistry to add primary amino groups to their surfaces. After FIB milling of nanopores, the NPAs were aggressively cleaned and oxidized in piranha (1 part 30% H_2O_2 added to 3 parts 96% H_2SO_4 at 100 °C) for 1 h. The NPAs were rinsed with deionized water and blown dry with nitrogen. Piranha cleaning produces

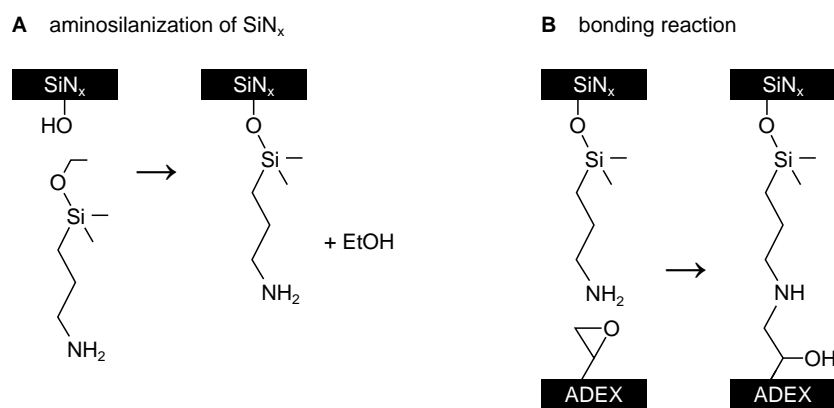


Figure 6.15 Chemistry of dry bonding. **A** APDMES reacts with silanol-terminated SiN_x. **B** Amine and epoxide groups react to form a stable covalent bond between ADEX and SiN_x structures.

hydrophilic surfaces with silanol groups on the surface of SiN_x.²

A solution-based reaction modified the surfaces with a monofunctional silane (3-aminopropyltrimethoxysilane, APDMES) (Figure 6.15A) [159]. The NPAs were immersed in a 1% v/v solution of APDMES in toluene. After immersion overnight or longer, the NPAs were rinsed with toluene, immersed in fresh toluene for at least 30 min, then rinsed with acetone and isopropanol, dried with nitrogen, and baked at 120 °C for at least 30 min. Nanopores were confirmed to be unblocked after monofunctional silane treatment and bonding (section 6.5.1).

Earlier NPMEAs used a vapour-phase reaction with a trifunctional silane (3-aminopropyltrimethoxysilane, APTMS) [246]. However, measurements suggested that this reaction blocked the nanopores. Trifunctional silanes can form thick layers even on planar surfaces [247], which could be exacerbated in the confined structures of nanopores. The confined hydrophilic nanopores may have provided an ideal moisture reservoir for silane polymerization. Furthermore, the delicate membranes did not withstand ultrasonic cleaning, which is commonly performed after silane reactions. No differences in appearance or stability of membranes bonded with tri- or monofunctional silanes were observed.

ADEX is more reactive than SU-8,³ so its post-exposure bake was kept 10 °C below that used by Zhang et al. to maintain unreacted epoxy groups. ADEX was prepared as in section 6.2.2, with a post-exposure bake at 85 °C. After developing, the substrate was exposed to vacuum in a desiccator for at least 15 min to remove solvents.

The NPA was manipulated by exploiting van der Waals forces to pick up the chip directly by the membrane (Figure 6.16). Square PDMS manipulators with side lengths of 1.9 mm were fluorinated with PFOTCS to prevent covalent bonding to the NPA. The manipulator was mounted on the bonder, aligned with the membrane, and the membrane was carefully picked up. This step was performed manually under visual observation, and required direct contact with the membrane. The membrane's frame was supported by an O-ring to avoid contact between the membrane and any surfaces. Sensitive handling was required to avoid breaking the membrane. The NPA was then aligned and placed on the ADEX microfluidic structures on the MEA, and the applied force was adjusted. The temperature was increased at 1 °C s⁻¹ to 100 °C, held for 45 min, then decreased at the same rate. This caused amine groups and epoxide groups to covalently bond (Figure 6.15B). Forces of up to 4 N were safely applied but 5 N shattered the membranes. Bonding at 2.5–3 N, or approximately 700–800 kPa, achieved successful bonding of the membrane (Figure 6.17, Figure 6.18). Substrates were hard baked for several hours at 200 °C to fully cross-link the microfluidic layers and improve adhesion to the SiN_x surface.

This process relied on visually-guided manual handling of the SiN_x membrane. Approximately half of NPAs were cracked after bonding (Figure 6.19) although this allowed for easy removal of the Si frame (Figure 6.19A) and the membrane itself remained mostly unaffected (Figure 6.19B). Microfluidic apertures were successfully covered by the membrane even with cracks within a few micrometres (Fig-

²Surfaces of SiN_x oxidize quickly in air, forming silicon oxide [244]. Piranha treatment of silicon oxide produces silanol functional groups [245].

³Personal communication with Don Johnson (DJ MicroLaminates, formerly DJ DevCorp) on September 4, 2014.

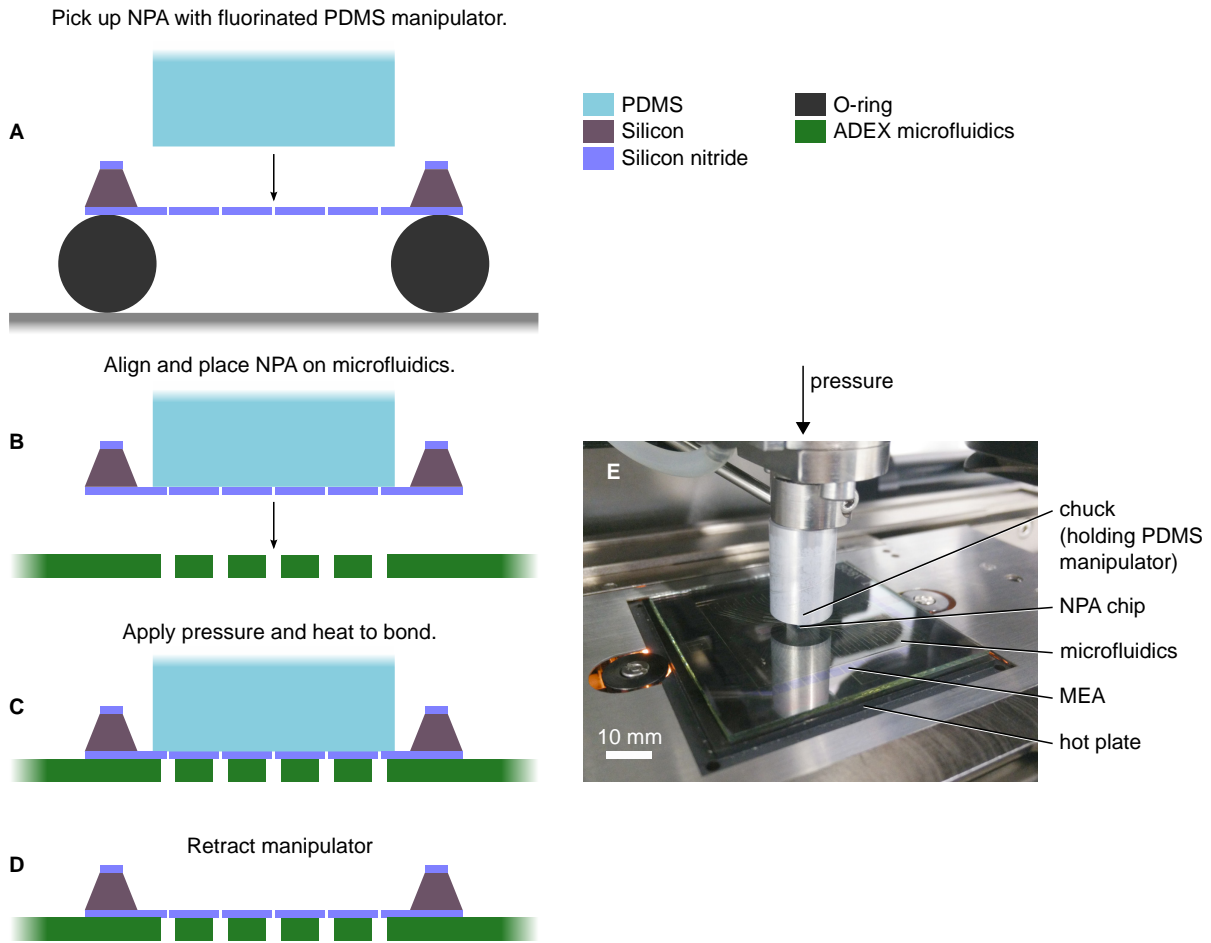


Figure 6.16 Dry bonding of nanopore arrays. **A–D** Bonding process. **E** Photograph during bonding (step **C**). The manipulator is manually lowered to bring the NPA chip and microfluidic structures into contact.

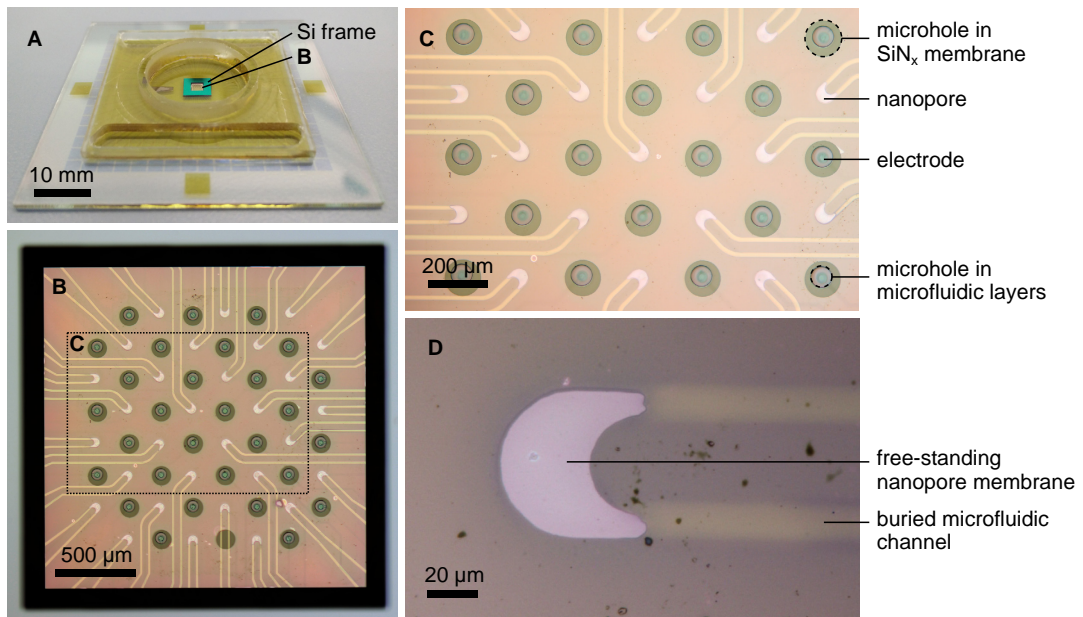


Figure 6.17 Dry bonding results. **A** The bonded SiN_x membrane is visible in the centre of the Si frame (green). **B, C** Bonding was consistent across the membrane, visible by its homogeneous colour. Any bonding defects were readily visible by interference patterns. A small defect is visible in the bottom right of **B**. Circles around the electrodes are holes in the microfluidic layers and nanopore membrane. **D** The dry bonding process forms a good seal around the microfluidic apertures. The membrane is bonded to the edge of the microfluidic structure, leaving the bright crescent area free-standing above the microfluidic channel.

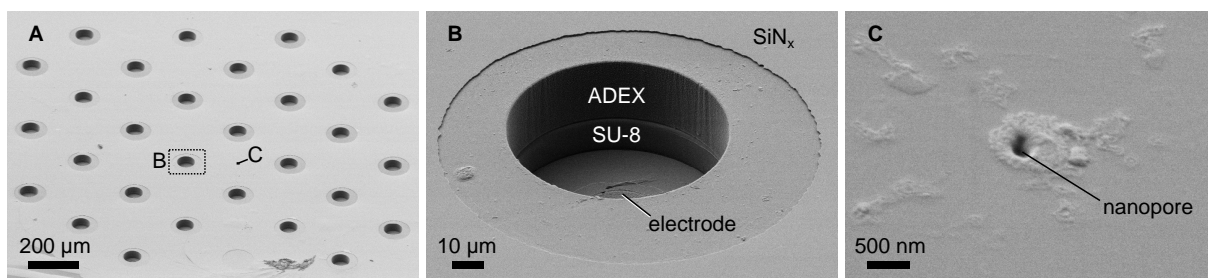


Figure 6.18 SEM of NPA bonded on microfluidic channels on MEA. **A** Wide view of the bonded membrane. **B** SU-8 and ADEX layers are visible at an exposed electrode, as well as the bonded SiN_x membrane. **C** A single nanopore. Bonding of this membrane used a trifunctional silane, so the unidentified substance near the nanopore may have been polymerized APTMS.

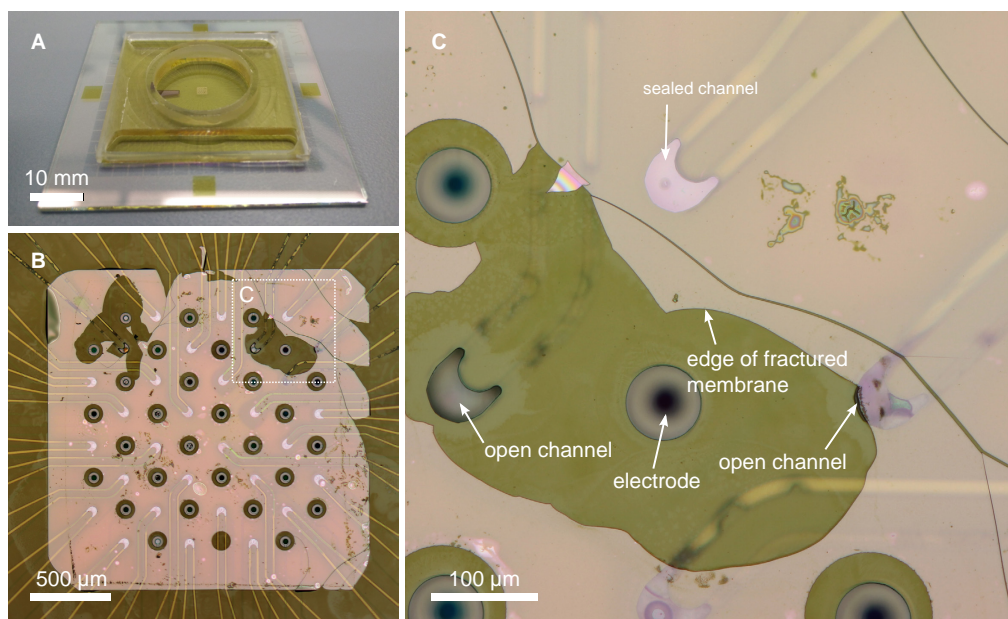


Figure 6.19 Dry bonding results with a fractured membrane. **A** The membrane was bonded in the centre of the device, and the Si frame was removed. **B** The membrane was successfully bonded, despite cracking around its perimeter and small regions being broken off. **C** Cracks caused problems only when directly contacting the microfluidic apertures. Other apertures are successfully sealed even with fractures within 20 μm .

ure 6.19C). Improved bonding could be achieved by a system which allows microscopic observation and pressure control of the bonding process.

This bonding method was rigorously evaluated during testing of the microfluidic structures. Pressures up to 300 kPa were applied to air- or water-filled channels without any problems. An upper pressure limit was not investigated. Channels were filled with water for many days and no change in bonding of the NPA was observed. Substrates were also exposed to cell culture medium and kept in an incubator at 37 °C for 16 days without visible changes to bonding (Figure 6.20). Rinsing with water, ethanol, isopropanol, and acetone did not cause problems, nor did aggressive blowing with nitrogen. Brief exposure to an ultrasonic bath fractured the suspended membranes, as was expected.

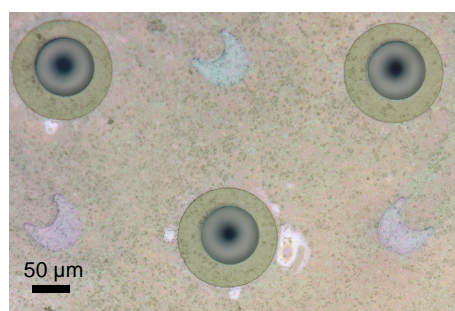


Figure 6.20 Dry bonding was stable after 16 days with culture medium at 37 °C. The visible debris is the soma and dendrites of dead neurons.

6.4 How to connect tubes

This section moves to a larger scale. A connector was required to reversibly interface with the microfluidic channels. Biological experiments require user-friendly methods. For example, positioning and insertion of individual tubes would be too cumbersome. The connector must be compatible with the electrophysiology recording systems for the MEA (Figure 6.3) and reversible to mount the NPMEA in the recording system. Long-term culture in an incubator requires that the NPMEA can be disconnected

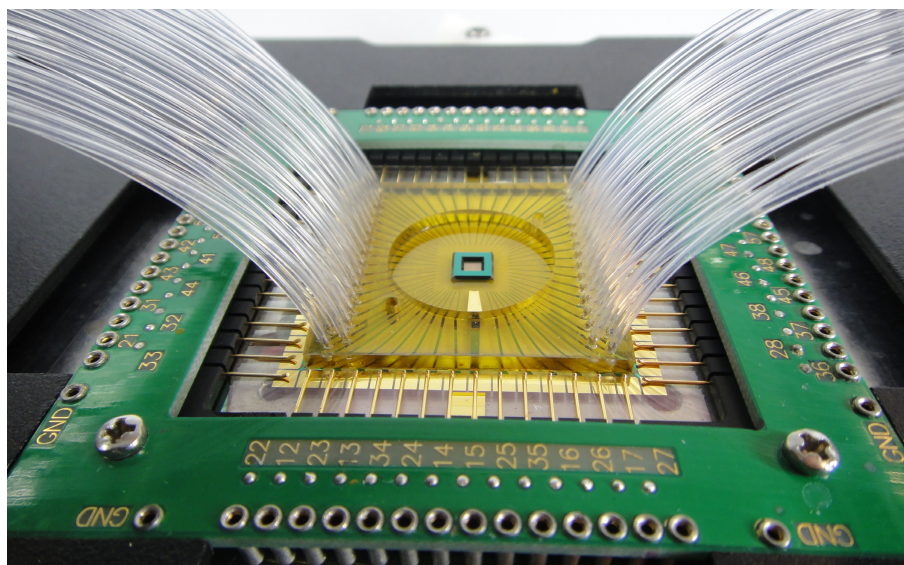


Figure 6.21 Silicone connectors bonded on the surface of the NPMEA with 60 tubes connected in a recording system.

and reconnected as needed for recording. The outer limits of the microfluidic region are 33 mm and may be further restricted by specific recording systems. The channel outlets with diameters of $150\ \mu\text{m}$ were arranged with a pitch of 2 mm along two sides of this region (Figure 6.5) to maintain accessibility to the culture chamber. This chamber must be large enough to accommodate culture of cells or tissues. At a minimum, the electrode array and reference electrode must be exposed. The high hydraulic resistance of the channels requires that high pressures can be supplied, which will be discussed further in the following section.

Despite the simplicity suggested by this section's title, interfacing remains a notorious challenge in all fields of microfluidic research. As recently reviewed by Temiz et al. [248], "Although the importance of fluidic interconnects is sometimes neglected in the microfluidics community, they are typically the least reliable components of a [lab-on-a-chip] device and often limit the overall performance of these devices."

Methods for reversible, parallel microfluidic connectors were recently reviewed [249]. None of these methods were suitable for the current application. Presented alongside this review was a new method which enabled connection of 35 tubes, based on silicone connectors covalently bonded to Si substrates. Single tubes could be reversibly inserted and removed from the silicone connectors. Mated female and male connectors were also demonstrated for parallel connection of multiple tubes, which had previously been demonstrated for 9 channels [250]. Conceptually similar connectors are commercially available for up to 12 channels with a pitch as small as 1.5 mm for 0.8 mm tubes (Dolomite, Royston, UK). These connectors use a fluorinated elastomeric gasket in which tubes are inserted. The gasket and tubes are pressed against the microfluidic device, sealing the gasket against the device while also compressing the gasket around the tubes.

My first efforts produced silicone connectors directly on the NPMEA (Figure 6.21) before the method of Wagler et al. was published, but failed due to poor bonding of silicone to ADEX. Moulds were produced by CNC milling, and used to cast silicone connectors from PDMS. Dry bonding had been intended by exploiting the capabilities of OSTE+, but adhesive was required for bonding to ADEX. This solution was challenging as the adhesive could flow into the microfluidic channels. These connectors were compatible with the recording device, but required manual insertion of individual tubes. Small movements of the tubes put sufficient strain onto the connector to detach it from the NPMEA.

A second design (Figure 6.22) was inspired by the Dolomite connectors (for example, part number 3000067, Dolomite Microfluidics). Viton elastomer sheets were laser cut to form gaskets. Tubes were positioned and held vertically by a polyamide piece produced by selective laser sintering (Dick & Dick GmbH, Leipzig, Germany). A CNC-milled aluminium frame pressed the connector against the NPMEA with screws or magnets.

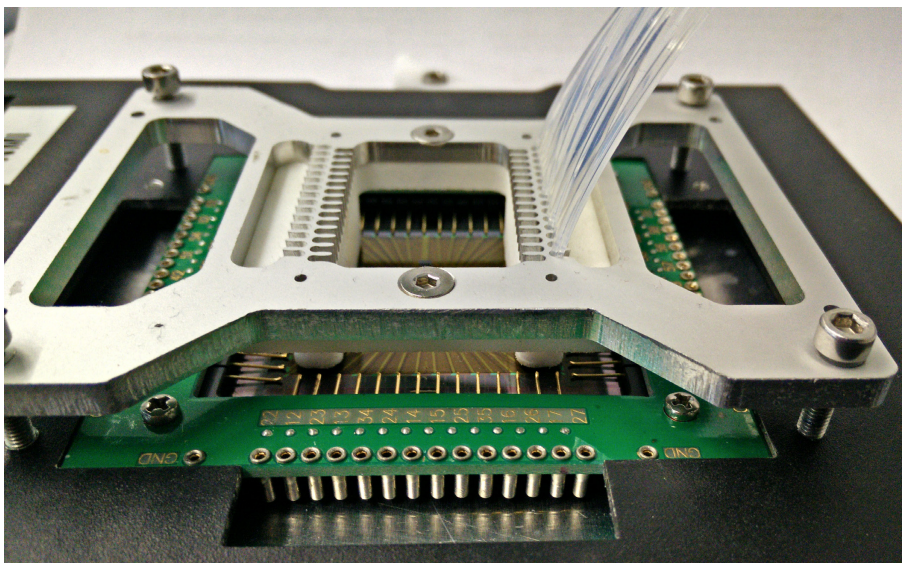


Figure 6.22 Dolomite-inspired tubing connector interfacing the NPMEA in a recording system. Only fifteen tubes were connected here.

This design allowed for robust connections with the NPMEA so that channels could be filled. However, sub-millimetre movements of the NPMEA tolerated by the recording system prevented reliable alignment of the connectors with the microfluidic outlets. Also, various recording systems have physical differences which required individual customization of the aluminium frame.

The final successful design (Figure 6.23) was inspired by a timely publication describing connectors [249] and combined the concept of silicone connectors with the pressure-enabled sealing of the Dolomite-inspired connectors. It achieved excellent alignment with the microfluidic outlets, and was compatible with various recording systems or could be used without a recording system.

A mould for the silicone connectors was produced similarly to Wagler et al. by milling of polycarbonate and PTFE (Figure 6.24). Needles (0.6 mm diameter, Pryn, Stolberg, Germany) were inserted through the top PTFE piece. Each needle was inserted in a 5 mm piece of silicone tube (inner diameter 0.51 mm, VWR International GmbH, Darmstadt, Germany). Air plasma activated the silicone surfaces before assembly of the polycarbonate and PTFE pieces. Each needle was positioned by being pressed into a corresponding dimple in the polycarbonate base. A second PTFE piece defined the outer dimensions and height of the silicone connectors. The assembly was filled with PDMS around the silicone tube pieces and allowed to cure at room temperature to avoid shrinkage [251].

Cell culture chambers were produced by milling of cyclic olefin copolymer (Topas 6015, TOPAS Advanced Polymers GmbH, Frankfurt-Höchst, Germany), and included screw holes and a contoured outer edge to assist with alignment of the connectors. The bottom edges of the piece were chamfered to minimize spreading of adhesive during bonding. A jig was produced to accurately align the culture chamber with the NPMEA. Bonding was achieved with a UV epoxy. Initially, NOA81 (Norland Products Inc., Cranbury, NJ, USA) was used, which has been reported to be biocompatible [252]. Later, Vitralit 6108 (Panacol-Elosol GmbH, Steinbach/Taunus, Germany) was used, which is certified for biocompatibility according to USP Class VI and ISO 10933-5, and has excellent moisture and chemical resistance and is compatible with several sterilization methods [253]. No functional difference was noticed between the two epoxies. The epoxy was applied to the perimeter of the culture chamber and filled the space between chamber and SUEX layer by capillary action.⁴ The epoxy was cured by UV exposure through the UV-transparent COC. Curing according to the supplier's instructions was important to avoid debonding.

An aluminium clamp was milled to fit the outer dimensions of the COC piece and the silicone connectors. The connector assembly consisted of the aluminium clamp, two silicone connectors, and 60 tubes (FEP, 0.8 mm outer diameter, IDEX H&S, Wertheim-Mondfeld, Germany) inserted into the silicone and

⁴I have since discovered that a similar method has been applied to bond microfluidic structures [254].

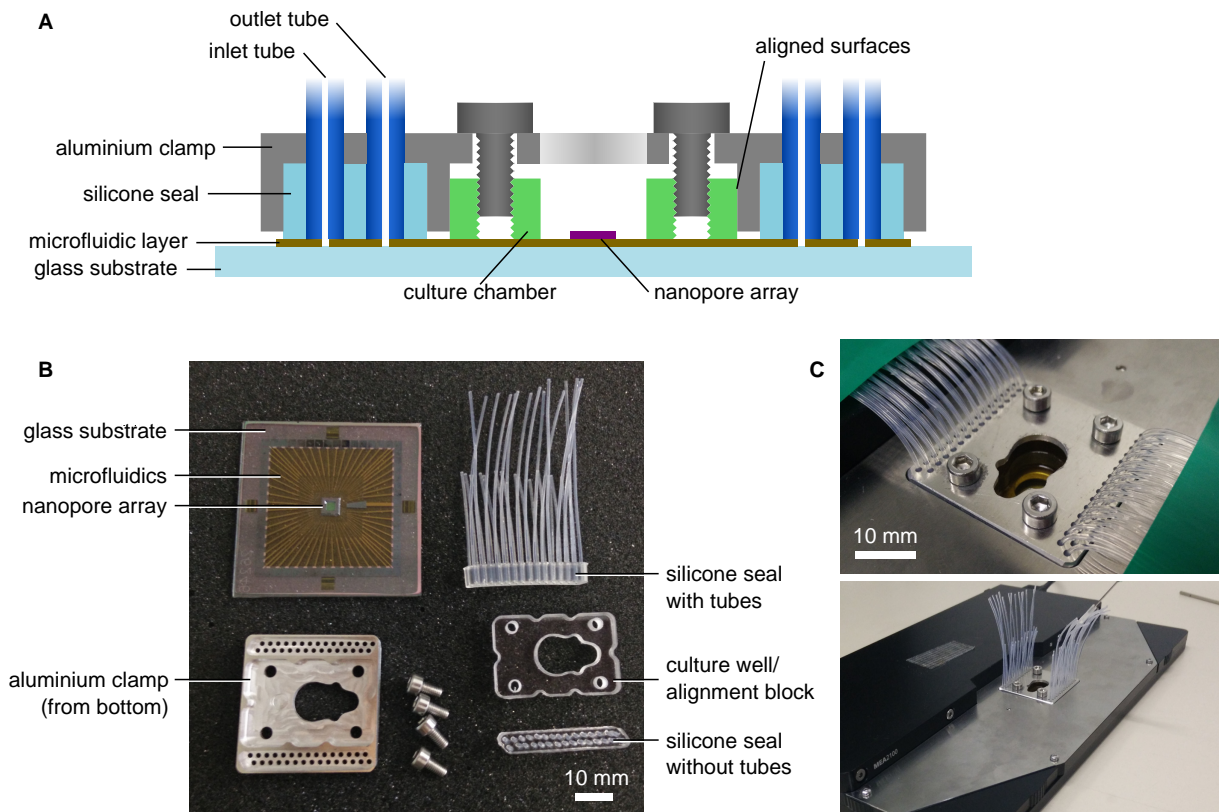


Figure 6.23 Final connector design. **A** Schematic cross-section. **B** Individual components. The alignment block was bonded to the NPMEA with an adhesive. The other components were reversibly assembled. **C** Photos of a NPMEA in a standard MEA recording setup with the final connector. The small form factor enabled dense fluidic connections without obstructing access to the culture well. The asymmetrical shape of the culture well was chosen to accommodate the field of nanopores and microelectrodes as well as the large integrated reference electrode.

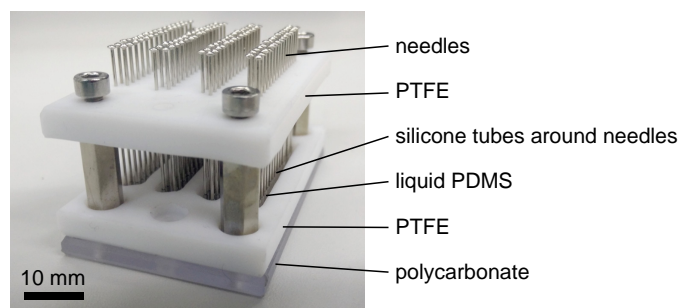


Figure 6.24 Mould for silicone seals.

stabilized by the aluminium clamp. This assembly fit over the COC piece bonded on the NPMEA to align the connectors with the microfluidic outlets. Four screws pressed the silicone connectors against the NPMEA. Visual observation of the silicone–microfluidic interface during tightening of the screws was sufficient to achieve a good seal of all tubes. A possible improvement would replace the screws with a clasp mechanism to quickly and reliably applying appropriate pressure.

The connector was tested extensively with several NPMEAs. Leakage was tested by submerging the assembled connector and NPMEA in water and supplying up to 300 kPa pressurized air. An upper pressure limit was not evaluated. Connection to specific single channels was evaluated by applying pressurized air to a single inlet, and observing that bubbles were released only from the corresponding outlet tube. The connector proved reliable to produce the results presented in the next section.

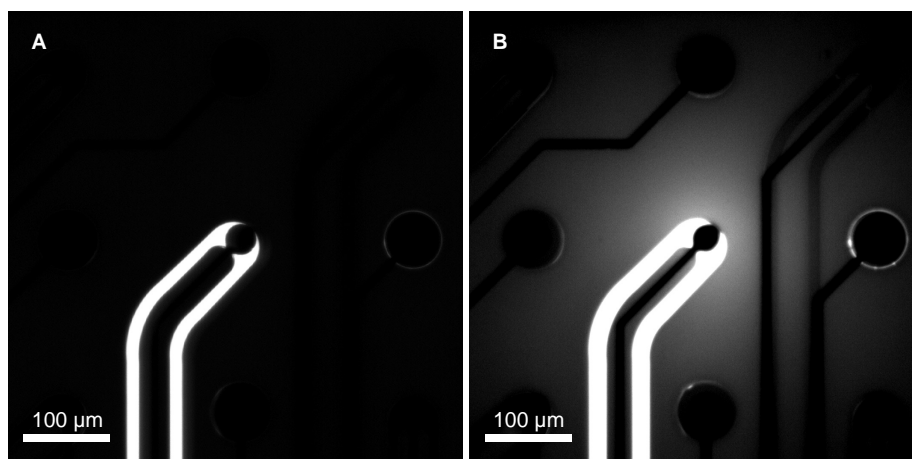


Figure 6.25 Release from a nanopore observed by fluorescence microscopy. **A** A single channel was filled with a carboxyfluorescein solution. The top of the membrane was dry, and no spreading of fluorescence was observed. **B** The top of the membrane was covered with water. Diffusion of carboxyfluorescein resulted in a visible fluorescence spreading away from the nanopore. The channels filled with concentration dye were overexposed to observe the released dye. Contrast was enhanced in both images.

6.5 Microfluidic control of chemical release from nanopores

Microfluidic control was necessary to apply desired solutions in the channels, as well as for rinsing and emptying of the channels. Chemical release can be controlled by switching of the microfluidic channel contents. Release of chemicals through the nanopores occurs by diffusion or may be driven by pressure or voltage application (see chapter 4). Figure 6.25 shows fluorescent dye released by diffusion through a single nanopore.⁵ Future development of gated nanopores will enable each channel to be continuously filled with a stimulant solution for on-demand release without unwanted leakage.

Switching of applied liquids or gas was performed off-chip for simplicity. Until now, provisional methods were sufficient for characterization of the device and initial experiments, and provided important results for the whole system. Addressing each channel on the NPMEA was achieved using the connectors described in the previous section. Earlier connectors were difficult, but still provided useful results. The final design has provided the most results with excellent reproducibility, and was easy to use.

The provisional control setup is illustrated in Figure 6.26. The connector was used to interface 60 tubes to the 30 microfluidic channels. Segments of FEP tubes (outer diameter 0.8 mm, inner diameter 75 μm) with lengths of 30–50 mm were fixed to the connector with their opposite ends free. Individual channels were addressed as illustrated in Figure 6.26B. Connection to a blunt needle (outer diameter 0.8 mm) was made with a short segment of silicone tubing whose smaller inner diameter formed a tight fit against the FEP tube and needle. Microlitre quantities of liquid were preloaded in the needle tip with a pipettor. The needle was connected to a pressurized air line through a regulator, and was used with pressures up to 300 kPa. Such pressures were sufficient for these experiments. No leakage was observed at these pressures. A higher pressure limit was not investigated.

Before interfacing with the NPMEA, dust and other contamination were removed by rinsing all tubing and components with isopropanol and drying with nitrogen. The pressurized air line was connected to a 0.2 μm filter before connection to the tubing. All liquids were filtered with a 0.2 μm filter before use, with the exception of biological dyes (section 6.6) which were available only in microlitre quantities. Experiments without rinsing tubing or filtering liquids often irreversibly clogged the microfluidic channels.

The possibility to fill, rinse, and dry channels was investigated (Figure 6.27). Pressurized air, deionized water, and several aqueous solutions were studied. Air was easy to flow, as its viscosity is ~ 50 times

⁵The nanopore membrane here was bonded with liquid adhesive which was not resistant to prolonged exposure to water. Later NPMEAs were baked at 200 $^{\circ}\text{C}$ to improve resistance of the microfluidic structures to water. A side-effect of this baking was increased autofluorescence of microfluidic structures, which complicated observation of dye release. Electrical characterization was adopted as a preferred method to measure nanopores, as explained in the following section.

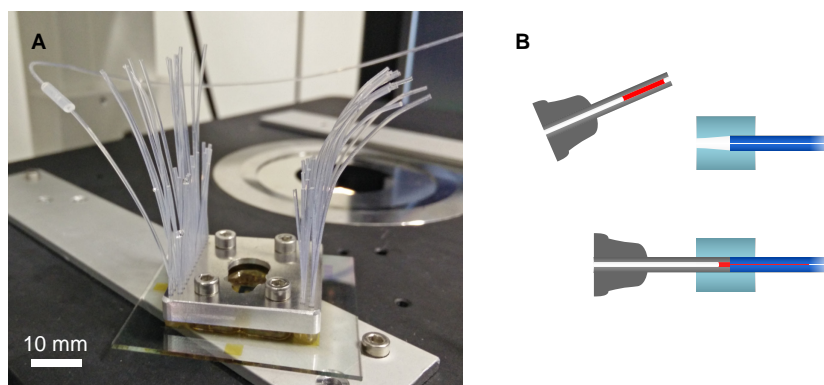


Figure 6.26 Provisional control setup. **A** The NPMEA and connector were assembled, and an individual channel was addressed by a syringe. **B** Microlitre volumes were loaded into the tip of a blunt needle, and the needle was connected to an inlet tube by insertion into a silicone tube. Pressure was applied to push the solution to the microfluidic channel.

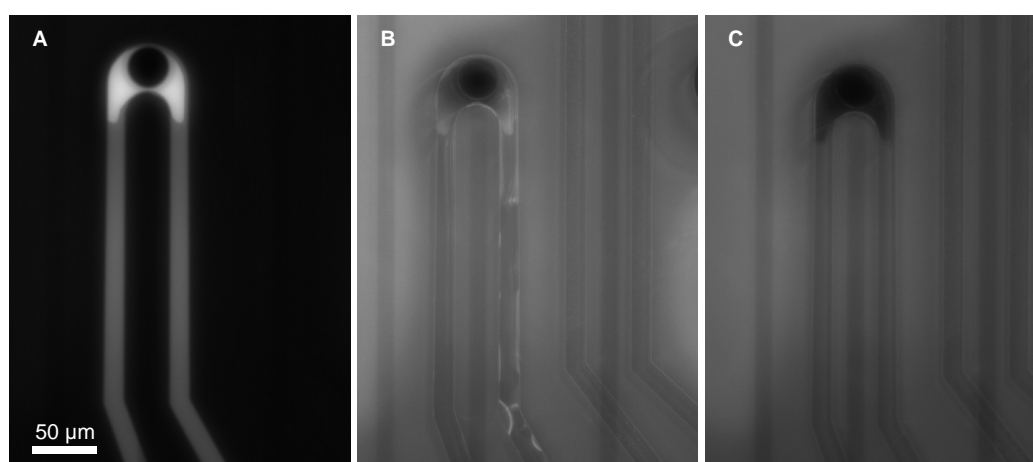


Figure 6.27 Filling and rinsing of a channel. **A** A single channel was filled with a fluorescence solution. **B** Purging with nitrogen could clear the channel. **C** Rinsing with deionized water removed any trace of the fluorescent salt. **B** and **C** were captured with maximum exposure settings, resulting in visible background fluorescence in comparison to **A**.

lower than water. However, air flow must consider the pressure difference which can be maintained across a meniscus according to the Young–Laplace equation. Pressurized air must exceed the Laplace pressure to push a meniscus forward within the microfluidic channel. Bubble release from nanopores would have required pressures higher than those applied here and was not observed.

To ensure a channel was not blocked, pressurized air was applied to the inlet tube. A microlitre of water was placed on the tip of the outlet tube; bubbling through the droplet confirmed flow through the channel. Small volumes of liquid were applied by disconnecting the needle, pipetting liquid into its tip, reconnecting, and applying air pressure (Figure 6.26B). Flow rates were measured by the linear movement of the meniscus through the inlet tube, and the movement of the meniscus and formation of droplets at the outlet tube. These droplets were removed manually, or the tube was inserted in a vial to collect waste. Flow in the microfluidic channels was observed with a fluorescence microscope (Nikon Eclipse Ti) and a carboxyfluorescein solution.

The diversity of length scales in the system can be better understood by considering the hydraulic resistance of the various elements (Figure 6.28, Table 6.1), analogous to electrical circuit analysis [101]. In this system, pressure-driven control generated appropriate flows based on hydraulic resistance under safe pressure limits. Conversely, applying defined flow rates could have quickly generated damaging pressures if channels became restricted. The hydraulic resistance of the elements of the system were calculated by equations 2.8 and 2.10 for nominal dimensions and water at 25 °C. Series combinations of two flow paths through the system are included in Table 6.1. The hydraulic resistance of the path comprising the inlet tube, microfluidic channel, and outlet tube is dominated by the microfluidic chan-

nel. The path along the inlet tube, microfluidic channel, and nanopore is dominated by the enormous hydraulic resistance of the nanopore, 10^4 times larger than that of the microfluidic channel. Also important is the volume of the elements, which is dominated rather by the larger tubes. Measurements of the pressure-driven flow rate in filled channels provided estimates of $13\text{--}15\text{ kPa s nl}^{-1}$ for hydraulic resistance, in reasonable agreement with the prediction in Table 6.1.

This analysis has important implications for controlling chemical release from the nanopore. If the system is filled with water, and a stimulant solution is applied at the inlet tube, 225 nl must be displaced for the stimulant to reach the nanopore, through a channel with a conductance of $0.052\text{ nl kPa}^{-1}\text{ s}^{-1}$. A pressure of 100 kPa would drive a flow rate of 5.2 nl s^{-1} and 43 s would pass before the stimulant reaches the nanopore.

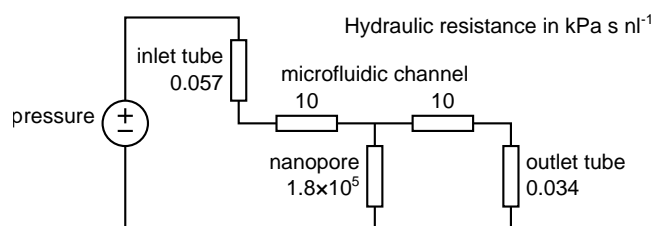


Figure 6.28 Fluidic resistance network of a single channel on the NPMEA.

Table 6.1 Hydraulic analysis of the microfluidic network.

Element	Dimensions	Volume (nl)	Resistance ^a (kPa s nl ⁻¹)	Conductance (nl kPa ⁻¹ s ⁻¹)	Flow rate ^b at 100 kPa
Inlet tube	length 50 mm diameter 75 μm	221	0.057	17	1.7 μl s^{-1}
Microfluidic channel	length ^c 30–42 mm width 10–50 μm height 10 μm	9	19	0.052	5.2 nl s^{-1}
Nanopore	length 500 nm diameter ^d 100 nm	4×10^{-9}	1.8×10^5	5.5×10^{-6}	0.6 pl s^{-1}
Outlet tube	length 30 mm diameter 75 μm	133	0.034	29	2.9 μl s^{-1}
Inlet tube, microfluidic channel, and outlet tube		362	19	0.05	5.2 nl s^{-1}
Inlet tube, half of microfluidic channel, and nanopore		225	1.8×10^5	5.5×10^{-6}	0.6 pl s^{-1}

^aHydraulic resistance is unintuitive. The values indicate the pressure (in kPa) required to produce a flow rate of 1 nl s^{-1} . The inverse (hydraulic conductance) provides a more intuitive value. ^bNote the different units for flow rates. ^cChannel length depends on the position of the inlet and outlet. Calculations used the maximum length. ^dThis microfluidic analysis assumed a diameter of 100 nm . The diameter greatly affects release from the nanopore, but has negligible effects on flow through the microfluidic channel.

In provisional experiments to study the behaviour of the system, such delays can be accommodated. Figure 6.27 illustrates switching of the liquid in a channel. The empty channel was filled by flowing 1 μl of $\sim 100\text{ mM}$ carboxyfluorescein solution (Figure 6.27A). Then, air pressure cleared the channel, leaving droplets on its walls (Figure 6.27B). Flowing 5 μl of deionized water rinsed the remaining carboxyfluorescein. Initially, the water appeared brighter due to the increased fluorescence (decreased quenching) of

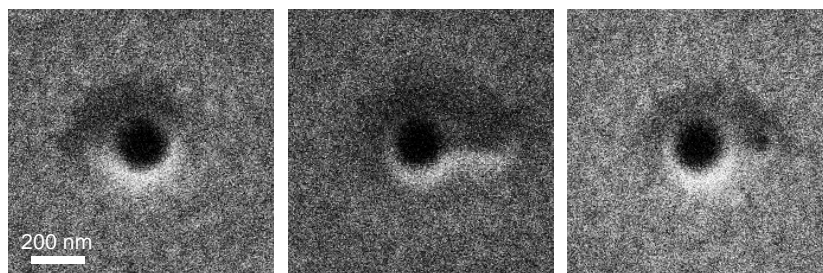


Figure 6.29 SEM of nanopores from a NPMEA. Three nanopores were imaged directly after milling. Apparent diameters were ~ 200 nm from the milling side, and would be narrower through the 500 nm membrane. Artefacts from the automated milling process were visible in the second and third nanopores.

carboxyfluorescein at lower concentrations. As flow continued, fluorescence disappeared (Figure 6.27C).

Absent from Figure 6.27 is any fluorescence from dye released from the nanopore. Uncontrolled silane polymerization may have blocked the nanopore, as discussed in section 6.3.2. Release of carboxyfluorescein from nanopores was observed when adhesive bonding method was used (Figure 6.25), but this method failed with longer exposure to water. Furthermore, later NPMEAs were baked at 200°C to improve their resistance to water. This increased the autofluorescence of the microfluidic structures; observing the small release from a single nanopore may not be possible against the increased autofluorescence. While bonding of later NPMEAs used monofunctional silanes and did not block the nanopores, observation of dye release was abandoned in favour of electrical characterization, as described in the following section.

Some biological investigations would be compatible with the slow switching speed introduced above. For example, effects of pharmacological blockers on neuronal activity are observed over longer time scales [28]. However, many interesting neurochemical processes occur much faster. Microfluidic control to generate more rapid chemical signals could exploit pulse code modulation [255] or on-chip valves [240].

This discussion has focused on controlling release from individual channels. Simultaneous control of 30 channels will require additional degrees of complexity. Computer-controlled microfluidic manifolds would be necessary. Nanopore control by hydrophobic gating should greatly simplify the required microfluidic control systems.

6.5.1 Electrical characterization of nanopore array functionality

Electrical measurements were used to characterize NPMEAs. Electrical measurements are quantitative, unlike fluorescence microscopy, and were well established through the work in chapter 5. Measurements from a NPMEA are described below. This NPMEA was later used in a retina experiment.

The nanopores on the NPMEA were each milled for 30 s with a beam current of 10 pA, to obtain large nanopores in the 500 nm membrane with a reduced risk of blockage and higher chemical release rate (Figure 6.29). The NPMEA was treated with air plasma for 2 min then interfaced with the tubing connector. The culture chamber was filled with phosphate-buffered saline (PBS). Each microfluidic channel was evaluated by flowing pressured gas (100 kPa) and observing bubbling from the outlet tube. After observing flow, channels were filled with $2\ \mu\text{l}$ of PBS, which was sufficient to fill the inlet and outlet tubes and the microfluidic channel. Electrical measurements were made between Ag/AgCl electrodes in the culture chamber and connected to the outlet tubes. The measurements therefore included series contributions of the nanopore, microfluidic channel, and outlet tube. Afterwards, the channels were rinsed with deionized water ($2\ \mu\text{l}$) and dried with pressurized gas.

On this NPMEA, gas could be flowed through 23 of the channels. The remaining seven channels had visible blockages in their tubes or at their microfluidic inlets. An additional five channels were blocked during filling with PBS, presumably by particles in the inlet tube flowing and blocking the microfluidic inlet. Therefore, eighteen nanopores were measured by impedance spectroscopy and voltage scanning (Figure 6.30). For each channel, low frequency impedance was resistive and in agreement with the conductance measured by voltage scanning. Fourteen channels had similar conductances with an average

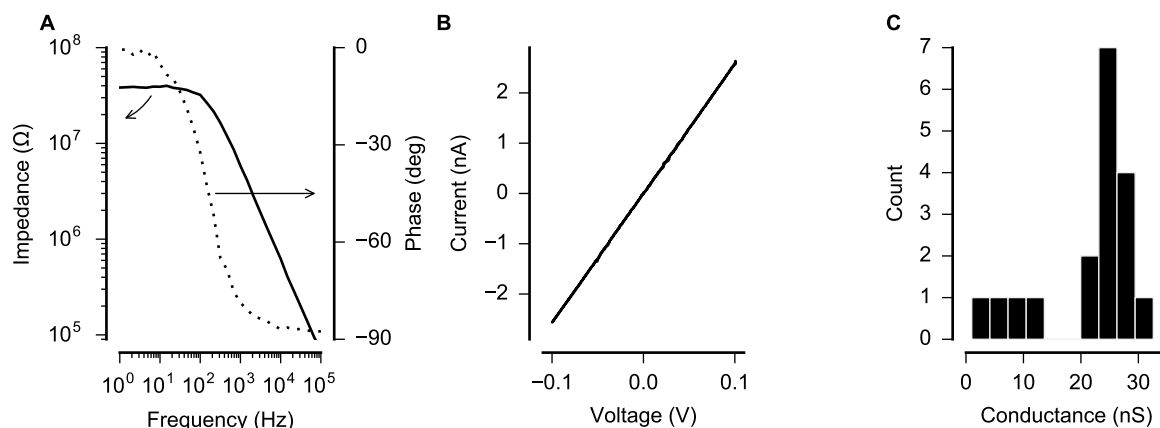


Figure 6.30 Electrical characterization of nanopores in a NPMEA. Electrodes were in the culture chamber and the outlet tube, so that measurements included the nanopore, microfluidic channel, and tube. **A** A typical impedance spectrum, showing an ohmic low frequency impedance of $38\text{ M}\Omega$ (26 nS), and high frequency capacitive behaviour corresponding to 26 pF . **B** A typical voltage cycle showing ohmic behaviour with a slope of 26 nS . **C** Conductance measured through 14 nanopores had an average of $25 \pm 3\text{ nS}$. Four outliers had much lower conductances, likely due to partial blockages in their microfluidic channels or tubing.

of $25 \pm 3\text{ nS}$. The remaining four channels had higher impedances, suggesting a partial blockage of their microfluidic channels or tubing. Two of these channels became blocked during rinsing with deionized water. All other channels were successfully rinsed and could be used in a retina experiment with results in Figure 6.35.

For the fourteen channels with high conductance, nanopore diameters were estimated by subtracting estimated tubing and channel impedance of $26\text{ M}\Omega$. This was a rough estimate, as the microfluidic channels varied in length ($15\text{--}21\text{ mm}$) and their individual impedances were not measured. According to this approximation, estimated nanopore diameters were $183 \pm 36\text{ nm}$, in agreement with images obtained after nanopore milling.

6.6 Towards stimulation of cells and tissues

Preliminary experiments for chemical modulation of neuronal cultures and explanted neural tissue have been developed. First experiments with cortical neurons were carried out, but poor adhesion of neurons on the substrates prevented cultivation for the required time ($2\text{--}3$ weeks) to observe spontaneous activity. Experiments with retinal preparations have been performed, but have not confirmed chemical release from nanopores.

The NPMEA, as a modification of the standard MEA, is intended for combined chemical stimulation with electrophysiological recording of neuronal responses. PEDOT-coated electrodes on the NPMEA with impedances of $60\text{--}100\text{ k}\Omega$ at 1 kHz were appropriate for neuronal recording [223]. Electrode quality was further tested in the MEA recording system. Low noise of $\sim 10\text{ }\mu\text{V}$ was recorded in PBS, which is appropriate for extracellular neuronal spikes which are typically recorded with peaks of $20\text{ }\mu\text{V}$ or greater.

The microfluidic channels must be maintained in cell culture conditions. If electrolyte evaporates from these channels, precipitation of dissolved salts will block the channels. Dissolution of these obstructions would only be possible by vacuum-assisted filling of dead-end channels,⁶ disrupting the biological experiment. In acute experiments, tubes will remain connected for the experiment duration and this issue can be neglected. However, long-term culture of neurons requires cultivation in an incubator for several weeks. It is not sufficient to leave the channels empty, as condensation and movement of water and salts through the nanopores may occur. Rather, the channels should be filled with a buffer solution and covered to prevent evaporation. Evaporation in MEAs has been solved by covering chambers with FEP

⁶An aqueous solution was accidentally allowed to evaporate in the channels of several NPMEAs, blocking any flow into the channels. By submerging them in deionized water and applying vacuum, the channels filled with water and the blockages were dissolved.

membranes, which are impermeable to water vapour [256]. At the end of an experiment, the channels should be flushed with deionized water to remove all salts before drying.

Many molecules in biological environments could block nanopores. For example, clogging of nanopores by amyloid-beta peptides has been observed [257]. Standard procedures to prepare MEAs for biological experiments involve coating with various chemicals such as polyelectrolytes or proteins [237]. This issue did not present a problem during acute retina experiments.

Another concern in these preliminary experiments was to minimize the use of animals. Close cooperation with other groups at the NMI made it possible to obtain cells and tissues in parallel with other experiments.

6.6.1 Cortical neurons

Experiments with central nervous system neurons were planned and carried out with Dr. Martin Kriebel and Christine Dürr. Cortical neurons from embryonic rats were cultured on two NPMEAs. The exposed surfaces of the NPMEAs are SiN_x and SU-8, both of which are commonly used in MEAs, so standard methods were used.

NPMEAs and membrane covers were sterilized by air plasma and UV, and coated by standard procedures to encourage cell adhesion [237]. The NPMEA was incubated with polyethylene imine (PEI) at room temperature for 1 h. PEI solution was repeatedly rinsed with deionized water and the NPMEA was allowed to dry in air before incubation with laminin for 1.5 h at 37 °C.

Meanwhile, a suspension of cortical neurons (embryonic day 17) was prepared according to standard procedures. A pregnant Sprague–Dawley rat was killed by terminal anaesthesia with carbon dioxide. Embryos were removed and dissected to remove their brains. The cortices were isolated and trypsinized, and the cells were washed and suspended in NMEM-B27 medium [258]. The laminin solution was aspirated and the NPMEAs were rinsed once with cell culture medium. Cells were plated and the NPMEAs were covered with membrane covers and placed in an incubator at 37 °C. Medium was replaced every 2–3 days.

On one NPMEA, the neurons did not adhere and were washed away with the first medium change after two days. The second MEA showed reduced density at the second medium change, and the majority of cells washed away with the third culture change. Such problems are occasionally encountered in normal MEA experiments. Further tests which would have been necessary to test chemical stimulation were deferred in favour of acute retina experiments.

The NPMEAs were kept in the incubator with culture medium for 16 days to evaluate their stability. The dry bonding process was stable as shown in Figure 6.20.

6.6.2 Retinas

First experiments with the NPMEA to chemically stimulate retinas have failed to demonstrate the success of chemical stimulation. The experiments demonstrated the readiness of NPMEAs for biological experiments and their compatibility with *in vitro* tissue preparations.

Experiments with explanted retinas were performed in collaboration with the Neurophysics research group of Dr. Günther Zeck. Mouse retinas were prepared by Florian Jetter and Henrike Stutzki. Fluorescence microscopy was performed by Anita Niedworok and supported by Dr. Paolo Cesare and Dr. Martin Kriebel.

Explanted retinas show spontaneous activity and response to light [28, 259], making them a useful experimental model. *In vitro* experiments with retinas are crucial for investigating electrical stimulation [22, 30] and chemical stimulation [31, 32] towards retinal neuroprostheses. Experiments of chemical stimulation were attempted but have not yet confirmed chemical release from nanopores. These efforts are discussed below.

Preliminary experiments evaluated the compatibility of the NPMEA with standard retina preparations. Devices were treated with air plasma for 1 min and incubated with a 1 mg ml⁻¹ aqueous solution of poly-L-lysine at 37 °C for at least 10 min. Measurements showed that nanopores remained open after coating with PLL.⁷ Retinas from blind rd1 mice were prepared according to established methods [259].

⁷Since these measurements, use of PLL to modify nanopores has been reported [260].

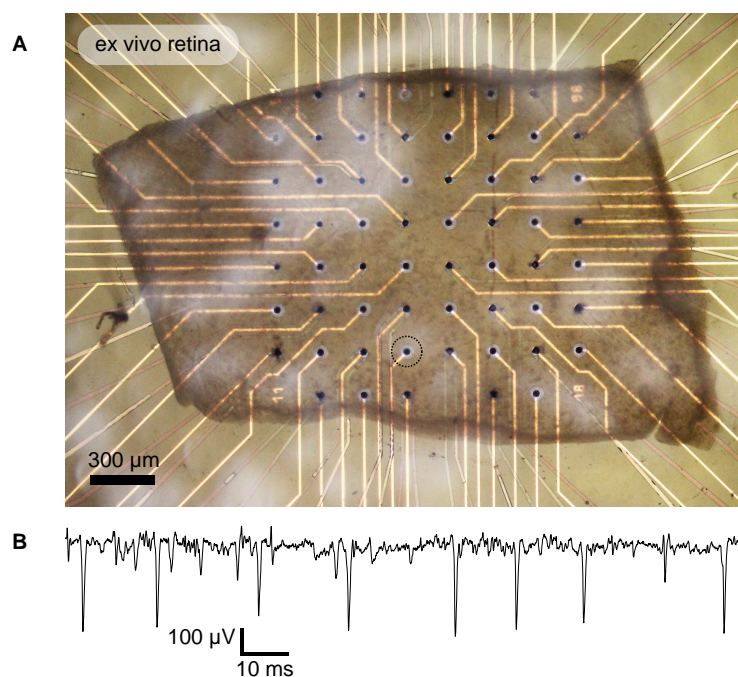


Figure 6.31 Retina electrophysiology. **A** A portion of an ex vivo retina was prepared on an incomplete NPMEA (lacking only the nanopore membrane). **B** Spontaneous activity was observed over more than 10 h. The addition of microfluidic structures did not compromise the ability to measure electrical activity.

The blind retinas exhibit robust spontaneous activity even when prepared under ambient light, unlike healthy retinas.

Complete NPMEAs were used, and the exposed electrodes recorded spontaneous activity; electrodes within the microfluidic channels did not record activity, as expected. Incomplete NPMEAs lacking the nanopore membrane were also used (Figure 6.31), in which all electrodes were exposed and the microfluidic channels were open in the centre of the device. Retinal portions were placed with the ganglion cell (epiretinal) side down on the device. Stimulation of photoreceptor cells would be more applicable for neuroprosthetic applications. However, current methods achieve better adhesion between the device and epiretinal side, in comparison to the subretinal side.⁸ Spontaneous action potentials were observed for at least 10 h (Figure 6.31B).

In devices lacking nanopore membranes, chemical release from the open microfluidic channels was attempted. By applying pressure to the tubing, medium released from the microfluidic opening under the retina formed a bubble, damaging the retina and lifting it from the substrate. This negative result demonstrated the need for the nanopore membrane to physically separate the microfluidic channel from the tissue.

Verification of chemical stimulation through single nanopores was attempted by a fluorescence staining method. Calcein acetoxymethyl ester (calcein AM or CAM) is a non-fluorescent cell-permeant calcein derivative which is reverted to the impermeant and fluorescent calcein by intracellular enzymes. CAM has previously been used for fluorescent observation of local chemical stimulation [57, 59, 61]. CAM is taken up by the first cells it encounters, and converted to calcein; it is therefore limited to staining outer cells of the retina [261].

For the experiments described below, NPMEAs were produced with SU-8 and ADEX microfluidics. Large nanopores were milled for 30 s with a beam current of 10 pA, which reliably produced diameters above 100 nm. Nanopore membranes were bonded to microfluidics using the dry bonding method with APDMES. Before chemical stimulation experiments, nanopores were confirmed to be open with conductivity measurements. Conductivity was measured again after biological experiments to confirm that nanopores remained open.

The first experiment attempted local release of CAM through a single nanopore (Figure 6.32). Before

⁸Ganglion cells are typically placed downwards to record their spiking electrical activity.

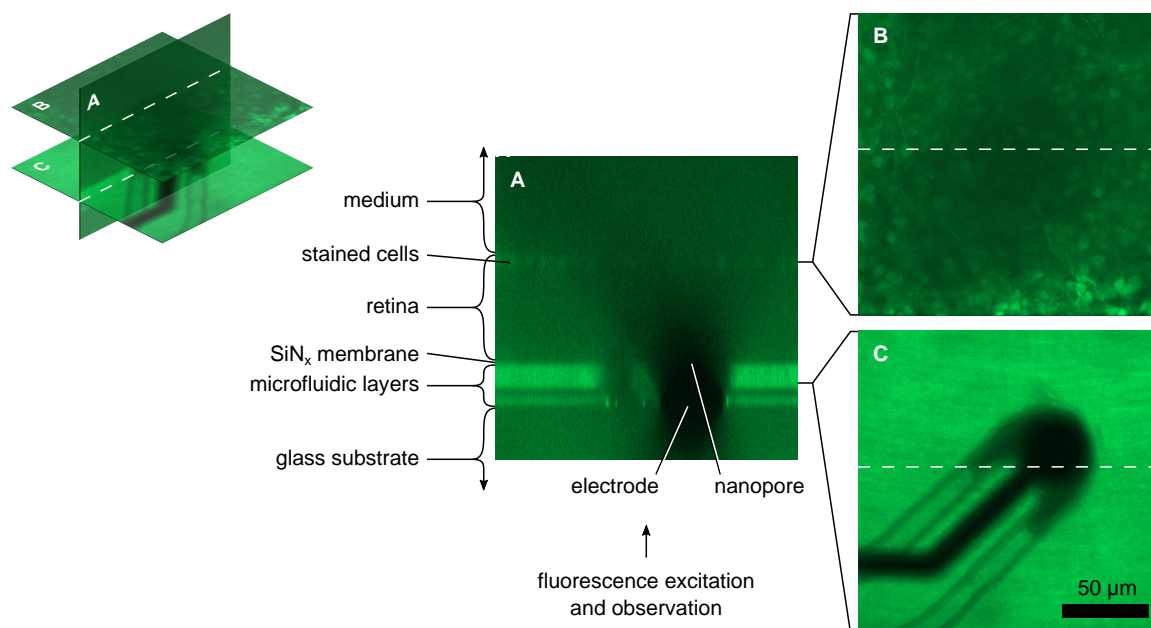


Figure 6.32 Calcein staining of a retina on a NPMEA. **A** A cross-section of stacked images, showing the shadow of the microelectrode. Any cells stained by release from the nanopore would have been within the shadow. **B** Cells exposed to CAM in the medium were stained. **C** Autofluorescence of microfluidic structures was visible. The electrode was visible as a shadow. The scale bar in **C** applies to all images. Excitation and emission wavelengths were 488 nm and 525 nm, respectively.

the experiment, four open nanopores were measured (conductances of 16–23 nS from culture chamber to outlet tube). The 26 other nanopores could not be measured, due to defects in the microfluidic channels.⁹ During the experiment, only one of the nanopores could be used (conductance of 20 nS). Three of the remaining microfluidic channels were blocked, likely by particles. Therefore, the results of this experiment were limited to a single nanopore.

A portion of an rd1 retina was positioned on the NPMEA over the nanopores and electrodes with the ganglion cells facing down. Spontaneous electrical activity was measured, confirming good adhesion of the retina on the device. The microfluidic channel was filled with 1 mM CAM in DMSO, allowing CAM to release from the nanopore by diffusion. After 30 min, the retina was imaged with a confocal fluorescence microscope. Autofluorescence of the microfluidics structures was visible, but no evidence of fluorescent cells was observed.

After this negative result, the entire retina on the NPMEA was stained by adding 10 μ M CAM to the medium for 30 min. Cells on top of the retina were stained (Figure 6.32B). CAM did not penetrate deeper within the retina, similar to previously reported results [261]. A key result from this experiment was the observation of the shadow cast by the microelectrode (Figure 6.32A). The microelectrode would have blocked excitation to and emission from cells near the nanopore, located directly above the microelectrode. Therefore, this experiment could not disprove chemical release from the nanopore.

Another observation was the strong autofluorescence of the SU-8 and ADEX structures. Previous fluorescence microscopy (for example, in Figure 6.25) used NPMEAs baked at 150 °C, but the microfluidic layers delaminated after extended exposure to water. Later NPMEAs, including here, were baked at 200 °C to improve their resistance to delamination. The hotter baking step changed the colour of the SU-8 and ADEX and increased its autofluorescence.

New experiments were undertaken to solve issues encountered above. The first problem was the electrode shadow. New devices were produced on SiN_x-coated glass substrates without electrodes. For continuity, these will be referred to as electrode-free NPMEAs. By removing the opaque electrodes, cells directly above the nanopore should be visible. A second problem was the absence of any visible cells, as possibilities such as detachment of the retina from the device or incorrect focus of the microscope had to

⁹Many channels were blocked at their inlets or outlets due to a short rest time before developing the ADEX layer, as discussed in section 6.2.2.

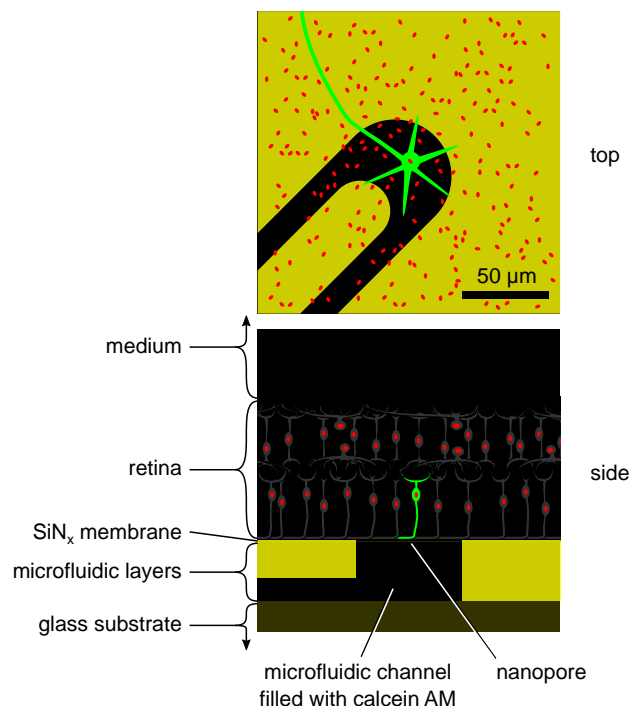


Figure 6.33 Concept for local fluorescence staining by chemical release from a nanopore. All cells would be identified by DRAQ5 nuclear staining (red) from the culture medium. CAM release near the nanopore should locally stain a single cell or a few cells (green). Autofluorescence of the microfluidic structures is expected (yellow).

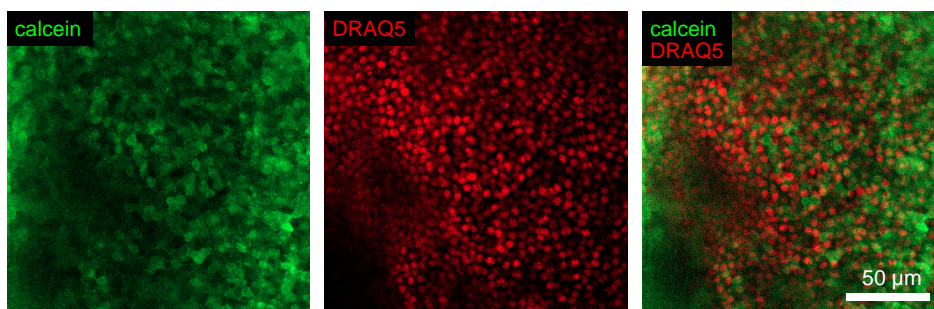


Figure 6.34 Retina stained with CAM and DRAQ5. Maximum intensity projections show cytoplasm (calcein) and nuclei (DRAQ5). Nuclei were stained throughout the retina, while CAM was taken up by outer cells. Excitation/emission wavelengths for calcein and DRAQ5 were 488 nm/525 nm and 639 nm/690 nm, respectively.

be addressed. Even the problem of the shadow cast by the microelectrode was not obvious until observing the cross-section of the z-stack (Figure 6.32A). Therefore, new experiments included a second dye to stain all cells in the retina. DRAQ5 was suggested by Martin Kriebel as a suitable membrane-permeant live-cell dye, with excitation and emission spectra compatible with calcein. Anticipated successful results are illustrated in Figure 6.33, with all cell nuclei stained red with DRAQ5 and local calcein staining near the nanopore. The broad autofluorescence of the microfluidic structures is illustrated in yellow.

In a control experiment, retina was imaged after staining with these two dyes (Figure 6.34). A portion of a retina was incubated for 30 min at room temperature in oxygenated Ames' medium with 4 μM CAM and 5 μM DRAQ5. The retina was rinsed with fresh Ames' medium, placed on a glass slide, covered with a cover slip, and imaged. Calcein fluorescence was limited to outer cells. Nuclei stained by DRAQ5 throughout the retina were visibly separated.

Results of an experiment on an electrode-free NPMEA are shown in Figure 6.35, and are representative of several nanopores on a single device. Nanopores were confirmed by conductivity measurements (section 6.5.1, Figure 6.30). The device was plasma treated and coated with PLL as described above, then rinsed with Ames' medium and a portion of an rd1 retina was placed over the nanopores. The

retina was stained with 5 μM DRAQ5 in Ames' medium. The retina was adhered to the device during staining, in contrast to the control experiment above, so the staining time was doubled to 60 min before rinsing with fresh medium.

In the control experiment, calcein fluorescence was observed after incubation in 4 μM CAM for 30 min. Considering the nanopore as a point source with unrestricted diffusion into water, equation 4.5 predicts a steady-state concentration greater than 4 μM within 2 μm of the nanopore. Restriction of diffusion by the adhered retina and removal of extracellular CAM by uptake into cells will affect its transport. Several microfluidic channels were filled with 1 mM CAM in DMSO, which was allowed to diffuse from the nanopores for 30–60 min before imaging.

No evidence of calcein-stained cells was observed; such cells would have been visible in the maximum intensity projections in Figure 6.35 (top left). Minimal DRAQ5 staining was observed (visible in the maximum intensity projection side view and the retina cross-section). Strong green and red autofluorescence of microfluidic structures was observed, with differences between SU-8 and ADEX. However, the nanopore membrane was suspended with no microfluidic structures below it; any stained cells should have been visible.

After the experiment, the microfluidic channels were rinsed. Measurements of the nanopores' conductivity verified that the nanopores remained open (Figure 6.36).

In the first attempt for local calcein staining by release of CAM, the shadow from the microelectrode could have prevented imaging of stained cells (Figure 6.32). Other factors could have also contributed. In the second attempt (Figure 6.35), no electrodes were present to cast shadows. Minimal DRAQ5 fluorescence in comparison to the control experiment suggests a biological problem could contribute; no electrical recording was possible to verify the retina's health. Alternatively, the weak DRAQ5 fluorescence could have resulted from absorbance of light by the microfluidic structures. However, the microfluidic-free area around the nanopore would have been expected to reveal DRAQ5 fluorescence. No calcein staining would be expected if CAM release was prevented by a blockage of the nanopores. Such a blockage would have to be transient, as the nanopores were measured to be conductive before and after the experiment. For example, blockages of glass micropipettes have been encountered when releasing lipophilic dyes in organic solvents into aqueous solutions [262]. However, DMSO is miscible with water and solubility of CAM in water should not be limiting.¹⁰ The use of DMSO as a solvent for CAM could have increased the permeability of cell membranes to calcein, allowing it to diffuse rather than remain concentrated in cells near the nanopore. DMSO acts on cell membranes to increase their permeability and at higher concentrations becomes toxic [263]. The experiment could be repeated with an aqueous CAM solution. Because CAM degrades in water, an aqueous solution should be prepared immediately before use.

A simpler explanation for these negative results is that the quantity of dye released was too low to achieve visible fluorescence. Equation 4.2 describes the release rate expected by diffusion from a nanopore. The nanopores in the experiment above had estimated diameters of 183 nm and lengths of 500 nm. The microfluidic channel was filled with 1 mM CAM in DMSO, and should diffuse into the aqueous culture medium. Diffusivity of CAM in DMSO or water is estimated to be $2 \times 10^{-10} \text{ m}^2 \text{ s}^{-1}$ [264]. Diffusion was predicted to release CAM from the nanopore at $1.5 \times 10^{-17} \text{ mol s}^{-1}$. The total amount released over 30 min was predicted to be 27 fmol.

In comparison, Zibek et al. observed fluorescence of cells within a 130 μm diameter, 4 min after application of 31 fmol CAM (0.25 mM, 125 μl) [59], and similarly within a diameter greater than 400 μm , 9 min after application of 100 fmol (0.25 mM, 400 μl) [61]. In these cases, CAM was applied across an area with a diameter of several tens of micrometres. Release of a similar quantity of CAM localized at a nanopore was therefore expected to produce a visible response.

Additional biological factors may affect CAM transport in the retina. The control experiment demonstrated calcein fluorescence, but did not examine whether staining occurred on both sides. Further experiments must specifically demonstrate staining of retinal ganglion cells before again attempting CAM staining by nanopore release.

¹⁰According to technical support from Life Technologies GmbH, solubility of CAM in water should be greater than 10 mM.

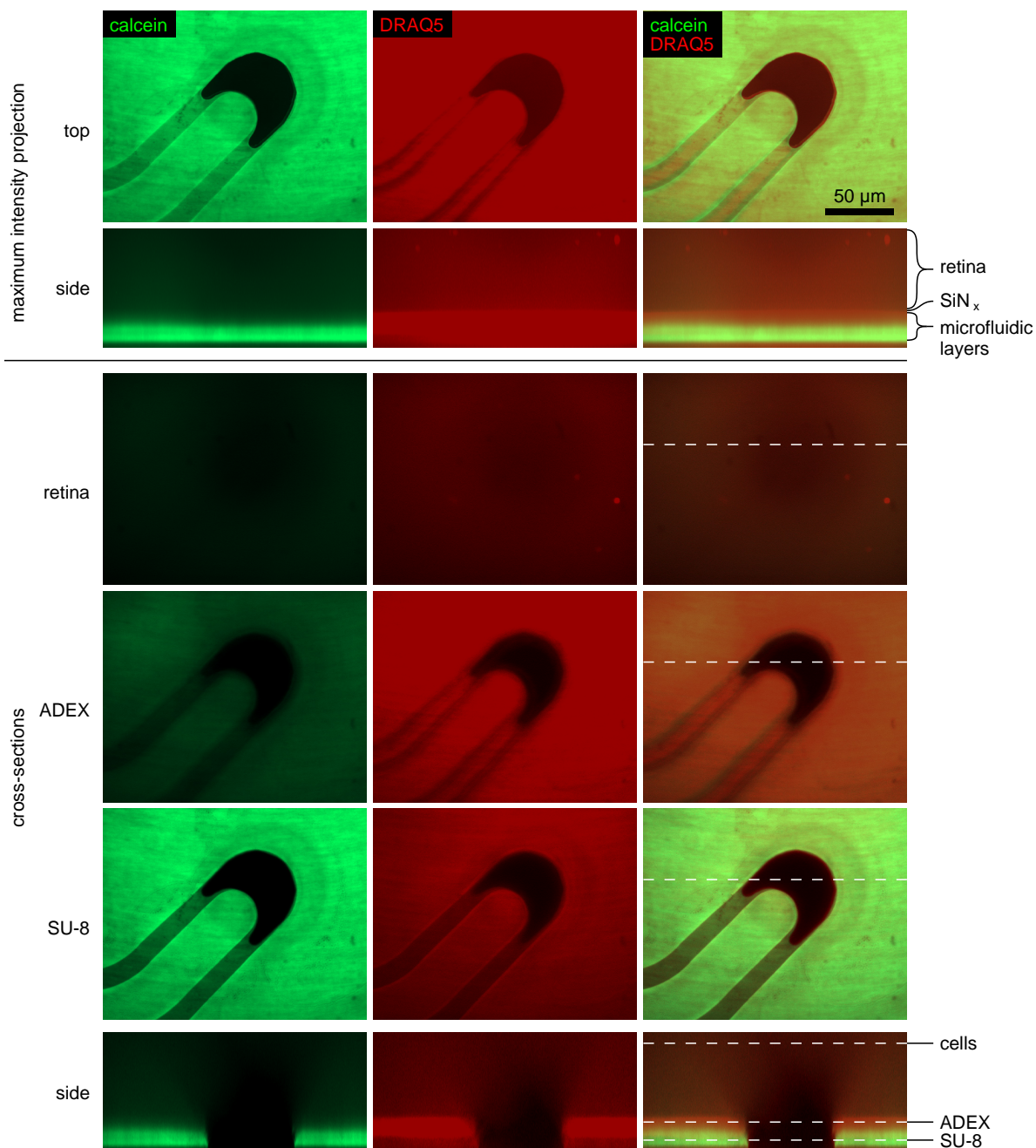


Figure 6.35 DRAQ5 and attempted local CAM staining with an electrode-free NPMEA. These results are representative of several nanopores on a single device. Maximum intensity projections are shown (top) as well as individual slices (bottom). The retina was broadly stained with 5 μM DRAQ5, but DRAQ5 fluorescence was weak compared to control experiments. The microfluidic channel was loaded with 1 mM CAM in DMSO. No local calcein fluorescence was observed near the nanopore. Microfluidic structures were autofluorescent. Excitation/emission wavelengths for calcein and DRAQ5 were 488 nm/525 nm and 639 nm/690 nm, respectively. Locations of the cross-sections are indicated by dashed white lines. The scale bar (top right) applies to all images.

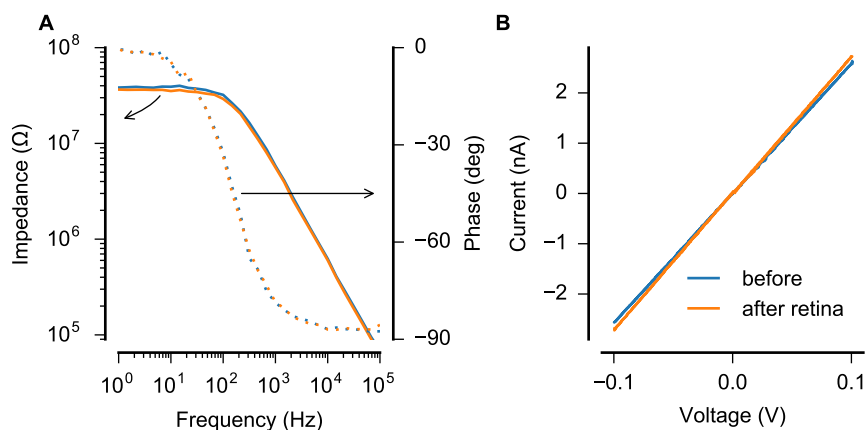


Figure 6.36 Electrical characterization before and after a retina experiment showed that nanopores were not blocked during the experiment. Before measurements were also shown in Figure 6.30.

6.7 Summary

This chapter has presented new technology for chemical stimulation of neurons. The technology was developed with the solid foundation of the established MEA platform. High-resolution microfluidics were produced which enabled manipulation of chemicals within MEA substrates at the scale of $\sim 10\ \mu\text{m}$. Integration of nanofluidic features on microfluidics was established. The integration method is stable against cell culture conditions, and may enable future exploitation of nanofluidic effects for advanced chemical stimulation of neurons or neural tissues. Reliable interfacing with the NPMEA was successfully achieved in a format compatible with standard electrophysiology recording systems.

Establishing this technology as a useful tool requires successful demonstration of local chemical stimulation. Fluorescence staining of acute retina preparations is a promising route to such a demonstration, and the preliminary experiments presented above should be pursued. Positive demonstration will allow consideration of experiments with biologically-relevant stimulation. Challenges of measuring cellular response to localized chemical signals must be solved.

The stability of nanopores in contact with biological matter was measured only after acute experiments. Longer experiments may require further development to ensure continued functionality. Development of microfluidic control systems will be required to simplify and automate experimental methods.

The dry bonding method was developed to ensure that the microfluidic and nanofluidic fabrication processes can be separated. Future development of hydrophobically gated nanopores may replace the uncontrolled nanopores in this chapter.

7 Outlook

This section will discuss the results presented above within the broader context of chemical neuroprostheses, giving an outlook towards future directions for this work and the challenges that remain. This work has presented conceptual and technological advances towards the goal of high-resolution chemical neurostimulation. The results do not, however, present a final state. A priority should be the pursuit of biological proof-of-concept experiments. The path to chemical neuroprostheses remains a long-term vision, and many future challenges, both known and unknown, remain to be investigated. Finally, potential applications of this work to other research fields will be mentioned.

7.1 Current results

The concepts and technology described in this work are significant developments towards nanopore-based chemical neurostimulation. A key aspect has been to bring together new nanotechnology with neurophysiology. By exploring the physics of micro- and nanofluidic chemical transport, concepts for nanofluidic technology to produce rapid, high-resolution chemical signals were developed. New nanofluidic mechanisms have been investigated which may eventually lead to improved neuroprosthetic technology, in ways which microfluidics cannot achieve. Achieving the goal of nanofluidic chemical neuroprostheses will require the realization of advanced technology, far beyond the scope of this work.

Towards this goal, nanopore arrays intended for chemical stimulation of neurons were developed. Fabrication processes were optimized to reliably produce nanopore arrays integrated with microfluidics on microelectrode arrays. A novel dry bonding process was developed to integrate nano- and microfluidic structures, without blocking nanofluidic channels. Compatibility with standard electrophysiology systems for MEAs enabled biological experiments according to standard procedures. Preliminary experiments showed that the nanopore arrays remain bonded to the microfluidics in cell culture conditions and that the microfluidic structures do not interfere with electrophysiological recording. The microfluidic interfacing system enabled the design and testing of chemical release in proof-of-concept chemical stimulation experiments with acute retina preparations. Positive results have not yet been obtained; repetition and optimization of these experiments is necessary.

Investigations towards hydrophobic gating in nanopores have not produced reversible gating in a controlled manner. Literature review and theoretical work have led to an improved understanding of electrowetting in nanopores. Maxwell stress on the liquid–vapour interface was identified as the underlying mechanism of nanopore electrowetting. Models based on the oversimplified contact-angle-based interpretation of electrowetting provided first estimates of electrowetting voltages, although limited validity was expected within nanopores. Promising methods for improved models by numerical solution of the electromechanical model were identified. Additionally, a new concept for reversible hydrophobic gating based on controlled bubble trapping was developed.

Fabrication of nanopores allowed experimental investigation of electrowetting and hydrophobic gating. SiN_x nanopores were fabricated and modified with a monofunctional silane. Gold nanopores were produced to enable use of thiol SAMs and for direct electrical addressing of the nanopores. Bubble traps in gold–thiol nanopores were also produced by etching of a sacrificial layer.

Fabrication of these nanopores demonstrated the success of monofunctional silanes. The stability of silanes and SiN_x made these an excellent system to study electrowetting. Measurements of SiN_x –silane nanopores showed evidence of electrowetting, and may be explained by the electromechanical model. Voltages were lower than predicted by a contact-angle-based model of electrowetting, but this model was expected to have limited validity at these dimensions. Flickering currents and dewetting in SiN_x nanopores could be explained by uncontrolled bubble trapping due to molecular roughness of silane-modified surfaces. Unique currents were also observed in these nanopores, which may be evidence

of field emission. These putative field emission currents led to wetting, which may be explained by charging of nanopore walls.

Challenges of gold nanopores were discovered, including their limited stability during piranha treatment and unexpected difficulties of etching thin sacrificial layers within the gold. Electrowetting of gold–thiol nanopores showed less flickering than SiN_x nanopores and no reversibility. Stability of thiols was insufficient to exploit electrowetting by the integrated electrode.

These results support the theory that trapped bubbles are necessary for reversibility of hydrophobic gating in large nanopores, and molecular effects must be considered. The expected smooth surfaces of thiol SAMs may not trap bubbles as on rough silane surfaces. Smoother surfaces should allow for controlled bubble trapping in engineered structures within nanopores. Avoidance of uncontrolled bubble trapping will be necessary to properly exploit the concept of controlled bubble trapping.

Because reliable mechanisms of hydrophobic gating are not yet established, the development of nanopore arrays was carried out to maximize compatibility with integration of future advances. Bonding nanopore arrays to microfluidic structures required only complementary amine groups on the bonding surfaces of the nanopore membrane. Otherwise, fabrication methods for microfluidic channels and nanopore arrays were independent. Future developments of hydrophobically gated nanopores may exploit novel fabrication methods without limitation due to the microfluidic structures.

7.2 Next steps towards hydrophobic gating in nanopores

Lessons from the hydrophobic nanopores studied in this work must guide continuing research to better understand and engineer hydrophobic gating mechanisms. Before undertaking further experimental work, numerical solutions of the electromechanical mechanism of electrowetting in nanopores should be solved. Predictions from this model may benefit experimental design as well as understanding of results.

New experiments with SiN_x nanopores should use smoother hydrophobic layers. Uncontrolled bubble trapping in the molecularly rough monofunctional-silane-modified surfaces complicates analysis of experimental results. Promising liquid-like hydrophobic surface modifications with low contact angle hysteresis have been reported, but use chemicals capable of polymerization [158, 265, 266]. Similar liquid-like hydrophobic monolayers would be promising for use in nanopores, but must avoid blocking the nanopores.

Experiments with electrode-gated nanopores should explore new materials to improve precision of fabrication and increase electrochemical stability or decrease necessary voltages. Experiments with gold electrodes may provide further useful results. Thin Cr adhesion layers resist piranha etching. Cleaning by oxygen plasma or electrochemical cleaning in dilute H_2SO_4 could allow the use of materials which are etched by piranha. Sacrificial materials for etching of bubble traps require materials which do not interdiffuse with the electrode material. For example, reliable etching of nanofluidic structures as small as 7 nm has been achieved with SiO_2 [267]. Materials with higher electrochemical stability will be necessary for electrode-gated control of nanopores. No known polymer materials or SAMs possess sufficient electrowetting capabilities. Atomic layer deposition (ALD) of high-K dielectric materials could be investigated. As a singular example, smooth BaO films with a relative permittivity of 35 and thickness of 4.5 nm have been produced [268]. Based on these values and a contact angle of 105° , equation 5.3 predicts a wetting voltage of 0.7 V according to the contact-angle-driven model. Stability and biocompatibility of any materials must be considered. Another intriguing possibility is diamond. While intrinsically insulating, doped diamond is electrically conductive [269]. It is chemically and electrochemically inert, with a wide voltage window. Surface modification, such as hydrophobic fluorination [270] could enable low-voltage electrowetting without an insulating layer. However, no reports of nanopores in diamond or electrowetting on diamond surfaces have been published. Electrowetting on planar diamond substrates could indicate with minimal effort whether further evaluation of diamond nanopores should be undertaken.

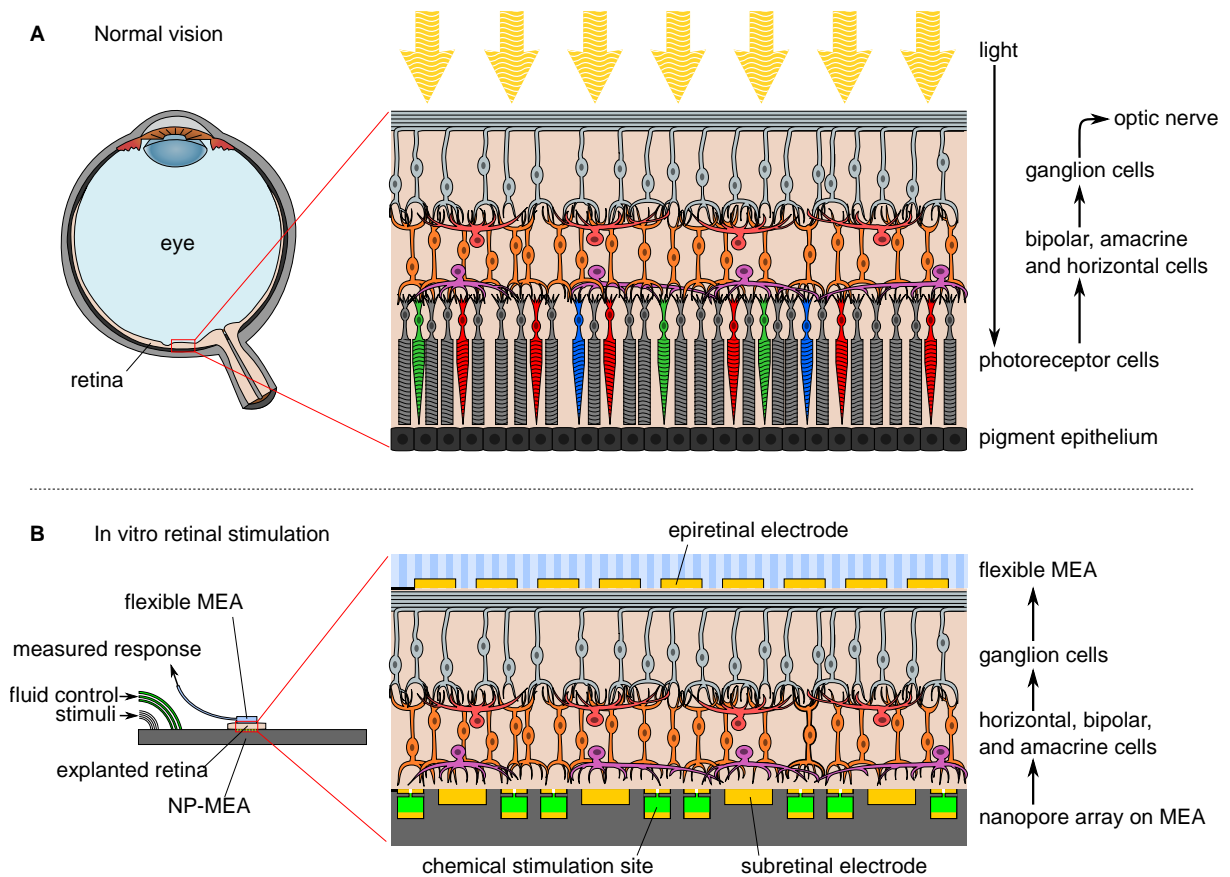


Figure 7.1 A proposed experiment for chemical stimulation of the retina. **A** In healthy retinas, light passes through several cell layers before being received by photoreceptor cells. The information then flows through a network of horizontal, bipolar, and amacrine cells, and is integrated by ganglion cells which form the optic nerve. **B** In vitro investigations with explanted retinas can evaluate artificial retinal stimulation. Here, a degenerate retina lacking photoreceptor cells would be placed on the NPMEA to directly stimulate the retinal circuitry. Elicited responses would be recorded by an epiretinal microelectrode array, which is flexible and perforated to protect the vitality of the retina. This model has been used to study electrical retinal stimulation, and can be adapted to evaluate the proposed neurotransmitter-based stimulation from a nanopore array.

7.3 Next steps towards local chemical stimulation of cells

Biological experiments must verify the functionality of the current nanopore array. Proof-of-concept experiments should be continued with acute retina preparations to demonstrate local fluorescent staining. After demonstration of local chemical release from nanopores, biologically-relevant experiments may be planned. Until controllable nanopores are available, interesting experiments may be accomplished with uncontrolled nanopores. Improved microfluidic control as discussed in chapter 6 would be helpful for controlling chemical release with high temporal resolution.

A proposed experiment to study chemical stimulation of the retina is illustrated in Figure 7.1. Placing an explanted retina on the NPMEA will allow electrical recording and multimodal chemical, electrical, or optical stimulation. Glutamate release from nanopores according to the mechanisms discussed in chapter 4 will locally stimulate the retinal cells. Applied pressure would release glutamate through nanopores, while leakage by diffusion should be accommodated by the retinal cells' glutamate transporters. With the ganglion cells on the exposed side of the retina, a flexible MEA can be placed on top to record elicited activity.

Many other biological experiments will be possible by controlling local chemical environments. For example, a simpler device was used to study neurite outgrowth in response to chemical gradients with only one release source [271]. The NPMEA could be used to establish arbitrary chemical gradients to study, for example, mechanisms of dendritic branching and synaptogenesis.

Quantitative measurement of chemical release would be beneficial to complement the demonstrated

electrical characterization of nanopore arrays. Observation of chemical release from nanopores was recently reported by combined atomic force/scanning electrochemical microscopy [272]. This method would be especially useful to quantify the spatiotemporal dynamics of chemical release in future experiments with gated nanopores.

7.4 Future challenges

Many challenges must be investigated on the course towards producing chemical neuroprostheses. An introduction to some of these is given here. A review of the concept of neurotransmitter release for retinal prostheses discussed many biological issues [27]. Others challenges, especially on the technical side, remain to be discovered.

7.4.1 Materials for nanopores

Nanopores in SiN_x are not stable, and widen due to dissolution [214]. Diamond may be an alternative, as suggested above. Rare earth oxide ceramics are stable in harsh environments and are natively hydrophobic [273]. Integrating such materials would require novel developments, as they are not commonly used in microfabrication.

Nanopores may eventually be blocked by biofouling during exposure to cells and tissues, for example by irreversible protein adsorption [274]. It is not known how long the nanopores will remain functional for chemical release. Modification of the nanopore surfaces to decrease biofouling may be necessary. Yusko et al. prepared nanopores with fluid walls which showed no clogging during experiments with amyloid beta peptides, in contrast to native SiN_x nanopores which clog after a few minutes of exposure [257]. Filling of hydrophobic porous structures with a fluorinated liquid has also been demonstrated to reduce fouling [275]. Although reported in macroscopic membranes, this effect could be transferred to single nanopores.

7.4.2 Individual control of large numbers of nanopores

Control of the 30 microfluidic channels in the present device is challenging. Further increases are impractical and would quickly reach a breaking point. Therefore, higher density integration of nanopores will be limited by how the nanopores can be controlled. Further increases in density and parallelization of hundreds or thousands of nanopores must rely on individual electrical control. This will require control by electrodes integrated to address individual nanopores, as electrical control through a shared microfluidic channel cannot control nanopores individually. Research towards reversible hydrophobic gating by gate electrodes must be continued if high-resolution artificial chemical stimulation is to be achieved.

7.4.3 Chemical elimination

Methods for elimination of the exogenously released chemicals must be considered for specific applications. Neurotransmission is usually terminated by reuptake or enzymatic removal of neurotransmitters. Artificial release of neurotransmitters without artificial removal could cause neurotoxicity. However, biological removal mechanisms may be sufficient even with artificial stimulation. For example, excitatory amino acid transporters are the primary mechanism for removal of glutamate from the extracellular fluid [155]. All retinal cells express these transporters to remove extracellular glutamate. In degenerate retinas without functional photoreceptors, these transporters have a reduced workload, and may have sufficient capacity to remove exogenous glutamate delivered by an artificial device [27, 31].

7.4.4 In vivo chemical neurostimulation technology

Many of the materials and methods used for the in vitro nanopore device have already been applied for in vivo applications. SU-8 has been used for in vivo neural probes [48, 49, 232], although it is not approved for use in implantable medical devices [276]. It is often recognized as biocompatible [229],

although specific cases of cytotoxicity have been reported which can be avoided by proper processing [230]. SU-8 has been used in 'injectable electronics' whose flexible mesh structures minimize immune responses [277]. It is anticipated that the nanopore integration methods in this work can be extended to similar in vivo probes based on SU-8. Microfluidic connections for in vivo probes will also provide a formidable challenge.

An implanted device must contain sufficient chemical for its lifetime, or a means to replenish a reservoir. This challenge has been solved for intrathecal drug delivery devices, which can be refilled by in situ injection into the implanted device through a septum localized by x-ray markers [45].

Future medical use would require clinical trials to achieve regulatory approval. Implantable neuroprostheses must be safe for many years of continuous use. From a regulatory perspective, a chemical neuroprosthesis which comprises both a medical device and drug would be a drug/device combination product. Regulation and approval of combination products is more complex than for non-combination products, such as electrical neuroprostheses.

7.4.5 The structural component of synapses

The concept of a chemical release device functioning as an artificial synapse was proposed more than a decade ago [54]. With pores closer in size to the soma of a neuron, such reports have not approached the function of real synapses. However, even an artificial device which can mimic synaptic release would be a poor imitation of a synapse. Synapses require advanced molecular connections between pre- and post-synaptic neurons, which provide structure and contribute to development, maintenance, and plasticity [278]. Specific biochemical functionalization of a future chemical stimulation device may promote acceptance by neurons, which could encourage the necessary proximity for rapid signalling between chemical release sites and target structures. Perhaps such a connection would satisfy the definition of an artificial synapse.

7.5 Other applications

Single nanopores are typically studied in isolation, but parallelization is currently in demand to improve throughput of single molecule analysis. According to a recent review of nanopore-based DNA sequencing, "Full realization of nanopore sequencing's potential will require additional progress in areas including nanopore parallelization, channel setup and microfluidics" [238].

Recent results of microfluidic integration have produced an array of 5 artificial nanopores [94]. The work presented here surpasses that number by a factor of 6. Furthermore, this work has been restricted to keeping one side of the nanopore membrane open for cell or tissue culture. Many more nanopores could be integrated with individual control if microfluidic channels addressed both sides of the nanopore membrane. Alignment and the risk of blocking the nanopores would be eliminated by in situ fabrication by the controlled breakdown method [95].

Developments in microfluidic fabrication also extend to other applications. Lamination and patterning of multiple dry film resist layers enables production of microfluidic structures which can replace and extend the capabilities of PDMS. The discovery that hard baking at 200 °C prevented delamination on SiN_x (in contrast to 150 °C) will enable new biological applications. An optimized baking temperature between 150 °C and 200 °C may minimize autofluorescence while maintaining adhesion.

8 Methods

Experimental methods are described here to support the discussions in the preceding chapters.

8.1 Nanopore fabrication

The methods developed for the study of hydrophobic nanopores are described here.

8.1.1 Nanopore membranes

Free-standing SiN_x membrane chips were purchased from Silson Ltd. (Blisworth, England). Low stress SiN_x was deposited and patterned on both sides of a silicon wafer (200 or 560 μm thick). Wet etching in potassium hydroxide produces free-standing SiN_x membranes in square 5 mm silicon frames. Single nanopore experiments were performed with 100 μm -square membranes, with thicknesses of 100, 200, and 500 nm. Integration of nanopore arrays used 2 mm-square, 500 nm membranes, additionally patterned with an array of holes to avoid blocking access to the electrodes.

8.1.2 Metal deposition

Metal layers were sputtered or evaporated on the SiN_x membranes. Sputtering of thin layers is limited to thicknesses of tens of nanometres required to form continuous layers. Thick (~450 nm) gold layers were preceded by a 30–50 nm Ti adhesion layer (Leybold Heraeus Z550). Low resolution masking was accomplished by manually applying Kapton adhesive tape to the chips. For finer control, metal layers were evaporated (Pfeiffer PLS 570) by Dr. Ronny Löffler at the Center for Light-Matter Interaction, Sensors & Analytics (LISA+) at the University of Tübingen. Evaporation can produce continuous nanometre-thin layers with real-time monitoring. Chromium (8 nm) was used for adhesion and gold and titanium layers were used for specific nanopore designs. Shadow masks with 100 μm feature sizes were laser cut from metal foil.

8.1.3 Nanopore milling

Nanopores were produced in free-standing membranes by FIB milling using the gallium beam of either an AURIGA CrossBeam FIB-SEM or a Leo 1540XB FIB-SEM (both from Carl Zeiss AG, Oberkochen, Germany). Nanopores were milled from the bottom (Si) side of the nanopore chip. Before milling, the membranes were sputtered for ~20 s with AuPd for conductivity; this layer came off later during piranha cleaning. The FIB current was controlled by measurement with a Faraday cup. Focus, alignment and astigmatism were manually adjusted. Nanopore milling was controlled by a script to hold the beam at a spot for a specified time. Scripts were also used to produce arrays of nanopores. Shifting the beam could produce arrays over tens of micrometres with high accuracy. Over larger areas, the stage was moved which reduced the accuracy. FIB currents of 1–20 pA and times of up to 60 s per nanopore were typical. Dimensions were determined by FIB cross-sections.

8.1.4 Nanopore cleaning

After milling, hydrocarbon coating on nanopore walls inhibits reliable wetting [183]. Nanopores were cleaned in hot piranha solution (sulphuric acid and hydrogen peroxide) to fully oxidise and hydrophilize their surfaces. Piranha solution is extremely dangerous, can spontaneously heat up to at least 170 °C, and may explode if proper precautions are not observed. Piranha will oxidise the surface of SiN_x but not etch it. Therefore, SiN_x nanopores without metal layers can be cleaned aggressively with a 3:1

mixture of 96 % H_2SO_4 and 30 % H_2O_2 above 100 °C for extended times. Nanopores with metal layers required more care, as piranha etches Ti (and to a lesser extent Cr) and also damaged gold nanopores. H_2SO_4 was heated to 100 °C, and H_2O_2 was added to make a 50:1 mixture. Nanopore membranes were submerged for typically 3–5 min, although sometimes repetition was required before nanopores were completely hydrophilic. Complete wetting was confirmed by recording stable and linear ionic currents at low transmembrane voltages (± 100 mV), with conductance corresponding to nanopore dimensions observed after nanopore milling.

8.2 Thiol modification

Hydrophobic gold–thiol nanopores were produced by formation of PFDT SAMs. Nanopores were cleaned with piranha solution (section 8.1.4) and rinsed thoroughly with deionized water. Glassware was cleaned thoroughly, with acetone, isopropanol, water, and dried. A flask was filled with 50 ml pure ethanol, sealed with a septum, and bubbled for several minutes with nitrogen to remove oxygen. A 1 mM solution was prepared by adding 14.7 μl PFDT. Individual nanopore chips were placed in 4 ml scintillator vials covered with PTFE septa and flushed with nitrogen. PFDT solution was withdrawn from the flask and injected into the vials with nanopore chips. The vials were kept in the dark during immersion. After a prescribed time, the chips were removed, rinsed thoroughly with ethanol and water and dried with nitrogen.

The same process was used to produce PFDT SAMs on planar gold substrates for contact angle measurements. A gold-coated Si wafer (643262, Sigma-Aldrich) was diced, cleaned aggressively with piranha, rinsed and placed into a deoxygenated ethanol solution of PFDT. High contact angles and low sliding angle of water droplets on the SAM-coated gold were readily apparent. Advancing and receding contact angles of $113^\circ \pm 1^\circ$ and $103^\circ \pm 6^\circ$ were measured, and representative images are shown in Figure 8.1.

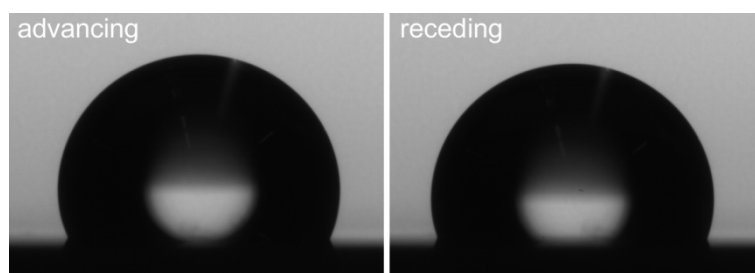


Figure 8.1 Droplets of water show the advancing (left) and receding (right) contact angles on a gold surface coated with PFDT.

8.3 Hydrophobic silane modification of nanopores

After piranha cleaning, SiN_x nanopores were immersed in a 1 % v/v ODMCS solution in toluene. The ODMCS solution was prepared in a glove box under nitrogen atmosphere to reduce contamination or influence of moisture. However, strict moisture control was not necessary for the monofunctional silane, which only has one functional group on the silicon atom available to react with SiN_x surfaces. Nanopores were immersed in silane solution typically overnight, but sometimes for several days or longer. No difference was apparent for these different immersion times. After removal from the solution, nanopore chips were rinsed thoroughly with fresh toluene and kept in fresh toluene for at least 30 min. They were then dried and baked in an oven at 120 °C for 30 min.

8.4 Non-sticking coating for soft lithography

Surfaces to be modified were treated with air plasma until they were hydrophilic (2–4 min), confirmed by low water contact angles. Substrates were heated on a hot plate to 150 °C on a piece of aluminium

foil. A droplet of PFOTCS was placed on the foil and a glass cover was placed over the hotplate. After 30 min, the hotplate was turned off. The substrate was allowed to cool and then rinsed with isopropanol and water.

8.5 Photolithographic microfluidic fabrication

Microfluidic structures were produced on MEAs by deposition and patterning of two layers. The first layer defined the channels in SU-8, while the second covered the channels by lamination of thin-film photoresist. Photomasks were designed in nanocad (Nanosoft, Moscow, Russia) and produced by Delta Mask B.V. (Enschede, the Netherlands).

MEAs (NMI TT GmbH, Reutlingen, Germany) were dehydrated at 150 °C for at least 3 h. SU-8 3005 was spin-coated for 10 s at 500 rpm and 30 s at 1000 rpm, to a nominal thickness of 10 μm , and soft-baked at 65 °C for 1 min, 95 °C for 3 min, and 65 °C for 1 min. Exposure was performed with an i-line filter on an MA6 mask aligner (SÜSS MicroTec AG, Garching, Germany) for a dose of 430 mJ cm^{-2} , usually at 12–15 mW cm^{-2} . A post-exposure bake at 65 °C for 1 min, 95 °C for 5 min, and 65 °C for 1 min was followed by a rest period of at least 20 min. Substrates were developed in mr-Dev 600¹ (micro resist technology GmbH, Berlin, Germany) for 1 min, then rinsed with isopropanol and dried with nitrogen. Substrates were baked at 150 °C for at least 1 h to make the structures resistant against later developing with cyclohexanone.

The channels defined in SU-8 were covered by lamination of 20 μm -thick ADEX A20 (DJ MicroLaminates, formerly DJ DevCorp, Sudbury, MA, USA). ADEX A20 was laminated at ~ 80 °C and a speed of 3 mm s^{-1} . The supporting foil was removed and ADEX was exposed with an i-line filter and a dose of 1000 mJ cm^{-2} . Exposed substrates were baked at 65 °C for 1 min, 85 °C for 10 min, and 65 °C for 1 min, and then allowed to rest for 2 h. Substrates were developed in cyclohexanone for 3 min, then were sprayed with fresh cyclohexanone, rinsed with isopropanol, and blown dry with nitrogen. Aiming the nitrogen at the aperture array in the centre of the substrate cleared solvents from the channels, which could be visually observed by the reflectance of the empty channels. The microfluidic structures were then ready for bonding with nanopore membranes. After bonding, the whole structure was baked in an oven at 200 °C for at least 1 h to complete cross-linking for improved stability. The substrates were ramped from room temperature and cooled in the oven.

8.6 Amine modification of silicon nitride for bonding

SiN_x membranes were prepared for bonding with SU-8 and ADEX microfluidic structures by reaction with 3-aminopropyltrimethylethoxysilane (APDMES) [159]. Membrane chips were oxidised in 3:1 piranha prepared at 100 °C for 60 min, then rinsed with deionized water and blown dry with nitrogen. The chips were immersed in a 1 % v/v solution of APDMES in toluene. The silane reaction was prepared in a nitrogen glovebox to avoid contamination, but strict moisture control was unnecessary for the monofunctional silane. After immersion overnight or longer,² the NPAs were rinsed with toluene, immersed in fresh toluene for at least 30 min, then rinsed with acetone and isopropanol, dried with nitrogen, and baked at 120 °C for at least 30 min.

8.7 PDMS soft lithography

Polydimethylsiloxane (PDMS) precursors (Sylgard 184, Dow Corning GmbH, Wiesbaden, Germany) were mixed at a 10:1 ratio by weight. The mixture was degassed in a desiccator to remove bubbles and dissolved gases. Negative moulds for desired structures were filled with PDMS, with care taken to avoid introducing bubbles. If necessary, the filled moulds were degassed again to remove bubbles. Curing

¹propylene glycol methyl ether acetate (PGMEA)

²Multiple membranes were prepared simultaneously, and kept in silane solution until needed. Results with immersion for several months were indistinguishable from membranes immersed overnight.

was done at elevated temperatures or for longer times at room temperature. Higher temperatures cause shrinkage, which must be considered when the cured PDMS must be aligned with other structures [251].

8.8 CNC milling

Computer numerical control (CNC) milling enables rapid prototyping of microfluidic structures and supporting systems. Milling cutters of various sizes can create arbitrary features in planar substrates quickly, but dimensions and precision are limited. A cutting diameter of 1 mm can achieve aspect ratios of at least 12. Cutters are commercially available with minimum diameters as small as 50 μm but aspect ratios are limited. Further limitations are introduced by manual alignment and the mechanical precision of the CNC system, with best results achieving precision of tens of micrometres. CNC milling was used to produce the connectors for microfluidic interfacing (Figure 6.23) and PDMS moulds (Figure 6.24). Three-dimensional structures were designed in SolidWorks (Dassault Systèmes SolidWorks Corp., Waltham, MA, USA) and were exported as .dxf files for preparation with isyCAM (imes-icore GmbH, Eiterfeld, Germany). A three-axis machine controlled a milling tool (KRESS-elektrik GmbH & Co. KG, Bisingen, Germany).

8.9 Electrochemistry

Ag/AgCl electrodes were produced from Ag wire. Wires were first sanded and rinsed with ethanol. A potential of +1 V vs. an existing Ag/AgCl electrode was applied for 10 s, followed by a 2 s reverse pulse at -1 V. This was repeated for at least ten cycles, and finished with 30 s at +1 V. This process produced electrodes with offsets below 1.5 mV. Electrodes could be refreshed by repeating this process.

After fabrication of microfluidic structures and bonding of nanopore membranes, gold electrodes were coated with PEDOT by a standard procedure [223]. An electrolyte was prepared by mixing 6 μl ethylenedioxythiophene (EDOT) with 3 ml of 1 % 70 000 g mol^{-1} poly(sodium-p-styrenesulfonate) (PSS) solution, and a current of 14 nA was applied versus a Pt mesh counter electrode. Low impedance of the coated electrodes was confirmed by potentiometric electrochemical impedance spectroscopy, measuring 60–80 k Ω at 1 kHz.

Earlier devices were produced on MEAs with TiN electrodes, which have typical impedances of ~50 k Ω and are well-established for electrophysiology. After fabrication of SU-8 microfluidic layers, impedances greater than 500 k Ω were measured, which could prevent recording of action potentials. To remedy this, gold and PEDOT were deposited on the TiN electrodes. Electrodes were treated with air plasma to ensure hydrophilicity. Gold was deposited from a commercial gold electrolyte (NB Semi-plate Au 100, MicroChemicals GmbH, Ulm, Germany) by pulsed galvanostatic electrodeposition with 10 pulses of 0.1 s and pauses of 1 s, applying 850 nA at each electrode. The counter electrode was a Pt mesh. This process should produce a 130 nm gold layer. PEDOT was deposited as described above. Poor adhesion of PEDOT and gold on TiN was observed as the PEDOT and gold would fall off.

8.10 Nanopore measurements

Nanopores were measured by potentiometric electrochemical impedance spectroscopy and cyclic voltammetry, using a potentiostat controlled by EC-Lab software (Bio-Logic Science Instruments SAS, Claix, France). Nanopore chips were mounted in fluidic cells (see section 5.4.2) and connected to syringes with built-in Ag/AgCl electrodes. Syringes were used to fill the fluidic cell. Unless otherwise noted, the electrolyte was phosphate-buffered saline (PBS) without Ca^{2+} or Mg^{2+} (L 182, Biochrom GmbH, Berlin, Germany). Impedance spectra were measured with amplitudes of 10–50 mV from 100 kHz to as low as 10^{-3} Hz. Cyclic voltammetry was measured with maximum voltages of ± 10 V, and scan rates of 1 mV s^{-1} to 1 V s^{-1} . Two electrodes were usually used, and no difference was measured when voltage-sensing and current electrodes were separated. Polarity of the nanopore measurements was not reported, as it was not rigorously controlled. Similar effects were observed at both polarities.

Future experiments should control and report polarity of the nanopore measurements. During filling of the fluidic cell, opposing reservoirs should be electrically shorted with Ag/AgCl electrodes to avoid charging [208].

8.11 Fluorescence microscopy

Fluorescence microscopy was performed with an Eclipse Ti microscope (Nikon GmbH, Düsseldorf, Germany). A solution of 5-(and-6)-carboxyfluorescein (Life Technologies GmbH, Darmstadt, Germany) was used as a fluorescent tracer, and was observed with a fluorescein isothiocyanate (FITC) filter. High concentrations of this dye are self-quenching and have reduced fluorescence. For example, fluorescence appeared stronger at 100 μM than 100 mM. Loading a concentrated solution into a microfluidic channel allows observation of the diluted signal released from a nanopore.

Fluorescently-stained retinas were imaged with a Zeiss Axio Observer Z1 spinning disc confocal microscope (Carl Zeiss AG, Oberkochen, Germany). Staining of retinas was performed with calcein AM and DRAQ5 (both from Life Technologies GmbH, Darmstadt, Germany). Calcein was excited with a 488 nm laser and emission was captured through a 525 nm filter (bandwidth 50 nm). DRAQ5 was excited with a 639 nm laser and emission was captured through a 690 nm filter (bandwidth 50 nm).

8.12 Biological experiments

Devices were treated with air plasma for 1 min and incubated with an aqueous solution of poly-L-lysine (1 mg ml⁻¹, P1274, Sigma-Aldrich Chemie GmbH, Munich, Germany) at 37 °C for at least 10 min. Retinas from blind rd1 mice (Charles River Laboratories) were prepared according to established methods [259]. Portions of several square millimetres were placed with ganglion cells down on the devices. The retinas were perfused with Ames' medium, which was bubbled continuously with carbogen (95 % O₂, 5 % CO₂). Medium was not perfused during fluorescent staining but was bubbled with carbogen.

8.13 Data analysis, graphing, and document preparation

Figures were composed with Inkscape and GIMP. Illustrations are original unless otherwise noted. Graphs were produced with the matplotlib package [279, 280] and the Anaconda Python distribution (Continuum Analytics). This document was typeset with L^AT_EX. References were organized with Mendeley.

Bibliography

1. *Neuroscience* 3rd ed. en (eds Purves, D. *et al.*) (Sinauer Associates, Sunderland, MA, USA, 2004).
2. Azevedo, F. A. C. *et al.* Equal numbers of neuronal and nonneuronal cells make the human brain an isometrically scaled-up primate brain. *J. Comp. Neurol.* **513**, 532–41 (Apr. 2009).
3. Rusakov, D. A., Savtchenko, L. P., Zheng, K. & Henley, J. M. Shaping the synaptic signal: Molecular mobility inside and outside the cleft. *Trends Neurosci.* **34**, 359–369 (2011).
4. Van der Kloot, W. The regulation of quantal size. *Prog. Neurobiol.* **36**, 93–130 (Jan. 1991).
5. Schneggenburger, R., Meyer, A. C. & Neher, E. Released fraction and total size of a pool of immediately available transmitter quanta at a calyx synapse. *Neuron* **23**, 399–409 (June 1999).
6. Richards, D. A., Guatimosim, C., Rizzoli, S. O. & Betz, W. J. Synaptic vesicle pools at the frog neuromuscular junction. *Neuron* **39**, 529–41 (July 2003).
7. McCormick, D. A., Connors, B. W., Lighthall, J. W. & Prince, D. A. Comparative electrophysiology of pyramidal and sparsely spiny stellate neurons of the neocortex. *J. Neurophysiol.* **54**, 782–806 (1985).
8. Sätzler, K. *et al.* Three-dimensional reconstruction of a calyx of Held and its postsynaptic principal neuron in the medial nucleus of the trapezoid body. *J. Neurosci.* **22**, 10567–79 (Dec. 2002).
9. Regus-Leidig, H. & Brandstätter, J. H. Structure and function of a complex sensory synapse. *Acta Physiol. (Oxf)*. **204**, 479–86 (Apr. 2012).
10. Greenshaw, A. J. in *Gen. Neurochem. Tech.* (eds Boulton, A. A. & Baker, G. B.) 233–277 (Humana Press, Clifton, New Jersey, 1985).
11. Amirnovin, R., Williams, Z. M., Cosgrove, G. R. & Eskandar, E. N. Experience with microelectrode guided subthalamic nucleus deep brain stimulation. *Oper. Neurosurg.* **58**, 96–102 (Feb. 2006).
12. Grahn, P. J. *et al.* A neurochemical closed-loop controller for deep brain stimulation: toward individualized smart neuromodulation therapies. *Front. Neurosci.* **8**, 1–11 (June 2014).
13. Kringelbach, M. L., Jenkinson, N., Owen, S. L. F. & Aziz, T. Z. Translational principles of deep brain stimulation. *Nat. Rev. Neurosci.* **8**, 623–635 (2007).
14. Laxton, A. W. & Lozano, A. M. Deep brain stimulation for the treatment of Alzheimer disease and dementias. *World Neurosurg.* **80**, S28.e1–S28.e8 (Sept. 2013).
15. Zrenner, E. *Visual Prosthesis, Subretinal Devices* (eds Jaeger, D. & Jung, R.) New York, NY, 2013.
16. Zrenner, E. Fighting blindness with microelectronics. *Sci. Transl. Med.* **5**, 210ps16–210ps16 (Nov. 2013).
17. Zrenner, E. *et al.* in *Artif. Vis.* 65–83 (Springer International Publishing, Cham, 2017).
18. Chuang, A. T., Margo, C. E. & Greenberg, P. B. Retinal implants: a systematic review. *Br. J. Ophthalmol.* **98**, 852–856 (July 2014).
19. Flesher, S. N. *et al.* Intracortical microstimulation of human somatosensory cortex. *Sci. Transl. Med.* **8** (Oct. 2016).
20. Stingl, K. *et al.* Artificial vision with wirelessly powered subretinal electronic implant alpha-IMS. *Proc. R. Soc. B Biol. Sci.* **280** (Feb. 2013).
21. Curcio, C. A., Sloan, K. R., Kalina, R. E. & Hendrickson, A. E. Human photoreceptor topography. *J. Comp. Neurol.* **292**, 497–523 (1990).
22. Stett, A., Barth, W., Weiss, S., Haemmerle, H. & Zrenner, E. Electrical multisite stimulation of the isolated chicken retina. *Vision Res.* **40**, 1785–1795 (June 2000).

23. Palanker, D. *et al.* Migration of retinal cells through a perforated membrane: implications for a high-resolution prosthesis. *Invest. Ophthalmol. Vis. Sci.* **45**, 3266–70 (Sept. 2004).
24. Mathieson, K. *et al.* Photovoltaic retinal prosthesis with high pixel density. *Nat. Photonics* **6**, 391–397 (2012).
25. Spira, M. E. & Hai, A. Multi-electrode array technologies for neuroscience and cardiology. *Nat. Nanotechnol.* **8**, 83–94 (Feb. 2013).
26. Angle, M. R., Cui, B. & Melosh, N. A. Nanotechnology and neurophysiology. *Curr. Opin. Neurobiol.* **32**, 132–140 (2015).
27. Iezzi, R. & Finlayson, P. G. in *Vis. Prosthetics* (ed Dagnelie, G.) 173–191 (Springer US, Boston, MA, 2011).
28. Eickenscheidt, M., Jenkner, M., Thewes, R., Fromherz, P. & Zeck, G. Electrical stimulation of retinal neurons in epiretinal and subretinal configuration using a multicapacitor array. *J. Neurophysiol.* **107**, 2742–2755 (2012).
29. Twyford, P., Cai, C. & Fried, S. Differential responses to high-frequency electrical stimulation in ON and OFF retinal ganglion cells. *J. Neural Eng.* **11**, 025001 (2014).
30. Samba, R., Herrmann, T. & Zeck, G. PEDOT-CNT coated electrodes stimulate retinal neurons at low voltage amplitudes and low charge densities. *J. Neural Eng.* **12**, 016014 (Jan. 2015).
31. Finlayson, P. G. & Iezzi, R. Glutamate stimulation of retinal ganglion cells in normal and s334ter-4 rat retinas: a candidate for a neurotransmitter-based retinal prosthesis. *Invest. Ophthalmol. Vis. Sci.* **51**, 3619–28 (July 2010).
32. Inayat, S., Rountree, C. M., Troy, J. B. & Saggere, L. Chemical stimulation of rat retinal neurons: feasibility of an epiretinal neurotransmitter-based prosthesis. *J. Neural Eng.* **12**, 016010 (Dec. 2015).
33. Rountree, C. M., Inayat, S., Troy, J. B. & Saggere, L. Differential stimulation of the retina with subretinally injected exogenous neurotransmitter: A biomimetic alternative to electrical stimulation. *Sci. Rep.* **6**, 38505 (Dec. 2016).
34. Jones, P. D. & Stelzle, M. Can nanofluidic chemical release enable fast, high resolution neurotransmitter-based neurostimulation? *Front. Neurosci.* **10** (Mar. 2016).
35. Buchthal, F. & Lindhard, J. Direct application of acetylcholine to motor endplates of voluntary muscle fibres. *J. Physiol.* **90**, 82–83 (1937).
36. Lalley, P. M. in *Mod. Tech. Neurosci. Res.* (ed Pitman, R. M.) 193–212 (Springer Berlin Heidelberg, 1999).
37. Nahavandi, S. *et al.* Microfluidic platforms for the investigation of intercellular signalling mechanisms. *Small* **10**, 4810–4826 (2014).
38. Murnick, J. G., Dubé, G., Krupa, B. & Liu, G. High-resolution iontophoresis for single-synapse stimulation. *J. Neurosci. Methods* **116**, 65–75 (Apr. 2002).
39. Belle, A. M., Owesson-White, C., Herr, N. R., Carelli, R. M. & Wightman, R. M. Controlled iontophoresis coupled with fast-scan cyclic voltammetry/electrophysiology in awake, freely moving animals. *ACS Chem. Neurosci.* **4**, 761–771 (2013).
40. Babakinejad, B. *et al.* Local delivery of molecules from a nanopipette for quantitative receptor mapping on live cells. *Anal. Chem.* **85**, 9333–42 (Oct. 2013).
41. Wang, G. *et al.* An optogenetics- and imaging-assisted simultaneous multiple patch-clamp recording system for decoding complex neural circuits. *Nat. Protoc.* **10**, 397–412 (2015).
42. Penn, R. D. & Kroin, J. S. Continuous intrathecal baclofen for severe spasticity. *Lancet* **2**, 125–127 (1985).
43. Penn, R. D. *et al.* Intrathecal baclofen for severe spinal spasticity. Tech. rep. 23 (1989), 1517–1521.
44. *iPRECIO®*, Innovative Drug Infusion Technology for Laboratory Animals. 2015. <<http://www.iprecio.com/>> (visited on 2015-06-15).

45. *Medtronic SynchroMed II Drug Pump and ITB Therapy for Severe Spasticity*. 2014. <<http://www.medtronic.com/patients/severe-spasticity/therapy/itb-therapy/synchromed-ii-pump/>> (visited on 2015-05-16).
46. Johnson, B. C., Norgon, D. & Kratoska, P. *Fluid delivery system and propellant mixture therefor*. 1996.
47. Pongrácz, A. *et al.* Deep-brain silicon multielectrodes for simultaneous in vivo neural recording and drug delivery. *Sensors Actuators B Chem.* **189**, 97–105 (Dec. 2013).
48. Frey, O. *et al.* Simultaneous neurochemical stimulation and recording using an assembly of biosensor silicon microprobes and SU-8 microinjectors. *Sensors Actuators B Chem.* **154**, 96–105 (June 2011).
49. Altuna, A. *et al.* SU-8 based microprobes for simultaneous neural depth recording and drug delivery in the brain. *Lab Chip* **13**, 1422–30 (2013).
50. Spieth, S. *The NeuroMedicator – an intra-cerebral drug delivery system for neural research*. PhD (University of Freiburg, 2013).
51. Mehenti, N. Z., Fishman, H. A. & Bent, S. F. A model neural interface based on functional chemical stimulation. *Biomed. Microdevices* **9**, 579–86 (Aug. 2007).
52. Sun, M., Kaplan, S. V., Gehringer, R. C., Limbocker, R. A. & Johnson, M. A. Localized drug application and sub-second voltammetric dopamine release measurements in a brain slice perfusion device. *Anal. Chem.* **86**, 4151–6 (2014).
53. Peterman, M. C., Noolandi, J., Blumenkranz, M. S. & Fishman, H. A. Fluid flow past an aperture in a microfluidic channel. *Anal. Chem.* **76**, 1850–6 (Apr. 2004).
54. Peterman, M. C., Noolandi, J., Blumenkranz, M. S. & Fishman, H. A. Localized chemical release from an artificial synapse chip. *Proc. Natl. Acad. Sci. U. S. A.* **101**, 9951–4 (July 2004).
55. Mernier, G., De Keersmaecker, K., Bartic, C. & Borghs, G. On-chip controlled release of neurotransmitter molecules. *Microelectron. Eng.* **84**, 1714–1718 (2007).
56. Mernier, G. *et al.* On-chip chemical stimulation of neurons by local and controlled release of neurotransmitter. in *IEEE Eng. Med. Biol. Soc.* (2008), 2745–2748.
57. Scott, A. *et al.* A microfluidic microelectrode array for simultaneous electrophysiology, chemical stimulation, and imaging of brain slices. *Lab Chip* **13**, 527–35 (Feb. 2013).
58. Papageorgiou, D. P., Shore, S. E., Bledsoe, S. C. & Wise, K. D. A shuttered neural probe with on-chip flowmeters for chronic in vivo drug delivery. *J. Microelectromechanical Syst.* **15**, 1025–1033 (2006).
59. Zibek, S. *et al.* Localized functional chemical stimulation of TE 671 cells cultured on nanoporous membrane by calcein and acetylcholine. *Biophys. J.* **92**, L04–6 (Jan. 2007).
60. Hu, M. *et al.* Discrete chemical release from a microfluidic chip. *J. Microelectromechanical Syst.* **16**, 786–794 (Aug. 2007).
61. Zibek, S., Hagemeyer, B., Stett, A. & Stelzle, M. Chemical stimulation of adherent cells by localized application of acetylcholine from a microfluidic system. *Front. Neuroeng.* **3**, 113 (Jan. 2010).
62. Wangler, N. *et al.* Bubble Jet agent release cartridge for chemical single cell stimulation. *Biomed. Microdevices* **15**, 1–8 (Feb. 2013).
63. Santini, J. T., Cima, M. J. & Langer, R. A controlled-release microchip. *Nature* **397**, 335–8 (Jan. 1999).
64. Chung, A. J., Kim, D. & Erickson, D. Electrokinetic microfluidic devices for rapid, low power drug delivery in autonomous microsystems. *Lab Chip* **8**, 330–8 (Feb. 2008).
65. Farra, R. *et al.* First-in-human testing of a wirelessly controlled drug delivery microchip. *Sci. Transl. Med.* **4**, 122ra21–122ra21 (Feb. 2012).
66. Metz, S., Bertsch, A., Bertrand, D. & Renaud, P. Flexible polyimide probes with microelectrodes and embedded microfluidic channels for simultaneous drug delivery and multi-channel monitoring of bioelectric activity. *Biosens. Bioelectron.* **19**, 1309–18 (May 2004).
67. Simon, D. T. *et al.* Organic electronics for precise delivery of neurotransmitters to modulate mammalian sensory function. *Nat. Mater.* **8**, 742–6 (Sept. 2009).

68. Tybrandt, K. *et al.* Translating electronic currents to precise acetylcholine-induced neuronal signaling using an organic electrophoretic delivery device. *Adv. Mater.* **21**, 4442–4446 (Nov. 2009).
69. Isaksson, J. *et al.* Electronic control of Ca^{2+} signalling in neuronal cells using an organic electronic ion pump. *Nat. Mater.* **6**, 673–9 (Sept. 2007).
70. Williamson, A. *et al.* Controlling epileptiform activity with organic electronic ion pumps. *Adv. Mater.* **27**, 3138–3144 (May 2015).
71. Jonsson, A. *et al.* Bioelectronic neural pixel: Chemical stimulation and electrical sensing at the same site. *Proc. Natl. Acad. Sci.* **113**, 9440–9445 (Aug. 2016).
72. Spieth, S., Schumacher, A., Kallenbach, C., Messner, S. & Zengerle, R. The NeuroMedicator—a micropump integrated with silicon microprobes for drug delivery in neural research. *J. Micromech. Microeng.* **22**, 065020 (June 2012).
73. Spieth, S. *et al.* An intra-cerebral drug delivery system for freely moving animals. *Biomed. Microdevices* **14**, 799–809 (Oct. 2012).
74. Aravanis, A. M. *et al.* An optical neural interface: in vivo control of rodent motor cortex with integrated fiberoptic and optogenetic technology. *J. Neural Eng.* **4**, S143–S156 (2007).
75. Yakushenko, A. *et al.* On-chip optical stimulation and electrical recording from cells. *J. Biomed. Opt.* **18**, 111402 (2013).
76. Boyden, E. S., Zhang, F., Bamberg, E., Nagel, G. & Deisseroth, K. Millisecond-timescale, genetically targeted optical control of neural activity. *Nat. Neurosci.* **8**, 1263–1268 (2005).
77. Pan, Z.-h., Bi, A. & Lu, Q. in *Optogenetics* (eds Yawo, H., Kandori, H. & Koizumi, A.) 353–365 (Springer Japan, Tokyo, 2015).
78. RetroSense Therapeutics. *RST-001 Phase I/II Trial for Retinitis Pigmentosa*. Dallas, Texas, USA, 2016.
79. Gilbert, F., Harris, A. R. & Kapsa, R. M. I. Controlling brain cells with light: ethical considerations for optogenetic clinical trials. *AJOB Neurosci.* **5**, 3–11 (July 2014).
80. Go, M. A., Stricker, C., Redman, S., Bachor, H.-A. & Daria, V. R. Simultaneous multi-site two-photon photostimulation in three dimensions. *J. Biophotonics* **5**, 745–53 (Oct. 2012).
81. Van Gelder, R. N. Photochemical approaches to vision restoration. *Vision Res.* (Feb. 2015).
82. Jayakody, S. A., Gonzalez-Cordero, A., Ali, R. R. & Pearson, R. A. Cellular strategies for retinal repair by photoreceptor replacement. *Prog. Retin. Eye Res.* (Feb. 2015).
83. Sparreboom, W., van den Berg, A. & Eijkel, J. C. T. Principles and applications of nanofluidic transport. *Nat. Nanotechnol.* **4**, 713–20 (Nov. 2009).
84. Haywood, D. G., Saha-Shah, A., Baker, L. A. & Jacobson, S. C. Fundamental studies of nanofluidics: nanopores, nanochannels, and nanopipets. *Anal. Chem.* **87**, 172–187 (2015).
85. Miles, B. N. *et al.* Single molecule sensing with solid-state nanopores: novel materials, methods, and applications. *Chem. Soc. Rev.* **42**, 15–28 (Jan. 2013).
86. Bai, J. *et al.* Fabrication of sub-20 nm nanopore arrays in membranes with embedded metal electrodes at wafer scales. *Nanoscale* **6**, 8900–6 (2014).
87. Yang, J. *et al.* Rapid and precise scanning helium ion microscope milling of solid-state nanopores for biomolecule detection. *Nanotechnology* **22**, 285310 (July 2011).
88. Wu, M. Y., Krapf, D., Zandbergen, M., Zandbergen, H. & Batson, P. E. Formation of nanopores in a SiN/SiO_2 membrane with an electron beam. *Appl. Phys. Lett.* **87**, 114–116 (2005).
89. Li, J. *et al.* Ion-beam sculpting at nanometre length scales. *Nature* **412**, 166–9 (July 2001).
90. Wei, R., Pedone, D., Zürner, A., Döblinger, M. & Rant, U. Fabrication of metallized nanopores in silicon nitride membranes for single-molecule sensing. *Small* **6**, 1406–14 (July 2010).
91. Nam, S.-W., Rooks, M. J., Kim, K.-B. & Rossnagel, S. M. Ionic field effect transistors with sub-10 nm multiple nanopores. *Nano Lett.* **9**, 2044–8 (May 2009).

92. Mussi, V., Fanzio, P., Firpo, G., Repetto, L. & Valbusa, U. [Size and functional tuning of solid state nanopores by chemical functionalization](#). *Nanotechnology* **23**, 435301 (Oct. 2012).
93. Wei, R., Gatterdam, V., Wieneke, R., Tampé, R. & Rant, U. [Stochastic sensing of proteins with receptor-modified solid-state nanopores](#). *Nat. Nanotechnol.* **7**, 257–63 (Apr. 2012).
94. Tahvildari, R., Beamish, E., Tabard-Cossa, V. & Godin, M. [Integrating nanopore sensors within microfluidic channel arrays using controlled breakdown](#). *Lab Chip* **15**, 1407–1411 (2015).
95. Kwok, H., Briggs, K. & Tabard-Cossa, V. [Nanopore fabrication by controlled dielectric breakdown](#). *PLoS One* **9** (2014).
96. Kwok, H., Waugh, M., Bustamante, J., Briggs, K. & Tabard-Cossa, V. [Long passage times of short ssDNA molecules through metallized nanopores fabricated by controlled breakdown](#). *Adv. Funct. Mater.* **24**, 7745–7753 (2014).
97. Ayub, M. *et al.* [Precise electrochemical fabrication of sub-20 nm solid-state nanopores for single-molecule biosensing](#). *J. Phys. Condens. Matter* **22**, 454128 (2010).
98. Bearden, S., Simpanen, E. & Zhang, G. [Active current gating in electrically biased conical nanopores](#). *Nanotechnology* **26**, 185502 (2015).
99. Sharp, K. V., Adrian, R. J., Santiago, J. G. & Molho, J. I. in *MEMS Handb.* (ed Gad-el-Hak, M.) 2nd ed. Chap. 10 (CRC Press, 2002).
100. Bruus, H. in *Microscale Acoustofluidics* (eds Laurell, T. & Lenshof, A.) 1–28 (Royal Society of Chemistry, Cambridge, 2014).
101. Oh, K. W., Lee, K., Ahn, B. & Furlani, E. P. [Design of pressure-driven microfluidic networks using electric circuit analogy](#). *Lab Chip* **12**, 515 (2012).
102. Cottin-Bizonne, C., Cross, B., Steinberger, A. & Charlaix, E. [Boundary slip on smooth hydrophobic surfaces: Intrinsic effects and possible artifacts](#). *Phys. Rev. Lett.* **94**, 1–4 (2005).
103. Holt, J. K. *et al.* [Fast mass transport through sub-2-nanometer carbon nanotubes](#). *Science* **312**, 1034–1037 (May 2006).
104. Crank, J. *The mathematics of diffusion* 2nd (Oxford University Press, London, 1975).
105. Nicholson, C., Phillips, J. M. & Gardner-Medwin, A. R. [Diffusion from an iontophoretic point source in the brain: Role of tortuosity and volume fraction](#). *Brain Res.* **169**, 580–584 (1979).
106. Pennathur, S. & Santiago, J. G. [Electrokinetic transport in nanochannels. 1. Theory](#). *Anal. Chem.* **77**, 6772–81 (Nov. 2005).
107. Herr, N. R., Kile, B. M., Carelli, R. M. & Wightman, R. M. [Electroosmotic flow and its contribution to iontophoretic delivery](#). *Anal. Chem.* **80**, 8635–8641 (2008).
108. Bouzigues, C. I., Tabeling, P. & Bocquet, L. [Nanofluidics in the Debye layer at hydrophilic and hydrophobic surfaces](#). *Phys. Rev. Lett.* **101**, 12–15 (2008).
109. Firnkes, M., Pedone, D., Knezevic, J., Döblinger, M. & Rant, U. [Electrically facilitated translocations of proteins through silicon nitride nanopores: conjoint and competitive action of diffusion, electrophoresis, and electroosmosis](#). *Nano Lett.* **10**, 2162–7 (June 2010).
110. Pennathur, S. & Santiago, J. G. [Electrokinetic transport in nanochannels. 2. Experiments](#). *Anal. Chem.* **77**, 6782–9 (Nov. 2005).
111. Karnik, R., Duan, C., Castelino, K., Daiguji, H. & Majumdar, A. [Rectification of ionic current in a nanofluidic diode](#). *Nano Lett.* **7**, 547–51 (Mar. 2007).
112. Karnik, R. *et al.* [Electrostatic control of ions and molecules in nanofluidic transistors](#). *Nano Lett.* **5**, 943–8 (May 2005).
113. Ali, M., Mafe, S., Ramirez, P., Neumann, R. & Ensinger, W. [Logic gates using nanofluidic diodes based on conical nanopores functionalized with polyprotic acid chains](#). *Langmuir* **25**, 11993–11997 (Oct. 2009).
114. Araci, I. E. & Quake, S. R. [Microfluidic very large scale integration \(mVLSI\) with integrated micromechanical valves](#). *Lab Chip* **12**, 2803 (2012).

115. He, Z., Corry, B., Lu, X. & Zhou, J. [A mechanical nanogate based on a carbon nanotube for reversible control of ion conduction](#). *Nanoscale* **6**, 3686–94 (2014).
116. Hummer, G., Rasaiah, J. C. & Noworyta, J. P. [Water conduction through the hydrophobic channel of a carbon nanotube](#). *Nature* **414**, 188–90 (Nov. 2001).
117. Beckstein, O., Biggin, P. C. & Sansom, M. S. P. [A hydrophobic gating mechanism for nanopores](#). *J. Phys. Chem. B* **105**, 12902–12905 (Dec. 2001).
118. Miyazawa, A., Fujiyoshi, Y. & Unwin, N. [Structure and gating mechanism of the acetylcholine receptor pore](#). *Nature* **423**, 949–55 (June 2003).
119. Dzubiella, J., Allen, R. J. & Hansen, J.-P. [Electric field-controlled water permeation coupled to ion transport through a nanopore](#). *J. Chem. Phys.* **120**, 5001–4 (Mar. 2004).
120. Dzubiella, J. & Hansen, J.-P. [Electric-field-controlled water and ion permeation of a hydrophobic nanopore](#). *J. Chem. Phys.* **122**, 234706 (July 2005).
121. Aryal, P., Sansom, M. S. & Tucker, S. J. [Hydrophobic gating in ion channels](#). *J. Mol. Biol.* **427**, 121–130 (Jan. 2015).
122. Smirnov, S. N., Vlasiouk, I. V. & Lavrik, N. V. [Voltage-gated hydrophobic nanopores](#). *ACS Nano* **5**, 7453–61 (Sept. 2011).
123. Powell, M. R., Cleary, L., Davenport, M., Shea, K. J. & Siwy, Z. S. [Electric-field-induced wetting and dewetting in single hydrophobic nanopores](#). *Nat. Nanotechnol.* **6**, 798–802 (Oct. 2011).
124. Lochovsky, C., Yasotharan, S. & Günther, A. [Bubbles no more: in-plane trapping and removal of bubbles in microfluidic devices](#). *Lab Chip* **12**, 595 (2012).
125. Smeets, R., Keyser, U., Wu, M., Dekker, N. & Dekker, C. [Nanobubbles in solid-state nanopores](#). *Phys. Rev. Lett.* **97**, 1–4 (Aug. 2006).
126. Lefevre, B. *et al.* [Intrusion and extrusion of water in hydrophobic mesopores](#). *J. Chem. Phys.* **120**, 4927–38 (Mar. 2004).
127. Hagemeyer, B., Zechall, F. & Stelzle, M. [Towards plug and play filling of microfluidic devices by utilizing networks of capillary stop valves](#). *Biomicrofluidics* **8**, 056501 (Sept. 2014).
128. Gao, L. & McCarthy, T. J. [Wetting 101](#). *Langmuir* **25**, 14105–14115 (Dec. 2009).
129. Mugele, F. [Fundamental challenges in electrowetting: from equilibrium shapes to contact angle saturation and drop dynamics](#). *Soft Matter* **5**, 3377 (2009).
130. Panciera, F. *et al.* [Controlling nanowire growth through electric field-induced deformation of the catalyst droplet](#). *Nat. Commun.* **7**, 12271 (2016).
131. Mugele, F. & Baret, J.-C. [Electrowetting: from basics to applications](#). *J. Phys. Condens. Matter* **17**, R705–R774 (July 2005).
132. Quinn, A., Sedev, R. & Ralston, J. [Contact angle saturation in electrowetting](#). *J. Phys. Chem. B* **109**, 6268–75 (Apr. 2005).
133. Liu, J., Wang, M., Chen, S. & Robbins, M. O. [Uncovering molecular mechanisms of electrowetting and saturation with simulations](#). *Phys. Rev. Lett.* **108**, 216101 (May 2012).
134. Vallet, M., Berge, B. & Vovelle, L. [Electrowetting of water and aqueous solutions on poly\(ethylene terephthalate\) insulating films](#). *Polymer (Guildf)*. **37**, 2465–2470 (1996).
135. Vallet, M., Vallade, M. & Berge, B. [Limiting phenomena for the spreading of water on polymer films by electrowetting](#). *Eur. Phys. J. B* **11**, 583–591 (1999).
136. Nelson, W. C. & Kim, C.-J. C. [Droplet Actuation by Electrowetting-on-Dielectric \(EWOD\): A Review](#). *J. Adhes. Sci. Technol.* **26**, 1747–1771 (Jan. 2012).
137. Yang, J. S., Kwon, J. O., Chae, J. B., Choi, M. & Chung, S. K. [Electrowetting-on-dielectric \(EWOD\) induced flow analysis](#). *J. Micromech. Microeng.* **25**, 087001 (2015).
138. Jones, T. B. [Electromechanical interpretation of electrowetting & relationship to liquid dielectrophoresis](#). Rochester, NY, 2007. <http://www.ece.rochester.edu/~jones/electromech_of_EWOD.pdf>.

139. Sedev, R. [Electrowetting: Electrocapillarity, saturation, and dynamics](#). *Eur. Phys. J. Spec. Top.* **197**, 307–319 (2011).
140. Blake, T. D. [Discussion notes on “Electrowetting: Electrocapillarity, saturation, and dynamics”](#), by R. Sedev. *Eur. Phys. J. Spec. Top.* **197**, 323–324 (2011).
141. Gupta, R., Olivier, G. K. & Frechette, J. [Invariance of the solid-liquid interfacial energy in electrowetting probed via capillary condensation](#). *Langmuir* **26**, 11946–11950 (2010).
142. Mugele, F. & Buehrle, J. [Equilibrium drop surface profiles in electric fields](#). *J. Phys. Condens. Matter* **19**, 375112 (Sept. 2007).
143. Jones, T. B. [An electromechanical interpretation of electrowetting](#). *J. Micromech. Microeng.* **15**, 1184–1187 (June 2005).
144. Buehrle, J., Herminghaus, S. & Mugele, F. [Interface profiles near three-phase contact lines in electric fields](#). *Phys. Rev. Lett.* **91**, 086101 (Aug. 2003).
145. Roghair, I. *et al.* [A numerical technique to simulate display pixels based on electrowetting](#). *Microfluid. Nanofluidics* **19**, 465–482 (2015).
146. Bratko, D., Daub, C. D., Leung, K. & Luzar, A. [Effect of field direction on electrowetting in a nanopore](#). *J. Am. Chem. Soc.* **129**, 2504–10 (Mar. 2007).
147. Vanzo, D., Bratko, D. & Luzar, A. [Dynamic control of nanopore wetting in water and saline solutions under an electric field](#). *J. Phys. Chem. B* **119**, 8890–8899 (July 2015).
148. Iwami, Y., Hobara, D., Yamamoto, M. & Kakiuchi, T. [Determination of the potential of zero charge of Au\(111\) electrodes modified with thiol self-assembled monolayers using a potential-controlled sessile drop method](#). *J. Electroanal. Chem.* **564**, 77–83 (Mar. 2004).
149. Abbott, N. L., Gorman, C. B. & Whitesides, G. M. [Active control of wetting using applied electrical potentials and self-assembled monolayers](#). *Langmuir* **11**, 16–18 (Jan. 1995).
150. Stett, A. *et al.* [Biological application of microelectrode arrays in drug discovery and basic research](#). *Anal. Bioanal. Chem.* **377**, 486–95 (Oct. 2003).
151. De Luca, G. & Glavinović, M. I. [Glutamate, water and ion transport through a charged nanosize pore](#). *Biochim. Biophys. Acta* **1768**, 264–79 (Feb. 2007).
152. Invernizzi, R. W. & Esposito, E. *Microiontophoresis and Related Methods* (ed Stolerman, I. P.) Berlin, Heidelberg, 2010.
153. Kirkpatrick, D. C., Edwards, M. A., Flowers, P. A. & Wightman, R. M. [Characterization of solute distribution following iontophoresis from a micropipet](#). *Anal. Chem.* **86**, 9909–16 (2014).
154. Clements, J., Lester, R., Tong, G., Jahr, C. & Westbrook, G. [The time course of glutamate in the synaptic cleft](#). *Science* **258**, 1498–1501 (Nov. 1992).
155. Danbolt, N. C. [Glutamate uptake](#). *Prog. Neurobiol.* **65**, 1–105 (Sept. 2001).
156. Geng, J. *et al.* [Stochastic transport through carbon nanotubes in lipid bilayers and live cell membranes](#). *Nature* **514**, 612–615 (Oct. 2014).
157. Vlassioux, I., Rios, F., Vail, S. A., Gust, D. & Smirnov, S. [Electrical conductance of hydrophobic membranes or what happens below the surface](#). *Langmuir* **23**, 7784–92 (July 2007).
158. Krumpfer, J. W. & McCarthy, T. J. [Contact angle hysteresis: a different view and a trivial recipe for low hysteresis hydrophobic surfaces](#). *Faraday Discuss.* **146**, 103 (2010).
159. Yadav, A. R., Sriram, R., Carter, J. A. & Miller, B. L. [Comparative study of solution-phase and vapor-phase deposition of aminosilanes on silicon dioxide surfaces](#). *Mater. Sci. Eng. C* **35**, 283–290 (2014).
160. Jones, P. D., Toimil Molares, M. E., Trautmann, C. & Stelzle, M. [Nanofluidic gates for diffusion-free controlled release from microfluidic devices](#). in *Proc. Mikrosystemtechnik Kongress* (Aachen, Germany, 2013). <<https://www.vde-verlag.de/proceedings-de/453555154.html>>.

161. Nagashima, G., Levine, E. V., Hoogerheide, D. P., Burns, M. M. & Golovchenko, J. A. [Superheating and homogeneous single bubble nucleation in a solid-state nanopore](#). *Phys. Rev. Lett.* **113**, 024506 (July 2014).
162. Levine, E. V., Burns, M. M. & Golovchenko, J. A. [Nanoscale dynamics of Joule heating and bubble nucleation in a solid-state nanopore](#). *Phys. Rev. E* **93**, 013124 (2016).
163. Li, Y. *et al.* [Photoresistance switching of plasmonic nanopores](#). *Nano Lett.* **15**, 776–782 (Dec. 2015).
164. Chen, Q., Luo, L. & White, H. S. [Electrochemical generation of a hydrogen bubble at a recessed platinum nanopore electrode](#). *Langmuir* **31**, 4573–4581 (Apr. 2015).
165. Trick, J. L., Wallace, E. J., Bayley, H. & Sansom, M. S. P. [Designing a hydrophobic barrier within biomimetic nanopores](#). *ACS Nano* **8**, 11268–11279 (Nov. 2014).
166. Guillemot, L., Biben, T., Galarneau, A., Vigier, G. & Charlaix, É. [Activated drying in hydrophobic nanopores and the line tension of water](#). *Proc. Natl. Acad. Sci. U. S. A.* **109**, 19557–62 (Nov. 2012).
167. Beckstein, O. & Sansom, M. S. P. [Liquid-vapor oscillations of water in hydrophobic nanopores](#). *Proc. Natl. Acad. Sci. U. S. A.* **100**, 7063–8 (June 2003).
168. Birkner, J. P., Poolman, B. & Koçer, A. [Hydrophobic gating of mechanosensitive channel of large conductance evidenced by single-subunit resolution](#). *Proc. Natl. Acad. Sci. U. S. A.* **109**, 12944–9 (Aug. 2012).
169. Yoshimura, K., Batiza, A., Schroeder, M., Blount, P. & Kung, C. [Hydrophilicity of a single residue within MscL correlates with increased channel mechanosensitivity](#). *Biophys. J.* **77**, 1960–72 (Oct. 1999).
170. Smirnov, S., Vlassiouk, I., Takmakov, P. & Rios, F. [Water confinement in hydrophobic nanopores. Pressure-induced wetting and drying](#). *ACS Nano* **4**, 5069–75 (Sept. 2010).
171. Schönherr, H., Hain, N., Walczyk, W., Wesner, D. & Druzhinin, S. I. [Surface nanobubbles studied by atomic force microscopy techniques: Facts, fiction, and open questions](#). *Jpn. J. Appl. Phys.* **55**, 08NA01 (Aug. 2016).
172. Tyrrell, J. W. G. & Attard, P. [Images of nanobubbles on hydrophobic surfaces and their interactions](#). *Phys. Rev. Lett.* **87**, 176104 (Oct. 2001).
173. Poynor, A. *et al.* [How water meets a hydrophobic surface](#). *Phys. Rev. Lett.* **97**, 266101 (Dec. 2006).
174. No nanobubbles. *Nature* **445**, 129 (2007).
175. Zhang, X. & Lohse, D. [Perspectives on surface nanobubbles](#). *Biomicrofluidics* **8**, 041301 (2014).
176. Zhang, X. & Winnik, F. M. [Preface to the Nanobubbles Special Issue](#). *Langmuir* **32**, 11071–11071 (Nov. 2016).
177. Öner, D. & McCarthy, T. J. [Ultrahydrophobic surfaces. Effects of topography length scales on wettability](#). *Langmuir* **16**, 7777–7782 (2000).
178. Miura, Y. F. *et al.* [Wettabilities of self-assembled monolayers generated from CF₃-terminated alkanethiols on gold](#). *Langmuir* **14**, 5821 (1998).
179. Fadeev, A. Y. & McCarthy, T. J. [Trialkylsilane monolayers covalently attached to silicon surfaces: Wettability studies indicating that molecular topography contributes to contact angle hysteresis](#). *Langmuir* **15**, 3759–3766 (1999).
180. Chechik, V. & Stirling, C. J. M. [Gold-Thiol Self-Assembled Monolayers](#). *Patai's Chem. Funct. Groups* (ed Rappoport, Z.) (Dec. 2009).
181. Zenasni, O., Jamison, A. C. & Lee, T. R. [The impact of fluorination on the structure and properties of self-assembled monolayer films](#). *Soft Matter* **9**, 6356 (2013).
182. Flynn, N. T., Tran, T. N. T., Cima, M. J. & Langer, R. [Long-term stability of self-assembled monolayers in biological media](#). *Langmuir* **19**, 10909–10915 (2003).
183. Tong, H. D. *et al.* [Silicon nitride nanosieve membrane](#). *Nano Lett.* **4**, 283–287 (Feb. 2004).

184. Roghair, I. *Source code of EHD and multi-region EHD solvers*. 2015. <<http://www.cfd-online.com/Forums/openfoam-programming-development/105182-ehdfoam-2.html>> (visited on 2016-10-15).
185. Piccirillo, A. & Gobbi, A. L. *Physical-electrical properties of silicon nitride deposited by PECVD on III–V semiconductors*. *J. Electrochem. Soc.* **137**, 3910–3917 (1990).
186. Boubour, E. & Lennox, R. B. *Insulating properties of self-assembled monolayers monitored by impedance spectroscopy*. *Langmuir* **16**, 4222–4228 (May 2000).
187. Crudden, C. M. *et al.* *Ultra stable self-assembled monolayers of N-heterocyclic carbenes on gold*. *Nat. Chem.* **6**, 409–14 (2014).
188. *CRC Handbook of Chemistry and Physics* (ed Lide, D. R.) 6–8 (CRC Press, Boca Raton, Florida, 2005).
189. Lee, J. & Karnik, R. *Desalination of water by vapor-phase transport through hydrophobic nanopores*. *J. Appl. Phys.* **108**, 044315 (2010).
190. Orr, F. M., Scriven, L. E. & Rivas, A. P. *Pendular rings between solids: meniscus properties and capillary force*. *J. Fluid Mech.* **67**, 723 (Mar. 1975).
191. Marmur, A. *The radial capillary*. *J. Colloid Interface Sci.* **124**, 301–308 (July 1988).
192. Cao, L., Hu, H. A. & Gao, D. *Design and fabrication of micro-textures for inducing a superhydrophobic behavior on hydrophilic materials*. *Langmuir* **23**, 4310–4314 (2007).
193. Liu, T. L. & Kim, C.-J. C. *Turning a surface superrepellent even to completely wetting liquids*. *Science* **346**, 1096–1100 (Nov. 2014).
194. Giacomello, A., Schimmele, L., Dietrich, S. & Tasinkevich, M. *Perpetual superhydrophobicity*. *Soft Matter* **12**, 8927–8934 (2016).
195. Radha, B. *et al.* *Molecular transport through capillaries made with atomic-scale precision*. *Nature* (Sept. 2016).
196. Agostinho, L. L. F. *et al.* *Morphology of water electrosprays in the simple-jet mode*. *Phys. Rev. E* **86**, 066317 (Dec. 2012).
197. Fuchs, E. C. *et al.* *The floating water bridge*. *J. Phys. D: Appl. Phys.* **40**, 6112–6114 (Oct. 2007).
198. Men, Y., Zhang, X. & Wang, W. *Capillary liquid bridges in atomic force microscopy: formation, rupture, and hysteresis*. *J. Chem. Phys.* **131**, 184702 (Nov. 2009).
199. Garcia, R. in *Nanoscale Liq. Interfaces Wetting, Patterning Force Microsc. Mol. Scale* (eds Ondaçuhu, T. & Aimé, J.-P.) 1st, 493–527 (Pan Stanford Publishing, 2013).
200. Rossi, M. P. *et al.* *Environmental scanning electron microscopy study of water in carbon nanopipes*. *Nano Lett.* **4**, 989–993 (2004).
201. Mattia, D. & Gogotsi, Y. *Review: static and dynamic behavior of liquids inside carbon nanotubes*. *Microfluid. Nanofluidics* **5**, 289–305 (Apr. 2008).
202. Shin, D. *et al.* *Growth dynamics and gas transport mechanism of nanobubbles in graphene liquid cells*. *Nat. Commun.* **6**, 6068 (2015).
203. Kowalczyk, S. W., Grosberg, A. Y., Rabin, Y. & Dekker, C. *Modeling the conductance and DNA blockade of solid-state nanopores*. *Nanotechnology* **22**, 315101 (Aug. 2011).
204. Beamish, E., Kwok, H., Tabard-Cossa, V. & Godin, M. *Fine-tuning the size and minimizing the noise of solid-state nanopores*. *J. Vis. Exp.* e51081 (2013).
205. *The Axon Guide* (ed Sherman-Gold, R.) **2500** (Axon Instruments, Inc., Foster City, CA, 1993).
206. Arafat, A., Schroën, K., de Smet, L. C. P. M., Sudhölter, E. J. R. & Zuillhof, H. *Tailor-made functionalization of silicon nitride surfaces*. *J. Am. Chem. Soc.* **126**, 8600–1 (July 2004).
207. Tabard-Cossa, V., Trivedi, D., Wiggin, M., Jetha, N. N. & Marziali, A. *Noise analysis and reduction in solid-state nanopores*. *Nanotechnology* **18**, 305505 (Aug. 2007).
208. Matsui, K., Yanagi, I., Goto, Y. & Takeda, K.-I. *Prevention of Dielectric Breakdown of Nanopore Membranes by Charge Neutralization*. *Sci. Rep.* **5**, 17819 (2015).

209. Vericat, C., Vela, M. E., Benitez, G., Carro, P. & Salvarezza, R. C. Self-assembled monolayers of thiols and dithiols on gold: new challenges for a well-known system. *Chem. Soc. Rev.* **39**, 1805–1834 (2010).
210. Godin, M. *et al.* Surface stress, kinetics, and structure of alkanethiol self-assembled monolayers. *Langmuir* **20**, 7090–7096 (2004).
211. Forbes, R. G. Refining the application of Fowler-Nordheim theory. *Ultramicroscopy* **79**, 11–23 (1999).
212. Bruggeman, P. J. *et al.* Plasma–liquid interactions: a review and roadmap. *Plasma Sources Sci. Technol.* **25**, 053002 (2016).
213. Papadakis, A. P., Rossides, S. & Metaxas, A. C. Microplasmas: a review. *Open Appl. Phys. J.* **4**, 45–63 (Dec. 2011).
214. Rollings, R. *et al.* The effects of geometry and stability of solid-state nanopores on detecting single DNA molecules. *Nanotechnology* **26**, 044001 (Jan. 2015).
215. Yang, C., Hinkle, P., Menestrina, J., Vlasiouk, I. V. & Siwy, Z. S. Polarization of gold in nanopores leads to ion current rectification. *J. Phys. Chem. Lett.* **7**, 4152–4158 (Oct. 2016).
216. Fosdick, S. E., Knust, K. N., Scida, K. & Crooks, R. M. Bipolar electrochemistry. *Angew. Chemie Int. Ed.* **52**, 10438–10456 (Sept. 2013).
217. Pradhan, S. K., Tanyi, E. K., Skuza, J. R., Xiao, B. & Pradhan, A. K. Electrical behavior of atomic layer deposited high quality SiO₂ gate dielectric. *J. Vac. Sci. Technol. A Vacuum, Surfaces, Film.* **33**, 01A107 (2015).
218. Cahill, B. P. *et al.* Reversible electrowetting on silanized silicon nitride. *Sensors Actuators B Chem.* **144**, 380–386 (Feb. 2010).
219. Williams, K., Gupta, K. & Wasilik, M. Etch rates for micromachining processing-part II. *J. Microelectromechanical Syst.* **12**, 761–778 (Dec. 2003).
220. Martinez, W. E., Gregori, G. & Mates, T. Titanium diffusion in gold thin films. *Thin Solid Films* **518**, 2585–2591 (2010).
221. Liu, Y. *et al.* Nanoscale wet etching of physical-vapor-deposited titanium nitride and its application to sub-30-nm-gate-length fin-type double-gate metal–oxide–semiconductor field-effect transistor fabrication. *Jpn. J. Appl. Phys.* **49**, 06GH18 (2010).
222. Stett, A., Mai, A. & Herrmann, T. Retinal charge sensitivity and spatial discrimination obtainable by subretinal implants: key lessons learned from isolated chicken retina. *J. Neural Eng.* **4**, S7–S16 (Mar. 2007).
223. Gerwig, R. *et al.* PEDOT-CNT composite microelectrodes for recording and electrostimulation applications: fabrication, morphology, and electrical properties. *Front. Neuroeng.* **5**, 8 (Jan. 2012).
224. Samba, R. *Development and characterization of PEDOT-CNT microelectrode arrays for advanced neuronal recording, stimulation and sensing.* Dr. rer. nat. (Eberhard Karls Universität Tübingen, 2013).
225. Carlborg, C. F., Haraldsson, T., Öberg, K., Malkoch, M. & van der Wijngaart, W. Beyond PDMS: off-stoichiometry thiol-ene (OSTE) based soft lithography for rapid prototyping of microfluidic devices. *Lab Chip* **11**, 3136–47 (Sept. 2011).
226. Saharil, F. *et al.* Dry adhesive bonding of nanoporous inorganic membranes to microfluidic devices using the OSTE(+) dual-cure polymer. *J. Micromech. Microeng.* **23**, 025021 (Feb. 2013).
227. Errando-Herranz, C. *et al.* Biocompatibility of OSTE polymers studied by cell growth experiments. *17th Int. Conf. Miniaturized Syst. Chem. Life Sci.* 143–145 (2013).
228. Errando-Herranz, C. *et al.* Integration of polymer microfluidic channels, vias, and connectors with silicon photonic sensors by one-step combined photopatterning and molding of OSTE. in *Transducers Eurosensors XXVII 17th Int. Conf. Solid-State Sensors, Actuators Microsystems* (IEEE, June 2013), 1613–1616.
229. Nemani, K. V., Moodie, K. L., Brennick, J. B., Su, A. & Gimi, B. In vitro and in vivo evaluation of SU-8 biocompatibility. *Mater. Sci. Eng. C* **33**, 4453–4459 (2013).

230. Vernekar, V. N. *et al.* SU-8 2000 rendered cytocompatible for neuronal bioMEMS applications. *J. Biomed. Mater. Res. Part A* (2008).
231. Heuschkel, M., Guérin, L., Buisson, B., Bertrand, D. & Renaud, P. Buried microchannels in photopolymer for delivering of solutions to neurons in a network. *Sensors Actuators B Chem.* **48**, 356–361 (1998).
232. Frey, O. *et al.* Biosensor microprobes with integrated microfluidic channels for bi-directional neurochemical interaction. *J. Neural Eng.* **8**, 066001 (Dec. 2011).
233. Kentsch, J., Breisch, S. & Stelzle, M. Low temperature adhesion bonding for BioMEMS. *J. Micromech. Microeng.* **16**, 802–807 (Apr. 2006).
234. Zhang, Z., Zhao, P. & Xiao, G. The fabrication of polymer microfluidic devices using a solid-to-solid interfacial polyaddition. *Polymer (Guildf).* **50**, 5358–5361 (Nov. 2009).
235. DJ MicroLaminates. *ADEX Epoxy Thin Film Rolls/Sheets Data Sheet*. Sudbury, MA, 2017. <<http://djmicrolaminates.com/datasheets/DJ-MicroLaminates-ADEX-Data-Sheet.pdf>>.
236. MicroChem. *SU-8 3000*. <<http://microchem.com/pdf/SU-8%203000%20Data%20Sheet.pdf>> (visited on 2016-08-24).
237. *Microelectrode Array Manual*. Reutlingen, 2016. <http://www.multichannelsystems.com/sites/multichannelsystems.com/files/documents/manuals/MEA_Manual.pdf> (visited on 2016-08-24).
238. Laszlo, A. H. *et al.* Decoding long nanopore sequencing reads of natural DNA. *Nat. Biotechnol.* 2–7 (June 2014).
239. Jain, T., Guerrero, R. J. S., Aguilar, C. A. & Karnik, R. Integration of solid-state nanopores in microfluidic networks via transfer printing of suspended membranes. *Anal. Chem.* **85**, 3871–3878 (Apr. 2013).
240. Tahvildari, R. *et al.* Manipulating electrical and fluidic access in integrated nanopore-microfluidic arrays using microvalves. *Small*, 1602601 (Dec. 2016).
241. Panacol-Elosol GmbH. *Technical Datasheet Vitralit® 1655*. Tech. rep. (2017).
242. Zhang, Z., Zhao, P., Xiao, G., Watts, B. R. & Xu, C. Sealing SU-8 microfluidic channels using PDMS. *Biomicrofluidics* **5**, 46503–465038 (Dec. 2011).
243. Watts, B. R. *et al.* Fabrication and performance of a photonic-microfluidic integrated device. *Micromachines* **3**, 62–77 (Feb. 2012).
244. Raider, S. I., Flitsch, R., Aboaf, J. A. & Pliskin, W. A. Surface oxidation of silicon nitride films. *J. Electrochem. Soc.* **123**, 560 (1976).
245. Acres, R. G. *et al.* Molecular structure of 3-aminopropyltriethoxysilane layers formed on silanol-terminated silicon surfaces. *J. Phys. Chem. C* **116**, 6289–6297 (Mar. 2012).
246. Hamlett, C. A. *et al.* Vapour phase formation of amino functionalised Si₃N₄ surfaces. *Surf. Sci.* **602**, 2724–2733 (Aug. 2008).
247. Vandenberg, E. T. *et al.* Structure of 3-aminopropyl triethoxy silane on silicon oxide. *J. Colloid Interface Sci.* **147**, 103–118 (1991).
248. Temiz, Y., Lovchik, R. D., Kaigala, G. V. & Delamarche, E. Lab-on-a-chip devices: How to close and plug the lab? *Microelectron. Eng.* **132**, 156–175 (2015).
249. Wagler, P. F., Tangen, U., Ott, J. & McCaskill, J. S. General-purpose, parallel and reversible microfluidic interconnects. *IEEE Trans. Components, Packag. Manuf. Technol.* **5**, 291–300 (2015).
250. Scott, A., Au, A. K., Vinckenbosch, E. & Folch, A. A microfluidic D-subminiature connector. *Lab Chip* **13**, 2036–9 (June 2013).
251. Madsen, M. H., Feidenhans'l, N. A., Hansen, P.-E., Garnæs, J. & Dirscherl, K. Accounting for PDMS shrinkage when replicating structures. *J. Micromech. Microeng.* **24**, 127002 (2014).
252. Morel, M., Bartolo, D., Galas, J.-C., Dahan, M. & Studer, V. Microfluidic stickers for cell- and tissue-based assays in microchannels. *Lab Chip* **9**, 1011–1013 (2009).

253. Panacol-Elosol GmbH. *Technical Datasheet Vitralit® 6108*. Tech. rep. (2017).
254. Lu, C., Lee, L. J. & Juang, Y. J. [Packaging of microfluidic chips via interstitial bonding technique](#). *Electrophoresis* **29**, 1407–1414 (2008).
255. Azizi, F., Lu, H., Chiel, H. J. & Mastrangelo, C. H. [Chemical neurostimulation using pulse code modulation \(PCM\) microfluidic chips](#). *J. Neurosci. Methods* **192**, 193–8 (Oct. 2010).
256. Potter, S. M. & DeMarse, T. B. [A new approach to neural cell culture for long-term studies](#). *J. Neurosci. Methods* **110**, 17–24 (2001).
257. Yusko, E. C. *et al.* [Controlling protein translocation through nanopores with bio-inspired fluid walls](#). *Nat. Nanotechnol.* **6**, 253–260 (2011).
258. [NMEM-B27 Transfection medium \(pH 7.4\)](#). *Cold Spring Harb. Protoc.* **2006**, pdb.rec10321 (June 2006).
259. Stutzki, H., Leibig, C., Andreadaki, A., Fischer, D. & Zeck, G. [Inflammatory stimulation preserves physiological properties of retinal ganglion cells after optic nerve injury](#). *Front. Cell. Neurosci.* **8**, 38 (2014).
260. Lepoitevin, M. *et al.* [Fast and reversible functionalization of a single nanopore based on layer-by-layer polyelectrolyte self-assembly for tuning current rectification and designing sensors](#). *RSC Adv.* **6**, 32228–32233 (2016).
261. Grieshaber, P., Lagrèze, W. A., Noack, C., Boehringer, D. & Biermann, J. [Staining of fluorogold-prelabeled retinal ganglion cells with calcein-AM: A new method for assessing cell vitality](#). *J. Neurosci. Methods* **192**, 233–239 (Oct. 2010).
262. Gan, W. B., Bishop, D. L., Turney, S. G. & Lichtman, J. W. [Vital imaging and ultrastructural analysis of individual axon terminals labeled by iontophoretic application of lipophilic dye](#). *J. Neurosci. Methods* **93**, 13–20 (1999).
263. Yu, Z. W. & Quinn, P. J. [The modulation of membrane structure and stability by dimethyl sulphoxide \(review\)](#). *Mol. Membr. Biol.* **15**, 59–68 (1998).
264. Evans, R. *et al.* [Quantitative interpretation of diffusion-ordered NMR spectra: Can we rationalize small molecule diffusion coefficients?](#) *Angew. Chemie - Int. Ed.* **52**, 3199–3202 (2013).
265. Krumpfer, J. W. & McCarthy, T. J. [Rediscovering silicones: "unreactive" silicones react with inorganic surfaces](#). *Langmuir* **27**, 11514–11519 (2011).
266. Wang, L. & McCarthy, T. J. [Covalently attached liquids: instant omniphobic surfaces with unprecedented repellency](#). *Angew. Chemie Int. Ed.* **55**, 244–248 (Jan. 2016).
267. Martin, F. *et al.* [Tailoring width of microfabricated nanochannels to solute size can be used to control diffusion kinetics](#). *J. Control. Release* **102**, 123–33 (Jan. 2005).
268. Acharya, S. *et al.* [Self-limiting atomic layer deposition of barium oxide and barium titanate thin films using a novel pyrrole based precursor](#). *J. Mater. Chem. C* **4**, 1945–1952 (2016).
269. Macpherson, J. V. [A practical guide to using boron doped diamond in electrochemical research](#). *Phys. Chem. Chem. Phys.* **17**, 2935–2949 (2015).
270. Guan, B., Zhi, J., Zhang, X., Murakami, T. & Fujishima, A. [Electrochemical route for fluorinated modification of boron-doped diamond surface with perfluorooctanoic acid](#). *Electrochem. Commun.* **9**, 2817–2821 (2007).
271. Nakashima, Y. & Yasuda, T. [Cell differentiation guidance using chemical stimulation controlled by a microfluidic device](#). *Sensors Actuators A Phys.* **139**, 252–258 (Sept. 2007).
272. Liu, Y. *et al.* [Visualization of diffusion within nanoarrays](#). *Anal. Chem.* **88**, 6689–6695 (July 2016).
273. Azimi, G., Dhiman, R., Kwon, H.-M., Paxson, A. T. & Varanasi, K. K. [Hydrophobicity of rare-earth oxide ceramics](#). *Nat. Mater.* **12**, 315–20 (2013).
274. Niedzwiecki, D. J. & Movileanu, L. [Monitoring protein adsorption with solid-state nanopores](#). *J. Vis. Exp.* 1–9 (Jan. 2011).

275. Hou, X., Hu, Y., Grinthal, A., Khan, M. & Aizenberg, J. [Liquid-based gating mechanism with tunable multiphase selectivity and antifouling behaviour](#). *Nature* **519**, 70–73 (2015).
276. Hassler, C., Boretius, T. & Stieglitz, T. [Polymers for neural implants](#). *J. Polym. Sci. Part B Polym. Phys.* **49**, 18–33 (2011).
277. Liu, J. *et al.* [Syringe-injectable electronics](#). *Nat. Nanotechnol.* **10**, 629–636 (2015).
278. Dalva, M. B., McClelland, A. C. & Kayser, M. S. [Cell adhesion molecules: signalling functions at the synapse](#). *Nat. Rev. Neurosci.* **8**, 206–220 (2007).
279. Hunter, J. D. [Matplotlib: A 2D graphics environment](#). *Comput. Sci. Eng.* **9**, 99–104 (2007).
280. Matplotlib Developers. [matplotlib: v1.5.3](#). 2016.

About the author

Peter D. Jones studied nanotechnology engineering at the University of Waterloo, Canada, obtaining his Bachelor of Applied Science with Distinction in Honours Nanotechnology Engineering in 2011. During his studies, he explored diverse research fields as a research assistant at the TRIUMF particle physics laboratory in Vancouver, at Sunnybrook Hospital in Toronto, at the Centre for Theoretical Neuroscience in Waterloo, and studying semiconductor materials with Prof. Thorsten Hesjedal and Prof. Pavle Radovanovic at the University of Waterloo.

In January 2012, Peter joined the BioMEMS & Sensors group of Dr. Martin Stelzle at the Natural and Medical Sciences Institute (NMI) at the University of Tübingen in Reutlingen, Germany. His doctoral studies were cosupervised by Prof. Dr. Dieter P. Kern at the University of Tübingen. His project to develop nanofluidic technology for chemical neurostimulation began as part of the NAMASEN Marie Curie Initial Training Network, supported by the 7th Framework Programme of the European Commission, and continued with the support of the “Experiment!” program of the Volkswagen Foundation. Since completing the research presented in this dissertation, he has continued developing biomedical technology as part of NMI TT GmbH and the Microsystems & Nanotechnology group of Dr. Claus Burkhardt.

Scientific works related to this dissertation are listed below.

Journal articles

Jones, P. D. & Stelzle, M. [Can nanofluidic chemical release enable fast, high resolution neurotransmitter-based neurostimulation?](#) *Front. Neurosci.* **10** (Mar. 2016)

Conference contributions

- 10/2015 **Neuroscience** (Chicago, USA)
“Artificial synapse chip: A nanopore array for local chemical modulation of neuronal activity” (poster)
- 07/2014 **International Meeting on Substrate-Integrated Microelectrode Arrays** (Reutlingen, Germany)
“Towards local chemical stimulation through a nanopore array on a microelectrode array” (poster)
- 05/2014 **International Conference on Micro & Nanofluidics** (Enschede, the Netherlands)
“Controlled release through gated nanopores integrated with microfluidics on a microelectrode array, towards chemical stimulation of cells” (poster)
- 10/2013 **Mikrosystemtechnik Kongress** (Aachen, Germany)
“Nanofluidic gates for diffusion-free controlled release from microfluidic devices” (poster)
- 09/2013 **International Conference on Micro and Nano Engineering** (London, UK)
“Hydrophobic gating of artificial nanopores for diffusion-free fluidic valves” (poster)